Chemical Bonding and Catalysis

Molecular Orbital Perspectives on Catalyst Design and Halogen Bonds

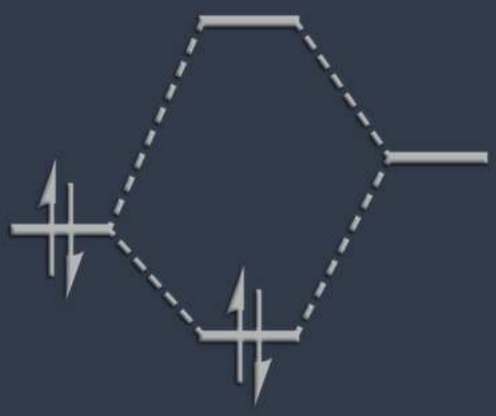

Lando P. Wolters

VRIJE UNIVERSITEIT

Chemical Bonding and Catalysis

Molecular Orbital Perspectives on Catalyst Design and Halogen Bonds

ACADEMISCH PROEFSCHRIFT

ter verkrijging van de graad Doctor aan
de Vrije Universiteit Amsterdam,
op gezag van de rector magnificus
prof.dr. V. Subramaniam,
in het openbaar te verdedigen
ten overstaan van de promotiecommissie
van de Faculteit der Exacte Wetenschappen
op dinsdag 22 maart 2016 om 13.45 uur
in de aula van de universiteit,
De Boelelaan 1105

door

Lando Peter Wolters

geboren te Zaanstad

promotor: prof.dr. F.M. Bickelhaupt

Chemical Bonding and Catalysis

Molecular Orbital Perspectives on Catalyst Design and Halogen Bonds

Lando Peter Wolters

This work has been financially supported by the National Research School Combination – Catalysis (NRSC-C) and the Netherlands Organization for Scientific Research (NWO).

Chemical Bonding and Catalysis
Molecular Orbital Perspectives on Catalyst Design and Halogen Bonds
Lando P. Wolters
ISBN: 978-90-6464-975-2
2015

Apophenia

The experience of seeing meaningful patterns in random data.

Contents

1 Introduction **11**

1.1 Theoretical Chemistry 11
1.2 Oxidative Addition 12
1.3 Hydrogen Bonds and Halogen Bonds 15

2 Theories, Models and Methods **23**

2.1 Semantics 23
2.2 Quantum Chemistry 24
2.3 Density Functional Theory 25
2.4 Computational Details 27
2.5 Activation Strain Model of Chemical Reactivity 30
2.6 Molecular Orbital Theory & Interaction Energy Decomposition 33

3 Nonlinear d^{10}-ML_2 Complexes **39**

3.1 Introduction 39
3.2 Structures and Energetics 40
3.3 General Bonding Mechanism 44
3.4 Bonding Mechanism: Variation of Ligands 46
3.5 Bonding Mechanism: Variation of Metals 49
3.6 Walsh Diagrams 51
3.7 Conclusions 53

4 Steric Attraction and Steric Repulsion: The Effect of Bulky Ligands **57**

4.1 Introduction 57
4.2 $Pd(PR_3)_2$ Geometries and Pd–PR_3 Bond Analyses 59
4.3 The Effect of Steric Attraction on Oxidative Addition 65
4.4 Conclusions 70

5 Electronic and Steric Effects on Bite-Angle Flexibility and Nonlinearity 73
5.1 Introduction 73
5.2 $Pd(PX_3)_2$ Geometries and Pd–PX_3 Bond Analyses 74
5.3 Reactivity of $Pd(PX_3)_2$ Towards the Methane C–H Bond 77
5.4 Conclusions 81

6 New Design Concepts for d^{10}-ML_n Catalysts 83
6.1 Introduction 83
6.2 General Reaction Profiles and Exceptions 85
6.3 Metal Variation from Group 9 to Group 11 88
6.4 Metal Variation from Row 1 to Row 3 92
6.5 Variation from σ-Donating to π-Accepting Ligands 94
6.6 Alternative Reaction Pathways for $M(NH_3)_2$ Catalysts 96
6.7 Catalyst Design Principles: d Regime versus s Regime 98
6.8 Conclusions 102

7 Rational Catalyst Design: Selective C–H and C–C Bond Activation 105
7.1 Introduction 105
7.2 General Energy Profiles for Ethane C–H and C–C Activation 106
7.3 Trends in Reaction Barriers for Ethane C–H Activation 110
7.4 Trends in Reaction Barriers for Ethane C–C Activation 113
7.5 Selective C–C or C–H Bond Activation 115
7.6 Selective Methane C–H versus Ethane C–H Bond Activation 118
7.7 Ethane C–C Activation via Ethane C–H Activation 120
7.8 Conclusions 122

8 Halogen Bonding versus Hydrogen Bonding: A Molecular Orbital Perspective 125
8.1 Introduction 125
8.2 Hydrogen Bonds: Strength and Structure 126
8.3 Halogen Bonds: Strength and Structure 128
8.4 Bond Analyses: Variation of the Accepting Halide 130
8.5 Bond Analyses: Variation of the Donating Group 135
8.6 Bond Analyses: Variation of the Central Atom 137
8.7 Conclusions 139

9 Resonance Assistance and Cooperativity in Halogen-Bonded Complexes 143
9.1 Introduction 143
9.2 Bond Analyses: B-DNA Base Pairs 145
9.3 Bond Analyses: G-DNA Quadruplexes 147
9.4 The Origin of Cooperativity in G_4 and X-G_4 Quartets 151
9.5 Conclusions 158

10 Summary **161**

11 Samenvatting **169**

12 References **177**

13 Acknowledgements **189**

14 List of Publications **191**

1 Introduction

Parts of this chapter previously appeared as

Activation Strain Model & Molecular Orbital Theory
L. P. Wolters, F. M. Bickelhaupt
WIREs Comput. Mol. Sci. **2015**, *5*, 324–343

The Many Faces of Halogen Bonding: A Review of Theoretical Models and Methods
L. P. Wolters, P. Schyman, M. J. Pavan, W. L. Jorgensen, F. M. Bickelhaupt, S. Kozuch
WIREs Comput. Mol. Sci. **2014**, *4*, 523–540

1.1 Theoretical Chemistry

Chemistry is, roughly speaking, the branch of the natural sciences investigating the properties, composition and transformation of matter. Within theoretical chemistry, this is done not by observation, but by a mathematical description of the physical system of interest. The field is also referred to as 'quantum chemistry' or 'computational chemistry', because often the descriptions are derived from quantum mechanics, and a large amount of computer power is required to solve the complicated equations. The constant improvement in the quality of mathematical descriptions, combined with the enormous advancement of computer technology in the past decades, has allowed the field of theoretical chemistry to advance as well. Nowadays, it is feasible to computationally study a large variety of molecular systems and chemical processes with, for many purposes, sufficient accuracy.

Although some of the romance of doing practical experiments is lost, theoretical chemistry opens up a whole new world of research by eliminating many practical limitations. Theoreticians can, for example, safely study explosives, recklessly experiment on expensive materials, investigate processes on timescales too short to be measured, or too long

to be observed, or obtain insight into interstellar processes from a comfortable office chair. Theoretical models can also be helpful to gain insight into a synthetically useful chemical reaction that, however, does not occur, and therefore cannot be studied experimentally. Such a process can be studied *in silico* to reveal the reasons why it is not viable, and what can be done to change this situation for the better.

Moreover, one can achieve a fundamental understanding of a certain chemical aspect based on the theoretical description itself. Whereas many experimental studies are only descriptive of a phenomenon, theoretical sciences can go one step further and often provide an explanation, and thereby understanding, of the phenomenon. Within this thesis, such an understanding is sought for several aspects of the oxidative addition reaction, as well as for the mechanism of halogen bonding interactions. Both phenomena involve the stretching, and eventually breaking, of a chemical bond, and involve charge transfer from one molecular moiety to another.

1.2 Oxidative Addition

Catalysis is typically described as increasing the rate of a chemical reaction due to the participation of an additional substance, without changing its outcome. The additional substance then acts as a catalyst, and must not be consumed in the process. The increased rate of the chemical reaction is achieved by lowering its activation energy: the minimum energy needed for a chemical reaction to occur. Thus, catalysis can lead to significant energy savings. Besides, when the rate of the desired reaction is enhanced compared to that of an unwanted side reaction, catalysis can lead to significant waste reduction. In an era of growing human energy demands and environmental concern, the importance of catalysis is therefore evident.

An important class of chemical reactions involving catalysis is that of coupling reactions.[1-22] These reactions are carried out to form carbon-carbon bonds, which are the basis of organic molecules, and thereby the very basis of the chemistry of life itself. In these reactions, often a homogeneous catalyst is used, meaning that the catalyst is codissolved in a solvent with the reactants. Figure 1.1 shows a schematic representation of a generic catalytic cycle for a coupling reaction catalyzed by a transition metal complex ML_n. More specifically, the scheme features an example of a cross-coupling reaction, since the coupling partners in this case are not identical.

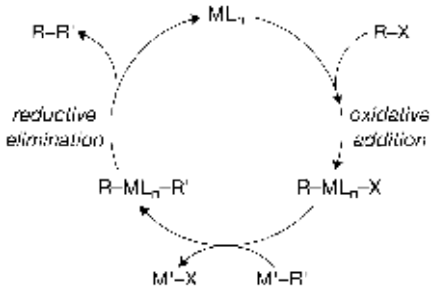

Figure 1.1 General catalytic cycle for a metal-catalyzed cross coupling.

The first step in many coupling reactions is the oxidative addition of a substrate RX to the metal center of a catalyst, thereby breaking the R–X bond, while simultaneously forming new M–R and M–X bonds. In subsequent steps X is replaced by R', and by reductive elimination, which is the reverse reaction of oxidative addition, the product RR' is obtained, and the catalyst ML_n recovered.

The oxidative addition step is of crucial importance for both the efficiency and selectivity of the process, and also plays a role in, for example, hydroformylations, hydrogenations and [2+2+2] cyclotrimerizations.[2] This reaction step has therefore been studied extensively using experimental,[9,13,23-31] as well as theoretical techniques.[7,8,32-35] The catalysts used in practice are typically based on a late transition metal, such as palladium, to which ligands are attached. The activity of the catalyst complex depends on the electronic nature of the metal center, which is affected by the number and type of ligands, as well as the structural properties of the catalytic complex.[36-48] Of these structural parameters, the bite angle, that is, the ligand-metal-ligand angle, is probably the most notable parameter that is adjusted in attempts to achieve the desired reactivity.[49-56]

Besides these examples, there are several other parameters that influence the characteristics of a catalytic complex. Therefore, the reactivity of a catalyst is, unfortunately, difficult to predict, and selecting a catalyst is still too often a process of trial-and-error. Theoretical chemistry can play an important role in facilitating this selection process, because it allows systematic variation of one parameter at a time, under strictly controlled conditions and without any experimental limitation. Simultaneously, the added benefit of available analysis tools allows for an explanation of the observed effects and eventually their interplay. A significant part of this thesis is therefore dedicated to the oxidative addition reaction and the role of the catalyst. It is part of an extensive research line, which aims at

achieving a fundamental understanding of the reactivity of catalyst complexes in the activation of different target bonds. This strategy of gradually building up insight into catalytic activity, starting from detailed studies on the effect of one variation in small model systems and eventually proceeding towards combinations of several effects in more realistic, larger systems, has been termed 'Fragment-oriented Design of Catalysts'.[57-60] Its aim is to allow chemists in the future to rationally design catalysts with the desired selectivity and optimized efficiency.

The purpose of several of the following chapters is to explain how reaction barriers and reaction energies change when certain aspects of the catalysts are modified in a systematic manner. To explain the observed effects, the bonding mechanism between molecular fragments had to be further elucidated, in order to obtain a better understanding of the intrinsic structural properties of the catalyst complex. Thus, in chapter 3, the geometries of a number of dicoordinated d^{10}-ML_2 complexes are investigated. The metal center M is varied along the metals from group 9, 10 and 11 from the first three transition metal rows of the periodic table, that is, Co^-, Rh^-, Ir^-, Ni, Pd, Pt, Cu^+, Ag^+ and Au^+. The ligands are varied along NH_3 (a strong σ donor), PH_3 (a σ donor and π acceptor) and CO (a strong π acceptor). Although such d^{10}-ML_2 complexes are generally assumed to have linear ligand-metal-ligand angles, this chapter describes a variety of ML_2 complexes with significantly smaller angles, and, by careful studies on the bonding mechanism of the metal-ligand bonds, the origin of this nonlinearity is uncovered. It is shown that steric effects favor a linear ligand-metal-ligand angle, but that π-backbonding interactions favor nonlinear geometries. When the latter are sufficiently strong, d^{10}-ML_2 complexes can become bent. Chapters 4 and 5 elaborate on these findings by including more bulky ligands, namely the series PH_3, PMe_3, $PiPr_3$, $PtBu_3$, PCy_3 and PPh_3, and the series along PF_3, PCl_3, PBr_3 and PI_3. These chapters provide insights into how to achieve a nonlinear ligand-metal-ligand angle and how to adjust this bite angle via both electronic, as well as steric mechanisms. These chapters also include a brief discussion on the consequences of this nonlinearity for the reactivity of the catalyst complexes in oxidative addition reactions.

Chapter 6 then discusses how the reaction barrier for oxidative addition of the methane C–H bond is affected by the nature of the metal center and the presence of different types of ligands. To this end, a large and consistent set of 72 model reactions is studied. Based on the results, combined with those of the preceding chapters, new light is shed on the nature of the bite angle in oxidative addition reactions. Interestingly, it is not the value of the bite angle itself that is important, but rather the flexibility of the catalyst towards

assuming a nonlinear ligand-metal-ligand angle during the bond activation process. Furthermore, the results show that the choice of metal and ligands not only determines the bite-angle flexibility, but also the catalyst's binding capability towards the substrate. The concepts of the d regime and the s regime of catalysts are introduced. In the former, the primary mode of catalyst-substrate interaction is electron donation from the catalyst's d hybrid orbitals to the σ* acceptor orbital of the substrate, whereas in the latter the catalyst's s hybrid orbital acts as an acceptor for electrons donated from the σ orbital of the substrate. The results indicate that ligands affect the electronic nature of the catalyst similarly within each regime. Importantly, however, since the catalyst takes opposite roles in the dominating donor-acceptor interactions present in these regimes, the effect of ligands on the reaction barrier can be reversed when switching between d-regime and s-regime catalysts. Altogether, the results reveal causal relationships between oxidative addition reaction barriers and the orbital-electronic and structural properties of the catalyst complex.

In chapter 7 the oxidative addition of the ethane C–H and C–C bonds is studied, using the same large and consistent set of catalyst complexes. The concepts introduced in chapter 6 are validated, but, more importantly, also subtle differences are revealed between the ethane C–H and C–C bond, as well as between the methane and ethane C–H bonds. Based on a careful understanding of the differences between these bonds and by applying the previously introduced design principles, catalyst complexes are devised that allow selective activation of each of these bonds.

Although there are several important new insights discussed in these chapters, additional studies will be required for the actual optimization of a catalyst for a specific process. This is only in part because there are still many more possible combinations of metal centers and ligands that can be included, as well as a plethora of variations of the substrate, and also the effects of different reaction conditions and possible side reactions. Note, however, that one should not only consider the reaction step in which the overall reaction barrier occurs, but also take into account the stability of intermediate species that occur during the catalytic cycle. For kinetic assessments of catalytic cycles, which is not pursued in this thesis, the energetic span model has been developed.[44,61-63]

1.3 Hydrogen Bonds and Halogen Bonds

Hydrogen bonds are one of the most important intermolecular interactions known.[64,65] Being responsible for unique features of water, as well as playing a key role in the structure

of DNA and its replication, the importance of hydrogen bonds for human life can hardly be overestimated. A hydrogen bond, DH···A, is a bonding interaction that typically occurs between a hydrogen, H, bound to an electronegative atom D, such as nitrogen, oxygen, or a halogen atom, and a second electronegative atom A. Of course, D and A can be part of a larger molecular structure, as for example in the Watson-Crick base pairs in DNA. In a hydrogen-bonded molecular moiety, some of the electron density around hydrogen will be shifted towards the electronegative atom D, leading to a partial positive charge δ^+ located on the hydrogen atom. Based on this feature, hydrogen bonds are often considered to arise due to the electrostatic attraction that occurs between this partial positive charge on the hydrogen, and the partial negative charge δ^- on the electronegative atom A (see Figure 1.2a). It should be noted, however, that although the electrostatic component of the bonding interaction is important, it has been shown that a description based on merely Coulomb attraction is incomplete.[66]

In analogy to the hydrogen bond in DH···A, a halogen bond can occur in DX···A, where the hydrogen atom H is replaced by a halogen atom X. Halogen bonds are known for already more than 150 years,[67] and nowadays receive interest from chemists working in various fields,[68,69] such as supramolecular chemistry,[70-77] and biochemistry.[78-83] Often it is found that halogen bonds can, both in terms of practical applications and bond strength, compete with hydrogen bonds.[84-92] This has led to a comparison of the nature of their bonding mechanism, but applying a similar explanation based on electrostatics to halogen bonds makes little sense, as a partial positive charge would then be assigned to the central halogen X. This directly opposes chemical intuition, since halogens are well known to be electronegative elements.

However, experimental studies[85,93-95] on intermolecular interactions involving halogen atoms suggest that the electron density around a covalently bound halogen is not isotropic, but, in fact, oblate: it is slightly flattened along the extension of the D–X bond. Around the halogen atom X, the electrostatic potential therefore often shows a region of positive sign at this flattened area, meaning that a negative point charge at that location would experience net Coulomb attraction in the direction of the nuclei of the X atom.[96] Based on this finding, the region of positive electrostatic potential, termed the σ-hole,[97] has been put forward as an explanation of the halogen bond, similar to the hydrogen bond, in electrostatic terms, as shown schematically in Figure 1.2.

Interestingly, there is indeed often a correlation between the magnitude of the σ-hole and the strength of the halogen bond, as well as between the location of the σ-hole and the

directionality of the halogen bond. Carefully conducted numerical control experiments, however, demonstrated a number of failures of the σ-hole description. It has been shown that, when the D–X···A angle in the halogen-bonded compound is bent around the central X, the electrostatic attraction often increases in strength, despite the fact that the electronegative A is no longer facing the σ-hole. Thus, the directionality of the halogen bond is a result of minimizing repulsive interactions, and is not related to the electrostatic interactions with the σ-hole.[98-100] Furthermore, there are documented examples of series of halogen-bonded compounds with increasingly strong interaction energies and electrostatic attraction, even though the maximum potential at the position of the σ-hole becomes less positive.[101] Taking into account a polarization-induced strengthening of the σ-hole[102] does not resolve the discrepancy.

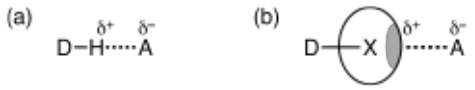

Figure 1.2 Schematic depiction of (a) a hydrogen bond DH···A with partial charges indicated, and (b) an analogous halogen bond DX···A showing the anisotropic charge density around the halogen atom X which gives rise to a region of positive electrostatic potential, indicated by the shaded area.

The σ-hole description fails primarily because the molecular electrostatic potential on an isodensity surface of the DX fragment reveals the Coulomb interaction with a point charge, while, on the scale of atoms, the properties of fragment A are significantly different from those of a point charge: it has a three dimensional, diffuse electron density extending in all directions in space. The shortcomings of a description in which both fragments are perceived as point charges (Coulomb attraction between partial atomic charges) can not be completely resolved by treating one fragment as a three dimensional structure, while still treating the other one as a point charge, as is done in the σ-hole model. Ironically, however, the erroneous conceptual reduction of atoms to point charges is sometimes presented as an argument in favor of a description based on the molecular electrostatic potential![103] Furthermore, descriptions using the molecular electrostatic potential neglect the overlap of the wavefunctions of the interacting fragments. The interactions are not only electrostatic in nature: quantum mechanical effects and properties have to be considered as well.

Proponents of the σ-hole hypothesis have argued in favor of a simplified description of the bonding mechanism, limited to mainly electrostatics (with some contributions from

polarization and dispersion[104]), and to omit the contribution of charge transfer, because it is hard to make a physical distinction between charge transfer and polarization. Also, it has been argued that, ultimately, the two are the same, because they can both be described by overlapping an occupied orbital with an unoccupied one.[105] The two arguments are not particularly strong. Indeed, it is true that the boundary between charge transfer and polarization is not easy to define, but this might also be perceived as an argument to abandon this dichotomous view, and to consider the terms as describing two parts of a continuous spectrum. Furthermore, within a fragment-based description, which is not an unreasonable starting point to describe the bonding between molecular moieties, these terms refer to two effects that can be separated conceptually: polarization can be regarded as the reorganization of the density of one fragment due to the electric field induced by the presence of the other fragment, whereas charge transfer is used to indicate a net depletion of density on one fragment, because part of its density is transferred to the other fragment. Still, this does not mean that the two effects can be rigorously separated and their individual importance can be uniquely quantified (which is therefore also not attempted in many energy decomposition schemes, such as the EDA method applied throughout this thesis and discussed in section 2.6). However, this also does not constitute a valid reason to leave charge transfer out of the description of the bonding mechanism, and most certainly not when the purpose of this omission is to reduce the description to one that is based on misleading, and conceptually flawed molecular electrostatic potential plots.

In a number of instances, also the principle of Occam's razor (also known as Ockham's razor, or *lex parsimoniae* in Latin) has been inferred as an argument to limit the description of halogen bonds to mainly electrostatics.[105] Sometimes, this argument is accompanied by an appeal to authority, quoting J. W. Gibbs: "*One of the principal objects of theoretical research in any department of knowledge is to find the point of view from which the subject appears in its greatest simplicity*".[104,105] However, to state that Occam's razor dictates that the most simple explanation should be preferred, is a misrepresentation of this important principle. Modern-day science philosophers more commonly interpret the principle as stating that, out of several competing possible explanations, the one that introduces the fewest new assumptions should be preferred. But, most importantly, this principle only applies after the first selection procedure, which is the assessment of (i) the agreement between the description and empirical data, and (ii) the quality of the predictions that are made using the model. Therefore, it seems unlikely that Gibbs would have advocated a literal interpretation of his cited quote. A more suitable, but of course equally fallacious

appeal to authority, would be "*Everything should be kept as simple as possible, but no simpler*", which is commonly attributed to Albert Einstein, although its origin has never been verified.

Although the mechanism of halogen bonds (and probably many other chemical interactions) cannot be accurately described by molecular electrostatic potential plots, investigating these plots has nevertheless led to the improvement of force fields to describe halogen bonding interactions with classical molecular mechanics (MM) methods.[106-109] These methods are unable to account for the quantum chemical effects that play such an important role in halogen bonds. By adding a virtual particle with a partial positive charge within the Van der Waals region of the halogen atom to mimic the σ-hole, some of the stabilization due to quantum chemical effects (charge transfer) can be recovered by the induced additional electrostatic interactions.

To obtain not only a truly satisfying level of understanding for these interactions, but also to consolidate the physical description with results obtained by studies on other subjects in chemistry, many studies have been performed to unravel the nature of hydrogen bonds,[110-117] and halogen bonds.[84,86,99-101,118-127] A number of studies directly compared the two interactions.[85,90-92,128-131] In chapter 8 a detailed comparison of the bonding mechanisms of both halogen bonds and hydrogen bonds is presented in terms of molecular orbital theory. To this end, a range of strongly halogen-bonded trihalides $DX\cdots A^-$ and analogous strongly hydrogen-bonded hydrogen bihalides $DH\cdots A^-$ (with D, X and A being one of the halogens F, Cl, Br or I) is subjected to extensive computational analyses. Through a variety of analysis tools, it is shown that both bonding interactions can be explained at a satisfactory level with molecular orbital theory: both types of bonds arise because of significant donor-acceptor orbital interactions, which occur on top of electrostatic interactions.

Chapter 9 demonstrates the similarities between hydrogen bonds and halogen bonds even further. Earlier work already provided a detailed description of the hydrogen bonds in Watson-Crick base pairs in terms of molecular orbital theory.[114,132,133] More recently, also the cooperative effect observed in guanine quartets has been elegantly explained.[115] Guanine quartets consist of four essentially coplanar guanine bases that interact via hydrogen bonds in a circular pattern. These quartets occur in the telomeric part of the chromosome and play a crucial role in protecting the genetic code. It is known that the total bonding energy of such guanine quartets is more strongly stabilizing than four times the hydrogen bond energy of one pair of guanine bases. Within this chapter, it is investigated whether these characteristics are retained when the hydrogen bonds in the naturally occurring hy-

drogen-bonded base pairs and quartets are replaced by halogen bonds. The resulting halogen-bonded *N*-halo-base pairs and *N*-halo-guanine quartets are found to indeed possess the same characteristics, again indicating that hydrogen bonds and halogen bonds are similar in nature. Moreover, these results provide evidence that the physical description given in chapter 8 is equally valid for more realistic, and more weakly interacting complexes, and that a description in purely electrostatic terms is insufficient.

2 Theories, Models and Methods

Parts of this chapter previously appeared as

Activation Strain Model & Molecular Orbital Theory
L. P. Wolters, F. M. Bickelhaupt
WIREs Comput. Mol. Sci. **2015**, *5*, 324–343

2.1 Semantics

The terms 'theory' and 'model' are regularly used throughout this thesis. Before proceeding with a more detailed discussion of the specific theories and models applied in this work, it is therefore appropriate to give some attention to the meaning of these terms, as this is often a source of confusion. The purpose of this brief section is not to provide a thorough and definitive view on theories and models and their application within the scientific method. Instead, it is meant as a word of caution, that should be in the back of one's mind when reading the brief explanation of the theories and models as applied within this thesis, and especially when discussing the interpretation of data in the following chapters.

Probably the most common example of misunderstanding the scientific term 'theory' is a creationist pointing out that "*the biological theory of evolution is just a theory*". This is a non-sensical statement, because it fallaciously equivocates on two different (in fact, almost opposite) meanings of the term 'theory'. In this argument the term is used in its colloquial sense, which in the Oxford English Dictionary is described as "*a hypothesis proposed as an explanation; hence, a mere hypothesis, speculation, conjecture; an idea or set of ideas about something; an individual view or notion*".[134] But in the case of the 'theory of evolution', the term refers to a scientific theory, which is aptly described by the American Association for the Advancement of Science as "*a well-substantiated explanation of some aspect of the natural world, based on a body of facts that have been repeatedly confirmed through observation and ex-*

periment".[135] A creationist might argue that this latter definition does not apply to evolution, but, apart from being factually wrong, that is not the point the initial statement was intended to make.

The results within this thesis are largely obtained using density functional theory. Density functional theory itself does not directly explain anything, and therefore does not fit any of the definitions given above. Instead, 'theory' here refers to a mathematical framework, derived from a set of postulates, which is intended to make predictions of physical results. In the case of density functional theory, it aims at reproducing the exact electronic density of a molecular fragment, from which physical properties of the fragment can be derived.

Within the scientific community, most of the discussions result not from this ambiguity of the word 'theory', but because of different views on the applied models. Models are used to interpret the data obtained from, for example, density functional theory. A model, within scientific context, is "*a simplified or idealized description of a particular system, situation, or process, often in mathematical terms, that is put forward as a basis for theoretical or empirical understanding*".[136] Within the field of theoretical chemistry, there are many discussions centered around the use of models. Given that a model is an idealized, often simplified description, and therefore inherently false, it should be judged on the basis of its usefulness: the quality of its predictions, general applicability, ease of understanding, etc. Interestingly, however, many of these discussions focus on the truth of particular individual components of a model, such as the different energy components in the interaction energy decomposition scheme discussed in section 2.6. It is therefore often not the model itself that is causing the debate, but rather the overinterpretation of its results.

2.2 Quantum Chemistry

The goal of quantum chemistry is to obtain insight into a molecular system by solving the Schrödinger equation,[137] which in the non-relativistic, time-independent form is[138-140]

$$H\Psi = E\Psi \,. \tag{2.1}$$

In this equation, the Hamiltonian operator H represents the total energy of a system of atomic nuclei and electrons, of which the quantum mechanical motions are described by the wavefunction Ψ. The Hamiltonian includes terms for the kinetic energy of all nuclei N (T_N) and electrons e (T_e), as well as potential energy terms to describe the electrostatic at-

traction between nuclei and electrons (V_{Ne}), and the repulsive nucleus-nucleus (V_{NN}) and electron-electron interactions (V_{ee}):

$$H = T_N + T_e + V_{NN} + V_{Ne} + V_{ee} \,. \tag{2.2}$$

According to the postulates of quantum mechanics, the wavefunction Ψ contains all information about the state of the system it describes. Unfortunately, this equation can only be solved exactly for one-electron atoms. Most chemical problems, of course, involve many more atoms and electrons, and require approximations to obtain solutions. The most regularly applied approximation is the Born-Oppenheimer approximation, which is based on the significant mass difference between the nuclei and electrons (the mass of a proton is roughly 1800 times that of an electron). Thus, the nuclei move much slower than electrons, and the electrons are therefore assumed to move around fixed nuclei. Effectively, the kinetic energy of the nuclei is then zero, the nucleus-nucleus repulsion is reduced to a constant, and the electrons experience a fixed potential from the positively charged nuclei. The Hamiltonian in Equation 2.2 then reduces to the electronic Hamiltonian H_{elec}, working on the electronic wavefunction Ψ_{elec}:

$$H_{elec}\Psi_{elec} = (T_e + V_{Ne} + V_{ee})\Psi_{elec} \,. \tag{2.3}$$

The electronic wavefunction Ψ_{elec} is usually approximated as an antisymmetric product of one-electron wavefunctions, such as in the Hartree-Fock scheme. Using this scheme, it is possible to recover roughly 99% of the total energy of the molecular system. Most importantly, it is missing a large part of V_{ee} because the correlation of the movements of electrons is not completely accounted for. Unfortunately, total energies are large quantities and chemists are generally interested in energy changes that are of the order of magnitude of the remaining 1%, or even smaller. More elaborate schemes, such as the configuration interaction (CI) method, or the coupled cluster (CC) method, are based on similar principles as Hartree-Fock, but have superior accuracy due to an improved approximation of the wavefunction.

2.3 Density Functional Theory

Instead of attempting to improve the wavefunction, as is done in wavefunction theory, a different approach has led to the development of density functional theory (DFT).[141,142] Its essential basis is a theorem proven by Hohenberg and Kohn,[143] which states that the

electron density ρ uniquely determines all properties of the molecular system, including the electronic energy:

$$E = E[\rho] \,. \tag{2.4}$$

Thus, the electronic energy has a functional dependence on the electron density, which is a function of only 3 spatial variables. This translates into a considerable reduction in computational cost compared to wavefunction methods, where the electronic energy has a functional dependence on the electronic wavefunction, which contains three spatial variables for each electron (and a fourth variable if spin is taken into account).

A practical approach to put this idea to work has been provided by Kohn and Sham.[144] They introduced the concept of a reference system of non-interacting electrons, moving in an effective potential V_S. This Kohn-Sham potential is constructed such that the density of the reference system equals the density of the real, interacting system. Thus, in Kohn-Sham DFT, the electronic wavefunction of the reference system is expressed by a single Slater determinant, consisting of one-electron wavefunctions. These wavefunctions are the Kohn-Sham orbitals φ, from which the electron density can be constructed by taking a linear combination of their densities:

$$\rho(r) = \sum_i |\varphi_i|^2 \,. \tag{2.5}$$

The electronic energy is obtained from the density by the energy functional

$$E[\rho(r)] = T_S[\rho(r)] + E_{Ne}[\rho(r)] + E_C[\rho(r)] + E_{XC}[\rho(r)] \,. \tag{2.6}$$

The first term in this expression, $T_S[\rho(r)]$, describes the kinetic energy of the electrons in the non-interacting reference system. $E_{Ne}[\rho(r)]$ represents the electrostatic attraction between the electron density and the nuclei. The third term, $E_C[\rho(r)]$, is the classical Coulomb repulsion between the electrons, that is, the repulsion each electron experiences from the average field due to all electrons, including itself. The final term, $E_{XC}[\rho(r)]$ is the exchange-correlation energy, which corrects for the deficiencies of $T_S[\rho(r)]$ and $E_C[\rho(r)]$. The kinetic energy of the electrons in the Kohn-Sham reference system, $T_S[\rho(r)]$, is different from the kinetic energy of the real system, $T[\rho(r)]$. For the third term, $E_C[\rho(r)]$, there are a number of deficiencies that have to be corrected. Firstly, electrons do not repel themselves, thus, the Coulomb repulsion computed from the average field of all electrons, contains a self-interaction error. Secondly, following from the Pauli exclusion principle, the probability of finding two same-spin electrons at the same point in space should be zero. Thirdly,

the motions of electrons are correlated: they avoid each other due to mutual Coulomb repulsion. Unfortunately, the form of the exchange-correlation functional is not known exactly, and has to be approximated. Nowadays, there is an incredible amount of functionals to choose from, and a large number of benchmark studies upon which the decision can be based.

The one-electron Kohn-Sham orbitals are determined by

$$\hat{h}^{KS}\varphi_i = (-\tfrac{1}{2}\nabla^2 + V_S)\varphi_i = \varepsilon_i\varphi_i \tag{2.7}$$

where $\hat{h}^{KS}$ is the one-electron Kohn-Sham Hamiltonian operator, which consists of a kinetic energy operator and the Kohn-Sham potential V_S. This potential comprises the potential V_{Ne} due to the charged nuclei, an effective Coulomb potential V_C due to the charge density and an exchange-correlation potential V_{XC}. The Kohn-Sham operator works on the one-electron Kohn-Sham orbitals φ_i, and the corresponding ε_i can be interpreted as the orbital energies of φ_i. Although these orbitals were originally developed only to construct the density, they appear to be suitable for qualitative chemical application.[145-148] The Kohn-Sham equations have to be solved iteratively, since, in order to obtain the orbitals, one needs the density, which is constructed from the very same orbitals. This is done using the self-consistent field (SCF) procedure. Starting from an initial guess of the density, the potentials are calculated and the Kohn-Sham equations are solved, yielding a set of orbitals from which a (hopefully) improved density is constructed. This procedure is repeated until the difference between the input density and output density drops below a specified threshold: the density is then approximately self-consistent and the computation converged to within certain criteria.

2.4 Computational Details

All computations within this thesis are based on density functional theory (DFT),[141,142] and have been carried out using the Amsterdam Density Functional program, developed by Baerends and co-workers,[149-151] and the Quantum-regions Interconnected by Local Descriptions (QUILD) program.[152-154] The numerical integration is performed using the procedure developed by Te Velde *et al.*[155,156] For some of the potential energy surfaces in chapter 4, the fuzzy cells integration scheme developed by Becke[157] was applied, as implemented in the ADF2013 release.[158] The molecular orbitals (MOs) are expanded in a large uncontracted set of Slater-type orbitals (STOs), no Gaussian functions are involved. This

basis set, denoted TZ2P, is of triple-ζ quality for all atoms and has been augmented with two sets of polarization functions.[159] The polarization functions are 2p and 3d on H, 3d and 4f on C, N, O, F, P and Cl, 4d and 4f on Br and 5d and 4f on I. For the transition metals, the polarization functions are 4p and 4f on Co, Ni, Cu, 5p and 4f on Rh, Pd and Ag and 6p and 5f on Ir, Pt and Au. An auxiliary set of s, p, d, f and g STOs is used to fit the molecular density and to represent the Coulomb and exchange potentials accurately in each self-consistent field (SCF) cycle. For the work on catalysis (chapters 3 to 7), all electrons are included in the variational treatment. For the work on halogen bonds in chapters 8 and 9, a frozen core approximation is applied. In these studies, the core shells comprised the 1s for C, N, O and F; 1s2s2p for Cl and K; up to 3p for Br and up to 4p for I.

Equilibrium structures and transition state geometries are obtained by optimizations using analytical gradient techniques.[160] Geometries and energies are calculated using functionals based on the generalized gradient approximation (GGA). For all chapters, except chapter 8, the BLYP functional is used, in which exchange is described by Slater's Xα potential,[161] with nonlocal corrections due to Becke[162,163] added self-consistently. Correlation is treated using the gradient-corrected functional of Lee, Yang and Parr.[164] The results in chapter 8 are obtained with the BP86 functional, using again Becke's corrections[162,163] on Slater's Xα potential,[161] but the correlation is now treated using the Vosko-Wilk-Nusair (VWN) parameterization[165] with nonlocal corrections due to Perdew[166] added, again, self-consistently.[167]

For a number of studies, mainly those in chapters 4, 5 and 9, dispersion interactions are included by means of additional corrections to the functional. In chapters 4 and 5, Grimme's third generation DFT-D3 method is applied.[168] In this approach, the density functional is augmented with an empirical term correcting for long-range dispersion effects, described by a sum of damped interatomic potentials of the form C_6R^{-6} added to the usual DFT energy. In chapter 9, the DFT-D3(BJ) method is applied,[169] which is a revised version of the DFT-D3 method, with a damping function of the form $C_6/(R^6+c)$ as proposed by Becke and Johnson.[170] Scalar relativistic effects are accounted for using the zeroth order regular approximation (ZORA).[171,172] These approaches have all been carefully tested and agree well with experimental results or high-level coupled cluster reference data.[113,161-166,173-182]

Energy minima and transition states have been verified through vibrational analysis,[183-185] except for the quadruplexes in chapter 9. All minima were found to have zero imaginary frequencies, whereas all transition states have one. The character of the normal

mode associated with the imaginary frequency has been analyzed to ensure it resembles the reaction under consideration. In a number of instances intrinsic reaction coordinate (IRC) calculations[186,187] have been performed to obtain the potential energy surface (PES) of the chemical process. In some cases, these potential energy surfaces have been approximated by means of the Transition-Vector Approximation to the IRC (TV-IRC). In this approach, the PES around the transition state is approximated using the transition vector, that is, the normal mode associated with a negative force constant leading from the saddle point on the PES to the steepest descent paths.[188] The PyFrag program was used to facilitate the analyses along the PES.[189]

Throughout this thesis, the focus lies on the electronic energies of the molecular systems. In a number of instances (mainly chapters 6 and 8), enthalpies or Gibbs free energies at 298.15 K and 1 atm. have been calculated using standard statistical mechanics relationships, and the computed partition functions, assuming an ideal gas.[138,190] The thermodynamic effects were found to have only a small influence on the energies and do not alter any of the encountered trends. It should be noted, however, that small barriers for either the forward or backward reaction that are present on the electronic potential energy surface, may vanish when thermodynamic effects are taken into account. For clarity, the results are therefore not discussed, but available in the supplementary information of the publications corresponding to these chapters.

The distribution of the electron density is analyzed using the Voronoi deformation density (VDD) method[191,192] for computing atomic charges. Within this method, the atomic charge on an atom A (Q_A^{VDD}) is computed as the integral of the deformation density in the volume of the Voronoi cell of atom A:

$$Q_A^{VDD} = -\int_{\substack{\text{Voronoi cell}\\ \text{of atom A}}} \left(\rho(r) - \sum_B \rho_B(r) \right) \mathrm{d}r \ . \tag{2.8}$$

The Voronoi cell of atom A is defined as the compartment of space bounded by the bond midplanes on, and perpendicular to, all axes between the nucleus of atom A and the nuclei of its neighboring atoms. The deformation density is the difference between the density $\rho(r)$ of the molecular system and the superposition of spherically averaged atomic densities $\rho_B(r)$ for neutral atoms B. The interpretation of VDD charges is rather straightforward: it measures how much charge flows out of ($Q_A^{VDD} > 0$) or into ($Q_A^{VDD} < 0$) the Voronoi cell of atom A, due to chemical interactions. Within a fragment-based approach, the VDD charge

of a molecular fragment can be calculated as the sum of the VDD charges of the individual atoms belonging to that fragment.

2.5 Activation Strain Model of Chemical Reactivity

The energy profile of a chemical process, that is, the change in energy of the molecular system as a function of the progress of the chemical process, can be obtained using, for example, density functional theory. However, to explain why molecular fragments interact, or react, requires a deeper understanding. The activation strain model of chemical reactivity[193-196] can be used to get insights into the features of an energy profile, and, for this purpose, has been applied in all research contained in this thesis. It is a fragment-based approach, dissecting the relative energy ΔE into two separate terms. For example, one can obtain insight into the height of the reaction barrier by splitting its energy, $\Delta E^{\ddagger}$, in the strain energy $\Delta E^{\ddagger}_{\text{strain}}$, and the interaction energy $\Delta E^{\ddagger}_{\text{int}}$:

$$\Delta E^{\ddagger} = \Delta E^{\ddagger}_{\text{strain}} + \Delta E^{\ddagger}_{\text{int}} \,. \tag{2.9}$$

The strain energy $\Delta E^{\ddagger}_{\text{strain}}$ is the energy required for the geometrical deformation of the fragments from a reference geometry (often, but not necessarily, their equilibrium geometry) to the geometry they acquire at the transition state. It is therefore strongly related to the structural rigidity of the fragments. Since the reference geometries are usually not distorted, this term is typically destabilizing. It can gain significant values when deformations are large, such as the substrate undergoing bond cleavage during oxidative addition. However, for the formation of metal-ligand bonds M–L, such as discussed in chapter 3, or some of the DX···A$^-$ halogen bonds in chapter 8, there is only a moderate change in the geometry of the ligand, or DX fragment, respectively. In these cases, the strain energy term is only moderately destabilizing. In principle, the strain term can also incorporate excitations to electronic configurations that are better suited or required for the interaction studied, but most often the reference fragments are chosen as already having the correct valence configuration.

The strain term can be split further into separate contributions from each fragment, as is done, for example, in some of the chapters on catalysis, where the contributions from catalyst deformation and substrate deformation are computed separately, to show that a significant part of the reaction barrier originates from the rigidity of the catalyst. Furthermore, note that in the formation of the metal-ligand bond M–L, as well as the DX···A$^-$

halogen bond formation, there is a monatomic fragment (M or A^-), for which the strain energy is zero by definition, because there are no possible geometric changes.

The interaction energy $\Delta E_{\text{int}}^{\ddagger}$ accounts for all chemical interactions as they arise when the deformed reactants are brought from infinity to their positions in the transition state geometry. This term can be further dissected using an energy decomposition scheme, of which there are several available. The EDA method[147,197,198] used within this thesis will be discussed in section 2.6.

The activation strain model can be generalized to any point along an energy profile.[193,194,199-202] The relative energy ΔE, as well as its components, then become functions of the reaction coordinate ζ and Equation 2.9 generalizes to

$$\Delta E(\zeta) = \Delta E_{\text{strain}}(\zeta) + \Delta E_{\text{int}}(\zeta) \ . \tag{2.10}$$

When applied to an energy profile of a chemical reaction with a central reaction barrier, as for example encountered for most oxidative addition reactions in this thesis, all terms start at a value close to zero, but not necessarily at zero. This is because a reaction (in the gas phase) typically starts from a precursor complex, in which the fragments are slightly distorted (small ΔE_{strain}) and interact only weakly (small ΔE_{int}). From there on, the reactants become increasingly deformed along the reaction coordinate, leading to a continuously increasing strain energy ΔE_{strain}. Concomitantly, the interaction between the fragments usually strengthens, which leads to the interaction energy ΔE_{int} becoming more stabilizing along the reaction profile. At the point where the destabilization from the strain term increases at the same rate as the stabilization from the interaction energy term strengthens, that is, $dE_{\text{strain}}/d\zeta = -dE_{\text{int}}/d\zeta$, the derivative of the total energy profile with respect to the reaction coordinate is zero ($dE/d\zeta = 0$). At this point, the energy profile achieves either a maximum (the reaction barrier), where the transition state occurs, or a stable minimum.

It follows that, to elucidate the height of a reaction barrier, or the stability of a stationary point, one should not only consider the rigidity of the fragments and the strength of their mutual interaction, but also the position along the reaction coordinate, and therefore the slopes of the strain and interaction terms. Depicted in Figure 2.1 is a comparison of the activation strain analyses of two generic chemical reactions to exemplify this. In this comparison, the strain curves ΔE_{strain} resulting from both reactions are chosen to be equal, while the interaction curves ΔE_{int} are different. From this figure, it is easily concluded that, upon going from the first reaction (black lines) to the second reaction (red lines), the energy profile $\Delta E(\zeta)$ is shifted up in energy, due to a weaker interaction between the fragments. This

results in a higher reaction barrier, which is shifted to the product side because the interaction energy curve is descending less steeply. This is in agreement with the Hammond postulate,[203] which indeed follows naturally from the activation strain model. Note, however, that an analysis at the transition state geometries only, as indicated by the dashed lines in Figure 2.1, can be misleading, as in this case one would conclude that the reaction barrier becomes higher due to a significant increase in strain energy, and even despite (!) a slightly more stabilizing interaction between the fragments.

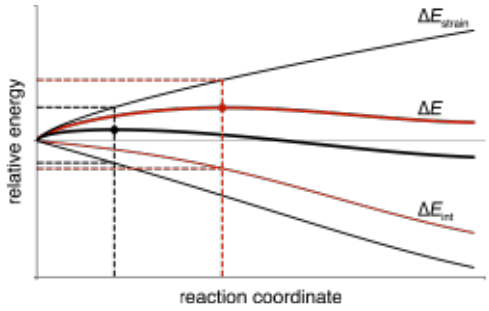

Figure 2.1 Comparison of generic activation strain analyses of two different reactions.

Although analyses along full reaction paths (or critical sections thereof) are more insightful than single point analyses at the transition state only, there are still a number of important factors to take into account in order to avoid misleading results. Firstly, analyses of two similar reactions are more readily compared when the energy profiles are projected onto a critical geometrical parameter. This parameter should be well-defined along the reaction profile and be sufficiently descriptive for the overall reaction process, but also undergo considerable changes in the transition state region.[188] Secondly, within this model, the total energy profile results from two opposing contributions, but these contributions are not orthogonal and thus influence each other. The strain term, for example, is almost always positive as a consequence of its very definition. Eliminating the strain term by freezing the geometries of the fragments and pushing them towards each other, however, would not lead to a lower total energy profile. Instead, the interaction term would weaken and, since it includes a repulsive component as well, eventually become repulsive, likely raising the total energy profile to higher values than the initial energy profile that was obtained with relaxed geometries. Thus, a significant part of the interaction energy that is built up during the

reaction, requires a certain amount of geometrical deformation, and thereby strain energy. This balance between mutually dependent terms usually does not cause problems, but should be kept in mind when applying any model that contains interacting and opposing components. To get insight into the importance of this interplay, it can be useful to use additional analyses where (part of) the geometries are fixed. In chapters 3 and 5 the geometries of the fragments are entirely fixed in the analyses of the bonding interactions as function of the ligand-metal-ligand angle. This is done to prevent any perturbation stemming from geometry changes of the fragments that could easily hide the small, though significant, variations in the components of the bonding mechanism that occur when the ligand-metal-ligand angle is varied.

So far, the activation strain model is discussed in the context in which it is most often applied, namely bimolecular reactions via a transition state, such as oxidative additions, as in this thesis, S_N2 reactions[193,204-206] or pericyclic reactions.[207,208] The model is, however, equally useful for the analyses of barrier-free bond formations, such as the hydrogen and halogen bonds discussed in chapters 8 and 9, and has also been generalized to study unimolecular processes.[209-211]

2.6 Molecular Orbital Theory & Interaction Energy Decomposition

The activation strain model reveals great insight into relative energies and even entire reaction energy profiles, as it provides the very relevant question *why* a certain geometrical deformation leads to an energetic destabilization, or *why* molecular fragments can build up a particular mutual interaction. Thus, to achieve a genuine explanation of the phenomena of interest, the reasons behind the changes in strain and interaction energy can be subjected to further investigation. In the following chapters, both the strain energy and the interaction energy are further analyzed, often using (Kohn-Sham) molecular orbital (MO) theory.[212-215]

As discussed in the previous section, the strain energy of a fragment is the energy needed for the geometric deformations, relative to a reference geometry. Since this reference geometry is typically the equilibrium geometry of the fragment, the amount of strain energy is often directly related to the amount of geometrical distortion, and can be readily linked to the extent to which, for example, bonds are stretched or angles have changed. Further explanation is therefore not always needed. However, when required, MO theory can help to understand why a certain geometric deformation leads to a less stable molecular

species. This is because changes in the total energy of the molecular fragment tend to parallel the changes in the sum of its orbital energies, and the orbital energies are again altered by changes in the molecular geometry. Thus, by investigating the dependence of the orbital energies on a geometrical parameter of interest, as is done in Walsh diagrams, one can explain why a certain molecular deformation leads to a destabilization of the molecular fragment. In a subsequent step, one can of course divide the fragment itself into smaller fragments, and provide an explanation for, for example, a rise in the orbital energy in terms of a decreased in-phase or increased out-of-phase overlap of the orbitals on the smaller fragments. Likewise, a lowered orbital energy can be ascribed to an increased in-phase overlap or decreased out-of-phase overlap. This process can be repeated until the explanation is provided in terms of atomic orbitals, which no longer have any geometry dependence. Often, however, a satisfactory level of understanding is achieved already at an earlier stage, based on the transferability of properties of common functional groups.

Studying the how and why of chemical interactions between molecular fragments is, in essence, chemical bond analysis, and constitutes a core aspect of this thesis, and theoretical chemistry in general. In the following chapters, the interaction energy is usually split into separate terms arising from different types of interactions, to get a quantitative idea of their contributions to the total interaction energy. This is done using the energy decomposition analysis (commonly abbreviated EDA) scheme as implemented in the ADF software suite.[147,149] This scheme is chosen for its transparent, easy-to-understand nature, as it dissects the interaction energy into terms that directly correspond to concepts from MO theory, thus revealing causal bonding mechanisms. The approach is based on that of Morokuma[216,217] and the extended transition state (ETS) method developed by Ziegler and Rauk.[197,198,218] Within this scheme, the interaction energy ΔE_{int} is decomposed into three terms, which can be interpreted physically in the framework of the molecular orbitals (MOs) arising from Kohn-Sham DFT:

$$\Delta E_{\text{int}} = \Delta V_{\text{elstat}} + \Delta E_{\text{Pauli}} + \Delta E_{\text{oi}} \,. \tag{2.11}$$

Similar to the generalization of the ΔE_{int} term to any point along an energy profile (as discussed in section 2.5, see Equations 2.9 and 2.10) also this equation can be generalized to the entire reaction profile. Each term then becomes a function of the reaction coordinate ζ.

For the discussion of the individual terms contributing to the interaction energy ΔE_{int}, the formation of AB is considered from two fragments A and B, which, as discussed in the previous section, already have the geometry and electronic configuration corresponding to

the combined complex AB. These fragments have electronic densities ρ_A and ρ_B, with corresponding wavefunctions Ψ_A and Ψ_B and energies E_A and E_B. The first term, ΔV_{elstat}, is the classical electrostatic interaction between the fragments as they are brought from infinity to their positions in the complex AB, giving rise to the sum density $\rho_{A+B} = \rho_A + \rho_B$, and corresponding Hartree product wavefunction $\Psi_A\Psi_B$. It consists of the Coulombic repulsion between the nuclei α and β (at positions R, with charges Z) of the fragments A and B, respectively, as well as the repulsion between their unperturbed electron densities ρ_A and ρ_B, and the attractive interactions between the nuclei of one fragment with the electron density of the other fragment:

$$\begin{aligned}\Delta V_{elstat} = & \sum_{\alpha \in A} \sum_{\beta \in B} \frac{Z_\alpha Z_\beta}{R_{\alpha\beta}} \\ & - \int \sum_{\alpha \in A} \frac{Z_\alpha \rho_B(r)}{|R_\alpha - r|} dr - \int \sum_{\beta \in B} \frac{Z_\beta \rho_A(r)}{|R_\beta - r|} dr \\ & + \int\int \frac{\rho_A(r_1)\, \rho_B(r_2)}{r_{12}}\, dr_1\, dr_2 \,.\end{aligned} \tag{2.12}$$

It is known from elementary electrostatics that two interpenetrating charge clouds have a repulsion that is smaller than the one between point charges at their centers, from which follows that fragments consisting of electronic densities around positive nuclei will typically experience a net attraction. Thus, ΔV_{elstat} is usually attractive for molecular fragments at chemically relevant distances. For discussions in later sections, it is important to note that this term is computed from frozen electron densities ρ_A and ρ_B, obtained by optimizations in absence of the other fragment.

The Pauli repulsion, ΔE_{Pauli}, is the energy change that occurs upon going from the product wavefunction $\Psi_A\Psi_B$ to an intermediate wavefunction Ψ^0 that, after antisymmetrization by an operator $\mathcal{A}$ and renormalization by a constant N, properly obeys the Pauli principle: $\Psi^0 = N\mathcal{A}\{\Psi_A\Psi_B\}$. This intermediate state, with density ρ^0, has energy E^0, such that $\Delta E^0 = E^0 - E_A - E_B = \Delta V_{elstat} + \Delta E_{Pauli}$ and $\Delta E_{Pauli} = \Delta E^0 - \Delta V_{elstat}$. The Pauli repulsion comprises the repulsive interaction between electrons having the same spin. It is responsible, for example, for the 4-electron destabilizing interactions between doubly occupied orbitals from the different fragments. This is the origin of steric repulsion: when two occupied valence orbitals from different fragments overlap, antisymmetrization results in a nodal plane.

The large gradients in this region lead to a significant increase in the kinetic component of the orbital energies (Equation 2.7).

In the final step of the bond formation between fragments A and B, the system is allowed to relax from Ψ^0, and corresponding ρ^0, to the final Ψ^{AB} and optimized density ρ of the molecular complex AB. The accompanying energy change is the orbital interaction term: $\Delta E_{oi} = E^{AB} - E^0$. This term is by definition stabilizing, because it involves an optimization. More specifically, it allows the virtual orbitals on the fragments to be mixed in. As a result of this mixing, the orbital interaction component contains the stabilizing contributions from polarization of the fragments A and B, as well as charge transfer between the fragments. It is hard, if not impossible, to rigorously distinguish polarization from charge transfer, and this is therefore not attempted in this interaction energy decomposition scheme (in contrast to the scheme of Morokuma[216,217]). However, when using a fragment-based approach and further orbital analyses, it is possible to get insight into the two individual contributions at least partially. Both polarization and charge transfer will show up as occupied-virtual orbital mixing, but in the case of polarization, the occupied and virtual orbitals will be localized on the same fragment, whereas charge transfer will show up as the mixing of occupied orbitals on one fragment with unoccupied orbitals on the other fragment. When using very large basis sets, care must be taken since the basis functions of one fragment can extend into the domain of the other fragment. Besides detailed orbital analyses, additional electron density analyses (based on atomic charge analyses, the deformation density, etc.) can be helpful to distinguish polarization from charge transfer.

Furthermore, it follows from group theory that only orbitals of the same symmetry, that is, having the same character under the available symmetry operations, can interact and mix. This allows for a further decomposition of the total orbital interaction energy ΔE_{oi} into contributions from each irreducible representation (irrep) Γ of the point group of the molecular system:[198]

$$\Delta E_{oi} = \sum_{\Gamma} \Delta E_{oi}^{\Gamma} . \tag{2.13}$$

Finally, when the functional is augmented with an explicit correction to account for dispersion interactions, the contribution ΔE_{disp} from this term can simply be added to Equation 2.11 as an additional component of the interaction energy ΔE_{int}.

In Figure 2.2, schematic orbital interaction diagrams are shown for the different types of orbital interactions that play a main role throughout the following chapters.

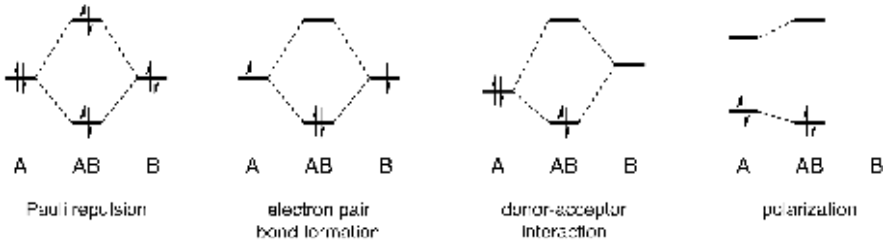

Figure 2.2 Orbital interaction diagrams for the interactions most commonly appearing throughout this thesis.

There are many other schemes available that divide the interaction energy into separate terms,[219-227] and one could argue that some of them give more realistic representations of, for example, the electrostatic attraction between fragments. Also, the Pauli repulsion term has been criticized for being based on an "*arbitrarily chosen, non-physical reference state*", and resulting from "*first violating the Pauli principle and then imposing it*".[210,228-230] Such statements may, at times, be relevant reminders for the overenthusiastic user of the decomposition scheme, but serve no further purpose: the scheme is a quantitative analysis tool that, preferably accompanied by results from additional analyses, assists in explaining a certain result using MO theory. All terms are defined as they are, and produce the numbers that follow from these clear and transparent definitions. The results provided by the decomposition scheme should therefore not be interpreted as the final answer to a question, nor be presented as such.

After this rigorous numerical treatment, the explanations in this thesis are often presented schematically, using generic hydrogen-like atomic orbitals and a few core concepts from MO theory, further aided by symmetry considerations derived from group theory. A number of elementary atomic properties, such as electronegativity and atomic radii, can easily be taken into account using what is in essence a perturbative treatment. Thus, although the results are derived from state-of-the-art DFT computations and detailed analyses, the final explanation often shows the essence of the phenomenon of interest in a pictorial manner that is easy to memorize, to communicate and to apply to new situations. Such representations nevertheless accurately account for the observations made, and provide important insights. In the past, this approach, and MO theory in general, has proven to be a very powerful tool for explaining many observations made in a variety of fields in chemistry, limited not only to molecules, but also including solids.[212-215,231]

3 Nonlinear d^{10}-ML_2 Complexes

Previously appeared as

Nonlinear d^{10}-ML_2 Transition Metal Complexes
L. P. Wolters, F. M. Bickelhaupt
ChemistryOpen **2013**, *2*, 106–114

3.1 Introduction

Dicoordinated d^{10}-ML_2 transition metal complexes in general have a linear ligand-metal-ligand angle (or bite angle), although exceptions have been observed.[232-236] The preference for such a linear geometry can be easily understood for a closed-shell d^{10} configuration. In most cases, the dominant bonding orbital interaction is σ donation from the ligand's lone pair orbitals into the empty metal (n+1)s atomic orbital (AO), which has ligand-metal bond overlap that is more or less independent of the L–M–L' angle, as shown in Figure 3.1.[213] At the same time, the steric repulsion associated with the overlap of the lone pairs (and other closed shells) on the ligands yields a force that maximizes their mutual distance and thus yields the commonly observed L–M–L' arrangement.

Figure 3.1 σ Donation has no preference (left and middle), whereas sterics favor linear L–M–L angles (right).

The same conclusion follows from valence shell electron pair repulsion (VSEPR) theory adapted for treating transition metal complexes[237-240] or a more sophisticated treatment based on molecular orbital (MO) theory. Proceeding from the latter, one can deduce the preference for linear over bent ML_2 complexes from the number of electrons in the valence orbitals and the dependence of the orbital energies on the geometrical parameter of interest (here, the L–M–L angle) in Walsh diagrams.[213] These diagrams show again that dicoordinated d^{10}-ML_2 transition metal complexes, for example, $Ag(NH_3)_2^+$, adopt a linear geometry due to the significant destabilization of the metal d_{xz} atomic orbital by the ligand lone pair orbitals in combination with steric repulsion between the latter upon bending. Nearly all instances with substantial deviations of the L–M–L bite angle from linearity are complexes in which this distortion is imposed by structural constraints in bidentate ligands, in which a bridge or scaffold forces the two coordinating centers L towards each other.[52,54,241] However, nonlinear geometries are also observed for some complexes that do not have such constraints, as for example, for $Ni(CO)_2$.[235,236]

In this chapter, we show that d^{10}-ML_2 complexes are not necessarily linear and may even have a pronounced intrinsic preference to adopt a nonlinear equilibrium geometry. To this end, we have investigated the molecular geometries and electronic structure of a series of d^{10}-ML_2 complexes, where the metal center is varied along Co^-, Rh^-, Ir^-, Ni, Pd, Pt, Cu^+, Ag^+ and Au^+, and the ligands along NH_3, PH_3 and CO. Some of these d^{10}-ML_2 complexes are found to deviate substantially from linearity, featuring bite angles as small as 131° or even less. All that is necessary for d^{10}-ML_2 complexes to become bent is sufficiently strong π backdonation. This emerges from our detailed metal-ligand bonding analyses in the conceptual framework of quantitative molecular orbital theory contained in Kohn-Sham DFT. Based on our findings, we can augment the textbook Walsh diagram for bending ML_2 complexes involving only σ donation with an extended Walsh diagram that also includes π backbonding. Understanding this phenomenon is crucial, because, as we will show in chapter 6, it partly determines the reaction barrier for oxidative addition to these transition metal complexes.

3.2 Structures and Energetics

The structural and energetic results that emerge from our ZORA-BLYP/TZ2P computations are collected in Table 3.1 to 3.4. Most ML_2 complexes have a linear L–M–L angle, which leads to either D_{3h}-symmetric complexes $M(NH_3)_2$ and $M(PH_3)_2$ or $D_{\infty h}$-symmetric

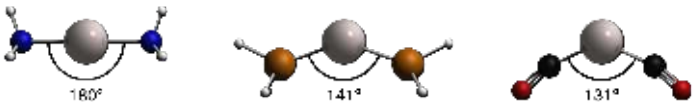

Figure 3.2 From left to right: equilibrium geometries of $Rh(NH_3)_2^-$, $Rh(PH_3)_2^-$ and $Rh(CO)_2^-$.

complexes $M(CO)_2$. However, numerous significantly smaller angles appear throughout Table 3.1 as well, where the symmetry of the complexes is lowered to C_{2v}. For instance, the complexes become increasingly bent when the ligands are varied along NH_3 (a strong σ donor), PH_3 (a σ donor and π acceptor) and CO (a strong π acceptor). This is most clearly seen for the group 9 complexes, where the angle decreases, for example, along $Rh(NH_3)_2^-$, $Rh(PH_3)_2^-$ and $Rh(CO)_2^-$ from 180.0° to 141.2° and 130.8° (see Figure 3.2). As will be discussed in section 3.3, the π-backbonding properties of the complexes constitute a prominent part of the explanation of why d^{10}-ML_2 complexes can adopt nonlinear geometries. The increasingly strong π backbonding along this series also results in stronger metal-ligand bonds, as indicated by the bond dissociation energies (BDEs) in Table 3.2, and the results from the energy decomposition analysis (EDA) for monoligated ML complexes in Table 3.3.

Table 3.1 L–M–L angle (in degrees) and linearization energy ΔE_{lin} (in kcal mol^{-1}) for d^{10}-ML_2 complexes.[a]

Group 9			Group 10			Group 11		
	L–M–L	ΔE_{lin}		L–M–L	ΔE_{lin}		L–M–L	ΔE_{lin}
$Co(NH_3)_2^-$	180.0	0.0	$Ni(NH_3)_2$	180.0	0.0	$Cu(NH_3)_2^+$	180.0	0.0
$Co(PH_3)_2^-$	131.8	6.4	$Ni(PH_3)_2$	180.0	0.0	$Cu(PH_3)_2^+$	180.0	0.0
$Co(CO)_2^-$	128.6	19.9	$Ni(CO)_2$	144.5	2.1	$Cu(CO)_2^+$	180.0	0.0
$Rh(NH_3)_2^-$	180.0	0.0	$Pd(NH_3)_2$	180.0	0.0	$Ag(NH_3)_2^+$	180.0	0.0
$Rh(PH_3)_2^-$	141.2	2.0	$Pd(PH_3)_2$	180.0	0.0	$Ag(PH_3)_2^+$	180.0	0.0
$Rh(CO)_2^-$	130.8	10.2	$Pd(CO)_2$	155.6	0.5	$Ag(CO)_2^+$	180.0	0.0
$Ir(NH_3)_2^-$	180.0	0.0	$Pt(NH_3)_2$	180.0	0.0	$Au(NH_3)_2^+$	180.0	0.0
$Ir(PH_3)_2^-$	144.1	2.4	$Pt(PH_3)_2$	180.0	0.0	$Au(PH_3)_2^+$	180.0	0.0
$Ir(CO)_2^-$	134.2	13.4	$Pt(CO)_2$	159.0	0.6	$Au(CO)_2^+$	180.0	0.0

[a] The linearization energy ΔE_{lin} is the energy of the linear ML_2 complex relative to its equilibrium geometry.

The extent of bending systematically decreases when the π-backbonding capability of the metal center decreases from the group 9 anions, via neutral group 10 atoms, to the group 11 cations. This is clearly displayed by the series of iso-electronic complexes $Rh(CO)_2^-$, $Pd(CO)_2$ and $Ag(CO)_2^+$ along which the L–M–L angle increases from 130.8° to 155.6° to 180.0° (Table 3.1). The data in Table 3.3 for the corresponding monocoordinated $RhCO^-$, PdCO and $AgCO^+$, nicely show how along this series the distortive π-orbital interactions ΔE_{oi}^{π} indeed become weaker, from –120 to –51 to –11 kcal mol^{-1}, respectively. In the case of group 9 metals, both phosphine and carbonyl complexes are bent, whereas for group 10 metals only the carbonyl complexes deviate from linearity. Complexes with a metal center from group 11 all have linear L–M–L angles.

Table 3.2 M–L bond length (in Å) and bond dissociation energy (BDE, in kcal mol^{-1}) in monocoordinated d^{10}-ML and dicoordinated d^{10}-ML_2 complexes.[a]

Group 9			Group 10			Group 11		
	M–L	BDE		M–L	BDE		M–L	BDE
$CoNH_3^-$ [b,c]	1.845	217.1	$NiNH_3$[c]	1.827	77.0	$CuNH_3^+$	1.911	70.0
$CoPH_3^-$ [b,c]	1.971	240.6	$NiPH_3$[c]	1.979	88.0	$CuPH_3^+$	2.163	68.7
$CoCO^-$ [b,c]	1.630	280.6	NiCO[c]	1.663	109.3	$CuCO^+$	1.833	50.2
$Co(NH_3)_2^-$ [b,c]	1.908	24.0	$Ni(NH_3)_2$[c]	1.888	36.2	$Cu(NH_3)_2^+$	1.919	61.1
$Co(PH_3)_2^-$ [c]	2.051	48.2	$Ni(PH_3)_2$[c]	2.108	36.3	$Cu(PH_3)_2^+$	2.232	48.0
$Co(CO)_2^-$ [c]	1.715	76.3	$Ni(CO)_2$[c]	1.765	48.6	$Cu(CO)_2^+$	1.882	45.0
$RhNH_3^-$ [c]	2.001	55.5	$PdNH_3$	2.115	21.6	$AgNH_3^+$	2.212	48.7
$RhPH_3^-$ [c]	2.068	89.9	$PdPH_3$	2.172	39.4	$AgPH_3^+$	2.415	47.9
$RhCO^-$ [c]	1.750	122.0	PdCO	1.861	47.4	$AgCO^+$	2.137	28.4
$Rh(NH_3)_2^-$ [c]	2.089	22.6	$Pd(NH_3)_2$	2.106	28.6	$Ag(NH_3)_2^+$	2.172	45.2
$Rh(PH_3)_2^-$ [c]	2.196	38.2	$Pd(PH_3)_2$	2.287	28.6	$Ag(PH_3)_2^+$	2.444	38.1
$Rh(CO)_2^-$ [c]	1.866	58.1	$Pd(CO)_2$	1.949	34.7	$Ag(CO)_2^+$	2.113	30.7
$IrNH_3^-$ [c]	1.967	85.0	$PtNH_3$[c]	1.981	50.1	$AuNH_3^+$	2.085	71.4
$IrPH_3^-$ [c]	2.056	126.5	$PtPH_3$[c]	2.095	77.3	$AuPH_3^+$	2.240	84.2
$IrCO^-$ [c]	1.734	166.3	PtCO[c]	1.776	87.9	$AuCO^+$	1.927	55.0
$Ir(NH_3)_2^-$ [b,c]	2.071	23.6	$Pt(NH_3)_2$[c]	2.061	41.6	$Au(NH_3)_2^+$	2.088	64.6
$Ir(PH_3)_2^-$ [c]	2.190	44.1	$Pt(PH_3)_2$[c]	2.249	38.7	$Au(PH_3)_2^+$	2.351	52.6
$Ir(CO)_2^-$ [c]	1.845	66.3	$Pt(CO)_2$[c]	1.911	47.1	$Au(CO)_2^+$	2.002	40.4

[a] Bond dissociation energies (BDEs) are given for the complexes in the electronic configuration corresponding to a $d^{10}s^0$ electron configuration, and relative to closed-shell $d^{10}s^0$ metal atoms. [b] The $d^{10}s^0$-type configuration is an excited state of the complex. [c] The $d^{10}s^0$ configuration is an excited state of the atomic metal fragment.

Table 3.3 Energy decomposition analyses (in kcal mol^{-1}) for the metal-ligand bonds and orbital energies ε (in eV) of the monoligated transition metal complexes M–L.[a]

	ΔE	ΔE_{int}	ΔV_{elstat}	ΔE_{Pauli}	ΔE_{oi}	ΔE_{oi}^{σ}	ΔE_{oi}^{π}[b]	$\varepsilon(d_\sigma)$	$\varepsilon(d_\pi)$	$\varepsilon(d_\delta)$
$CoNH_3^-$	−217.1	−218.4	−110.0	+166.3	−274.7	−241.8	−32.9	+1.84	+2.91	+3.99
$CoPH_3^-$	−240.6	−241.7	−197.9	+204.5	−248.2	−123.9	−124.4	+1.67	+1.81	+3.38
$CoCO^-$	−280.6	−286.4	−233.4	+274.5	−327.5	−141.7	−185.8	+1.34	+1.17	+3.20
$RhNH_3^-$	−55.5	−56.2	−143.2	+202.1	−115.1	−110.8	−4.3	+1.72	+1.83	+2.53
$RhPH_3^-$	−89.9	−90.3	−269.7	+311.7	−132.3	−61.7	−70.6	+1.49	+0.91	+2.20
$RhCO^-$	−122.0	−126.0	−273.3	+364.1	−216.8	−96.7	−120.1	+1.05	−0.09	+1.56
$IrNH_3^-$	−85.0	−85.8	−196.9	+268.9	−157.8	−142.9	−14.9	+1.54	+2.16	+2.91
$IrPH_3^-$	−126.5	−127.2	−349.2	+396.0	−174.1	−85.9	−88.2	+1.18	+0.73	+2.28
$IrCO^-$	−166.3	−171.3	−353.5	+461.5	−279.2	−129.6	−149.7	+0.63	−0.26	+1.68
$NiNH_3$	−77.0	−77.3	−116.2	+139.8	−100.8	−94.5	−6.3	−3.28	−2.99	−2.21
$NiPH_3$	−88.0	−88.7	−161.3	+173.3	−100.7	−50.8	−49.9	−3.79	−3.93	−2.90
NiCO	−109.3	−110.4	−171.6	+210.3	−149.1	−60.4	−88.7	−4.89	−5.40	−4.14
$PdNH_3$	−21.6	−21.7	−88.0	+105.1	−38.8	−34.5	−4.4	−3.46	−3.81	−3.47
$PdPH_3$	−39.4	−39.8	−166.2	+190.3	−63.8	−35.3	−28.5	−4.49	−5.29	−4.56
PdCO	−47.4	−47.8	−161.4	+213.3	−99.7	−48.0	−51.8	−5.28	−6.48	−5.53
$PtNH_3$	−50.1	−50.4	−170.1	+211.4	−91.7	−82.0	−9.7	−4.19	−4.46	−3.72
$PtPH_3$	−77.3	−78.9	−273.9	+310.3	−115.3	−70.5	−44.8	−4.92	−5.72	−4.53
PtCO	−87.9	−88.7	−271.6	+356.9	−174.0	−91.6	−82.4	−5.97	−7.28	−5.77
$CuNH_3^+$	−70.0	−70.1	−104.5	+86.0	−51.7	−41.9	−9.8	−11.80	−12.13	−12.02
$CuPH_3^+$	−68.7	−73.5	−101.7	+94.0	−65.8	−51.8	−14.0	−11.99	−12.44	−12.15
$CuCO^+$	−50.2	−50.3	−89.8	+100.7	−61.2	−38.8	−22.4	−13.70	−14.28	−13.90
$AgNH_3^+$	−48.7	−48.7	−73.3	+58.8	−34.2	−28.5	−5.8	−12.56	−13.60	−13.57
$AgPH_3^+$	−47.9	−51.8	−84.3	+81.3	−48.8	−39.9	−8.9	−12.41	−13.67	−13.85
$AgCO^+$	−28.4	−28.6	−59.1	+67.2	−36.7	−26.2	−10.6	−14.08	−15.07	−14.86
$AuNH_3^+$	−71.4	−71.6	−124.8	+123.2	−70.0	−60.3	−9.7	−12.49	−13.32	−12.92
$AuPH_3^+$	−84.2	−91.0	−177.9	+187.2	−100.3	−80.9	−19.4	−12.52	−13.70	−13.06
$AuCO^+$	−55.0	−55.1	−149.0	+188.4	−94.5	−64.9	−29.7	−14.20	−15.53	−14.73

[a] See Equations 2.9, 2.11 and 2.13. [b] Also includes small contributions from δ orbital interactions, which can only be separated for $C_{\infty v}$-symmetric MCO complexes. There, the δ term amounts at most to 3.5% of the π term.

The reduced π backbonding also leads to weaker metal-ligand bonds. For the cationic metal centers, for which π backdonation plays a much smaller role, the metal-ligand BDEs decrease in the order NH_3 > PH_3 > CO (see Table 3.2). This trend originates directly from the σ-donating capabilities of the ligands as reflected by the energy ε(LP) of the lone pair

orbital, which decreases in this order (see Table 3.4). Note that, for the same reason, the basicity of the ligand as measured by the proton affinity (PA) decreases along NH_3 > PH_3 > CO.[242] For the anionic group 9 metal centers, the opposite order is found, that is, metal-ligand BDEs decrease in the order CO > PH_3 > NH_3, following the π-accepting capabilities of the ligands.

Linearity also increases if one descends in a group. For example, from $Ni(CO)_2$ to $Pd(CO)_2$ to $Pt(CO)_2$, the L–M–L angle increases from 144.5° to 155.6° to 159.0°. Interestingly, this last trend is opposite to what one would expect proceeding from a steric model. If one goes from a larger to a smaller metal center, *i.e.*, going up in a group, the ligands are closer to each other and thus experience stronger mutual steric repulsion. But instead of becoming more linear to avoid such repulsion, the complexes bend even further in the case of the smaller metal. For example, when the palladium atom in $Pd(CO)_2$ is replaced by a smaller nickel atom, the L–M–L angle decreases from 155.6° in $Pd(CO)_2$ to 144.5° in $Ni(CO)_2$. Later on, we show that this seemingly counterintuitive trend also originates from enhanced π backbonding, which dominates the increased steric repulsion.

Table 3.4 Ligand orbital energies ε (in eV) and proton affinities (in kcal mol^{-1}).[a]

	ε(LP)	$\varepsilon(\pi^*)$	PA
NH_3	–6.05	+1.42	+201.4
PH_3	–6.63	–0.24	+185.2
CO	–8.93	–1.92	+141.5

[a] LP: lone pair; π^*: acceptor orbital. Proton affinities (PA) from enthalpies at 298.15 K and 1 atm.

3.3 General Bonding Mechanism

The bending of our ML_2 model complexes can be understood in terms of a monocoordinated complex to which a second ligand is added either in a linear or a bent arrangement, $ML + L \rightarrow ML_2$. Using $Pd(CO)_2$ as an example, we start from a PdCO fragment, and consider the addition of the second CO ligand both at a 180° angle, and at a 90° angle. Our Kohn-Sham MO analyses show that, in PdCO, the degeneracy of the five occupied d orbitals on palladium is lowered by interactions with the ligand (see Figure 3.3). Choosing the M–L bond along the z axis, the d_{xz} and d_{yz} orbitals act as donor orbitals for π backdonation into the two π^* acceptor orbitals on the CO ligand, resulting in two stabilized "d_π"

orbitals at –6.5 eV (value not shown in Figure 3.3). The d_{xy} and $d_{x^2-y^2}$ (or "d_δ") orbitals at –5.5 eV do not overlap and interact with the ligand. The d_{z^2} orbital is destabilized due to the antibonding overlap with the lone pair on the ligand, resulting in a "d_σ" orbital that is relatively high in energy, at –5.3 eV.

When the second CO ligand coordinates opposite the first one (in a linear L–M–L arrangement), its π^* acceptor orbitals interact with the d_π orbitals on the PdCO fragment.

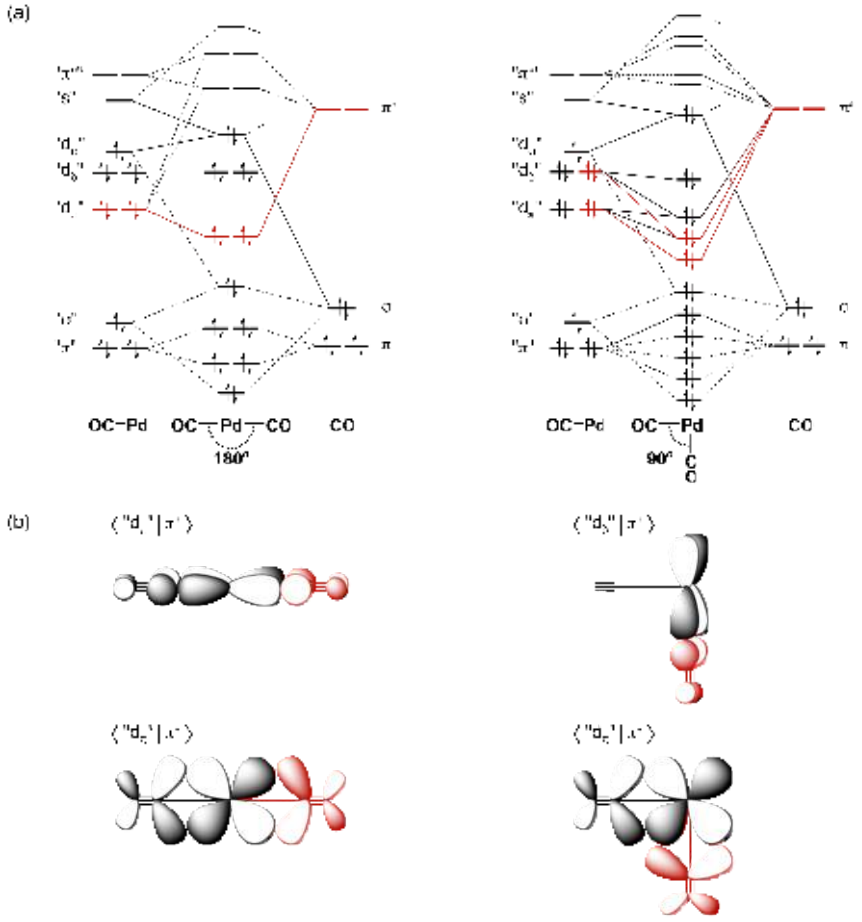

Figure 3.3 (a) Schematic MO diagrams for the bonding mechanism between PdCO and CO in linear $Pd(CO)_2$ (left) and at a L–M–L angle of 90° (right): dominant interactions in black, other interactions dashed and π backbonding in red. (b) Schematic representation of the bonding overlaps of the donating orbital on PdCO (black) with the π-accepting orbital on the second CO ligand (red).

The latter are already considerably stabilized by π backdonation to the first carbonyl ligand (Figure 3.3, left). When, instead, the second ligand is added at an angle of 90°, its π* orbitals overlap with only one d_π orbital, and with one d_δ orbital (Figure 3.3, right). This d_δ orbital is essentially a pure metal d orbital that has not yet been stabilized by any coordination bond. Consequently, this orbital has a higher energy and is, therefore, a more capable donor orbital for π backdonation into the π* orbital of the second CO ligand. This results in a stronger, more stabilizing donor-acceptor interaction of this pair of orbitals in the 90° (Figure 3.3, right) than in the 180° ML_2 geometry (Figure 3.3, left: compare red-highlighted π interactions). σ Donation is affected less by bending. It is therefore π backdonation that favors nonlinearity. The more detailed energy decomposition analyses in the following sections consolidate this picture.

3.4 Bonding Mechanism: Variation of Ligands

To understand the trends in nonlinearity of our ML_2 complexes (see Table 3.1), we have quantitatively analyzed the metal-ligand bonding between ML and the second ligand L as a function of the L–M–L angle. The results are collected in Figure 3.4 and 3.5 (BDEs in Table 3.2). Most of our model complexes have a d^{10}-type ground state configuration, but not all of them, as indicated in detail in Table 3.2. Yet, all model systems discussed here have been kept in their d^{10}-like configuration, to achieve a consistent comparison and because, on the longer term, we are interested in understanding more realistic dicoordinated d^{10}-ML_2 transition metal complexes that feature, for example, as catalytically active species in metal-mediated bond activation reactions.

We start in all cases from the optimal linear ML_2 structure (*i.e.*, the complex optimized in either D_{3h} or $D_{\infty h}$ symmetry) and analyze the bonding between ML and L' as a function of the L–M–L angle, from 180° to 90°, while keeping all other geometry parameters frozen. The analyses are done in C_s symmetry, bending the complexes in the mirror plane, with the out-of-plane hydrogen atoms of $M(NH_3)_2$ and $M(PH_3)_2$ towards each other. Thus, using Equation 2.13, we are able to separate the orbital interactions symmetric to the mirror plane (A' irrep) from the orbital interactions antisymmetric to the mirror plane (A" irrep):

$$\Delta E_{oi}(\zeta) = \Delta E_{oi}^{A'}(\zeta) + \Delta E_{oi}^{A''}(\zeta) \; . \qquad (3.1)$$

The use of frozen fragment geometries allows us to study purely how the interaction energy changes as the angle is varied, without any perturbation due to geometrical relaxation. Any change in ΔE therefore stems exclusively from a change in $\Delta E_{int} = \Delta V_{elstat} + \Delta E_{Pauli} + \Delta E_{oi}^{A'} + \Delta E_{oi}^{A''}$. Note that rigid bending of the linearly optimized L–M–L complexes causes minima on the energy profiles to shift to larger angles than in fully optimized complexes, but this does not alter any relative structural or energy order.

In Figure 3.4a, we show the energy decomposition analyses (Equation 2.11) and how they vary along the palladium complexes $Pd(NH_3)_2$, $Pd(PH_3)_2$ and $Pd(CO)_2$. Upon bending the LM–L' complex from 180° to 90°, the average distance between the electron density on LM and the nuclei of L' decreases (the Pd–P distance, however, remains constant), which results in a more stabilizing electrostatic attraction ΔV_{elstat}. Likewise, the Pauli repulsion ΔE_{Pauli} increases because of a larger overlap of the lone pair on L' with the d_{z^2}-derived d_σ orbital on the ML fragment. The latter is the antibonding combination of the metal M d_{z^2} orbital and the ligand L lone pair, with a fair amount of metal s character admixed in an L–M bonding fashion. The resulting hybrid orbital is essentially the d_{z^2} orbital with a relatively large torus. The increase in Pauli repulsion that occurs as the L–M–L' angle decreases, stems largely from the overlap of the lone pair on the second ligand L' with this torus. For $Pd(CO)_2$ for example, the overlap of the L' lone pair with the d_σ hybrid orbital on ML increases from 0.05 to 0.28 upon bending from 180° to 90°. We note that this repulsion induces a secondary relaxation, showing up as a stabilizing $\Delta E_{oi}^{A'}$, by which it is largely canceled again. The mechanism through which this relief of Pauli repulsion occurs is that, in the antibonding combination with the L' lone pair, the d_σ orbital is effectively pushed up in energy and (through its L' lone pair component) interacts in a stabilizing fashion with the metal s-derived LUMO on ML.

The aforementioned π backbonding that favors bending (see Figure 3.3) shows up as an increased stabilization in the antisymmetric $\Delta E_{oi}^{A''}$ component upon decreasing the L–M–L angle. To more clearly reveal the role of the orbital interactions with A" symmetry, we separate the interaction energy ΔE_{int} into the corresponding term $\Delta E_{oi}^{A''}$ plus the remaining interaction energy $\Delta E'_{int}$ which combines the other interaction terms comprising electrostatic attraction ΔV_{elstat}, Pauli repulsion ΔE_{Pauli} and the symmetric orbital interactions ($\Delta E_{oi}^{A'}$):

$$\begin{aligned}\Delta E_{int}(\zeta) &= \Delta V_{elstat}(\zeta) + \Delta E_{Pauli}(\zeta) + \Delta E_{oi}^{A'}(\zeta) + \Delta E_{oi}^{A''}(\zeta) \\ &= \Delta E'_{int}(\zeta) + \Delta E_{oi}^{A''}(\zeta)\ .\end{aligned} \tag{3.2}$$

Thus, the interaction energy is split into two contributions which are both stabilizing along a large part of the energy profiles studied, and which vary over a significantly smaller range. Therefore, this decomposition allows us to directly compare the importance of $\Delta E_{oi}^{A''}$ with respect to the combined influence of all other terms, contained in $\Delta E'_{int}$. The latter contains the aforementioned counteracting and largely canceling terms of strong Pauli repulsion between A' orbitals and the resulting stabilizing relaxation effect $\Delta E_{oi}^{A'}$.

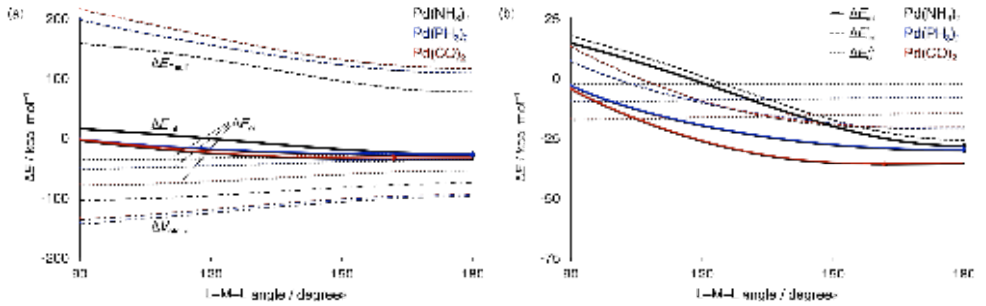

Figure 3.4 Analyses of the interaction between PdL and L in dicoordinated palladium complexes PdL_2 as a function of the L–M–L angle (L = NH_3, PH_3, CO) using (a) the regular energy decomposition scheme (Equation 2.11) and (b) the modified terms as in Equation 3.2. A dot designates the position of the energy minimum.

The results of this alternative decomposition appear in Figure 3.4b, again for the series of palladium complexes $Pd(NH_3)_2$, $Pd(PH_3)_2$ and $Pd(CO)_2$. In each of these complexes, bending begins at a certain point to weaken the $\Delta E'_{int}$ energy term and, at smaller L–M–L angles, makes it eventually repulsive as the Pauli repulsion term becomes dominant (see also Figure 3.4a). Numerical experiments in which we consider the rigid bending process of a complex in which the metal is removed show that steric repulsion between ligands does contribute to this repulsion especially at smaller angles. Thus, direct Pauli repulsion between the L and L' in LM–L' goes, upon bending from 180° to 90°, from 0.3 to 4.6 kcal mol^{-1} for $Pd(NH_3)_2$ and from 0.4 to 9.0 kcal mol^{-1} for $Pd(CO)_2$ (data not shown). This finding confirms that ligands avoid each other for steric reasons, but it also shows that the effect is small compared to the overall change in the ΔE_{int} curves (see Figure 3.4b). The dominant term that causes ΔE_{int} to go up in energy upon bending is the increasing Pauli repulsion that occurs as the ligand L' lone pair overlaps more effectively with the LM d_σ orbital.

In a number of cases, the stabilization upon bending from the antisymmetric orbital interactions $\Delta E_{oi}^{A''}$ dominates the destabilization from the $\Delta E'_{int}$ term. These cases are the complexes that adopt nonlinear equilibrium geometries. This $\Delta E_{oi}^{A''}$ term gains stabilization upon bending LM–L' because the π* acceptor orbital on the ligand L' moves from a position in which it can overlap with a ligand-stabilized LM d_π orbital to a more or less pure metal, and thus up to 1 eV higher in energy, d_δ orbital (see Table 3.3), which leads to a more stabilizing donor-acceptor orbital interaction (see Figure 3.4b). The gain in stabilization of $\Delta E_{oi}^{A''}$ upon bending, and thereby the tendency to bend, increases along NH_3 to PH_3 to CO. The reason is the increasing π-accepting ability of the ligands, as reflected by the energy $\varepsilon(\pi^*)$ of the ligand π* orbital, which is lowered from +1.42 to –0.24 to –1.92 eV, respectively (see Table 3.4). Thus, for $Pd(NH_3)_2$, where π backdonation plays essentially no role, the $\Delta E_{oi}^{A''}$ term is stabilized by less than 0.5 kcal mol^{-1} if the complex is bent from 180° to 90°. For PH_3, known as a moderate π-accepting ligand, this energy term is stabilized by 1.5 kcal mol^{-1} from 180° to 90° and for CO this stabilization amounts to 2.5 kcal mol^{-1}. Thus, in the case of palladium complexes, the energy profile for bending the complexes becomes more flat as the ligands are better π acceptors, but only the carbonyl ligand generates sufficient stabilization through increased π backbonding in $\Delta E_{oi}^{A''}$ to shift the equilibrium geometry to an angle smaller than 180°.

3.5 Bonding Mechanism: Variation of Metals

Applying the same analysis along the series $Rh(CO)_2^-$, $Pd(CO)_2$ and $Ag(CO)_2^+$, reveals a similar, but clearer picture (see Figure 3.5a). Along this series of iso-electronic complexes, the equilibrium geometries have L–M–L angles of 130.8°, 155.6° and 180.0°. Similar to the results obtained for the series discussed above, we find again a $\Delta E'_{int}$ term that is relatively shallow and eventually, at small angles, dominated by the Pauli repulsion. The $\Delta E'_{int}$ term does not provide additional stabilization upon bending the complex. We do observe, however, a $\Delta E_{oi}^{A''}$ component that, from $Rh(CO)_2^-$ to $Pd(CO)_2$ to $Ag(CO)_2^+$, becomes more stabilizing and also gains more stabilization upon bending from 180° to 90°. That is, whereas for $Ag(CO)_2^+$ the $\Delta E_{oi}^{A''}$ remains constant at a value of –5.4 kcal mol^{-1} as the complex is bent from 180° to 90°, the same component for $Pd(CO)_2$ starts already at a more stabilizing value of –15.1 kcal mol^{-1} at 180° and is stabilized more than 2.5 kcal mol^{-1} as the complex is bent to 90°. For $Rh(CO)_2^-$, the effect of the additional stabilization upon bending is strongest, almost 10 kcal mol^{-1}, as $\Delta E_{oi}^{A''}$ goes from –28.4 kcal mol^{-1} at 180° to

–37.3 kcal mol^{-1} at 90°. The mechanism behind this trend is that the donor capability of the metal d orbitals increases as they are pushed up in energy from the cationic $AgCO^+$ to the neutral PdCO to the anionic $RhCO^-$ fragment (see Table 3.3). This trend of increasing d orbital energies leads to a concomitantly strengthening π backdonation and, therefore, an increasing energy difference in the LM fragment between the pure metal d_δ and the ligand-stabilized d_π orbitals. Thus, the "fresh" d_δ orbitals are higher in energy than the ligand-stabilized d_π orbitals by 0.21 to 0.96 to 1.65 eV along $AgCO^+$, PdCO and $RhCO^-$ (see Table 3.3). Consequently, the LM–L' complexes benefit progressively along this series from increasing the overlap of L' π* with the higher-energy d_δ orbitals in the bent geometry.

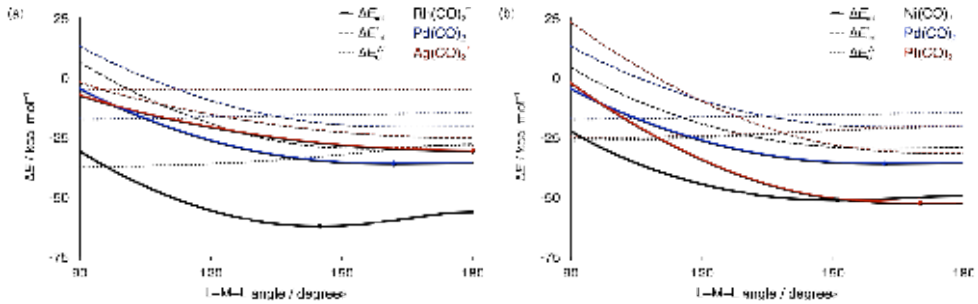

Figure 3.5 Analyses of the interaction (see Equation 3.2) between MCO and CO in transition metal complexes $M(CO)_2$ as a function of the L–M–L angle for (a) M = Rh^-, Pd and Ag^+ and (b) M = Ni, Pd and Pt. A dot designates the position of the energy minimum.

Variation of the metal down a group goes with a less pronounced increase of the L–M–L angle that originates from more subtle changes in the bonding mechanism. The largest variation in bite angle is observed along the group 10 complexes $Ni(CO)_2$, $Pd(CO)_2$ and $Pt(CO)_2$, which show L–M–L angles of 144.5°, 155.6° and 159.0° (see Table 3.1). Two factors are behind this trend: (i) a weakening in π backbonding as the metal orbital energy decreases from Ni 3d to Pd 4d; (ii) a steeper increase upon bending in Pauli repulsion between PtCO d_σ (which has a large torus due to strong admixture of the relativistically stabilized Pt 6s AO) and the lone pair of the other CO ligand. As can be seen in Figure 3.5b, the π-backbonding stabilization of $\Delta E_{oi}^{A''}$ upon bending is indeed stronger for $Ni(CO)_2$ than for $Pd(CO)_2$ and $Pt(CO)_2$. The difference between the latter is small because the greater (more favorable) overlap of the π* orbitals on the ligand with the more

extended platinum d orbitals on PtCO compensates for the lower (less favorable) platinum d orbital energy. Figure 3.5b also shows how the $\Delta E'_{int}$ term containing the aforementioned Pauli repulsion becomes more rapidly destabilizing at smaller angles for $Pt(CO)_2$ than for $Ni(CO)_2$ and $Pd(CO)_2$. Likewise, in the case of group 9 complexes, the more steeply increasing Pauli repulsion of the ligand lone pair with the large iridium d_σ torus pushes the equilibrium L–M–L angle of $Ir(CO)_2^-$ (134.2°) to a larger value than for $Rh(CO)_2^-$ (130.8°; see Table 3.1). Interestingly, here, the linearization energy ΔE_{lin} is nevertheless higher for the less bent $Ir(CO)_2^-$ (13.4 kcal mol^{-1}) than for $Rh(CO)_2^-$ (10.2 kcal mol^{-1}) because of the more favorable π-backbonding overlap between $IrCO^-$ and CO (see Table 3.1). This illustrates the subtlety of the interplay between the two features in the bonding mechanism.

3.6 Walsh Diagrams

Based on detailed Kohn-Sham molecular orbital analyses of individual complexes, we have constructed generalized Walsh diagrams corresponding to bending the ML_2 complexes from 180° to 90°. This choice comes down to an alternative perspective on the same problem and the emerging electronic mechanism why bending may occur is fully equivalent to the one obtained in the preceding analyses based on two interacting fragments LM + L', namely: bending ML_2 to a nonlinear geometry enables ligand π* orbitals (if they are available) to overlap with and stabilize metal d orbitals that are not stabilized in the linear arrangement.

The spectrum of different bonding situations has been summarized in two simplified diagrams that correspond to two extreme situations: weakly π-accepting ligands (Figure 3.6a) and strongly π-accepting ligands (Figure 3.6b). In these diagrams, we position the d_{z^2} orbital in linear ML_2 above the other d orbitals, a situation that occurs, for example, for $Pd(PH_3)_2$. The relative position of the d_{z^2} may change and in some complexes, such as $Rh(NH_3)_2^-$, it is located below the other d orbitals. These variations do not affect the essential property of the orbitals, namely, their change in energy upon bending the ML_2 complex. Furthermore, we speak about weakly π-accepting ligands, not just about (purely) σ-donating ligands, because it turns out that none of our model ligands has negligible π-accepting capability. The resulting Walsh diagrams summarize our results in a more easy-to-use, and pictorial manner which, in particular for the situation with strongly π-accepting ligands, is novel.

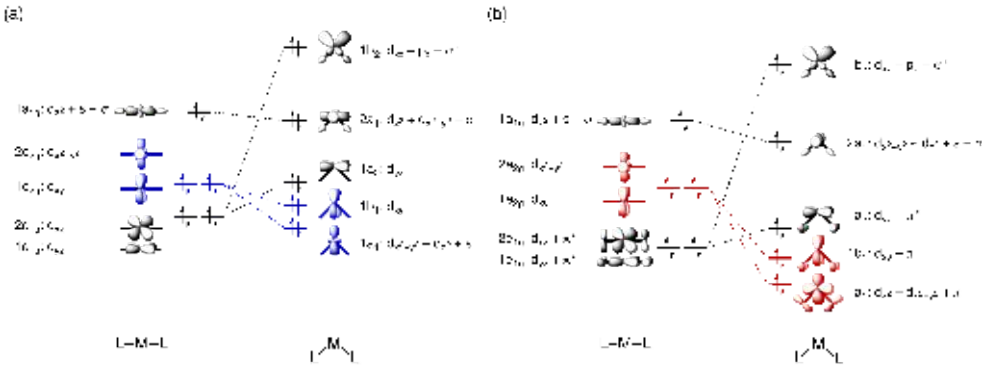

Figure 3.6 Simplified Walsh diagrams for bending ML_2 complexes (a) without π backbonding and (b) with π backbonding, that emerge from our Kohn-Sham MO analyses (+/– indicate bonding/antibonding).

We first examine the diagram with weakly π-accepting ligands (Figure 3.6a). Bending ML_2 from linear to nonlinear significantly destabilizes the d_{xz} orbital because of turning on overlap with the out-of-phase combination of ligand lone pairs. This effect is related to the overlap between the LM d_σ torus and the L' lone pair in the fragment approach (see section 3.4). At small angles, direct ligand-ligand antibonding interactions become important. The d_{z^2} orbital is slightly stabilized in the nonlinear situation due to a decreasing antibonding overlap with the in-phase combination of ligand lone pairs, augmented by admixing with the $d_{x^2-y^2}$ orbital (a detailed scheme of this intermixing is shown in Figure 3.7). Note that if our model ligands would have been purely σ donating, the d_{xy} and d_{yz} levels would not be affected by L–M–L bending. Yet, they are, although only slightly so. This is a manifestation of some π backbonding, which is discussed in more detail below for the strongly π-accepting ligands.

In the case of strongly π-accepting orbitals (Figure 3.6b), bending ML_2 from linear to nonlinear still goes with significant destabilization of d_{xz} and slight stabilization of d_{z^2} (for the same reasons as discussed above for weakly π-accepting ligands). π Backbonding stabilizes both d_{xz} and d_{yz} in the linear L–M–L arrangement; bending reduces π overlap, which causes also d_{yz} to go up in energy. A striking phenomenon in the ML_2 Walsh diagram with strongly π-accepting ligands is the significant stabilization of the $d_{x^2-y^2}$ and d_{xy} orbitals that occurs as bending moves ligand π* orbitals in the right orientation for π-accepting overlap with these orbitals. The resulting stabilization, if strong enough, can overcome the destabilization of the d_{xz} orbital and accounts for the observed bent complexes described in this

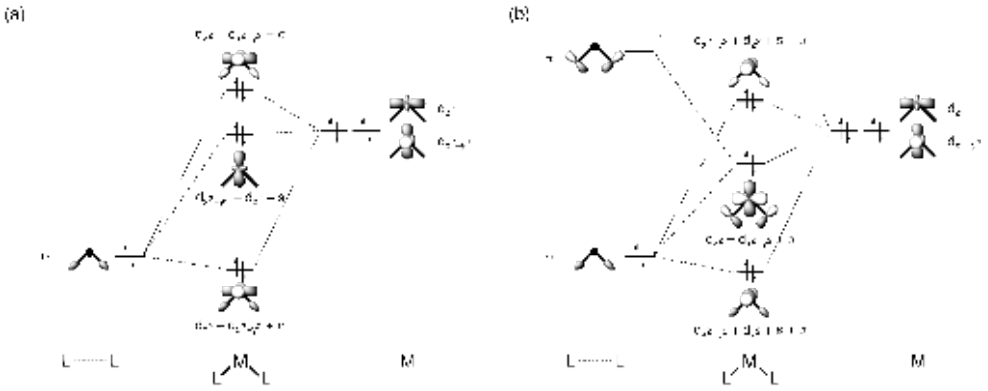

Figure 3.7 Molecular orbital diagram for the mixing of ligand orbitals with the metal $d_{x^2-y^2}$ and d_{z^2} orbitals, (a) without π backbonding and (b) with π backbonding. The lowest-energy molecular orbital that results from these interactions is not shown in the Walsh diagram in Figure 3.6.

chapter. This effect is related to the overlap between the ML d_δ orbital and the L' π* in the fragment approach, as discussed in section 3.3. The same effect also nicely accounts for the nonlinear structures observed in earlier studies for d^0 metal complexes with π-donating ligands.[243-247] For these complexes, a mechanism based on π bonding has been proposed, in which bending is favorable because it effectively increases the number of d orbitals that have non-zero overlap with the π-donating orbitals on the ligands.[244]

3.7 Conclusions

Dicoordinated d^{10} transition metal complexes ML_2 can very well adopt nonlinear geometries with bite angles that deviate significantly from the usually expected 180°. This follows from our relativistic DFT computations on a broad range of archetypal d^{10}-ML_2 model systems. The smallest bite angle encountered in our exploration among 27 model systems amounts to 128.6° for $Co(CO)_2^-$.

Nonlinear geometries appear to be a direct consequence of π backbonding. The geometry of d^{10}-ML_2 complexes results from two opposing features in the bonding mechanism, which we have analyzed in terms of the interaction between ML and L as a function of the L–M–L angle using quantitative MO theory and energy decomposition analyses. Bending destabilizes the interaction ΔE_{int} between ML and L through increasing steric

(Pauli) repulsion between the ligands' lone pair orbital lobes as well as a destabilization, by the latter, of the ML d_σ hybrid orbital; bending can also stabilize ΔE_{int} because of enhanced π backdonation. The reason is that the π-accepting orbital on the ligand L (*e.g.*, CO π*) interacts in the linear arrangement with an already stabilized ML d_π hybrid orbital, whereas in the bent geometry it enters into a more favorable donor-acceptor orbital interaction with an unstabilized, *i.e.*, higher-energy metal d_δ orbital.

Our analyses complement the existing textbook Walsh diagram for bending ML_2 complexes[213] with a variant that includes metal-ligand π backbonding. Our findings also contribute to a more rational design of catalytically active and selective ML_2 complexes, as will be demonstrated in chapters 6 and 7.

4 Steric Attraction and Steric Repulsion: The Effect of Bulky Ligands

Previously appeared as

Role of Steric Attraction and Bite-Angle Flexibility in Metal-Mediated C–H Bond Activation
L. P. Wolters, R. Koekkoek, F. M. Bickelhaupt
ACS Catal. **2015**, *5*, 5766–5775

4.1 Introduction

The active catalyst in cross-coupling reactions is often a dicoordinated palladium phosphine complex. An important geometric parameter of a catalyst is its bite angle, that is, the ligand-metal-ligand angle. It is known that a smaller bite angle leads to a lower barrier for the oxidative addition step,[35-37,44,49-54,248-250] because of less steric repulsion between the substrate and the ligands.[241,251] Also in other catalytic processes (*e.g.*, hydroformylation, hydrocyanation and Diels-Alder reactions) the bite angle is one of the parameters known to affect the activity, as well as regioselectivity of the catalyst complex.[250] Control over the bite angle is usually achieved using bidentate ligands in which the coordinating sites are bridged by, for example, a hydrocarbon chain of variable length. A study on palladium complexes with chelating ligands has addressed the precise nature of the bite-angle effect on oxidative addition reaction barriers.[241,251] The results clearly indicate that a catalyst with a smaller bite angle displays higher reactivity because it does not have to bend away its ligands to avoid repulsive interactions of the ligands with the substrate. Thus, the bite-angle effect on reaction barriers is primarily steric in nature. The electronic nature,[49,50,252] that is, stabilization of the transition state due to stronger donor-acceptor orbital interactions from metal d orbitals to the substrate σ^* orbital as one of the metal-ligand d hybrid orbitals is pushed up in energy at smaller bite angles (see section 3.6), has a much smaller effect on the reaction barrier.

The active catalytic species in cross-coupling reactions is, however, often a dicoordinated d^{10}-ML_2 complex where L is a non-chelating ligand. Geometries of d^{10}-ML_2 transition metal complexes are generally assumed to have linear ligand-metal-ligand angles.[36,213,253-255] In the previous chapter, however, we showed that this is not necessarily the case, as several complexes with significantly bent L–M–L geometries were encountered. Detailed analyses revealed that a number of d^{10}-ML_2 complexes prefer nonlinear geometries, because the two ligands then do not compete for π backdonation from the same metal d orbital. Of course, in order to prefer a nonlinear geometry the additional stabilization that results from this effect must be greater than the additional steric repulsion that occurs upon bending. Since most phosphine-ligated catalysts used in practical applications of cross couplings feature hydrocarbon substituents that are much bulkier than the hydrogens in our model catalysts, we here test if the previous findings still apply to catalyst complexes with more realistic ligands. Many studies have addressed the steric properties of such ligands[256-261] and their effect on reactivity.[47,262-275] One might expect that the propensity to bend is decreased, because the more bulky ligands will tend to avoid mutual steric repulsions. $Pd(P\textit{t}Bu_3)_2$ ($\textit{t}Bu_3$ = *tert*-butyl) is indeed known to have a 180° ligand-metal-ligand angle.[276] However, a crystal structure of $Pd(PPh(\textit{t}Bu)_2)_2$ (Ph = phenyl) obtained by Otsuka *et al.*[233] reveals a bite angle of 177.0°, and Immirzi and Musco reported a crystal structure of $Pd(PCy_3)_2$ (Cy = cyclohexyl) showing a bite angle of only 158.4°.[232] In addition, the analogous platinum complex, $Pt(PCy_3)_2$ appears to have a nonlinear L–M–L angle of 160.5°, as revealed by crystallographic data.[277] Leitner *et al.* have reported[234] computational results on the structures of dicoordinated palladium phosphine complexes, and found nonlinear P–Pd–P angles for a number of compounds. Notably, for $Pd(PCy_3)_2$ they obtained an angle of 162°, in reasonable agreement with the crystal structure. Many other computational studies, however, reported linear geometries, or deviations from linearity of only a few degrees.[45,46,278-281]

Despite the available experimental data, and numerous computational studies on palladium phosphine complexes, the observed nonlinearity has, to the best of our knowledge, never been explained. In this chapter, we discuss a series of dicoordinated palladium complexes $Pd(PR_3)_2$ with phosphine ligands PR_3 of varying steric bulk, in which the substituents R are hydrogen (H), methyl (Me), isopropyl ($\textit{i}Pr$), *tert*-butyl ($\textit{t}Bu$), cyclohexyl (Cy), or phenyl (Ph). Interestingly, although the expected linear geometries emerge for $Pd(PH_3)_2$, $Pd(PMe_3)_2$ and $Pd(P\textit{t}Bu_3)_2$, we find that $Pd(P\textit{i}Pr_3)_2$, $Pd(PCy_3)_2$ and $Pd(PPh_3)_2$ have nonlinear bite angles of 172.4°, 148.2° and even 132.2°, respectively. We relate these findings

to the precise steric properties of the ligands, that is, size but also shape. Activation strain analyses in combination with quantitative molecular orbital (MO) theory explain this dichotomy because they reveal that steric bulk may operate in two distinct ways: (i) one mechanism is the usual steric repulsion deriving from overlap between closed-shell orbitals of intimate and isotropically bulky ligands; (ii) the second mechanism embodies steric attraction,[282,283] which occurs as a result of dispersion interactions between anisotropically bulky ligands (*e.g.*, flat ligands with a large surface, "sticky pancakes") that are not yet in direct contact.

Although the importance of dispersion interactions has been noted by several research groups in the past,[46,284-290] it is often believed that its energetic effect is moderate, and arises only due to additional intermolecular attraction. Here, we show that intramolecular dispersion interactions can also be of paramount importance to obtain both qualitatively and quantitatively correct results. Furthermore, we reveal how steric attraction can result in nonlinear ligand-metal-ligand angles, and softens the resistance towards bending this angle, *i.e.*, it enhances what we designate the 'bite-angle flexibility'. This leads to surprisingly low reaction barriers for methane C–H activation, even for rather congested model catalysts such as $Pd(PCy_3)_2$ and $Pd(PPh_3)_2$. These results suggest that not the bite angle itself, but the intrinsic bite-angle flexibility of the catalyst is of relevance to the reaction barrier. This indicates that a single structural parameter based on the catalyst's equilibrium geometry (*e.g.*, the bite angle) is not necessarily sufficient to account for the catalyst's activation strain, let alone for predicting its activity.

4.2 $Pd(PR_3)_2$ Geometries and Pd–PR_3 Bond Analyses

Shown in Figure 4.1 are the equilibrium geometries for the series of $Pd(PR_3)_2$ complexes, obtained at the dispersion-corrected ZORA-BLYP-D3/TZ2P level of theory. We find linear bite angles for $Pd(PH_3)_2$, $Pd(PMe_3)_2$ and $Pd(P\textit{t}Bu_3)_2$, whereas $Pd(P\textit{i}Pr_3)_2$, $Pd(PCy_3)_2$ and $Pd(PPh_3)_2$ have bent equilibrium geometries. $Pd(P\textit{i}Pr_3)_2$ is bent slightly, having a bite angle of 172.4° and being less than 0.1 kcal mol^{-1} more stable than the linear geometry. For $Pd(PCy_3)_2$ we find an angle of 148.2°, in rather good agreement with the available X-ray structure.[233] $Pd(PPh_3)_2$ is even more bent, having a ligand-metal-ligand angle of only 132.2°. These latter angles are surprisingly small, given that the much less bulky $Pd(PH_3)_2$, for which one would expect even less resistance towards bending, is linear. We will show,

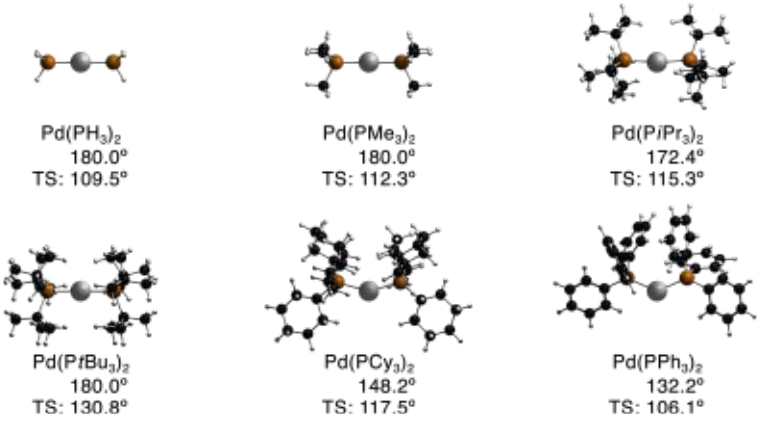

Figure 4.1 Equilibrium geometries and P–Pd–P angles (TS: value in TS for methane C–H activation) of palladium phosphine complexes.

however, that the greater steric dimension in $Pd(PCy_3)_2$ and $Pd(PPh_3)_2$ is, counterintuitively, of key importance to rationalize their nonlinearity.

In chapter 3, we have shown that most dicoordinated transition metal complexes have very flat potential energy surfaces for decreasing the ligand-metal-ligand angle to values smaller than 180°, due to enhanced π backbonding when the ligands interact with different d orbitals on the metal center. This additional stabilizing interaction can in some cases (*i.e.*, for strong π-accepting ligands at an electron-donating metal center) outweigh the increased steric repulsion that occurs for smaller ligand-metal-ligand angles, leading to nonlinear ML_2 complexes. To see if the same explanation holds for the $Pd(PR_3)_2$ complexes studied here, we have performed brief Pd–PR_3 bond analyses. The results (shown in Table 4.1) for the monocoordinated $PdPR_3$ complexes (R = H, Me, *i*Pr, *t*Bu, Cy, Ph) show that, in the present series, the trend in nonlinearity appears not to be caused by the π-backbonding capabilities. This is indicated by the small variation in the orbital interaction term (which for all complexes is between –61.1 and –63.6 kcal mol^{-1}) and the VDD charge on the palladium center changes irregularly instead of systematically. In the previous chapter, we found much larger and more systematic variations of these terms. Furthermore, the populations of the π-donating orbitals on Pd (*i.e.*, the d_{xz} and d_{yz} orbitals when the Pd–PR_3 bond is aligned with the z axis) are essentially equal for each complex and consistently between 1.88 and 1.90 electrons.

These results therefore indicate that, although π backbonding contributes to the bite-angle flexibility of these complexes, it is not the dominant factor for their bent equilibrium geometries. This is confirmed by geometry optimizations of the $Pd(PR_3)_2$ complexes at the dispersion-free, but otherwise similar ZORA-BLYP/TZ2P level of density functional theory, at which we find the angles of the bent complexes to be increased to 173.9° for $Pd(PiPr_3)_2$, 179.4° for $Pd(PCy_3)_2$ and 180.0° for $Pd(PPh_3)_2$. Thus, although the slightly bent ligand-metal-ligand angle for $Pd(PiPr_3)_2$ is indicative for an important contribution from the mechanism based on π backdonation in this complex, the bent geometries of $Pd(PCy_3)_2$ and $Pd(PPh_3)_2$ originate from dispersive ligand-ligand attraction. In the following, we will therefore elaborate on the steric characteristics of the ligands, and show that sterically repulsive bulk should be distinguished from sterically attractive bulk. The latter is of crucial importance to explain the observed ordering of the ligand-metal-ligand angles along the $Pd(PR_3)_2$ series in the present chapter.

Table 4.1 Pd-PR_3 bond analyses (in Å, electrons and kcal mol^{-1}) for the monocoordinated $PdPR_3$ complexes, relative to the ground state ($d^{10}s^0$) Pd atom and the ligand.[a]

	M–L	Q_{Pd}^{VDD}	ΔE	ΔE_{int}	ΔV_{elstat}	ΔE_{Pauli}	ΔE_{oi}	ΔE_{disp}
$PdPH_3$	2.174	−0.044	−40.9	−41.2	−165.6	+189.4	−63.6	−1.4
$PdPMe_3$	2.186	−0.125	−49.0	−49.5	−189.9	+208.0	−63.6	−4.0
$PdPiPr_3$	2.210	−0.064	−52.8	−53.4	−185.8	+202.1	−61.9	−7.8
$PdPtBu_3$	2.228	−0.042	−53.1	−53.7	−181.6	+198.2	−61.1	−9.2
$PdPCy_3$	2.209	−0.009	−53.5	−54.1	−187.0	+203.1	−61.8	−8.4
$PdPPh_3$	2.198	−0.055	−49.7	−50.0	−175.0	+195.1	−63.2	−7.0

[a] See Equations 2.8, 2.9 and 2.11.

To explain the different ways in which steric bulk can operate, we distinguish three situations that can occur for ML_2 complexes, schematically displayed in Figure 4.2. Firstly, when small, non-bulky ligands are present, there is no significant steric congestion, and the complex is relatively indifferent towards bending its ligand-metal-ligand angle. For these complexes the electronic effects, as mentioned before and described in chapter 3, are decisive. Secondly, for the larger, bulkier ligands, steric effects are obviously more important. These effects are generally considered to be unfavorable for bending. In a sterically crowded situation, displayed schematically in the center of Figure 4.2, there is already in the linear geometry some ligand-ligand repulsion. Bending the ligands towards each other strength-

ens this steric repulsion by increasing the number of closed shell-closed shell (Pauli, or steric) repulsions. Thirdly, however, as we have just seen, steric effects can also be favorable for bending. When the ligands are sizable, but not as sterically crowded, as displayed on the right of Figure 4.2, there is less steric congestion and bending barely induces repulsion between the ligands. Instead, decreasing the L–M–L angle brings the ligands closer to each other and strengthens attractive dispersion interactions between the contact surfaces of the ligands. This "sticky pancake" effect stabilizes a nonlinear geometry and becomes stronger as the shape of ligands becomes more flat, leading to larger contact surfaces.

In solution, this picture still applies. The presence of a solvent does not alter the situation for small ligands, or for ligands with isotropically bulky substituents, because there are no significant dispersion interactions to be quenched, and any repulsive interaction still persists. The effect of solvents on steric attraction, however, is moderate as well. In the linear situation the solvent molecules can occupy the space between the ligands, giving rise to some dispersion interactions between the ligand and the solvent (see Figure 4.2, at the very right). When the ligands are bent towards each other, these solvent molecules are pushed out from between the ligands, leading again to a situation similar to that of the gas phase, but now within a solvent shell. This may go with some quenching of the net ligand-ligand dispersion stabilization upon bending, when the ligand-solvent interaction becomes of comparable magnitude as the ligand-ligand interaction by which it is replaced in the bent configuration. The important point, however, is that the PES for L–M–L bending remains shallow. In other words, complexes with bulky, yet flat ligands remains flexible in solution.

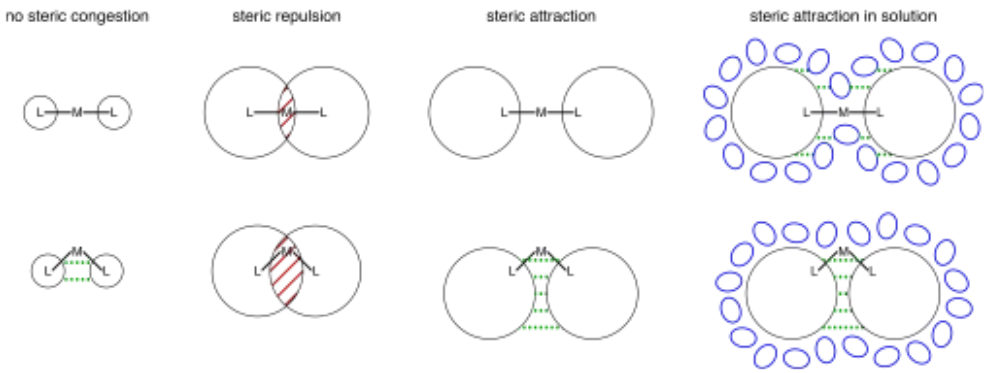

Figure 4.2 Schematic representation of different steric situations in ML_2 complexes. For the situation in solution, only the relevant interactions that occur in the region between the ligands are indicated.

Thus, especially for the small L–M–L angles encountered in chemical reactions of these complexes (as will be discussed in a later section), solvent effects can be expected to play no significant role, and the most important characteristics can be recovered from analyses in vacuum, which we therefore choose to discuss in the following sections.

These schematic representations allow us to rationalize the trend encountered along the series of $Pd(PR_3)_2$ complexes. To do so, it is important to consider the bite-angle flexibility of the catalyst complexes, instead of only the value of the ligand-metal-ligand angle in the equilibrium geometry. To investigate the flexibility of the bite angle, we have computed the energy profiles for bending the L–M–L angle of the complexes from 180° towards 90° while all other geometry parameters are allowed to relax (see Figure 4.3). We find for all complexes a rather flat energy profile between 180° and 150°, indicative for additional π backbonding upon bending, which compensates for (part of) the steric repulsion. Thereafter, the curves start to ascend due to dominating repulsive effects. The increase is least steep for $Pd(PH_3)_2$, because it has the smallest substituents and therefore is an example of a catalyst complex that is sterically indifferent towards bending. Going from $Pd(PH_3)_2$ to $Pd(PMe_3)_2$, $Pd(P\mathit{i}Pr_3)_2$ and $Pd(P\mathit{t}Bu_3)_2$, the steric bulk on the ligands is gradually increased and thereby also the bite-angle rigidity. This is indicated by the more steeply increasing energy profiles in Figure 4.3, and correlates well with the larger Tolman cone angles along this series of ligands, which are 87°, 118°, 160° and 182°, respectively.[38] Other parameters, such as the solid cone angles, reveal a similar trend for the series of ligands in this work.[291-293] Note that $Pd(P\mathit{i}Pr_3)_2$ is bent slightly also when dispersion is ne-

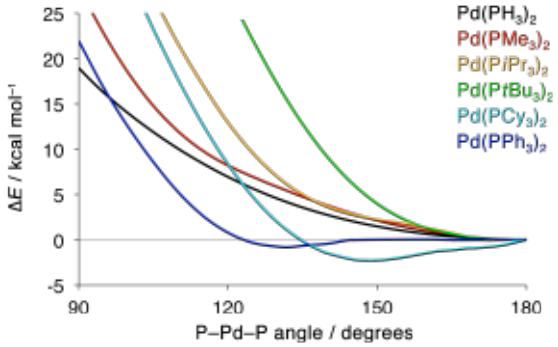

Figure 4.3 Potential energy surfaces for bending $Pd(PR_3)_2$ complexes, relative to the energy of the complex constrained to a 180° ligand-metal-ligand angle.

glected, but the bent equilibrium geometry is only marginally more stable than the linear geometry. We therefore conclude that its bending is the result of a delicate balance between the enhanced π backbonding and the opposing steric repulsion. On a flat potential energy surface, the position of the minimum is sensitive even to minor variations in the energy components.

Going from $Pd(PtBu_3)_2$ to $Pd(PCy_3)_2$ and $Pd(PPh_3)_2$, the ligands remain quite sizable, but the bulk is less isotropically distributed. The cyclohexyl substituents are not as bulky as *tert*-butyl substituents because they do not bind to the phosphorus atom via a tertiary carbon atom, and rotate to avoid steric repulsion when the ligands are bent towards each other. In addition, there is room between the ligands, allowing the cyclohexyl substituents to rotate such that the attractive dispersion interactions between the ligands are enhanced. Going to the phenyl substituents reduces the bulkiness even further because these cyclic substituents consist of planar sp^2-hybridized carbon atoms instead of tetrahedral sp^3-hybridized carbon atoms. This leads to even less steric crowding between the ligands, and therefore stronger steric attraction and consequently a smaller value of the bite angle. Again, this is in agreement with their Tolman cone angles, which for PCy_3 (170°) and PPh_3 (145°) are smaller than for $PtBu_3$ (182°).[38] The effect of steric attraction manifests itself also clearly when the bite-angle flexibility is considered: besides first descending to a minimum upon reducing the L–M–L angle from 180°, the bending energy profiles for these complexes are in general not strongly destabilized at smaller angles. The bending energy profile for $Pd(PCy_3)_2$ remains below that of $Pd(PiPr_3)_2$ even for angles as small as 100°, whereas that of $Pd(PPh_3)_2$ even remains below that of $Pd(PH_3)_2$ in this range.

Note that similar reasoning can be used to account for the recent finding by Zhang and Dolg that the sterically more crowded *syn* isomer of a double C_{60} adduct of pentacene is more stable than the *anti* isomer.[294] In addition, such sterically attracting substituents can be considered to act as dispersion energy donors, a term recently introduced by Grimme and Schreiner.[295]

The potential energy surfaces in Figure 4.3 contain only the geometries connected to the energetically lowest conformations found. For all but the smallest complexes (*i.e.*, all but $Pd(PH_3)_2$ and $Pd(PMe_3)_2$), we found other local minima at higher energies, in which one or more of the substituents have been rotated. Most notably, for $Pd(PiPr_3)_2$, we also encountered a linear L–M–L structure at 8.2 kcal mol^{-1} above the global minimum with its angle of 172.4°. For $Pd(PCy_3)_2$, a slightly more bent (146.8°) conformer was found at 2.7 kcal mol^{-1}, as well as a less bent geometry (158.3°) at 0.5 kcal mol^{-1} above the global mini-

mum which assumes a bite angle of 148.2° (see Table 4.2). The angle of 158.3° matches the value of 158.4° from the crystal structure[232] better than the angle of 148.2° in the global minimum. Note, however, that this is not true for more rigid geometry parameters, such as the Pd–P bond lengths and the orientation of the substituents, for which significantly better agreement is achieved between our global minimum and the crystal structure.

For $Pd(PPh_3)_2$, the global minimum is stabilized by three C–H···π interactions occurring in a 'Z' pattern between the phenyl rings on the different ligands. A different local minimum is obtained when the ligands are in nearly eclipsed positions and the phenyl rings on one ligand are oriented perpendicular to each other as well as to the phenyl rings on the other ligand. This leads to only two C–H···π interactions between the ligands and a corresponding geometry with a larger bite angle of 141.0° and 0.7 kcal mol^{-1} higher in energy. We have not further analyzed the exact nature of these interactions,[296] as this is beyond the scope of the present work, and, as noted before, the geometry assumes a linear bite angle if dispersion is not accounted for. This suggests that an eventual contribution from the C–H···π interactions to the stability of the nonlinear geometry is not as important as that from the dispersion interactions. Besides, when the complex is bent to smaller angles, as during the oxidative addition to which we will soon turn our focus, the phenyl rings more closely adopt a face-to-face orientation, further reducing the likelihood of any significant stabilizing contribution from C–H···π interactions.

4.3 The Effect of Steric Attraction on Oxidative Addition

In this section, we explore the consequences of steric attraction, and the resulting catalyst bite-angle flexibility or nonlinearity, on the energy profiles of methane oxidative addition reactions. For both oxidative addition and its reverse reaction, reductive elimination, it is well known that the bite angle of the catalyst complex has a great influence on the activity and selectivity of the process.[35-37,44,49-54,248-250] We here test if the effect of steric attraction is relevant when assessing a catalyst's activity. To this end, we have studied the addition of the methane C–H bond to the palladium center of the series of $Pd(PR_3)_2$ complexes (with R = H, Me, *i*Pr, *t*Bu, Cy and Ph) analyzed above. We chose the archetypal methane C–H bond as a simpler, but representative model for the aryl halide bonds used more commonly in practice. From previous work[241] it is known that prereactive catalyst-substrate complexes essentially do not exist for dicoordinated catalysts, or are held together only by weak dispersion interactions. We therefore have not attempted to locate these weakly bound

complexes, and will discuss only the transition states (TSs) and product complexes (PCs). These two stationary points, together with additional analyses, reveal sufficient insight into the reaction energy profiles for this series of catalysts.

Using again the dispersion-corrected ZORA-BLYP-D3/TZ2P level of theory, we find a barrier of +29.5 kcal mol^{-1} for $Pd(PH_3)_2$, followed by a slightly lower barrier of +28.4 kcal mol^{-1} for $Pd(PMe_3)_2$. Thereafter, the barriers increase to +30.0 kcal mol^{-1} for oxidative addition to $Pd(PiPr_3)_2$ and +43.1 kcal mol^{-1} for $Pd(PtBu_3)_2$. For $Pd(PCy_3)_2$ and $Pd(PPh_3)_2$, we find that the barrier decreases monotonically in rather large steps, to +31.1 and +20.9 kcal mol^{-1}, respectively (see Table 4.2). We have performed a preliminary exploration of solvent effects, by applying the COSMO (Conductor-like Screening Model) method,[297,298] as implemented in ADF,[299] on the gas phase geometries. Toluene was chosen as a solvent, and modeled with a dielectric constant of 2.38, a solvent radius of 3.48 Å. Atomic radii taken from the MM3 van der Waals radii[300] scaled by 0.8333.[301] Work by Riley *et al.* suggests that the dispersion correction does not need to be modified when combined with implicit solvation models.[302] With this approach, we find only slightly different reaction barriers (roughly 0.5 kcal mol^{-1}) in solvent.

Table 4.2 Geometries (in degrees and Å) and activation strain analyses (in kcal mol^{-1}) for the transition states of the oxidative addition of methane to $Pd(PR_3)_2$.[a]

	L–M–L[b]	C–H	$\Delta E^{\ddagger}$[c]	$\Delta E^{\ddagger}_{strain}$	$\Delta E^{\ddagger}_{strain}$[cat]	$\Delta E^{\ddagger}_{strain}$[sub]	$\Delta E^{\ddagger}_{int}$
$Pd(PH_3)_2$	109.5 (180.0)	1.734	+29.5 [+29.9]	+80.1	+16.4	+63.8	–50.7
$Pd(PMe_3)_2$	112.3 (180.0)	1.641	+28.4 [+28.8]	+72.3	+17.9	+54.4	–43.9
$Pd(PiPr_3)_2$	115.3 (172.4)	1.712	+30.0 [+29.7]	+79.6	+16.2	+63.4	–49.6
$Pd(PtBu_3)_2$	130.8 (180.0)	1.962	+43.1 [+42.7]	+108.9	+22.4	+86.6	–65.8
$Pd(PCy_3)_2$	117.5 (148.2)	1.729	+31.1 [+31.1]	+81.5	+17.9	+63.6	–50.3
$Pd(PPh_3)_2$	106.1 (132.2)	1.700	+20.9 [+20.8]	+71.0	+10.7	+60.3	–50.0

[a] See Equation 2.9. [b] In parentheses the value of the ligand-metal-ligand angle in the equilibrium geometry of the catalyst complex. [c] Values in square brackets include solvation effects, computed for toluene with the COSMO model.

A similar series of catalysts was studied by Liu and co-workers for the oxidative addition of aryl halides using dispersion-free DFT.[279] Interestingly, they found only a small decrease (2.3 kcal mol^{-1}) in barriers when going from $Pd(PiPr_3)_2$ to $Pd(PPh_3)_2$. Results obtained by Maseras *et al.* with dispersion-corrected DFT show that the barrier for CH_3Br addition to $Pd(PPh_3)_2$ is roughly 4 kcal mol^{-1} lower than the barrier for addition to

$Pd(PH_3)_2$.[280] Harvey and co-workers reported[284] that the reaction barrier for aryl halide addition to $Pd(PPh_3)_2$ is about 1 kcal mol^{-1} higher than for $Pd(PCy_3)_2$, and that the barrier for the small $Pd(PH_3)_2$ is similar to that of the larger complexes (for C–Cl activation) or slightly lower than the barrier for the larger complexes (for C–Br activation).

Table 4.3 Geometries (in degrees and Å) and activation strain analyses (in kcal mol^{-1}) for the product complexes of the oxidative addition of methane to $Pd(PR_3)_2$.[a]

	L–M–L[b]	C–H	ΔE[c]	ΔE_{strain}	ΔE_{strain}[cat]	ΔE_{strain}[sub]	ΔE_{int}
$Pd(PH_3)_2$	107.2 (180.0)	2.430	+24.3 [+23.2]	+134.5	+18.6	+115.8	–110.2
$Pd(PMe_3)_2$	107.6 (180.0)	2.512	+19.0 [+17.9]	+141.0	+21.9	+122.0	–122.0
$Pd(PiPr_3)_2$	111.8 (172.4)	2.341	+25.8 [+24.6]	+133.9	+20.5	+113.4	–78.8
$Pd(PtBu_3)_2$	129.7 (180.0)	2.112	+43.1 [+42.6]	+122.0	+24.0	+97.9	–78.8
$Pd(PCy_3)_2$	112.2 (148.2)	2.402	+26.3 [+25.4]	+139.8	+24.4	+115.4	–113.5
$Pd(PPh_3)_2$	102.6 (132.2)	2.417	+15.4 [+14.7]	+126.9	+14.0	+112.9	–111.4

[a] See Equation 2.9. [b] In parentheses is the value of the ligand-metal-ligand angle in the equilibrium geometry of the catalyst complex. [c] Values in square brackets include solvation effects, computed for toluene with the COSMO model.

The product complexes reveal a trend similar to that of the transition states, as shown by a comparison of Table 4.2 and 4.3. With the exception of $Pd(PMe_3)_2$ and $Pd(PtBu_3)_2$, all product complexes are roughly 5 kcal mol^{-1} lower in energy and have slightly more bent P–Pd–P angles than the transition states. For $Pd(PMe_3)_2$, the difference in energy is 9.4 kcal mol^{-1}. For $Pd(PtBu_3)_2$, we find a stable product complex (no imaginary frequencies) with a methane C–H stretch that is 0.16 Å greater than in the transition state geometry. However, the energy difference between the two is essentially zero (ca. 0.01 kcal mol^{-1}), within the precision of our numerical techniques. In other words, the reaction leads to a product plateau. Thus, for $Pd(PtBu_3)_2$, the reverse reaction, that is, reductive elimination, proceeds without a barrier. We find that solvation by toluene induces a slightly larger effect on the reaction energies (the energy of the product complex relative to reactants) than was found for the barriers (the energy of the transition state relative to reactants), but the solvent effect on the product complexes is still small, around 1 kcal mol^{-1}, and does not alter the trend.

In order to reveal the origin of the differences in oxidative addition barrier height along our series of model catalysts, we have performed activation strain analyses along the approximated partial reaction energy profiles in the transition state region, obtained by the

TV-IRC method[188] (Figure 4.4a). The harmonic approximation on which the TV-IRC method is based, appears to be only entirely valid for $Pd(PH_3)_2$. For the other catalyst complexes this approximation results in partial energy profiles in the TS region with energy maxima that are slightly higher, and shifted along the reaction coordinate as compared to the actual TS. In Figure 4.4, the positions of the actual transition states (*i.e.*, the fully optimized TS geometries) are indicated. It should be noted that the deviations of the TV-IRC maxima from the real transition states are small compared to the size of the effect we are seeking to explain, which is the overall increase in barrier height from $Pd(PH_3)_2$ to $Pd(P\textit{t}Bu_3)_2$, and the significant drop in barrier height along $Pd(P\textit{t}Bu_3)_2$, $Pd(PCy_3)_2$ and $Pd(PPh_3)_2$.

Firstly, we note that the energy profiles and activation strain analyses for $Pd(PH_3)_2$, $Pd(PMe_3)_2$ and $Pd(P\textit{i}Pr_3)_2$ are rather similar. Not only the energy profiles lie within a few kcal mol^{-1}, also the components ΔE_{strain} and ΔE_{int} show only subtle variations (Figure 4.4a). Apparently, there are only minor differences in bite-angle flexibility (see also values for $\Delta E^{\ddagger}_{strain}$[cat] in Table 4.2) and catalyst-substrate bonding capability among these three catalysts. We will not focus on these subtleties, but instead look at the significant increase in barrier height when going to $Pd(P\textit{t}Bu_3)_2$. For the latter, we find a much larger increase in barrier, caused by a more destabilizing strain term as well as less stabilizing catalyst-substrate interaction ΔE_{int} (see Figure 4.4a). Both these differences are directly related to the increased steric crowding associated with the isotropically bulky *t*Bu substituents. Decomposing the strain term into contributions from catalyst and substrate deformation ($\Delta E_{strain} = \Delta E_{strain}$[cat] + ΔE_{strain}[sub]) reveals that the increase stems primarily from the catalyst deformation ΔE_{strain}[cat] (see Figure 4.4b). The curves for substrate deformation (ΔE_{strain}[sub]) roughly coincide for all catalysts, whereas the catalyst deformation term is clearly higher for $Pd(P\textit{t}Bu_3)_2$. This can be attributed to the decreased bite-angle flexibility of the latter catalyst, which requires more energy to bend (see also Figure 4.3), even though the ligand-metal-ligand angle of 130.8° at the TS is more linear than for any other catalyst in this series. At the same time, the bulkier $\textit{t}Bu_3$ substituents on the phosphine ligands lead to more Pauli repulsive interactions with the substrate, thereby weakening the interaction ΔE_{int} significantly. Note that the values in Table 4.2 are not suitable for such an analysis because they refer to the quite different positions at which the various TSs occur along the reaction coordinate (see C–H distances of activated bond in TS), a condition that prevents a consistent comparison.[194]

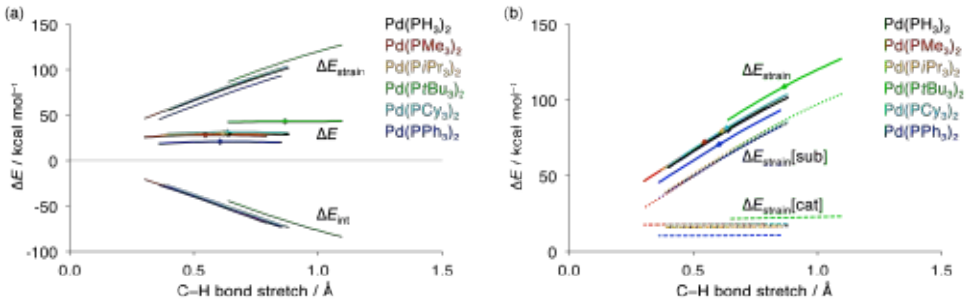

Figure 4.4 Activation strain analyses (a) and strain energy decomposition (b) along the reaction coordinate (see Equation 2.10) in the region around the TS for oxidative addition of CH_4 to $Pd(PR_3)_2$ catalyst complexes. A dot designates the position of the TS.

Continuing along the series of catalyst complexes, we find that, upon going from $Pd(PtBu_3)_2$ to $Pd(PCy_3)_2$, the transition state is stabilized again. This is because both factors causing the high reaction barrier for $Pd(PtBu_3)_2$ disappear in the case of $Pd(PCy_3)_2$, which is nonlinear and has a higher bite-angle flexibility. Firstly, there is a lower strain energy, which, as shown in Figure 4.4b, is the result of a smaller contribution from ΔE_{strain}[cat]. Thus, there is less deformation energy from bending the catalyst, although the catalyst's bite angle in the TS geometry is smaller than that of $Pd(PtBu_3)_2$ (see Table 4.2). Again, this is in line with the results shown in Figure 4.3, and a direct consequence of the steric attraction between the ligands. Secondly, when the ligands are bent further away from the substrate, there is, compared to $Pd(PtBu_3)_2$, a relief in Pauli repulsion between catalyst and substrate. This strengthens the interaction energy ΔE_{int} for $Pd(PCy_3)_2$ compared to that of $Pd(PtBu_3)_2$. Going to $Pd(PPh_3)_2$, we find that, although the ligand-metal-ligand is even smaller than for $Pd(PCy_3)_2$, again the catalyst deformation energy is lowered (Figure 4.4b) due to the increased steric attraction, and resulting bite-angle flexibility. Because the interaction energy is not much different from that of $Pd(PCy_3)_2$ (Figure 4.4a), it is the lower strain term that directly causes the lowering of the reaction barrier. Note that we find that the interaction energy term for $Pd(PPh_3)_2$ is only slightly more stabilizing, even though the PPh_3 ligand is known to be a stronger electron donor than, for example, the PH_3 ligand. From Figure 4.4a, it is clear that any electronic effect stemming from this increased electron-donating capability is small compared to the effect on the ΔE_{strain} curves that results from the bite-angle flexibility. Interestingly, the barrier for $Pd(PPh_3)_2$ ends up

as the lowest among this series of catalysts, being 8.6 kcal mol^{-1} lower than the barrier for addition to the much smaller, archetypal $Pd(PH_3)_2$.

It follows that applying dispersion corrections can have significant effects on reaction barriers. This is neither because the additional intermolecular dispersion strengthens the catalyst-substrate interaction (this contribution is strongest for $Pd(P\textit{t}Bu_3)_2$ and only around 9 kcal mol^{-1}), nor because of stronger donor-acceptor interactions between the catalyst and substrate, that would result from destabilized d hybrid orbitals upon increased bite-angle bending. These two effects would strengthen the catalyst-substrate interaction energy ΔE_{int}. Rather, it is the difference in the strain energy ΔE_{strain}, resulting from the variation among catalyst contributions, that causes the observed trends in reaction barriers.

Thus, the bite-angle flexibility of the catalyst, which is significantly increased by intramolecular dispersion interactions, leads to less destabilized reactants and therefore lower reaction energy profiles. This effect of steric attraction is reminiscent to the bite-angle effect as described for palladium complexes with chelating ligands[241,251] and which, as we will discuss in chapter 6, also occurs for certain complexes with non-chelating ligands. The catalyst complexes discussed in this chapter furthermore reveal that steric attraction as a result of dispersion interactions, is of paramount importance to obtain quantitatively and even qualitatively accurate results for realistic catalyst complexes.

4.4 Conclusions

More bulky ligands in d^{10}-ML_2 complexes may enhance, instead of counteract, L–M–L bite-angle bending. Traditional behavior is found for $Pd(PH_3)_2$, $Pd(PMe_3)_2$ and $Pd(P\textit{t}Bu_3)_2$ complexes, which have the expected linear L–M–L angle. Unexpectedly, however, $Pd(P\textit{i}Pr_3)_2$, $Pd(PCy_3)_2$ and $Pd(PPh_3)_2$ are bent. The more flexible or even nonlinear geometry translates into lower barriers for oxidative addition to these complexes. This follows from our quantum chemical analyses of the bonding in, and reactivity of bisphosphine palladium complexes $Pd(PR_3)_2$ with varying steric bulk, based on relativistic dispersion-corrected DFT computations in combination with the activation strain model and quantitative MO theory.

Our analyses explain this dichotomy as they reveal that steric bulk may operate in two distinct ways: one is the usual steric repulsion deriving from overlap between closed-shell orbitals of intimate and isotropically bulky ligands; the second is steric attraction, which occurs between large, but more planar, ligands. Such ligands can build up relatively strong

dispersion interactions between their large surfaces when they bend toward each other. The resulting stabilization favors bending and thus enhances nonlinearity or bite-angle flexibility. Thus, by introducing sizable ligands with anisotropically distributed bulk, one can enhance the bite-angle flexibility of a catalyst via a steric mechanism, on top of the electronic mechanisms that have been described previously (see chapter 3). This situation leads to relatively little catalyst activation strain and, thus, low reaction barriers for methane C–H activation by the rather congested $Pd(PCy_3)_2$ and $Pd(PPh_3)_2$ model catalysts. Interestingly, the lowest barrier among our series of model catalysts appears for the quite sizable $Pd(PPh_3)_2$ catalyst. Its C–H activation barrier of +20.9 kcal mol^{-1} is substantially below that of +29.5 kcal mol^{-1} that we find for the smallest catalyst complex, $Pd(PH_3)_2$. These results confirm the steric nature of the bite-angle effect on oxidative addition barriers.[241,251]

Furthermore, the results reveal how the concept of steric attraction can serve as a mechanism for tuning bite-angle flexibility and thereby activity of catalyst complexes. This suggests that not the bite angle itself, but the intrinsic bite-angle flexibility of the catalyst is of relevance to the reaction barrier. We will elaborate on this finding in chapter 6.

5 Electronic and Steric Effects on Bite-Angle Flexibility and Nonlinearity

Previously appeared as

d^{10}-ML_2 Complexes: Structure, Bonding, and Catalytic Activity
L. P. Wolters, F. M. Bickelhaupt
In *Structure and Bonding* (Eds.: O. Eisenstein, S. Macgregor), Springer, Berlin, **2016**

5.1 Introduction

In this chapter, we present a study on the activation of the methane C–H bond by halogen-substituted palladium phosphine complexes $Pd(PX_3)_2$, where X = F, Cl, Br or I. This topic has been briefly touched upon before,[241,249] but these studies only included $Pd(PCl_3)_2$. Here, we will therefore discuss not only the difference in reactivity upon going from $Pd(PH_3)_2$ to halogen-substituted $Pd(PX_3)_2$, but also the effect of the decreasing electronegativity of the substituents along $Pd(PF_3)_2$, $Pd(PCl_3)_2$, $Pd(PBr_3)_2$ and $Pd(PI_3)_2$, which is new. Furthermore, as the bulkiness of the ligands increases from PH_3 to PF_3, PCl_3, PBr_3 and PI_3, we do not only expect electronic effects to play a role, but steric effects as well. Thus, by studying the reactivity of this series of catalysts, we investigate both electronic and steric effects on catalytic activity, and their interplay.

In a previous study[241] the $Pd(PCl_3)_2$ complex was found to have a nonlinear equilibrium geometry. This feature was overlooked by Fazaeli and co-workers:[249] in an attempt to reproduce their results using the same computational methodology, we found $Pd(PCl_3)_2$ to have a P–Pd–P angle of 135.5°, and the linear conformer to be 1.4 kcal mol^{-1} higher in energy, with two degenerate imaginary frequencies that both correspond to bending the complex. We will therefore first present detailed bonding analyses to investigate the reasons behind this nonlinearity of $Pd(PCl_3)_2$, and compare its situation to the other halogenated phosphine catalysts in this series. Interestingly, the latter appear to have nonlinear geome-

tries as well. Furthermore, we will compare these findings to the results discussed in chapters 3 and 4.

5.2 $Pd(PX_3)_2$ Geometries and Pd–PX_3 Bond Analyses

Our dispersion-corrected computations at ZORA-BLYP-D3/TZ2P reveal that all halogen-substituted bisphosphine palladium complexes $Pd(PX_3)_2$ have nonlinear geometries. Initially, one may expect that the complexes become more linear from $Pd(PF_3)_2$ to $Pd(PI_3)_2$, based on stronger steric repulsions between the heavier halogens. We find, however, that the opposite is true: along this series the P–Pd–P angle in the equilibrium geometries decreases from 151.7° for X = F to 143.2° (X = Cl), 136.6° (X = Br) and 122.4° for X = I, as shown in Figure 5.1. Furthermore, we find that $Pd(PH_3)_2$, $Pd(PF_3)_2$, $Pd(PCl_3)_2$ and $Pd(PBr_3)_2$ have eclipsed geometries, leading to a D_{3h}-symmetric geometry for $Pd(PH_3)_2$ and C_{2v}-symmetric geometries for the halogenated $Pd(PX_3)_2$ complexes. In the latter, two halogens from different ligands point towards each other. For $Pd(PI_3)_2$, we find that the ligands are rotated, avoiding close contacts between the iodines on one ligand with the iodines on the other ligand, lowering the symmetry of the complex to C_2.

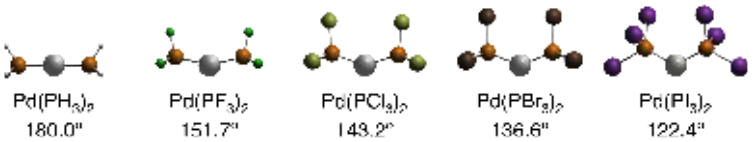

Figure 5.1 Equilibrium geometries and P–Pd–P angles of $Pd(PH_3)_2$ and halogen-substituted palladium phosphine $Pd(PX_3)_2$ complexes.

It is tempting to attribute the bending of these complexes to stronger dispersion interactions between the heavier halogen substituents on different ligands, basically pulling the ligands towards each other. However, dispersion-free computations at the otherwise same ZORA-BLYP/TZ2P level reveal that also without dispersion the angles decrease steadily from 153.9° for $Pd(PF_3)_2$ to 141.6° for $Pd(PI_3)_2$. Thus, although dispersion does contribute to bending, it is not exclusively responsible for this nonlinearity.

We recall from chapter 3 that sufficient π backbonding can lead to nonlinear ML_2 geometries, because, upon bending from 180° to 90°, this π backbonding is enhanced. In

order to investigate the π-accepting properties of the ligands included in this work, we have performed a bond energy analysis for the Pd–L bond in monocoordinated $PdPH_3$ and $PdPX_3$ (Table 5.1). We find a Pd–PH_3 bond energy of –40.9 kcal mol^{-1}, whereas the halogen-substituted phosphines bind a little stronger to Pd, with bonding energies between –43.8 and –46.1 kcal mol^{-1}. A further decomposition using Equations 2.11 and 2.13 reveals that, indeed, the halogen-substituted phosphines have a larger contribution from the π component of ΔE_{oi} and hence are apparently better π acceptors. This also follows from the lower π* orbital energies that decrease from –1.5 eV to –2.4 eV, –2.7 eV and –3.0 eV from PF_3 to PI_3, which are all lower than that of PH_3 at –0.2 eV. However, we do not find stronger π backbonding along the halogen-substituted series. The reason is that the π* orbital on PX_3 (which has antibonding character between P and X) is increasingly localized on the halogen substituents, and less on the phosphorus atom. Therefore, the overlap between the π* orbital and the Pd d orbitals decreases along this series, thereby counteracting the effect of the lower energy of the π* orbital. Thus, while the stronger π backbonding for the halogen-substituted phosphines may explain why the $Pd(PX_3)_2$ complexes are bent whereas $Pd(PH_3)_2$ is not, it does not explain the increased nonlinearity from $Pd(PF_3)_2$ to $Pd(PI_3)_2$.

Table 5.1 Metal-ligand bond energies and analyses (in kcal mol^{-1}) for the monocoordinated $PdPX_3$ complexes, relative to the ground state ($d^{10}s^0$) Pd atom and the ligand.[a]

	ΔE	ΔE_{strain}	ΔE_{int}	ΔE_{disp}	ΔV_{elstat}	ΔE_{Pauli}	ΔE_{oi}	ΔE_{oi}^{σ}	ΔE_{oi}^{π}[b]
$PdPH_3$	–40.9	0.3	–41.2	–1.4	–165.6	+189.4	–63.6	–35.2	–28.4
$PdPF_3$	–44.4	0.1	–44.5	–2.4	–157.8	+193.4	–77.7	–36.5	–41.3
$PdPCl_3$	–43.8	0.1	–43.9	–5.1	–141.8	+178.8	–75.9	–34.4	–41.5
$PdPBr_3$	–45.2	0.4	–45.6	–6.2	–133.7	+172.0	–77.7	–36.1	–41.6
$PdPI_3$	–46.1	0.6	–46.7	–7.0	–131.0	+169.0	–77.7	–36.8	–40.9

[a] See Equations 2.9, 2.11 and 2.13. [b] Also includes small contributions from δ orbital interactions.

We have also performed bonding analyses between ML and the second ligand, where we start from D_{3h}-symmetric $Pd(PH_3)_2$ or $Pd(PX_3)_2$ complexes optimized at the dispersion-free ZORA-BLYP/TZ2P level, and then bend the complex from 180° to 90° without further optimization. This way, we eliminate any geometric relaxation effects, allowing for a concise, and detailed investigation of the bonding mechanism. Thus, in Figure 5.2 we show the results of the interaction energy decomposition for $Pd(PH_3)_2$, as well as the series of

$Pd(PX_3)_2$ complexes. As this graph reveals, there is no significant difference between the orbital interaction curves within the halogen-substituted series. Also a further decomposition of this term into contributions from each respective irreducible representation (Equation 2.13; results not shown) does not reveal any factor contributing significantly to a preference for nonlinear geometries. Figure 5.2 does reveal however, that the minimum on the energy profiles shifts to smaller L–M–L angles from $Pd(PH_3)_2$ to $Pd(PF_3)_2$, and further to $Pd(PI_3)_2$, because the Pauli repulsion increases less steeply for the $Pd(PX_3)_2$ series than for $Pd(PH_3)_2$, and also along the $Pd(PX_3)_2$ series as the halogen substituents become heavier.

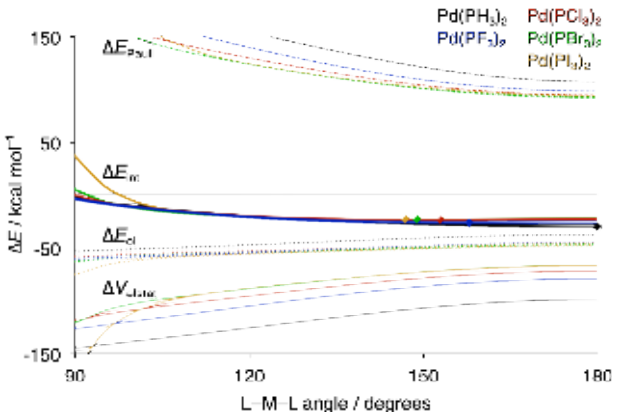

Figure 5.2 Bond energy decomposition (Equation 2.11) along the L–M–L angles for $Pd(PH_3)_2$ and halogen-substituted $Pd(PX_3)_2$ complexes. A dot designates the position of the energy minimum. Due to the use of frozen geometries and the omission of dispersion corrections, all minima are shifted to the right.

This, again counterintuitive, trend originates from the composition of the highest occupied MOs (HOMOs) on the L and ML fragments. The HOMO on the ligand L is the lone pair on phosphorus. For PH_3, this is the bonding combination of the hydrogen s orbitals and the phosphorus p_z orbital (with antibonding admixture of the phosphorus s orbital), which is strongly localized on phosphorus (see Figure 5.3). For the halogenated PX_3 ligands, the HOMO has considerably more admixture of the substituent halogen orbitals. It consists of the p_z orbitals on P and X, mixing in antibonding fashion. Thus, the larger amplitude is on the more electropositive phosphorus atom. As from F to I the halogen be-

comes less electronegative, this orbital becomes less localized on phosphorus (see Figure 5.3).

For $PdPH_3$ and $PdPX_3$, the HOMO is the antibonding combination of the ligand lone pair and the d_{z^2} orbital on Pd. Because from PH_3 to PF_3, PCl_3, PBr_3 and PI_3 the ligand lone pair becomes less localized on phosphorus, there is less destabilization from repulsions between this orbital and the palladium d_{z^2} orbital. Due to the decreased destabilization, there is less Pd 5s admixture in the $PdPH_3$ or $PdPX_3$ HOMO, resulting in the torus of the Pd d_{z^2} orbital becoming smaller (see Figure 5.3). It is this smaller torus from $PdPH_3$ to $PdPX_3$, and from $PdPF_3$ to $PdPI_3$, combined with the lone pair orbital on the second ligand being less localized on phosphorus, that results in a less steeply increasing Pauli repulsion term upon bending for the halogen-substituted catalysts compared to $Pd(PH_3)_2$, as well as along the $Pd(PX_3)_2$ series as the halogen becomes heavier (Figure 5.2).

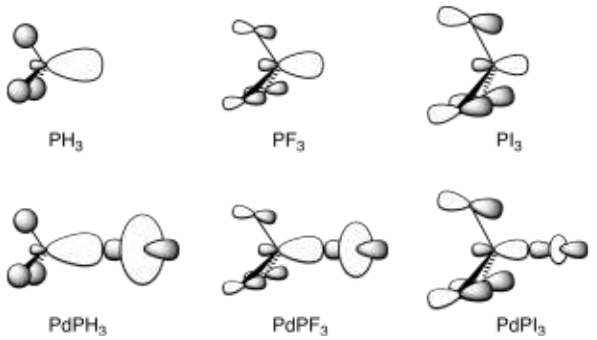

Figure 5.3 Schematic representations of the HOMO on PH_3, PF_3, and PI_3 (top, from left to right) and on monocoordinated $PdPH_3$, $PdPF_3$, and $PdPI_3$ (bottom, from left to right).

5.3 Reactivity of $Pd(PX_3)_2$ Towards the Methane C–H Bond

In this section, we investigate how the steric and electronic effects discussed in the previous section influence the activity of the $Pd(PX_3)_2$ catalyst complexes in the oxidative addition of methane. For all catalyst complexes the methane C–H bond activation starts from a reactant complex (RC) that is more strongly bound along the series of catalysts, from –1.9 kcal mol^{-1} for $Pd(PH_3)_2$ to –4.7 kcal mol^{-1} for $Pd(PI_3)_2$ (Table 5.2 and Figure 5.4). This is because, along this series, the catalyst complexes are bent further and therefore have a sterical-

ly less shielded metal center, allowing for a stronger catalyst-substrate interaction immediately at the beginning of the reaction. This interaction is further strengthened by increasingly stabilizing dispersion interactions between methane and the catalyst complexes with the heavier halogens.

Table 5.2 Relative energies (in kcal mol^{-1}) of the stationary points and transition states for methane C–H activation by the different palladium-based catalysts.

	RC	TS	PC
$PdPH_3$	−1.9	+29.5	+24.3
$PdPF_3$	−2.8	+26.6	+24.1
$PdPCl_3$	−3.7	+24.1	+22.1
$PdPBr_3$	−4.4	+23.7	+22.3
$PdPI_3$	−4.7	+25.1	+24.1

As the reaction proceeds, a transition state (TS) is encountered at +29.5 kcal mol^{-1} for $Pd(PH_3)_2$, and at slightly lower energies for the $Pd(PX_3)_2$ series, in line with findings of previous studies.[241,249] Along the $Pd(PX_3)_2$ series, the barriers first decrease from +26.6 kcal mol^{-1} for $Pd(PF_3)_2$ to +24.1 kcal mol^{-1} for $Pd(PCl_3)_2$ and +23.7 kcal mol^{-1} for $Pd(PBr_3)_2$, and then increase again to +25.1 kcal mol^{-1} for $Pd(PI_3)_2$.

Based on activation strain analyses along part of the reaction energy profile obtained using the Transition-Vector Approximation to the IRC (TV-IRC),[188] we find that this ordering of the barriers is the result of two counteracting trends (see Figure 5.5), namely: (i) a reduced strain energy from $Pd(PH_3)_2$ to the halogen-substituted catalysts, as well as a reduction when the halogens become heavier, and (ii) a simultaneous weakening of the interaction between the catalyst complex and methane substrate, which we address later on. Because the strain energy from $Pd(PH_3)_2$ to $Pd(PF_3)_2$ and onwards to $Pd(PI_3)_2$ decreases in progressively smaller steps, while on the other hand the interaction energy terms weaken with progressively larger steps, the oxidative addition barrier first decreases from $Pd(PH_3)_2$ to $Pd(PBr_3)_2$ and then increases again for $Pd(PI_3)_2$.

A further decomposition of the strain energy into individual contributions from the catalyst and substrate clearly reveals that the differences in catalyst strain are decisive. These differences are directly related to the bite-angle flexibility, or indeed nonlinearity, of the complexes, as we also encountered in the previous chapter. Thus, although the easier bend-

ing of the L–M–L angle contributes to the progressively decreasing catalyst strain from $Pd(PH_3)_2$ to $Pd(PI_3)_2$, the potential energy surfaces for bending these complexes are very flat. The bending itself therefore only contributes a few kcal mol^{-1} to the total catalyst strain. A significant contribution to the catalyst deformation energy stems from further tilting and rotation of the ligands, which accompanies the bending. These deformations are less needed when the L–M–L angle is intrinsically more bent, and therefore add to the lowering of the catalyst strain originating from the increased bite-angle flexibility. From $Pd(PBr_3)_2$ to $Pd(PI_3)_2$, however, this increase in flexibility is less important because it has

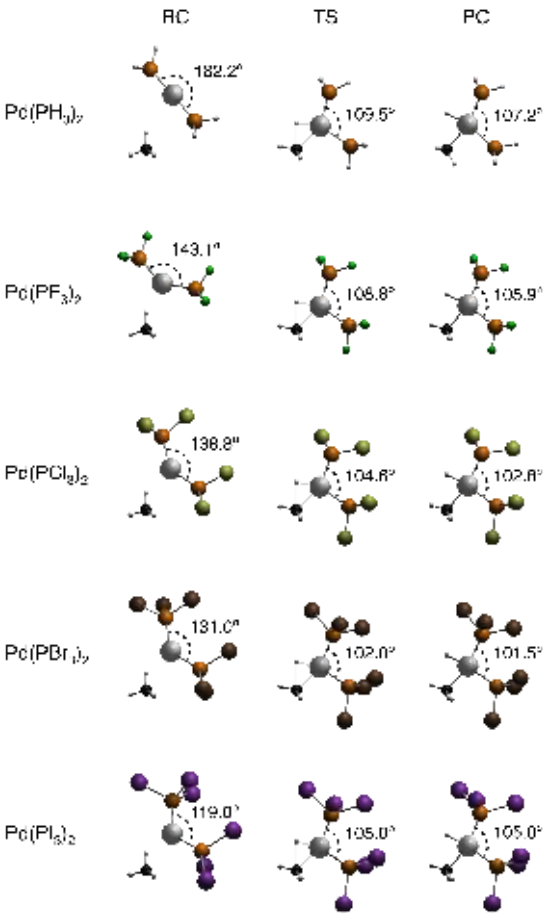

Figure 5.4 Geometries of the RC, TS, and PC along the energy profile for oxidative addition of methane to $Pd(PH_3)_2$, $Pd(PF_3)_2$, $Pd(PCl_3)_2$, $Pd(PBr_3)_2$, and $Pd(PI_3)_2$.

reached a point where the catalysts are sufficiently flexible, and the direct steric interaction between the ligands prevents further bending

This steric repulsion is also revealed in Figure 5.2 by the strong increase in Pauli repulsion that occurs at angles below 110°. Although only the beginning of this sharp increase of the Pauli repulsion term is visible in the graph and most of it is off the scale, its effect (even though partly masked by the more stabilizing electrostatic attraction and orbital interactions) is still clearly visible in the total interaction energy curve. Due to this direct ligand-ligand repulsion, the bite angle does not decrease any further from the TS to the PC of addition to $Pd(PI_3)_2$, but retains a value of 105.0°; slightly larger than for $Pd(PBr_3)_2$ (see Figure 5.4).

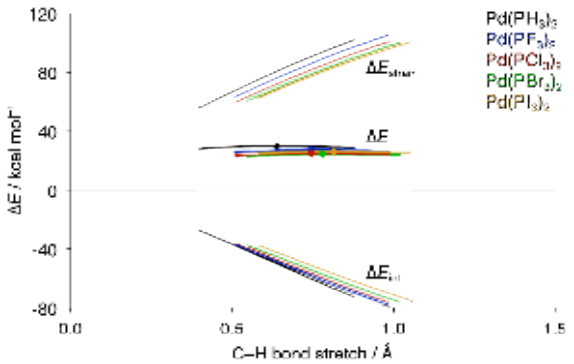

Figure 5.5 Activation strain analyses (Equation 2.10) along partial energy profiles for $Pd(PH_3)_2$ and $Pd(PX_3)_2$, obtained with the TV-IRC method. A dot designates the position of the TS.

Finally, we address the progressively weaker interaction between the fragments. From $Pd(PH_3)_2$ to the series of halogen-substituted catalysts, the interaction weakens mainly due to a less stabilizing orbital interaction term. This is caused by weaker catalyst-to-substrate backbonding, due to a lower orbital energy of the donating orbitals on the halogenated catalysts. The reason for these lower orbital energies is the better π backdonation to the halogenated phosphine ligands (Table 5.1). The stronger backdonation generates a more positive potential on the Pd center, which stabilizes the donating orbitals. This is accompanied by the fact that, upon bending, the HOMO on the catalyst is pushed up less in energy, because from PH_3 to the halogen-substituted PX_3, the lone pairs are less localized on the

phosphorus atom (see section 5.2 and Figure 5.3) and therefore have a weaker antibonding interaction with the palladium d orbitals.

Along the halogenated series, from $Pd(PF_3)_2$ to $Pd(PI_3)_2$, the orbital interaction term is remarkably similar, and the weakening of the catalyst-substrate interaction along this series results from an increasing Pauli repulsion. This destabilizing term is strengthened along the series because, from $Pd(PF_3)_2$ to $Pd(PI_3)_2$, there are more orbitals on the catalyst with energies in the vicinity of the methane HOMO energy, and therefore an increasingly large number of occupied catalyst orbitals enters a 2-center, 4-electron repulsion with the methane HOMO.[303]

5.4 Conclusions

Halogen-substituted palladium phosphine complexes $Pd(PX_3)_2$ with X = F, Cl, Br or I all have nonlinear ligand-metal-ligand angles, unlike $Pd(PH_3)_2$ which has a linear ligand-metal-ligand angle. Along the $Pd(PX_3)_2$ series the ligand-metal-ligand angle decreases from 151.7° for $Pd(PF_3)_2$, to 143.2°, 136.6° and 122.4° for $Pd(PCl_3)_2$, $Pd(PBr_3)_2$ and $Pd(PI_3)_2$, respectively. This follows from dispersion-corrected relativistic density functional computations. We found that the nonlinearity is the result of a combination of factors: firstly, the potential energy surfaces for bending the halogenated palladium phosphine complexes are flat due to the increased π backbonding that occurs upon bending from 180° to 90°. Secondly, from $Pd(PH_3)_2$ to $Pd(PF_3)_2$ and onwards to $Pd(PI_3)_2$, the Pauli repulsion between $PdPH_3$ or $PdPX_3$ and the second ligand increases less steeply, due to a smaller overlap of the highest occupied MOs upon bending. Thirdly, as along the $Pd(PX_3)_2$ series the halogen substituents become heavier, the stronger dispersion interactions between the ligands pull them more closely to each other.

When applied as catalysts for methane C–H bond activation, this nonlinearity leads to a lower reaction barrier for the halogenated catalysts $Pd(PX_3)_2$ compared to $Pd(PH_3)_2$, because there is less deformation energy needed to bend away the ligands in order to make room for the approaching methane. Along the $Pd(PX_3)_2$ series, there are two opposing trends, resulting in lower barriers from $Pd(PF_3)_2$ to $Pd(PBr_3)_2$, but a slightly higher barrier for $Pd(PI_3)_2$. The two trends are: (i) a less destabilizing catalyst strain energy due to increased nonlinearity; counteracted by (ii) a less stabilizing interaction energy due to a larger number of repulsive occupied-occupied orbital interactions. From $Pd(PBr_3)_2$ to $Pd(PI_3)_2$ this latter trend outweighs the effect of the decreased strain energy.

6 New Design Concepts for d^{10}-ML_n Catalysts

Previously appeared as

New Concepts for Designing d^{10}-$M(L)_n$ Catalysts:
d Regime, s Regime and Intrinsic Bite-Angle Flexibility
L. P. Wolters, W.-J. van Zeist, F. M. Bickelhaupt
Chem. Eur. J. **2014**, *20*, 11370–11381

6.1 Introduction

In this chapter, we wish to develop a generic understanding of how the type and charge of the metal center determines the reaction barrier height for methane C–H bond activation, and how these barriers are modulated by different types of ligands. Earlier work dealt with the insertion of palladium into several types of bonds,[201,304,305] with a variety of ligands.[241,251] These studies provided a detailed understanding of the electronic and steric mechanisms that govern trends in catalytic activity and selectivity, to which the previous chapters further contributed. However, besides a preliminary study on bare coinage metal cations,[306] the influence of the metal center on catalyst activity has never received much attention. Here, we bridge this gap by presenting a broad and deep analysis of the causal relationship between catalytic activity and the nature of the metal center, as well as the ligands.

To this end, we have explored and analyzed how and why the activity of catalyst complexes d^{10}-ML_n toward methane C–H oxidative addition varies along all nine metal centers of groups 9, 10 and 11 (M = Co^-, Rh^-, Ir^-, Ni, Pd, Pt, Cu^+, Ag^+, Au^+). We have done this for all metal centers in uncoordinated, monoligated, and bisligated systems (n = 0, 1, 2), for which the ligands are varied along L = NH_3, PH_3, and CO. These ligands provide

small yet representative models accounting for the electronic effects of the (often bulkier) ligands used in practice.

Reaction profiles are analyzed with respect to the metal centers in their $d^{10}s^0$ electronic configuration. This configuration most closely resembles the electronic configuration of these metals in molecular complexes, and is therefore the main electronic configuration of interest in order to understand the catalytic activity of these complexes.[307,308] This is an important difference with earlier work by other groups that focused on the ground state of the isolated atoms (often d^9s^1 or d^8s^2), which is, however, only relevant for gas-phase experiments involving bare metal atoms.[23,33,309-311] For each model catalyst we have located the minima and transition state on the energy profile of the oxidative addition of methane, thus arriving at a rather large set of results. Trends along these results have been analyzed by using the activation strain model, allowing us to explain the characteristics of each energy profile in terms of intrinsic properties of the catalyst and the substrate.

We will first discuss the effect of metal variation on oxidative addition, followed by an investigation of ligand effects. Thereafter, we will combine insights obtained from these sections, to show how the electronic nature of the metal center and the ligands influence each other, and consequently the reaction barrier for oxidative addition. The analyses enable us to unveil a number of new insights and concepts that are crucial for developing more rational approaches to catalyst design. At variance with textbook knowledge, bond activation reactions are not in all cases favored by pushing up metal d orbitals through ligand lone pairs, which, in principle, makes them better backdonating agents. We show that the supposedly lower bond activation barriers that may be expected only really occur if the catalyst complex is in what we designate the d regime. In addition, as will become clear from the results in this chapter, metals can also be in what we designate the s regime. In the latter, ligands that destabilize the metal d orbitals have no, or even the opposite, effect on the catalyst's activity toward bond activation, namely, a reduction in its bond-activating capability.

Furthermore, we elaborate on the concept of bite-angle flexibility that we mentioned already in chapter 4. Using this concept, we propose new ways of tuning the catalyst activation strain associated with the bond activation reaction. We show, using results from chapter 3, how the catalyst's activation strain can be tuned (reduced) electronically, without the help of structural constraints as imposed by a molecular scaffold. Such a scaffold is often applied, for example, in chelate complexes to pull the ligands in ML_2 toward each other in order to achieve a smaller bite angle.

The concepts that we propose herein constitute a set of generally applicable design principles for catalysts. In chapter 7, we will show how these principles manifest themselves in situations in which various bonds compete for activation, and how the design principles developed in the present work can be applied to achieve selective activation of one particular of these bonds.

6.2 General Reaction Profiles and Exceptions

ZORA-BLYP/TZ2P energies relative to the reactants of stationary points along all oxidative addition reactions are collected in Table 6.1. These energies are relative to the catalysts in a $d^{10}s^0$ (uncoordinated metal atoms) or d^{10}-like (coordinated metal centers) configuration, to be able to make a direct comparison with d^{10}-ML_n catalysts used in practice. Most of our model catalysts do indeed have a d^{10} ground state, but there are a few exceptions: according to our computations, Co^-, Rh^-, and Ir^- have d^8s^2 atomic ground states, whereas Ni and Pt have d^9s^1 ground states. For these uncoordinated metal centers, strong mixing with the low metal s orbital leads to an enhanced stability of the stationary points relative to reactants (see Table 6.1). The addition of ligands to these metal centers generally results in catalyst complexes with d^{10}-like electronic ground states. Only the monocoordinated cobalt complexes, as well as the dicoordinated $Co(NH_3)_2^-$ and $Ir(NH_3)_2^-$ have non-aufbau d^{10}-like configurations.

We will first systematically discuss the main trends in the reaction barriers that we find along the commonly encountered energy profiles, such as depicted in Figure 6.1 for the archetypal model systems Pd, $PdPH_3$ and $Pd(PH_3)_2$. In general, the reactions start from a reactant complex (RC), in which the methane coordinates in an η^2 fashion to the catalyst. For the bare and monoligated catalysts these complexes are stable, while for the bisligated catalysts they are essentially not bound, or the substrate coordinates only weakly (see Table 6.1). Moving onwards from the reactant complex, the catalyst migrates towards the C–H bond, which starts to elongate until it is, via a transition state (TS), effectively broken in the product complex (PC). Figure 6.2a shows a schematic representation of the potential energy surface (PES). We find, however, that a number of catalysts, mainly those based on a metal from group 9, insert into the methane C–H bond without barrier, leading to a PES as shown in Figure 6.2b. For most of the catalyst complexes based on a metal center from group 11, on the other hand, transition states do not occur, because the oxidative addition proceeds from the RC with an entirely uphill energy profile, and does not lead to a kinet-

ically stable product (PES as in Figure 6.2c). The reasons behind these different PESs will be discussed in more detail in section 6.3.

We also note that bond activation by monoligated catalysts proceeds with the ligand positioned either *trans* or *cis* to the methyl group of the activated methane substrate. For most transition state geometries, the *trans* isomer (as shown in Figure 6.1 for $PdPH_3$) is preferred, with differences in relative energies varying from 0.5 to 8 kcal mol^{-1}. Only the complexes containing $AgNH_3^+$, $AuNH_3^+$ and $AuCO^+$ are slightly more stable when the ligand is located *cis* to the methyl group, but the difference is less than 2 kcal mol^{-1}. A special situation occurs for NiCO, for which insertion of the catalyst with the ligand *trans* to

Table 6.1 Energies ΔE relative to reactants (in kcal mol^{-1}) for the oxidative addition of the methane C–H bond to various model catalysts. Square brackets indicate that constraints were applied (see text).

	Group 9				Group 10				Group 11		
	RC	TS	PC		RC	TS	PC		RC	TS	PC
Co^- [a]	[b]	[b]	−241.4	Ni[a]	−55.8	−54.2	−68.6	Cu^+	−30.8	[d]	[−3.1][d]
$CoNH_3^-$ [a]	[b]	[b]	−37.9	$NiNH_3$	−18.6	−12.7	−15.5	$CuNH_3^+$	−25.5	[d]	[+13.0][d]
$CoPH_3^-$ [a]	−18.8	−18.4	−36.5	$NiPH_3$	−16.8	−5.0	−5.9	$CuPH_3^+$	−21.5	[d]	[+20.3][d]
$CoCO^-$ [a]	−15.9	−14.4	−29.5	NiCO	−17.4	[d]	[−0.1][d]	$CuCO^+$	−29.2	[d]	[+11.2][d]
$CoNH_3^-(NH_3)$[a]	−2.4	−2.3	−20.6	$NiNH_3(NH_3)$	+12.0	+17.1	+14.5	$CuNH_3^+(NH_3)$	+20.0	[d]	[+57.7][d]
$Co(NH_3)_2^-$ [a]	0.0	+10.2[c]	+5.1[c]	$Ni(NH_3)_2$	−0.8	+24.1	+5.3	$Cu(NH_3)_2^+$	−1.5	[d]	[+42.2][d]
$Co(PH_3)_2^-$	−5.8	−1.0	−15.4	$Ni(PH_3)_2$	−0.4	+13.4	+10.7	$Cu(PH_3)_2^+$	−0.6	[d]	[+42.8][d]
$Co(CO)_2^-$	−2.2	+7.1	−4.1	$Ni(CO)_2$	−2.4	+19.9	+19.8	$Cu(CO)_2^+$	−6.1	[d]	[+38.9][d]
Rh^- [a]	−44.5	−44.4	−73.8	Pd	−6.7	+4.0	−3.6	Ag^+	−15.8	[d]	[+28.5][d]
$RhNH_3^-$	−13.9	−12.5	−26.8	$PdNH_3$	−12.2	+1.2	−0.8	$AgNH_3^+$	−14.2	[d]	[+34.6][d]
$RhPH_3^-$	−10.9	−3.8	−16.8	$PdPH_3$	−7.7	+15.7	+14.9	$AgPH_3^+$	−12.7	[d]	[+40.6][d]
$RhCO^-$	−9.5	−0.4	−11.8	PdCO	−9.9	+15.5	+15.4	$AgCO^+$	−17.0	[d]	[+32.2][d]
$RhNH_3^-(NH_3)$	−0.1	+1.4	−12.1	$PdNH_3(NH_3)$	+10.7	+23.5	+21.8	$AgNH_3^+(NH_3)$	+16.5	[d]	[+65.3][d]
$Rh(NH_3)_2^-$	−2.4	+28.2[c]	−5.5[c]	$Pd(NH_3)_2$	−0.1	[+29.0][e]	+14.7	$Ag(NH_3)_2^+$	−1.3	[d]	[+49.5][d]
$Rh(PH_3)_2^-$	0.0	+13.9	−2.8	$Pd(PH_3)_2$	0.0	+32.6	+27.3	$Ag(PH_3)_2^+$	−0.5	[d]	[+54.7][d]
$Rh(CO)_2^-$	−0.8	+22.1	+5.5	$Pd(CO)_2$	0.0	+33.9	+30.3	$Ag(CO)_2^+$	−2.5	[d]	[+48.3][d]
Ir^- [a]	[b]	[b]	−117.7	Pt[a]	[b]	[b]	−54.8	Au^+	−28.6	−22.5	−28.9
$IrNH_3^-$	[b]	[b]	−40.9	$PtNH_3$	−18.4	−17.2	−25.0	$AuNH_3^+$	−24.8	[d]	[−3.3][d]
$IrPH_3^-$	−10.4	−8.4	−32.4	$PtPH_3$	−10.0	+2.2	−4.5	$AuPH_3^+$	−17.6	[d]	[+15.7][d]
$IrCO^-$	−8.0	−3.7	−25.1	PtCO	−14.3	+0.7	−4.5	$AuCO^+$	−28.6	[d]	[+0.1][d]
$IrNH_3^-(NH_3)$[a]	[b]	[b]	−27.2	$PtNH_3(NH_3)$	+16.1	−17.3	+10.4	$AuNH_3^+(NH_3)$	+23.0	[d]	[+47.5][d]
$Ir(NH_3)_2^-$ [a]	−3.7	+22.4[c]	+10.3[c]	$Pt(NH_3)_2$	−0.3	[+43.1][e]	+0.8	$Au(NH_3)_2^+$	−1.6	+38.3	+27.5
$Ir(PH_3)_2^-$	0.0	+12.8	−17.8	$Pt(PH_3)_2$	−0.1	+30.3	+11.7	$Au(PH_3)_2^+$	−0.6	+44.1	+37.8
$Ir(CO)_2^-$	−0.9	+21.0	−8.2	$Pt(CO)_2$	0.0	+31.1	+14.6	$Au(CO)_2^+$	−1.2	+34.3	+29.8

[a] Catalyst complex with a non-aufbau $d^{10}s^0$ or d^{10}-like electronic configuration. [b] Inserts without barrier. [c] Energy refers to the complex with the ligands oriented out of the plane formed by the metal center and the C–H bond to be activated (see section 6.6). [d] No reverse barrier: energy of the labile PC within brackets. [e] One ligand dissociates during insertion: energy in brackets obtained by constraining both metal-ligand bond lengths to remain equal (see section 6.6).

the methyl group is a lower-energy pathway but does not lead to a kinetically stable product complex. A labile product complex on this energy profile was found at a relative energy of −0.1 kcal mol^{-1}, which is not separated by a reverse barrier from the reactant complex at −17.4 kcal mol^{-1}. When the ligand is positioned *cis* to the methyl group, a kinetically stable product complex exists (+8.4 kcal mol^{-1}) as well as a transition state (+8.6 kcal mol^{-1}) corresponding to C–H activation, which constitutes a reverse barrier of only +0.2 kcal mol^{-1}. However, when thermodynamic effects are included, this barrier for the reverse reaction vanishes as well.

Finally, we encountered several alternative pathways for a number of $M(NH_3)_2$ complexes, mainly those with metal centers from group 9 or 10. These pathways can involve dissociation of one M–NH_3 bond, such as for $Pd(NH_3)_2$, leading to stationary points as shown in Figure 6.1 where the catalyst complex is denoted $PdNH_3(NH_3)$ to emphasize that

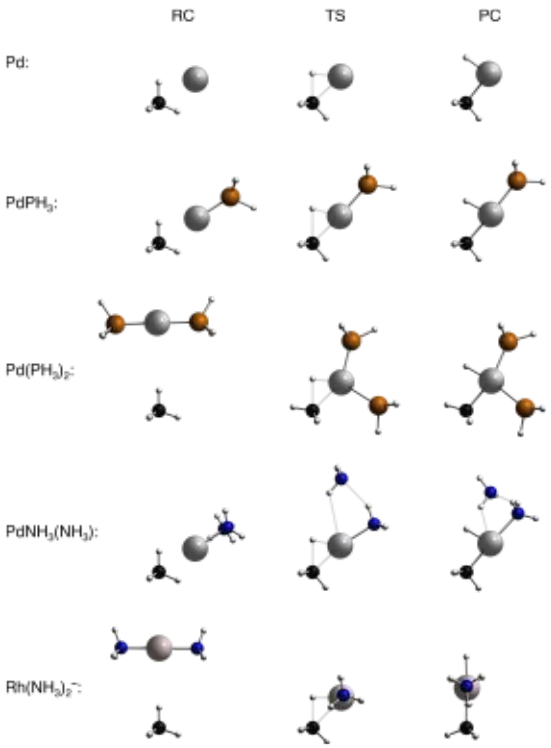

Figure 6.1 Representative geometries of the stationary points for the oxidative addition of methane to selected model catalysts.

one ligand is dissociated. Another possible alternative pathway occurs, for example, for $Rh(NH_3)_2^-$, also shown in Figure 6.1. This catalyst complex approaches the substrate with its ligands perpendicular to the plane formed by the targeted C–H bond and the metal center, in contrast to many other catalysts, including $Pd(PH_3)_2$. The occurrence of these pathways can be explained if the effects of both metal and ligand variation are known, and will therefore be discussed, along with other ligand effects in sections 6.5 and 6.6, after the sections on the effect of metal variation.

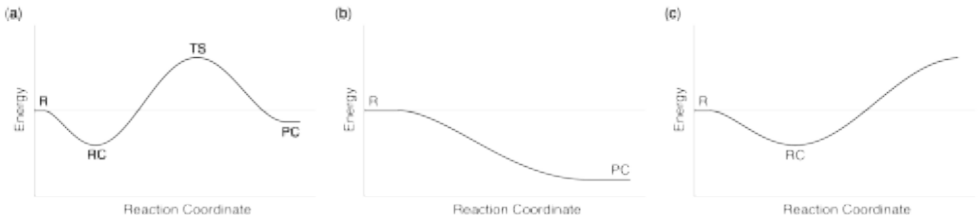

Figure 6.2 Reaction potential energy profiles occurring in this work: (a) the general profile with stable reactant complex, a transition state, and stable product complex; (b) profile with a labile reactant complex and stable product complex; and (c) profile with only a stable reactant complex and a labile product complex.

6.3 Metal Variation from Group 9 to Group 11

According to the results of our computations, collected in Table 6.1, the anionic catalysts based on a group 9 metal center have early transition states, at a significantly lower energy, compared to the catalysts with a group 10 metal center. In fact, a number of group 9 metal-based catalysts, as well as Pt from group 10, insert into the methane C–H bond without barrier, which leads to a PES as shown in Figure 6.2b. For most of the group 11 metal centers on the other hand, transition states do not occur, because the oxidative addition proceeds from the RC with an entirely uphill energy profile, and does not lead to a kinetically stable product (Figure 6.2c). For these group 11 catalysts, which do not experience a barrier for the reverse reaction, we have obtained a labile PC-like structure through optimization with the C–M–H angle fixed to its value in the product of the insertion of the analogous palladium-based catalyst. We have modeled, for example, the PC of addition to $AgPH_3^+$ by optimizing the complex with the C–Ag–H angle constrained to the value of the C–Pd–H angle in the resulting PC of the addition to $PdPH_3$. Only for some gold-based catalysts,

which activate methane with very high barriers (well above 30 kcal mol^{-1}), did we find stable product complexes.

Thus, in general, we find that from group 9 to group 11, reaction barriers increase and product complexes become less stable. From $Rh(PH_3)_2^-$ to $Pd(PH_3)_2$ to $Ag(PH_3)_2^+$, for example, barriers increase from +13.9 to +32.6 to +54.7 kcal mol^{-1} (see Table 6.1). Similar trends are observed for the other ligands, and with metal centers from the first or third transition metal row. We have compared the activation strain analyses for methane activation by $Rh(PH_3)_2^-$, $Pd(PH_3)_2$, and $Ag(PH_3)_2^+$ along the full reaction path, projected onto the stretch of the activated C–H bond (see activation strain diagrams in Figure 6.3a). From these analyses it is clear that, from group 9 to group 11 catalyst complexes, the energy pro-

Table 6.2 HOMO and LUMO energies (in eV) of model catalysts in their equilibrium geometry and an effective d^{10} electronic configuration.

Group 9			Group 10			Group 11		
	HOMO	LUMO		HOMO	LUMO		HOMO	LUMO
Co^- [a]	+12.0	+4.3	Ni[a]	+0.3	–2.8	Cu^+	–14.0	–12.3
$CoNH_3^-$ [a]	+4.0	+3.2	$NiNH_3$	–2.2	–2.0	$CuNH_3^+$	–11.8	–9.2
$CoPH_3^-$ [a]	+3.4	+2.5	$NiPH_3$	–2.9	–2.4	$CuPH_3^+$	–12.0	–8.9
$CoCO^-$ [a]	+3.2	+2.7	NiCO	–4.1	–3.0	$CuCO^+$	–13.7	–10.2
$Co(NH_3)_2^-$ [a]	+3.9	+3.2	$Ni(NH_3)_2$	–1.5	–0.7	$Cu(NH_3)_2^+$	–10.3	–5.9
$Co(PH_3)_2^-$	+2.0	+2.8	$Ni(PH_3)_2$	–2.9	–1.3	$Cu(PH_3)_2^+$	–10.9	–6.3
$Co(CO)_2^-$	+1.1	+2.5	$Ni(CO)_2$	–5.2	–3.1	$Cu(CO)_2^+$	–13.2	–9.2
Rh^- [a]	+4.7	+2.7	Pd	–4.1	–3.4	Ag^+	–15.6	–11.5
$RhNH_3^-$	+2.5	+2.6	$PdNH_3$	–3.5	–2.1	$AgNH_3^+$	–12.6	–9.0
$RhPH_3^-$	+2.2	+2.4	$PdPH_3$	–4.5	–2.3	$AgPH_3^+$	–12.4	–8.7
$RhCO^-$	+1.6	+2.4	PdCO	–5.3	–2.9	$AgCO^+$	–14.1	–9.7
$Rh(NH_3)_2^-$	+2.7	+3.0	$Pd(NH_3)_2$	–3.1	–0.9	$Ag(NH_3)_2^+$	–11.0	–6.2
$Rh(PH_3)_2^-$	+1.4	+2.7	$Pd(PH_3)_2$	–4.4	–1.2	$Ag(PH_3)_2^+$	–11.3	–5.9
$Rh(CO)_2^-$	+0.4	+2.4	$Pd(CO)_2$	–5.8	–3.1	$Ag(CO)_2^+$	–13.3	–8.6
Ir^- [a]	+4.3	+2.0	Pt[a]	–4.3	–4.8	Au^+	–15.3	–13.3
$IrNH_3^-$	+2.9	+3.0	$PtNH_3$	–3.7	–2.7	$AuNH_3^+$	–12.5	–9.9
$IrPH_3^-$	+2.3	+2.3	$PtPH_3$	–4.5	–2.9	$AuPH_3^+$	–12.5	–9.3
$IrCO^-$	+1.7	+2.5	PtCO	–5.8	–3.6	$AuCO^+$	–14.2	–10.8
$Ir(NH_3)_2^-$ [a]	+3.2	+3.2	$Pt(NH_3)_2$	–3.0	–0.7	$Au(NH_3)_2^+$	–11.1	–6.0
$Ir(PH_3)_2^-$	+1.5	+2.8	$Pt(PH_3)_2$	–4.4	–1.3	$Au(PH_3)_2^+$	–11.5	–6.1
$Ir(CO)_2^-$	+0.2	+2.4	$Pt(CO)_2$	–6.1	–3.4	$Au(CO)_2^+$	–13.5	–9.1

[a] Catalyst complex with a non-aufbau $d^{10}s^0$ or d^{10}-like electronic configuration.

files become progressively less exothermic due to weaker interactions between the catalysts and the substrate. Because the strain curves $\Delta E_{strain}(\zeta)$ are similar, the energy profile $\Delta E(\zeta)$, and thus the transition state, shifts up in energy. Also, because of the less steeply descending interaction energy curves $\Delta E_{int}(\zeta)$, the position of the transition state shifts towards the product complex geometry. Indeed, for many of the cationic catalysts, this effect is strong enough to make the transition state merge into the product complex, resulting in a disappearance of the barrier for the reverse reaction.

A further decomposition of the interaction energy (using Equation 2.11; results not shown) reveals that the weakening from group 9 to group 11 catalysts is primarily the result of the orbital interactions, which clearly show a trend from strongly stabilizing for $Rh(PH_3)_2^-$ to less stabilizing for $Pd(PH_3)_2$ and even less stabilizing if we go to $Ag(PH_3)_2^+$. This trend derives from the energies of the catalyst's frontier orbitals (see Table 6.2). For the group 9 catalysts the energies of the d orbitals are high, due to the negative potential that the electrons are confined in, while for the neutral group 10 catalysts, the orbital energies are much lower, and they again decrease significantly going to the group 11 catalysts, due to their net positive charge. As a result, the anionic $Rh(PH_3)_2^-$, with its high-energy d-derived HOMOs, is a better electron donor than $Pd(PH_3)_2$, which in turn is a better donor than the cationic $Ag(PH_3)_2^+$. Therefore, $Rh(PH_3)_2^-$ donates electrons into the antibonding σ^*_{C-H} orbital of the substrate more easily, which translates into a stronger orbital interaction term, and a lower barrier for methane C–H bond breaking. This is also reflected in the σ^*_{C-H} populations, which decreases from 1.06 electrons in the product complex of $Rh(PH_3)_2^-$, to 0.80 electrons in the product complex of $Pd(PH_3)_2$, to 0.52 electrons in the labile product complex obtained for $Ag(PH_3)_2^+$.

The strain curves associated with geometrical deformations more or less coincide, because these reactions proceed via very similar geometrical transformations. The strain energy originates predominantly from the deformation of the substrate, because breaking the covalent C–H bond induces more strain than bending the L–M–L bite angle to smaller values. However, as shown in Figure 6.3a, the strain energy for $Rh(PH_3)_2^-$ increases slowly at the beginning of the reaction and is lower than the strain curves for $Pd(PH_3)_2$ and $Ag(PH_3)_2^+$. For the last two, the strain curves increase steeply at an early stage of the reaction, thereby pushing up the total energy profile immediately. This is related to the intrinsic bite-angle flexibility of the catalysts, especially in the case of $Rh(PH_3)_2^-$, which already has a bent equilibrium geometry. This nonlinearity also occurs for $M(PH_3)_2$ in which M is Co^-, Rh^- or Ir^-, and for $M(CO)_2$ with all metal centers M from groups 9 or 10, such as

$Pd(CO)_2$, which has a ligand-metal-ligand (L–M–L) angle of 155°. We have elucidated the reason for this bending in chapter 3. Our analyses showed that L–M–L bending is favorable for d^{10}-ML_2 complexes with strong π backbonding, because the increase in steric repulsion is outweighed by a more strongly increasing stabilization that occurs when one of the two ligand π* acceptor orbitals overlaps and interacts with a different metal d orbital that is not yet stabilized by backbonding to the other ligand and therefore at a higher orbital energy.

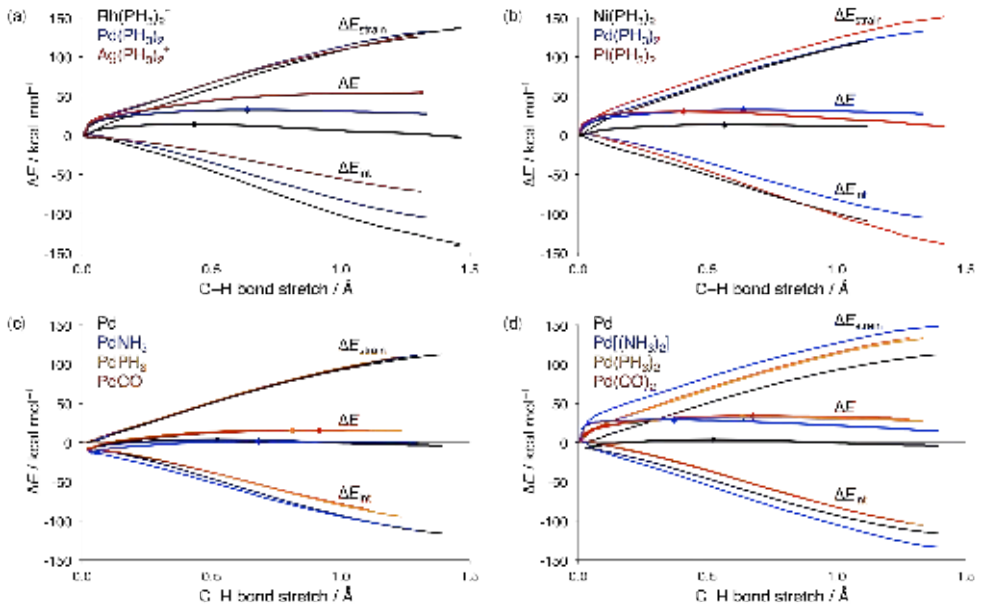

Figure 6.3 Comparison of activation strain analyses (see Equation 2.10) for the oxidative addition of methane to four different series of model catalysts (using constraints for $Pd(NH_3)_2$; see text). A dot designates the position of the TS.

Again, we find that the enhanced L–M–L bite-angle flexibility has the effect of lowering the strain curves in a manner that is related to, and yet also different from well-known bite-angle effects in chelate complexes. In earlier work[241,251] it was shown that smaller bite angles in chelate complexes enhance the catalyst's activity by reducing its contribution to the activation strain. The physical mechanism behind this reduced catalyst strain is that there is no longer a need for the bending away of ligands from the approaching substrate, a process that occurs in linear d^{10}-ML_2 complexes to relieve steric (Pauli) re-

pulsion between ligands and substrate, but which still causes the build-up of catalyst strain. Thus, in a sense, the deformation energy needed to bend the catalyst during the reaction is taken out of the strain term by building it into the catalyst with a structural constraint, such as the bridging scaffold in chelating ligands. In chapters 4 and 5, we already showed that such a bridging ligand is not needed when the catalyst complex adopts a bent geometry intrinsically. In the present case, such a bridging ligand is not needed as the catalyst complex becomes bent for electronic reasons (namely strong π backbonding, as described in chapter 3). Going from $Pd(PH_3)_2$ to $Ag(PH_3)_2^+$, we find a slightly more steeply increasing catalyst strain in an early stage of the reaction, despite the fact that both catalyst complexes have linear L–M–L angles in their equilibrium geometries. In accordance with the conclusions from chapter 4, this shows that not the bite angle itself, but the intrinsic bite-angle flexibility of the catalyst is of relevance to the reaction barrier. This also proves that a single structural parameter based on the catalyst's equilibrium geometry (*e.g.*, the bite angle) is not necessarily sufficient to account for the catalyst's activation strain, let alone for predicting its activity.

6.4 Metal Variation from Row 1 to Row 3

Considering the trend within a group, descending the periodic table, we find that the catalysts with a metal center from the second row (Rh^-, Pd, Ag^+) generally have higher barriers than their congeners with a first row (Co^-, Ni, Cu^+) or third row (Ir^-, Pt, Au^+) metal center. Thus, if we consider for example the triad $NiPH_3$, $PdPH_3$, $PtPH_3$, we find a significantly higher barrier for $PdPH_3$ (+15.7 kcal mol^{-1}), than for $NiPH_3$ and $PtPH_3$ (–5.0 and +2.2 kcal mol^{-1}, respectively). Although the differences in barrier heights within a certain group are generally smaller than the differences in barrier heights between groups, they can still be considerable. The barrier for $AgNH_3^+$, for example, is more than 30 kcal mol^{-1} higher than that of $AuNH_3^+$. This trend, combined with the general increase of reaction barriers going from group 9 to group 11 (see previous section), accounts for the earlier observation that addition to Cu^+ and Au^+ is more feasible than to Pd, for which it is again more feasible than to Ag^+.[306] The preliminary nature of this earlier work, however, did not allow for a careful analysis of this trend. Now, we have addressed its origin and, having already explained the general increase in barriers from group 9 to group 11, we turn to the activation strain diagrams for the triad of group 10 metal bisphosphine complexes shown in Figure 6.3b.

We find that the barrier for $Ni(PH_3)_2$ is the lowest in this series, while the barriers for $Pd(PH_3)_2$ and $Pt(PH_3)_2$ are much higher. Note that, although the last two barriers are comparable in height, the transition state for $Pt(PH_3)_2$ occurs at shorter C–H bond stretch, that is, in an earlier stage of the reaction. The barrier for $Ni(PH_3)_2$ is lowest for two reasons: (i) the strain curve is least destabilizing and (ii) the interaction curve is, along most of the reaction path, most stabilizing (see Figure 6.3b). The differences in strain energy originate again from the contributions of bending the catalysts, that is, we again recover the consequences of the intrinsic bite-angle flexibility. All three catalysts have linear L–M–L angles in their equilibrium geometries, which must decrease to a value around 110° as the methane substrate approaches and oxidatively adds. The concomitant catalyst deformation energy ΔE_{strain}[cat] is smallest for $Ni(PH_3)_2$ and largest for $Pt(PH_3)_2$, because a somewhat stronger π backbonding from the higher-energy nickel d orbitals causes $Ni(PH_3)_2$ to have a reduced resistance against bending the ligands away, as described in chapter 3. Therefore, the energy profiles of $Pd(PH_3)_2$ and $Pt(PH_3)_2$ rise faster in an early stage of the reaction than that of $Ni(PH_3)_2$. Later on, however, the interaction energy curve starts to descend more steeply for $Pt(PH_3)_2$ than for $Ni(PH_3)_2$ and $Pd(PH_3)_2$. As a result, the product side of the energy profile for $Pt(PH_3)_2$ is stabilized relative to the reactant side, which shifts the transition state towards a smaller C–H stretch. The interaction energy for $Pd(PH_3)_2$ does not descend as fast, and hence this addition reaction occurs with a relatively high barrier, and via a transition state appearing at a larger C–H stretch.

A closer look at the interaction energy curves for this series shows that, similar to the series from $Rh(PH_3)_2^-$ to $Pd(PH_3)_2$ to $Ag(PH_3)_2^+$, the orbital interactions are decisive for the final trend in the interaction energies (results not shown). Those interactions are weakest for $Pd(PH_3)_2$, more stabilizing for $Ni(PH_3)_2$ and most stabilizing for $Pt(PH_3)_2$. Our bonding analyses show that this is again related to the catalyst's capability to interact with and donate electrons to the substrate acceptor σ^*_{C-H} orbital. This is again reflected by the population of this orbital, which, at the same point near the TS of the reactions (*i.e.*, at a C–H stretch around 0.57 Å), has risen from zero to 0.50 electrons for the addition to $Ni(PH_3)_2$ and $Pt(PH_3)_2$, while for $Pd(PH_3)_2$ it is less, only 0.43 electrons. Compared to $Pd(PH_3)_2$, $Ni(PH_3)_2$ is a better electron donor because of its energetically higher d-derived HOMO (see Table 6.2). $Pd(PH_3)_2$ and $Pt(PH_3)_2$ have comparable orbital energies for their d-derived HOMO, but the platinum d orbitals are larger and, therefore, achieve a better overlap with the substrate's σ^*_{C-H} LUMO: 0.31 for $Pt(PH_3)_2$ as compared to 0.28 for $Ni(PH_3)_2$ and $Pd(PH_3)_2$ at the same point in the TS region (again at a C–H stretch of 0.57

Å). Furthermore, the energy profile for $Pt(PH_3)_2$ is additionally stabilized by a relatively strong substrate-to-catalyst donor-acceptor interaction. This interaction benefits from the relativistic contraction and stabilization of the platinum 6s orbital, which translates into a low orbital energy and thus favorable acceptor capability of the 6s-derived LUMO on $Pt(PH_3)_2$ (also listed in Table 6.2).[200,312-314] This description closely resembles a picture commonly put forward, based on competition between the $d^{10}s^0$ and d^9s^1 state of the catalyst complex.[8,248,315] However, as we will show and explain later on, it is important to consider the catalyst-to-substrate backdonation separately from the substrate-to-catalyst donation.

6.5 Variation from σ-Donating to π-Accepting Ligands

As shown by the results in Table 6.1, reaction barriers for oxidative addition to ML_n complexes increase in most cases along L = NH_3 < PH_3 < CO. For example, from $RhNH_3^-$ to $RhPH_3^-$ to $RhCO^-$ the barrier increases from –12.5 to –3.8 and to –0.4 kcal mol^{-1}. For the monoligated palladium-based catalysts, we find that the barrier increases substantially from $PdNH_3$ to $PdPH_3$ and PdCO. Note, however, that addition to the last two model catalysts goes via essentially equally high barriers; we will return to this in a later section. The relative energy of the product complexes, however, increases systematically and monotonically along NH_3 < PH_3 < CO.

In Figure 6.3c, we show the activation strain diagrams for the monoligated palladium-based catalysts and, for comparison, bare palladium. We find that the higher barriers and increased endothermicity for $PdPH_3$ and PdCO are the result of a less stabilizing catalyst-substrate interaction ΔE_{int}, compared to $PdNH_3$. This is related to the σ-donating and π-accepting properties of the ligands. NH_3 acts primarily as a σ-donating ligand, pushing up the metal d orbitals (see Table 6.2). This improves the catalyst-substrate interaction and thus reduces the reaction barrier. PH_3 and especially CO, on the other hand, have π* acceptor orbitals that stabilize the d orbitals on the metal center (see Table 6.2) and deplete some electron density from the metal center (the VDD atomic charge on Pd in these catalysts is –0.15 a.u. for $PdNH_3$, –0.04 a.u. for $PdPH_3$ and +0.14 a.u. for PdCO). This reduces the electron-donating capability of the catalyst and weakens the catalyst-substrate interaction ΔE_{int}, resulting in a higher barrier.

One might argue, that the $M(CO)_n$ catalysts are exceptions to this general trend, because they have relatively high barriers for metal centers from groups 9 or 10, while they

have the lowest barriers for group 11 metal centers. Indeed, although the effects of the ligands on the metal orbitals as just described also apply to metal centers from group 11, the effect on the reaction barrier is completely reversed as a consequence of the combined effect of the metal and the ligand. In section 6.7, we introduce the 'd regime' and 's regime' of catalysts, which serve as useful concepts to understand this intriguing reversal of ligand effects.

The same ligand effects can be recognized in the case of the bisligated catalysts, although these generally react via significantly higher barriers than the monocoordinated complexes (see Figure 6.3d for Pd and PdL_2). It is known that this is the result of additional catalyst strain induced by the need to bend the catalyst complex to avoid even stronger repulsive steric interactions between the catalyst and the substrate.[241,251] Although this is true in general, the concept needs refinement, because, as we encountered in previous sections, the amount of destabilization of the strain term also changes along linear catalysts when the metal center is varied along a row or a group of the periodic table. Here, we find a similar effect when varying the ligands, while keeping the same metal center. Thus, from $Pd(CO)_2$ to $Pd(PH_3)_2$ to $Pd(NH_3)_2$, the intrinsic bite-angle flexibility of the catalyst decreases, and therefore the catalyst strain becomes more destabilizing. This effect is small from $Pd(CO)_2$ to $Pd(PH_3)_2$, despite the fact that $Pd(CO)_2$ is intrinsically bent, while $Pd(PH_3)_2$ is not. From $Pd(PH_3)_2$ to $Pd(NH_3)_2$, however, the flexibility of the bite angle decreases significantly, while the metal-ligand bond weakens as well. Consequently, the search for a transition state for methane activation by $Pd(NH_3)_2$ with both ligands attached fails, as one of the NH_3 ligands dissociates from the metal. To obtain nevertheless an idea of how such a TS would look like, we have optimized and analyzed the fictitious reaction profile for methane activation by $Pd(NH_3)_2$ under the constraint that the two Pd–NH_3 bonds remain equal in length. The strain curve for $Pd(NH_3)_2$ is therefore significantly higher than those of the other two bisligated palladium catalysts, because not only does bending this more rigid catalyst (see chapter 3) lead to a larger deformation energy, but also the simultaneous elongation (but not rupture!) of both Pd–NH_3 bonds contributes to this term. Importantly, the same ligand effects as for monocoordinated PdL can still be observed: the catalyst-substrate interaction ΔE_{int} is strongest for $Pd(NH_3)_2$ and weaker for $Pd(PH_3)_2$ and $Pd(CO)_2$, because the metal d orbitals are more effectively stabilized in the last two due to the strong π-backbonding capability of PH_3 and especially CO.

Interestingly, we observe anti-Hammond behavior if we go from mono- to bisligated catalyst complexes. Thus, oxidative addition to PdL_2 proceeds with higher barriers and

higher endothermicity than to PdL, yet the TS of the former, more endothermic reaction is located more at the reactant side (at shorter C–H stretch) than the TS of the latter. The transition states for the monoligated catalysts occur at C–H bond lengths of 1.777 ($PdNH_3$), 1.908 ($PdPH_3$), and 2.012 Å (PdCO), whereas for the bisligated catalysts the transition states occur at 1.465 ($Pd(NH_3)_2$), 1.733 ($Pd(PH_3)_2$) and 1.770 Å ($Pd(CO)_2$; see Figure 6.3c and 6.3d). This anti-Hammond behavior results from the more steeply descending interaction curves for the PdL_2 catalysts. Thus, the catalyst-substrate interaction ΔE_{int} shows the same trend for bisligated catalysts as for the monoligated ones, because the orbital energies in both series of catalyst complexes, PdL and PdL_2, decrease in the same order along L = NH_3 > PH_3 > CO (see Table 6.2). However, all bisligated catalysts show a faster descending interaction energy than their monoligated analogues, because the electron-donating capability of bisligated catalysts ML_2 is improved with respect to ML as soon as L–M–L bending in the former begins and turns on the antibonding overlap of the ligand lone pairs with a metal d orbital. The effect of this phenomenon is that the resulting hybrid d orbital is pushed up in energy and oriented more towards the substrate σ^*_{C-H} orbital.[37,241,251] Thus, as we proceed along the reaction coordinate for oxidative addition to the bisligated metal complexes, the interaction curve experiences an additional reinforcement, becomes steeper and pulls the TS to an earlier, more reactant-like geometry.

6.6 Alternative Reaction Pathways for $M(NH_3)_2$ Catalysts

As alluded to in section 6.2, a number of reaction paths for $M(NH_3)_2$ catalysts deviate from the general path that is depicted in Figure 6.1 for the archetypal dicoordinated model catalyst $Pd(PH_3)_2$. We have found a viable alternative pathway for $Pd(NH_3)_2$ in which one ligand is dissociated (see Figure 6.1). Such hemilability has often been applied in ligand design and is a known feature of N-coordinating sites.[316-320] Expulsion of one of the NH_3 ligands avoids not only bending the L–M–L angle, which is unfavorable for $Pd(NH_3)_2$ due to its bite-angle rigidity, but also avoids steric repulsion between the dicoordinated catalyst and the substrate. Thus, this directly links our concept of intrinsic bite-angle flexibility (or rigidity) to that of hemilability. We have investigated these alternative pathways for all metal centers M, and listed the energies (relative to dicoordinated, linear $M(NH_3)_2$ and methane) of the stationary points on these pathways in Table 6.1. These are denoted as $MNH_3(NH_3)$, because when M–N dissociation occurs the dissociated ligand forms a complex with the remaining MNH_3 moiety through a hydrogen bond between its nitrogen lone

pair and an N–H bond of the still metal-coordinated ammine ligand. For the metal centers from groups 9 and 10, but not group 11, these complexes are further stabilized by an agostic interaction between one of the hydrogen atoms of the expelled NH_3 ligand and the metal center. The isolated catalyst complexes $RhNH_3^-(NH_3)$ and $IrNH_3^-(NH_3)$ are 13.9 and 12.8 kcal mol^{-1} higher in energy compared to the linear dicoordinated $M(NH_3)_2^-$ complexes, respectively. For $CoNH_3^-(NH_3)$, we could not reach full convergence, but based on a partially converged calculation, we estimate this complex to be around 12 kcal mol^{-1} higher in energy than the linear $Co(NH_3)_2^-$. For the neutral complexes $Ni(NH_3)_2$, $Pd(NH_3)_2$ and $Pt(NH_3)_2$, these rearrangements lead to species that are 30.3, 22.7 and 33.6 kcal mol^{-1} less stable than the linear dicoordinated complexes, respectively. For the cationic complexes such rearrangements are even less feasible, due to the stronger M^+–NH_3 bonds (see chapter 3) and the absence of agostic interactions. As a result, the complexes $CuNH_3^+(NH_3)$, $AgNH_3^+(NH_3)$ and $AuNH_3^+(NH_3)$ are 42.8, 29.1 and 44.1 kcal mol^{-1} less stable than the corresponding linear dicoordinated $M(NH_3)_2^+$ complexes.

Alternative pathways involving ligand dissociation are therefore feasible for catalysts based on a metal center from group 9 or 10, but not for the catalysts based on a metal center from group 11. In fact, we were unable to find planar tetracoordinated transition states for the $M(NH_3)_2$ complexes with M = Co^-, Rh^-, Ir^-, Pd and Pt. For $Ni(NH_3)_2$ we located a transition state and product complex with both ligands attached to the metal center, but an alternate path including the rearrangement of one ligand is also feasible. For $Ir(NH_3)_2^-$, we find no transition state for methane activation after the catalyst rearranges to $IrNH_3^-(NH_3)$, but instead a barrierless formation of the addition product (see Table 6.1, PES as in Figure 6.2b). In general, the geometries of the stationary points along these alternative reaction paths are similar to those of the corresponding monocoordinated MNH_3 catalyst complexes. Note also that the shape of reaction profiles is similar, although they have been shifted up due to the reorganization of $M(NH_3)_2$ to $MNH_3(NH_3)$.

Interestingly, in the case of $Co(NH_3)_2^-$, $Rh(NH_3)_2^-$ and $Ir(NH_3)_2^-$, we also find an additional pathway via a transition state in which the ligands remain coordinated to the metal, but the metal-ligand bonds are oriented perpendicular to the plane formed by the activated C–H bond and the metal center (see Figure 6.1 for $Rh(NH_3)_2^-$). This distorted tetrahedral arrangement also avoids steric repulsion between the ligands and the substrate, and allows the catalyst to remain almost linear, thereby avoiding the unfavorable strain energy that would be induced by decreasing its rigid bite angle (see chapter 3), or dissociating one of the two NH_3 ligands. Despite avoiding both destabilizing effects, these transition

states are relatively high in energy compared to the barriers for other catalyst complexes based on these metal centers (see Table 6.1), due to additional (Pauli) repulsion between the occupied orbitals of the reactants, which significantly weakens the catalyst-substrate interaction.

The nonplanar transition state for $Rh(NH_3)_2^-$ leads to a planar product at –5.5 kcal mol^{-1}, with the NH_3 ligands in *trans* positions (see Figure 6.1). In the product complexes for $Co(NH_3)_2^-$ and $Ir(NH_3)_2^-$ the ligands keep their almost perpendicular orientation to the plane containing the metal and the activated C–H bond, leading to complexes with a distorted tetrahedral geometry, with ligand-metal-ligand angles of 166.2° and 175.8°, respectively. These product complexes are at +5.1 kcal mol^{-1} for $Co(NH_3)_2^-$ and +10.3 kcal mol^{-1} for $Ir(NH_3)_2^-$ (see Table 6.1). For comparison, we have optimized planar *cis* products for these catalysts, similar to the product shown in Figure 6.1 for $Pd(PH_3)_2$. These *cis* complexes were found to have relative energies of –25.3, –11.2 and –25.4 kcal mol^{-1} for $Co(NH_3)_2^-$, $Rh(NH_3)_2^-$ and $Ir(NH_3)_2^-$, respectively.

Methane activation by group 10 catalysts $Pd(NH_3)_2$ and $Pt(NH_3)_2$ also proceeds via dissociation of one of the NH_3 ligands. To obtain an idea of how the reaction profile involving a tetracoordinated TS would look like, we have optimized and analyzed the fictitious reaction profile for methane activation under the constraint that the two M–NH_3 bonds remain equal in length, to prevent dissociation of one ligand; the resulting relative energies are collected in Table 6.1. For the product complexes, no such constraint was necessary as these complexes do have equilibrium structures $Pd(NH_3)_2(CH_3)(H)$ and $Pt(NH_3)_2(CH_3)(H)$ in which both M–NH_3 coordination bonds are intact. These product complexes have relative energies of +14.7 kcal mol^{-1} and +0.8 kcal mol^{-1}, respectively. These numbers fit the trends observed for the other bisligated catalyst complexes. For $Ni(NH_3)_2$, we found a regular planar tetracoordinated complex, such as that shown in Figure 6.1 for $Pd(PH_3)_2$. Its relatively high barrier compared to the other dicoordinated nickel-based catalysts again originates from the bite-angle rigidity of $M(NH_3)_2$ complexes.

6.7 Catalyst Design Principles: d Regime versus s Regime

The emerging insights about metal and ligand effects on catalyst activity may be combined to yield design principles for catalyst complexes that are tailor-made for activating particular bonds in a substrate. In most cases, we can even simply add up the different effects that we have uncovered. Barriers can be tuned down, for example, by making the metal complex

a better electron donor and by increasing its intrinsic bite-angle flexibility to accommodate the incoming substrate. These two effects cause the interaction curve ΔE_{int} to become more stabilizing, and the strain curve ΔE_{strain} to become less destabilizing, which both result in a lowering of the overall reaction profile and barrier. This is illustrated by the schematic activation strain diagrams in Figure 6.4. The electron-donating capability of ML_n can be enhanced, for example, by choosing an effectively negatively charged d^{10} metal center from group 9 (see section 6.3), introducing a strong σ-donating ligand or even a negatively charged ligand (anion assistance[201,304,305]). The bite-angle flexibility can be enhanced by increasing the intrinsic tendency of the complex to adopt a bent L–M–L geometry through enhanced π backbonding (see chapter 3), steric attraction (see chapter 4), or by introducing a short bridge between the two coordinating L moieties as a structural constraint to force the bite angle to smaller values, as in chelating ligands.[241,251]

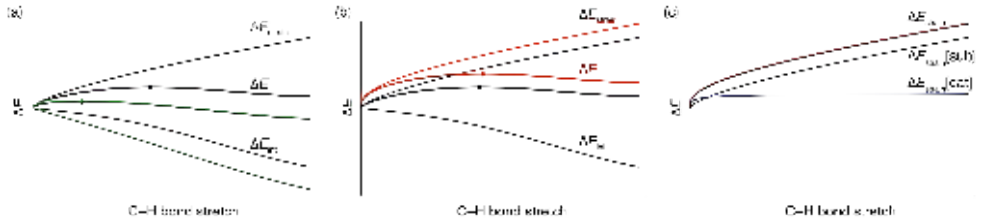

Figure 6.4 Schematic activation strain diagrams (Equation 2.10) showing how the reaction barrier can be reduced: (a) by strengthening the interaction ΔE_{int} (from black to green curves); and (b) by softening the activation strain ΔE_{strain} (from red to black curves); for example (c) by reducing the activation strain ΔE_{strain}[cat] contributed by the bending of the catalyst during the reaction (blue curve). A dot designates the position of the TS.

Interestingly, barriers cannot in all cases be lowered by pushing up metal d orbitals, as we already alluded to in previous sections. In the majority of model reactions, we do observe this relationship between a lower barrier and a higher catalyst d orbital energy. This more common situation is what we designate the 'd regime' (see Figure 6.5). Examples of d-regime catalysts are the anionic group 9 and neutral group 10 catalysts. For d-regime catalysts, the ammine-ligated complex has the lowest barrier because the ammine ligands slightly push the d orbitals up in energy through σ donation. Addition to carbonyl-ligated d-regime catalysts, on the other hand, goes with higher barriers, despite reduced bending strain, because the carbonyl ligand effectively stabilizes the d orbitals through π backbond-

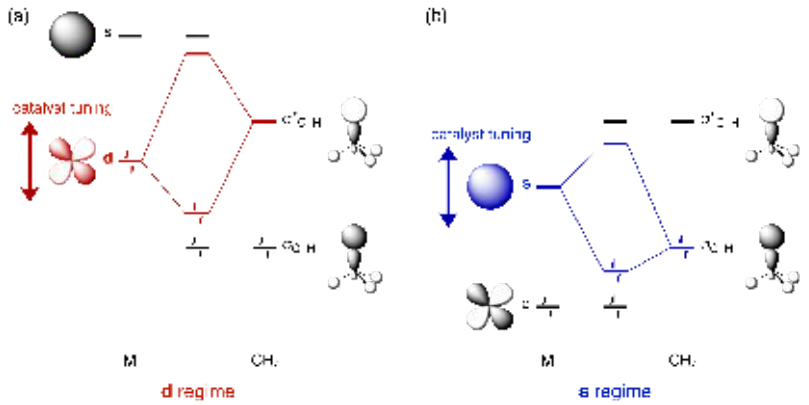

Figure 6.5 Schematic representation of key orbital interactions between the metal center M of the catalyst and the substrate CH_4, defining: (a) the d regime in which catalyst activity can be adjusted by tuning d orbitals (indicated in red) and (b) the s regime in which catalyst activity can be adjusted by tuning the s orbital (indicated in blue).

ing. Consequently, along $RhCO^-$, $RhPH_3^-$, and $RhNH_3^-$, the energy of the catalyst HOMO increases from +1.6 to +2.2 to +2.5 eV (see Table 6.2), which induces a more stabilizing interaction ΔE_{int} curve and therefore a lower and lower barrier $\Delta E^{\ddagger}$ for C–H bond activation. The latter goes down from $\Delta E^{\ddagger}$ = –0.4 to –3.8 to –12.5 kcal mol^{-1}, along $RhCO^-$, $RhPH_3^-$, and $RhNH_3^-$, respectively (see Table 6.1).

However, a different trend is obtained for group 11 complexes, which are in what we designate the 's regime'. Now, the lowest barrier no longer occurs for the ammine-ligated complexes, but for the carbonyl-ligated catalysts. The reason why this may seem unexpected is the fact that the ML_2 d hybrid orbitals are still highest in energy for the ammine-ligated catalysts and lowest for the carbon monoxide-ligated ones (see Table 6.2). Thus, according to the activation strain diagram in Figure 6.4, one might expect the lowest barrier to occur for the catalyst complex that can enter into the strongest π-backbonding interaction with the substrate, namely, the ammine-ligated complex with its high-energy d hybrid orbitals.

What has happened, however, is that a different catalyst-substrate bonding mechanism, with a different dependence on orbital energies, has joined the game for the group 11 complexes. Due to the net positive potential in these cationic species, all metal complex orbitals are at relatively low energy and π backbonding is no longer of much importance (see also chapter 3). The question whether the ligands push the d orbital energy up or not

still matters (for example, the C–H activation barrier for $Au(PH_3)_2^+$ is still a bit higher than for $Au(NH_3)_2^+$), but has become less important. On the other hand, the empty metal s orbitals have been stabilized significantly, such that donation from the substrate σ_{C-H} HOMO to this low-energy catalyst LUMO becomes important. We are now in the s regime (see Figure 6.5), for which trends in reaction barriers are dictated primarily by the metal s orbital and how this orbital is affected by the choice of ligands.

The concepts of d regime and s regime explain in a straightforward manner the inversion of ligand effects that we encountered for the group 11 complexes. The additional lowering of the metal LUMO that occurs via backbonding from metal to a π-accepting ligand, such as CO (*i.e.*, through the associated increase of the effective positive potential at M) makes the metal an even better acceptor for σ donation from the substrate. Thus, the interaction curve ΔE_{int} for these positively charged group 11 complexes becomes more stabilizing and the barrier goes down from values between +35 and +41 kcal mol^{-1} for $AgNH_3^+$ and $AgPH_3^+$, respectively, to +32 kcal mol^{-1} for $AgCO^+$ (see Table 6.1). Other prominent examples of s-regime catalysts are the bisligated gold catalysts, which achieve the lowest barrier for $Au(CO)_2^+$ (see Table 6.1 and 6.2). A closer inspection of the palladium-based catalysts shows that, already for the neutral complexes, this influence on ΔE_{int} of σ donation from substrate to catalyst begins to play a role. The interplay of electronic mechanisms is, however, rather subtle, leading to only a small energy difference between, for example, the barriers for $PdPH_3$ and PdCO (+15.7 and +15.5 kcal mol^{-1}, respectively).

It follows that, to rationally devise a catalyst with the desired reactivity, one should not only consider the effect of metal variation and ligand variation, but also their combined effect, as well as the primary mode of interaction with the target substrate: (i) for catalyst complexes from the d regime, in which bond breaking depends primarily on d orbital properties, modifications for tuning should be aimed at adjusting these d orbitals; and (ii) on the other hand, for catalysts from the s regime, one should aim at adjusting the metal s orbitals. For the latter category of catalysts, d orbital tuning has, at best, little effect on the reactivity, but is likely to induce effects opposite to what is attempted, as revealed by the unexpected lowering of barriers when π-backbonding ligands are attached to group 11 catalyst complexes. This picture is qualitatively different from the picture based on the splitting of the $d^{10}s^0$ to d^9s^1 states in the catalyst, as is commonly suggested.[8,248,315] Although the two bear resemblances, a description based on the splitting of the $d^{10}s^0$ and d^9s^1 states does not indicate when to tune the d orbitals or the s orbitals, because both affect the $d^{10}s^0$-d^9s^1 transition energy similarly.

6.8 Conclusions

We have developed three new concepts for catalyst design: (i) bite-angle flexibility, (ii) d-regime catalysts, and (iii) s-regime catalysts. These concepts, further detailed below, emerge from our activation strain analyses of 72 methane C–H bond activation reactions by d^{10}-ML_n complexes, based on relativistic density functional theory. The analyses of this vast set of reaction potential energy surfaces, all obtained consistently at the same level of theory, make it possible to examine systematically how and why the activity of d^{10}-ML_n catalysts toward methane C–H oxidative addition varies along all of the nine d^{10} metal centers of groups 9 to 11, combined with the effects of variations along uncoordinated, mono- and bisligated systems, involving σ-donating and π-accepting ligands.

The concept of bite-angle flexibility is a change of paradigm regarding the role of the bite angle in a catalyst complex. We have shown that the bite angle is not decisive for the catalyst's activity. What is decisive instead is the catalyst's flexibility towards assuming a nonlinear L–M–L geometry during the bond activation. Such a nonlinear geometry is crucial when the C–H bond to be activated is coordinating and breaking, because in that situation a bent L–M–L geometry avoids strong steric (Pauli) repulsion between the catalyst complex and the substrate. Traditionally, this factor is addressed by tuning (reducing) the bite angle with the help of a structural constraint, imposed by the molecular scaffold, that pulls the two coordinating sites closer to each other, thus making room for the incoming substrate. This indeed reduces the catalyst activation strain $\Delta E^{\ddagger}_{\text{strain}}[\text{cat}]$ and thus the reaction barrier $\Delta E^{\ddagger}$.[241,251] However, the catalyst activation strain can also be reduced simply by making the catalyst complex sufficiently flexible, that is, by designing the electronic structure of the d^{10}-ML_n complex, such that the PES for L–M–L bending becomes shallow. This can be done by amplifying metal-to-ligand π backdonation, for example, by improving the π-accepting capability of the ligands in the catalyst complex, as discussed in chapter 3.

The choice of ligands and metal determines not only the bite-angle flexibility, but also the catalyst's binding capability towards the substrate. In what we designate the d regime, the catalyst-substrate interaction is dominated by donor-acceptor orbital interactions between the catalyst d_π hybrid orbitals and the substrate $\sigma^*_{\text{C–H}}$ acceptor orbital. This situation is implicitly assumed in textbook examples about catalyst tuning. In this regime, the metal d orbitals are therefore the prime target for catalyst tuning (see Figure 6.5a). The d regime occurs for anionic group 9 and, to a lesser extent, for neutral group 10 ML_n catalyst com-

plexes. The catalyst-substrate interaction in this regime is enhanced by σ-donating ligands (*e.g.*, NH_3) that push the d orbitals up in energy, and it is weakened by π-backbonding ligands (such as CO, and to a lesser extent PH_3) that stabilize the d orbitals.

However, a breakdown of this textbook behavior occurs if we switch over to the s regime. For s-regime catalysts, such as the cationic group 11 ML_n complexes, the catalyst-substrate interaction is dominated by donor-acceptor orbital interactions between the substrate's HOMO (σ_{C-H} in the case of methane) and the catalyst's s-derived acceptor orbital. In this regime, catalyst tuning is achieved by influencing the metal s orbital (see Figure 6.5b). The d orbitals have little or no influence. Ligand effects in the s regime therefore work in opposite direction: the catalyst-substrate bonding is enhanced by π-backbonding ligands (most notably CO) and it is weakened by σ-donating ligands, such as NH_3.

The insights obtained in this chapter reveal causal relationships between barriers for bond activation, on one hand, and the orbital electronic structure of the catalyst's metal and ligands, on the other hand, and thus constitute new tools for a more rational design and tuning of catalysts. In the following chapter, we demonstrate how these design principles allow activation of selectively targeted bonds in substrates.

7 Rational Catalyst Design: Selective C–H and C–C Bond Activation

Previously appeared as

Selective C–H and C–C Bond Activation:
Electronic Regimes as Tool for Designing d^{10}-ML_n Catalysts
L. P. Wolters, F. M. Bickelhaupt
Chem. Asian J. **2015**, *5*, 2272–2282

7.1 Introduction

The purpose of this chapter is to unravel how a transition metal catalyst can be rationally designed such as to selectively activate one particular bond in a substrate. Here, the bonds between which we wish the model catalyst to be selective are in the first place the C–H and C–C bonds in ethane and, in the second place, the C–H bonds in ethane versus those in methane. The stability of C–H and C–C bonds is a prerequisite for human life, while, at the same time, the development of methods to break these chemical bonds in a selective manner is of great importance as well. Activation of C–H and C–C bonds has received considerable attention,[26,27,29,52,321-326] mainly because this is an important step towards efficient conversion of abundant and inert hydrocarbons into more useful products. Also, cleavage of C–C bonds can potentially lead to new synthetic pathways towards complex molecules.[321,327,328] Besides the efficiency, also the selectivity of the catalysts has been topic of a vast body of research.[329-336]

Previously, the reactivity of ethane towards palladium-based catalysts has been examined.[57,194,201,241,251,337] It was found that activation of the C–C bond occurs with higher barriers, despite the fact that this bond is weaker than the C–H bond. The reason for this is that, due to steric shielding by the C–H bonds as well as the additional nodal plane present in the C–C σ^* orbital, the C–C bond has to be stretched further in order to achieve a fa-

vorable overlap with the donating metal d orbital.[338] The orbital overlap situations are shown schematically in Figure 7.1. The resulting delay in overlap leads to a significant delay in the build-up of stabilizing catalyst-substrate interactions, and therefore a higher reaction barrier.[194]

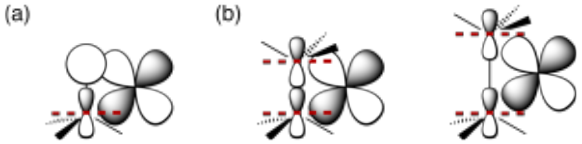

Figure 7.1 Schematic representation of the overlap of a metal d orbital with the σ* orbital of (a) a C–H bond and (b) a short and stretched C–C bond.

To obtain insight into the effect of the nature of the electronic structure of the catalyst on the energy barriers, we have analyzed the activity and selectivity of a large series of model catalysts towards ethane. The catalysts comprise the complexes that were also analyzed in chapters 3 and 6, namely the d^{10}-ML_n complexes with coordination number n = 0, 1 and 2, metal centers M = Co^-, Rh^-, Ir^-, Ni, Pd, Pt, Cu^+, Ag^+ and Au^+, and ligands L = NH_3, PH_3, and CO. For comparison, we will also make use of the results for methane activation, as discussed in the previous chapter.

In this way, we can compose and analyze model catalysts with a wide range of electronic and steric properties, which is important for our proof of concept for rationally designing and tuning a catalyst's activity and selectivity. Our analyses demonstrate that the rather subtle electronic differences between bonds can be exploited to induce a lower barrier for activating one or the other, depending, among others, on the catalyst's electronic regime (*i.e.* s-regime versus d-regime catalysts). Interestingly, the concepts and design principles emerging form this work appear to be successfully applicable to the more challenging problem of differentiating between activation of the C–H bonds in ethane versus those in methane.

7.2 General Energy Profiles for Ethane C–H and C–C Activation

The results of our computations at ZORA-BLYP/TZ2P on ethane C–H and C–C bond activation reactions are listed in Table 7.1 and 7.2, respectively. Similar to results in chap-

ters 3 and 6, these energies are relative to the catalysts in a $d^{10}s^0$ (uncoordinated metal atoms) or d^{10}-like (coordinated metal centers) configuration. We kept our model catalysts in this electronic configuration because it enables us to make a direct comparison with d^{10}-ML_n catalysts used in practice. Nearly all catalysts included in this study indeed have a d^{10} or d^{10}-like ground state, but there are exceptions: Co^-, Rh^- and Ir^- have s^2d^8 atomic ground states, whereas Ni and Pt have s^1d^9 ground states, according to our computations. For these uncoordinated catalysts, strong mixing with the low metal s orbitals stabilizes the entire energy profile with respect to the isolated reactants (see Table 7.1 and 7.2). When ligands are added to these metal centers, the resulting complexes generally have d^{10}-like electronic ground states. Only the monocoordinated cobalt complexes, as well as the dicoordinated $Co(NH_3)_2^-$ and $Ir(NH_3)_2^-$ have non-aufbau d^{10}-like configurations.

Oxidative addition of the ethane C–H and C–C bonds generally starts with the formation of a dihapto reactant complex (RC), in which the ethane substrate coordinates via two C–H bonds to the metal center. For the bisligated model catalysts, such pre-reactive complexes are not always bound, or only weakly. From here, the metal center of the catalyst moves towards the C–H or C–C bond to proceed with the oxidative addition. In a number of instances, mostly for the strongly d-donating catalysts with a group 9 metal center, the oxidative addition proceeds without reaction barrier, and stable reactant complexes do therefore not exist.

We find that there are three different orientations for the catalyst to approach the ethane C–H bond. Schematic representations of these orientations are shown in Figure 7.2. Not all of these three orientations are necessarily feasible for each catalyst. Most commonly, the oxidative addition pathway starts from the dihapto reactant complex, in which the metal coordinates to two C–H bonds of a methyl moiety, followed by the insertion of the catalyst into one of these bonds (Figure 7.2, left).

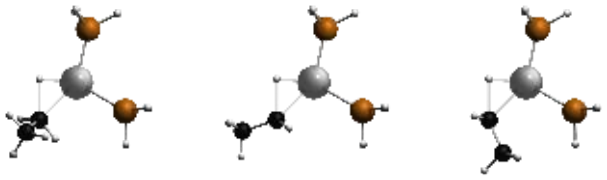

Figure 7.2 Schematic geometries of the different orientations of ethane in the transition state geometries for addition of the ethane C–H bond to the metal center of a catalyst.

Table 7.1 Energies ΔE relative to reactants (in kcal mol^{-1}) for the oxidative addition of the ethane C–H bond to various model catalysts. Square brackets indicate that constraints were applied (see text).

	Group 9				Group 10				Group 11		
	RC	TS	PC		RC	TS	PC		RC	TS	PC
Co^- [a]	[b]	[b]	−242.0[c]	Ni[a]	−55.9	−54.0	−69.7[c]	Cu^+	−31.1[c]	−15.7	−16.0
$CoNH_3^-$ [a]	[b]	[b]	−37.6[c]	$NiNH_3$	−18.6	−12.0	−14.7[c]	$CuNH_3^+$	−28.0	[h]	[+6.0][e,h]
$CoPH_3^-$ [a]	−18.8	−18.0	−34.7[c]	$NiPH_3$	−12.2[c,e]	−7.2 [e]	−12.7[e]	$CuPH_3^+$	−24.1	[h]	[+12.1][e,h]
$CoCO^-$ [a]	−16.3	−14.0	−27.4[c]	NiCO	−13.7[c]	−3.9 [e]	−7.0[e]	$CuCO^+$	−29.7[c]	[h]	[+3.1][e,h]
$Co(NH_3)_2^-$ [a]	0.0	+11.5[d]	+5.7[d]	$Ni(NH_3)_2$	−0.8	[+25.2][f]	+6.9	$Cu(NH_3)_2^+$	−2.1	[h]	[+40.0][h]
$Co(PH_3)_2^-$	−7.5	−0.4	−14.0	$Ni(PH_3)_2$	0.0[c]	+15.3	+12.3	$Cu(PH_3)_2^+$	−1.3	[h]	[+40.8][h]
$Co(CO)_2^-$	−1.4[b]	+8.2	−2.7	$Ni(CO)_2$	−3.2	+21.1	+21.0	$Cu(CO)_2^+$	−8.6	[h]	[+34.1][h]
Rh^- [a]	−44.4	−44.3	−74.4	Pd	−6.7	+4.5	−4.3[c]	Ag^+	−15.5[c]	+15.7	+15.6
$RhNH_3^-$	−14.3	−12.5	−26.4	$PdNH_3$	−12.1	+2.1	+0.1[c]	$AgNH_3^+$	−16.2	[h]	[+26.4][h]
$RhPH_3^-$	−11.1	−2.7	−15.1[c]	$PdPH_3$	−7.9	+16.5	+15.8[c]	$AgPH_3^+$	−14.8	[h]	[+32.5][h]
$RhCO^-$	−9.7	+0.7	−9.7[c]	PdCO	−10.3	+16.1	+16.1[c]	$AgCO^+$	−19.6	[h]	[+24.4][h]
$Rh(NH_3)_2^-$	−2.8	+29.5[d]	−3.8[d]	$Pd(NH_3)_2$	0.0	[+30.6][f]	+16.0	$Ag(NH_3)_2^+$	−1.8	+46.6	+46.6
$Rh(PH_3)_2^-$	0.0	+15.0	−1.0[c]	$Pd(PH_3)_2$	0.0	+34.2	+28.9	$Ag(PH_3)_2^+$	−1.0	[h]	[+52.0][h]
$Rh(CO)_2^-$	−1.0	+23.5	+7.2	$Pd(CO)_2$	−0.1	+35.2	+31.5	$Ag(CO)_2^+$	−4.0	[h]	[+43.1][h]
Ir^- [a]	[b]	[b]	−119.2	Pt[a]	[b]	[b]	−56.3 [c]	Au^+	−34.8	−30.5	−40.6
$IrNH_3^-$	[b]	[b]	−41.2[c]	$PtNH_3$	−18.6	−16.6	−24.1 [c]	$AuNH_3^+$	−27.8	−10.9	−11.2
$IrPH_3^-$	−10.6	−7.9	−30.7	$PtPH_3$	−10.4	+3.0	−2.5 [c]	$AuPH_3^+$	−20.1	[h]	[+7.6][h]
$IrCO^-$	−8.2	−2.9	−22.9	PtCO	−14.9	+1.2	−2.9 [c]	$AuCO^+$	−32.1	−8.7	−9.7
$Ir(NH_3)_2^-$ [a]	−4.7	+22.9[d]	+11.8[d]	$Pt(NH_3)_2$	−0.2	[g]	+1.9	$Au(NH_3)_2^+$	−2.1	+37.1	+25.7
$Ir(PH_3)_2^-$	0.0	+13.3	−16.5	$Pt(PH_3)_2$	0.0	+31.7	+13.2	$Au(PH_3)_2^+$	−0.9	+42.5	+36.3
$Ir(CO)_2^-$	−1.2	+22.0	−6.5	$Pt(CO)_2$	0.0	+32.0	+16.1	$Au(CO)_2^+$	−2.3	+31.3	+26.2

[a] Catalyst complex with a non-aufbau $d^{10}s^0$ or d^{10}-like electronic configuration. [b] Inserts without barrier. [c] Minimum directly connected to TS, rearrangement to more stable complex possible. [d] Energy refers to the complex with the ligands oriented out of the plane formed by the metal center and the C–H bond to be activated (see section 6.6). [e] Complex containing an agostic interaction between the metal center and a C–H bond. [f] One ligand dissociates during insertion: energy in brackets obtained by constraining both metal-ligand bond lengths to remain equal (see section 6.6). [g] Transition state not found (see text). [h] No reverse barrier, energy of the labile PC within brackets.

Alternatively, the metal can approach a methyl moiety from the back (opposite the other methyl moiety) and insert into one of its C–H bonds (Figure 7.2, middle), or the catalyst can approach with the metal center within the plane containing the C–C bond and a C–H bond, and insert into this C–H bond (Figure 7.2, right). Only for a few catalysts is this latter pathway found, and usually it is higher in energy owing to the additional deformation of the substrate that is required to avoid repulsion with the catalyst. There are some bare and monocoordinated catalysts for which this situation is feasible, because there is additional stabilization stemming from an agostic interaction between the metal center and a C–H bond of the adjacent methyl moiety. In those cases, this latter methyl moiety is rotated to an eclipsed position.[339,340] Within this work, we focus on the analysis of the pathway

Table 7.2 Energies ΔE relative to reactants (in kcal mol^{-1}) for the oxidative addition of the ethane C–C bond to various model catalysts. Square brackets indicate that constraints were applied (see text).

	Group 9				Group 10				Group 11		
	RC	TS	PC		RC	TS	PC		RC	TS	PC
Co^- [a]	−243.2[b]	−208.9[b]	−254.5	Ni[a]	−51.0[f]	−46.7	−80.4	Cu^+	−31.1[f]	−18.6	−26.0
$CoNH_3^-$ [a]	−45.5[b]	−11.1[b]	−47.0	$NiNH_3$	−9.3[f]	−2.2	−20.9	$CuNH_3^+$	−28.0	[h]	[−0.9][h]
$CoPH_3^-$ [a]	−40.8[c,d]	−9.2[c]	−40.5	$NiPH_3$	−12.2[f]	+2.4	−9.3	$CuPH_3^+$	−24.1	[h]	[+7.3][h]
$CoCO^-$ [a]	−33.8[c,d]	−3.5[c]	−33.3	NiCO	−13.7[f]	+4.0	−2.7	$CuCO^+$	−29.7[f]	[h]	[−1.5][h]
$Co(NH_3)_2^-$ [a]	0.0	+18.2[e]	−4.5[e]	$Ni(NH_3)_2$	−0.8	[+43.6][g]	+2.0	$Cu(NH_3)_2^+$	−2.1	−41.9	+35.3
$Co(PH_3)_2^-$	−7.5	+14.1	−18.1	$Ni(PH_3)_2$	0.0[f]	+28.5	+10.2	$Cu(PH_3)_2^+$	−1.3	−41.5	+39.5
$Co(CO)_2^-$	−1.4[f]	+24.3	−7.0	$Ni(CO)_2$	−3.2	+33.0	+19.4	$Cu(CO)_2^+$	−6.8[f]	[h]	[+32.1][h]
Rh^- [a]	−68.8[b]	−30.6[b]	−80.0	Pd	−6.7	+18.5	−9.4	Ag^+	−15.5[f]	+13.3	+8.5
$RhNH_3^-$	−14.3	+8.0	−30.8	$PdNH_3$	−12.1	+16.5	−3.2	$AgNH_3^+$	−16.2	+20.7	+20.7
$RhPH_3^-$	−11.1	+15.0	−16.7	$PdPH_3$	−7.9	+26.3	+13.6	$AgPH_3^+$	−14.8	[h]	[+28.4][h]
$RhCO^-$	−9.7	+18.4	−11.8	PdCO	−10.3	+24.4	+13.8	$AgCO^+$	−19.6	[h]	[+19.6][h]
$Rh(NH_3)_2^-$	−2.8	+43.6[e]	+17.2[e]	$Pd(NH_3)_2$	0.0	[+53.3][g]	+12.9	$Ag(NH_3)_2^+$	−1.8	+50.9	+41.8
$Rh(PH_3)_2^-$	−0.0	+36.2	−4.8	$Pd(PH_3)_2$	0.0	+51.7	+26.6	$Ag(PH_3)_2^+$	−1.0	+54.3	+48.7
$Rh(CO)_2^-$	−1.0	+44.5	+2.8	$Pd(CO)_2$	−0.1	+51.4	+29.0	$Ag(CO)_2^+$	−4.0	+42.8	+39.3
Ir^- [a]	−134.7[b]	−62.1[b]	−125.8	Pt[a]	−56.6[c]	−1.5 [c]	−60.0	Au^+	−34.8	−13.0	−45.9
$IrNH_3^-$	−55.4[b]	+6.6[b]	−46.1	$PtNH_3$	−18.6	+10.0	−25.9	$AuNH_3^+$	−27.8	+0.1	−11.7
$IrPH_3^-$	−30.2[c,d]	+14.0[c]	−31.0	$PtPH_3$	−10.4	+21.1	−3.9	$AuPH_3^+$	−20.1	+12.0	+6.4
$IrCO^-$	−22.4[c,d]	+19.1[c]	−23.8	PtCO	−14.9	+17.2	−5.0	$AuCO^+$	−32.1	−3.6	−10.7
$Ir(NH_3)_2^-$ [a]	−4.7	+44.3[e]	+5.0[e]	$Pt(NH_3)_2$	−0.2	+75.1 [e]	+0.6	$Au(NH_3)_2^+$	−2.1	[+60.8][g]	+23.7
$Ir(PH_3)_2^-$	0.0	+40.2	−19.1	$Pt(PH_3)_2$	0.0	+57.5	+12.2	$Au(PH_3)_2^+$	−0.9	+61.2	+34.8
$Ir(CO)_2^-$	−1.2	+47.3	−10.6	$Pt(CO)_2$	0.0	+55.0	+14.1	$Au(CO)_2^+$	−2.3	+49.1	+24.1

[a] Catalyst complex with a non-aufbau $d^{10}s^0$ or d^{10}-like electronic configuration. [b] Ethane C–C activation achieved via activation of two C–H bonds. [c] Ethane C–C activation achieved via activation of one C–H bond. [d] Complex containing an agostic interaction between the metal center and a C–H bond. [e] Energy refers to the complex with the ligands oriented out of the plane formed by the metal center and the C–C bond (see section 6.6). [f] Minimum directly connected to TS, rearrangement to more stable complex possible. [g] One ligand dissociates during insertion: energy in brackets obtained by constraining both metal-ligand bond lengths to remain equal (see section 6.6). [h] No reverse barrier, energy of the labile PC within brackets.

with the energetically lowest reaction barrier to the first C–H insertion product. In some cases a second, more stable product can be formed after rearrangement via a small barrier. The energetic difference with the second, more stable product is usually small, unless a favorable agostic interaction occurs within this second product complex. This is the case, for example, for some monocoordinated catalysts based on Co^- and Ni, for which the second product is 4.8 to 6.4 kcal mol^{-1} more stable than the first product (see Table 7.1).

The C–C oxidative addition pathway proceeds for most catalyst complexes from the dihapto RC to the C–C activation product via a single transition state. However, for some catalysts the only route to this C–C activation product involves the activation of one, or even two, C–H bonds. For the discussion of the trends in reaction barrier height, as well as

the demonstration for catalyst tuning, we will focus on the results obtained for the direct C–C activation pathways. A separate section is devoted to a brief discussion of the C–C activation pathways that proceed by prior C–H activation.

7.3 Trends in Reaction Barriers for Ethane C–H Activation

In general, the trends observed for ethane C–H activation closely resemble the trends previously obtained and described for activation of the rather similar methane C–H bond (see chapter 6, Table 6.1). Thus, starting with the effect of varying the metal center from group 9 to group 11, we find that the barrier increases monotonically. For example, the barrier increases from +15.0 kcal mol^{-1} for $Rh(PH_3)_2^-$ to +34.2 kcal mol^{-1} for $Pd(PH_3)_2$, and for $Ag(PH_3)_2^+$ there is not even a stable product complex. By optimization with the C–Ag–H angle constrained to the value of the analogous palladium-based product complex, we have modeled a labile product complex for $Ag(PH_3)_2^+$ at +52.0 kcal mol^{-1}. Also, while the reaction is exothermic for $Rh(PH_3)_2^-$, it is endothermic for $Pd(PH_3)_2$ and even more so for $Ag(PH_3)_2^+$. Activation strain analyses (see Figure 7.3a) revealed that the computed trend originates from decreased metal-to-substrate electron donation as the d orbital energies become lower along this series of catalyst complexes, in agreement with the results in chapter 6. This leads to a less stabilizing interaction energy, and therefore a higher reaction barrier and less stable product complex.

A comparison of catalyst complexes with metal centers from the same group, for example the group 10 triad $Ni(PH_3)_2$, $Pd(PH_3)_2$ and $Pt(PH_3)_2$, reveals that the barriers first increase from the first row to the second row transition metal center, and then again decrease for the catalyst complex with a metal center from the third transition metal row (for analyses, see Figure 7.3b). The barrier of +15.3 kcal mol^{-1} for $Ni(PH_3)_2$ is lower than that of +34.2 kcal mol^{-1} for $Pd(PH_3)_2$ because the d-derived orbitals on the former are higher in energy and therefore better electron donors. From $Pd(PH_3)_2$ to $Pt(PH_3)_2$, the electron-donating capability increases slightly due to the larger spatial extent of the Pt d orbitals, and resulting better overlap with the σ^*_{C-H} acceptor orbital. Furthermore, the third row transition metals are better electron acceptors as a consequence of the relativistic stabilization of the empty 6s atomic orbital. This leads to a low-lying virtual orbital on $Pt(PH_3)_2$ that enhances the substrate-to-catalyst donation during the oxidative addition process. The result is a strengthened interaction between the reactants, which also contributes to the

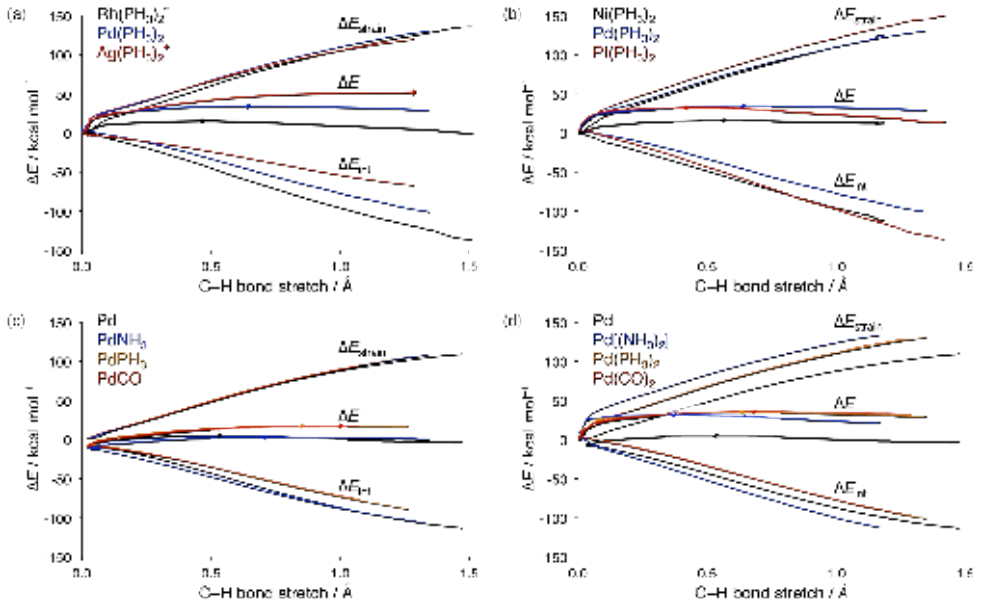

Figure 7.3 Comparison of activation strain analyses (see Equation 2.10) for the oxidative addition of the ethane C–H bond to four different series of model catalysts (using constraints for $Pd(NH_3)_2$; see text). A dot designates the position of the TS.

lower reaction barrier of +31.7 kcal mol^{-1} for $Pt(PH_3)_2$ compared to that of +34.2 kcal mol^{-1} for $Pd(PH_3)_2$, as well as a more stable product complex for the former model catalyst.

Finally, we sketch the main trends in ligand effects in ethane C–H activation (see Figure 7.3c and 7.3d), which are again similar to those found for methane C–H activation (see chapter 6). Typically, we find higher reaction barriers when the ligand is a better π acceptor, because these ligands deplete the electron density on the metal center and thereby reduce donation from the metal d orbitals to the substrate. In general, the carbonyl-ligated catalysts therefore have higher barriers than the phosphine-ligated catalysts, which in turn have higher barriers than the ammine-ligated catalysts. This is nicely illustrated by a comparison of NiCO, $NiPH_3$ and $NiNH_3$, which activate the ethane C–H bond via barriers of –3.9, –7.2 and –12.0 kcal mol^{-1}, respectively (see Table 7.1). In section 6.7, we have designated this the d regime of catalysts. In the d regime, the most important catalyst-substrate orbital interactions involve the d orbitals on the metal center of the catalyst, and ligand effects are therefore best described by considering the influence of the ligand on these d orbitals. For the model catalysts in our study, adding π-accepting ligands stabilizes the do-

nating d orbitals, which results in less electron donation to the substrate, and consequently a higher reaction barrier for the oxidative addition. Ligand effects can be completely reversed in the s regime, where the primary catalyst-substrate interaction is the donation of electrons from the substrate to the empty metal s orbitals. Many group 11 catalyst complexes are in the s regime, because their positive charge makes them good electron acceptors. This feature is improved when π-accepting ligands are attached, resulting in an even stronger substrate-to-metal donation, which leads to a lowering of the reaction barrier. This is most clearly seen for the bisligated gold complexes, comparing for example the barrier of +31.3 kcal mol^{-1} for $Au(CO)_2^+$ to that of +42.5 kcal mol^{-1} for $Au(PH_3)_2^+$ or +37.1 kcal mol^{-1} for $Au(NH_3)_2^+$.

Furthermore, also the dicoordinated group 9 catalysts with ammine ligands have relatively high barriers. These catalysts have poor bite-angle flexibility (see chapter 3), which prohibits the formation of a planar tetracoordinated transition state. Instead, for these catalyst complexes, transition state geometries are found in which the ligands point out of the plane containing the metal center and the C–H bond to be activated. In this perpendicular orientation, the unfavorable bending of the ligand-metal-ligand angle of the catalyst, which would be required if the ligands were oriented parallel to the C–H bond, is avoided. The reason that these perpendicular transition states nevertheless have high energies, is that the σ^*_{C-H} substrate orbital does not overlap with the high-energy b_2 orbital of a bent ML_2 complex, but with an essentially pure, lower-energy d orbital (the b_1 orbital) on the metal center. These orbital overlap situations are schematically depicted in Figure 7.4, for the case of overlap with the σ^*_{C-C} orbital. Also, whereas the high-energy b_2 orbital of a bent ML_2 complex is pushed towards the substrate due to the antibonding interactions with the ligand lone pair orbitals, this pure d orbital of the nearly linear ML_2 complex is not, leading to a decreased overlap with the σ^*_{C-H} orbital. To compensate for these two consequences and nevertheless build up sufficiently strong donor-acceptor interactions, the catalyst moves much closer to the substrate, which in turn induces additional Pauli repulsive occupied-occupied orbital interactions, and a relatively high reaction barrier. For the strongly d-donating group 9 catalysts, this situation is feasible, but for the group 10 $M(NH_3)_2$ catalysts, which also have poor bite-angle flexibility, such nonplanar transition state geometries are not found, because the stabilizing orbital interactions provided by donation from the d hybrid orbitals are not strong enough to overcome the additional Pauli repulsion.

The reaction barriers of $Ni(NH_3)_2$ and $Pd(NH_3)_2$ reported in Table 7.1 have been obtained by constraining the two M–NH_3 coordination bonds to remain mutually equal in

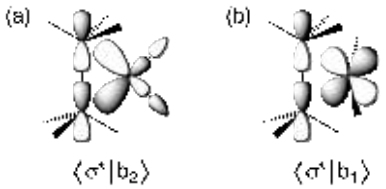

Figure 7.4 Schematic representation of the different catalyst-substrate orbital overlaps, depending on the orientation of the ML_2 catalyst complex.

length. This is done to avoid the expulsion of one of the NH_3 ligands, which otherwise occurs. In this way, we ensure direct comparability of analogous reaction pathways of bisligated catalyst complexes for all ligands, taking into account that a few of them have a fictitious character. We recall from section 6.7 that for $M(NH_3)_2$ catalyst complexes with metal centers from group 9 and group 10 an alternative pathway is viable, in which one of the NH_3 ligands is expelled from the metal center. Here, we have not further investigated these reaction paths, because none of these complexes plays a role in the discussion on selectivity, to which we will soon turn our focus.

Finally, for dicoordinated $Pt(NH_3)_2$, we were unable to locate a transition state corresponding to C–H activation. Our attempts either led to weakly interacting reactants (similar to the RC listed in Table 7.1), the product complex of C–H addition (similar to the PC listed in Table 7.1), or several possible transition states that, however, do not correspond to C–H activation, including one in which an M–NH_3 bond dissociates (results not shown).

7.4 Trends in Reaction Barriers for Ethane C–C Activation

The trends in reaction barriers along series of catalyst complexes are not significantly affected when going from the ethane C–H bond to the C–C bond (compare Table 7.1 and 7.2, and Figure 7.3 and 7.5), and are therefore largely similar to the trends discussed in the previous section. In general, barriers for C–C activation also increase when the metal center is varied from group 9 to group 11, and barriers within a group are usually highest for the second row transition metal. However, among the dicoordinated complexes, the barriers for the third row transition metal-based catalysts are highest, which is mainly due to the additional strain induced by the more rigid ligand-metal-ligand angles (see chapter 3). Also ligand effects are rather similar: transition states are destabilized when π-accepting ligands

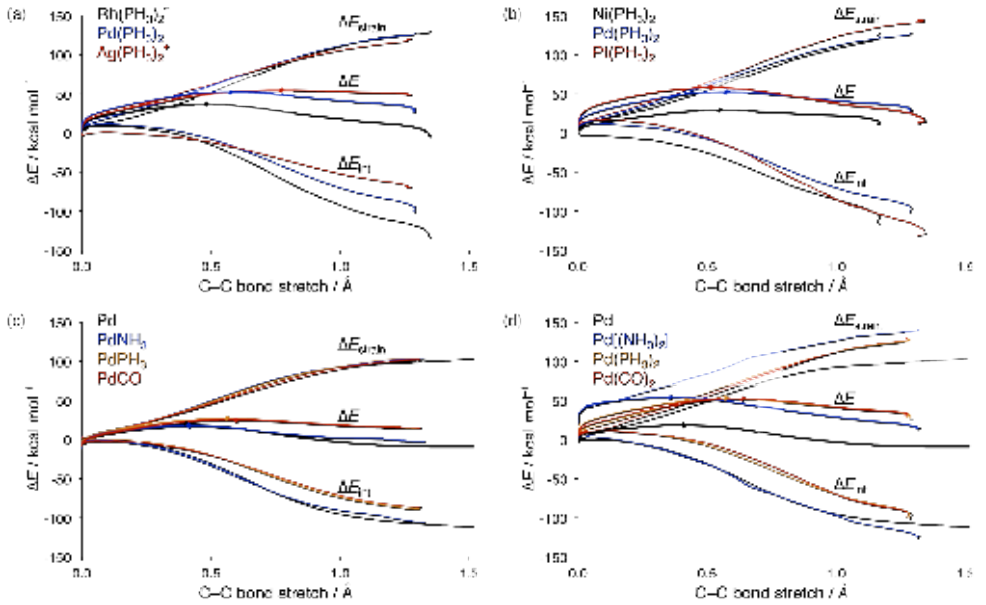

Figure 7.5 Comparison of activation strain analyses (see Equation 2.10) for the oxidative addition of the ethane C–C bond to four different series of model catalysts (using constraints for $Pd(NH_3)_2$; see text). A dot designates the position of the TS.

are added to a strongly d-donating catalyst, whereas such ligands tend to stabilize transition states when the catalyst belongs to the s regime. Again, we find transition state geometries with nearly linear ligand-metal-ligand angles (perpendicular to the activated C–C bond) for $Co(NH_3)_2^-$, $Rh(NH_3)_2^-$, $Ir(NH_3)_2^-$, and $Pt(NH_3)_2$. For $Ni(NH_3)_2$, $Pd(NH_3)_2$ and now also $Au(NH_3)_2^+$, we have located planar tetracoordinated transition states by constraining the metal-ligand bonds to remain equal in length. This is done in order to avoid the expulsion of one ligand, which would otherwise occur, as discussed in the previous section.

Furthermore, we note that nearly all barriers for ethane C–C activation are higher than the barriers for ethane C–H activation, despite the less destabilizing strain energy $\Delta E_{strain}(\zeta)$ associated with the lower BDE in the former. The reason turns out to be a delay in building up stabilizing interaction energy $\Delta E_{int}(\zeta)$ along the reaction coordinate for C–C activation, as compared to C–H activation. This effect was first discovered for palladium-based catalysts[194] and is shown here to occur also for other catalyst complexes. The delay in interaction energy for C–C activation is caused by the fact that the C–C bond is sterically shielded by C–H bonds from all sides. The model catalyst can only approach the C–C

bond after this bond partially elongates and the methyl groups have tilted away. The slightly elongated C–C bond that occurs at that later stage of the reaction also allows for a better overlap between the metal d_π (hybrid) orbital and the σ^*_{C-C} acceptor orbital (see Figure 7.1). Importantly, the strain curve is hardly affected by varying the model catalyst. It is a characteristic of the bond that is being activated, depending mainly on that bond's BDE.

7.5 Selective C–C or C–H Bond Activation

To achieve selective activation of either the C–H or C–C bond in ethane, we recall that the C–C bond is weaker (the purely electronic bond dissociation energies are 104.7 kcal mol^{-1} and 90.0 kcal mol^{-1}, respectively), but nevertheless reaction barriers are higher for addition of this bond due to the aforementioned delayed catalyst-to-substrate charge donation. These two features show up separately in our activation strain analyses: for C–C activation the strain term $\Delta E_{strain}(\zeta)$ is generally softer due to its lower bond dissociation energy, while the interaction term $\Delta E_{int}(\zeta)$ is weakened due to the delay in the build-up of stabilizing donor-acceptor interactions.[194] However, while the effect on the strain term is essentially equal for each catalyst complex (the strain originates primarily from stretching the C–H or C–C bond in the substrate), the effect on the interaction energy is catalyst dependent. If the latter effect is sufficiently diminished, the preferred reaction pathway would shift from the C–H to the C–C bond. Thus, understanding the catalyst dependency of the ΔE_{int} term, and relating it to the previously introduced concepts of d-regime and s-regime catalysts, turns it into a tool to rationally devise a selective catalyst that activates either the C–H or the C–C bond in ethane.

The build-up of stabilizing interactions is delayed because the C–C bond has to be stretched further, before a favorable overlap of the catalyst's d-derived orbital with the σ^*_{C-C} orbital is achieved for the d-donation to take place. Its effect can therefore be mitigated when (i) a catalyst with compact d-derived orbitals is applied, and (ii) catalyst-to-substrate donation plays only a moderate role. Candidates for selective C–C activation are therefore s-regime catalysts with a small metal center. This design principle is schematically illustrated in Figure 7.6a, in which we compare addition of the ethane C–H bond (solid lines) and C–C bond (dashed lines), considering two cases: (i) a catalyst from the d regime, such as the anionic, or most of the neutral complexes, and (ii) a catalyst from the s regime, such as one of the cationic complexes. For both d-regime and s-regime catalysts, activation of the C–C bond goes with less strain energy (black lines in Figure 7.6a). For the strongly d-

donating catalysts, however, the difference in the interaction energy due to the delay effect is greater than the difference in the strain term. This results in an increased reaction barrier (red lines in Figure 7.6a), which is the situation for most catalyst complexes. However, for an s-regime catalyst the delay in the build-up of favorable interaction energy can be smaller than the difference in strain energy (blue lines in Figure 7.6a), in which case a lower barrier for C–C activation than for C–H activation is obtained.

The most obvious candidates with the properties required by our design model are the copper-based catalyst complexes. Comparing the results in Table 7.1 and 7.2, we find indeed a lower barrier for addition of the C–C bond to Cu^+ (–18.6 kcal mol^{-1}, $\Delta G^{\ddagger}$ = –13.2 kcal mol^{-1}) than for the C–H bond (–15.7 kcal mol^{-1}, $\Delta G^{\ddagger}$ = –11.6 kcal mol^{-1}), while for the iso-electronic Ni, addition of the C–H bond is favored (–54.0 kcal mol^{-1} compared to –46.7 kcal mol^{-1}, or –50.1 and –42.6 kcal mol^{-1}, respectively, for Gibbs free energy barriers). The same shift in preferred reactivity is observed from Pd to Ag^+, for which the computed activation strain diagrams are shown in Figure 7.6b. This shift is also observed for many of the coordinated complexes based on these metal centers, such as the monocoordinated copper- and silver-based catalysts. However, the results for these monocoordinated complexes should be considered more carefully, since the results have been obtained from constrained optimizations.

The validity of our design approach is further supported by a tendency towards C–C activation that is observed throughout the entire set of catalysts. For example, when comparing the results of C–C activation to those of C–H activation, and going from anionic group 9 catalysts to cationic group 11 catalysts, we find that for catalysts from all three groups the interaction energy is delayed in the case of C–C activation, but that this effect is more pronounced for the more strongly d-donating catalysts.

For example, from $Ir(CO)_2^-$ to $Pt(CO)_2$ and $Au(CO)_2^+$, the difference between C–H and C–C activation barriers decreases from 25.3 kcal mol^{-1} to 23.0 kcal mol^{-1} to 17.8 kcal mol^{-1} (compare data in Table 7.1 and 7.2). Furthermore, when going from larger third row metal centers to the smaller first row metal centers, we find a tendency towards preferred C–C activation. This is true, for example, along the monocoordinated group 9-based catalysts: whereas for $IrPH_3^-$ the C–C activation barrier is 21.9 kcal mol^{-1} higher than the C–H activation barrier (+14.0 and –7.9 kcal mol^{-1}, respectively), this difference decreases to 17.7 kcal mol^{-1} for $RhPH_3^-$ and further to 8.8 kcal mol^{-1} for $CoPH_3^-$.

It should be noted that we limit ourselves here to gas-phase results. Previous studies have shown that including a dielectric model to account for solvation has only a moderate

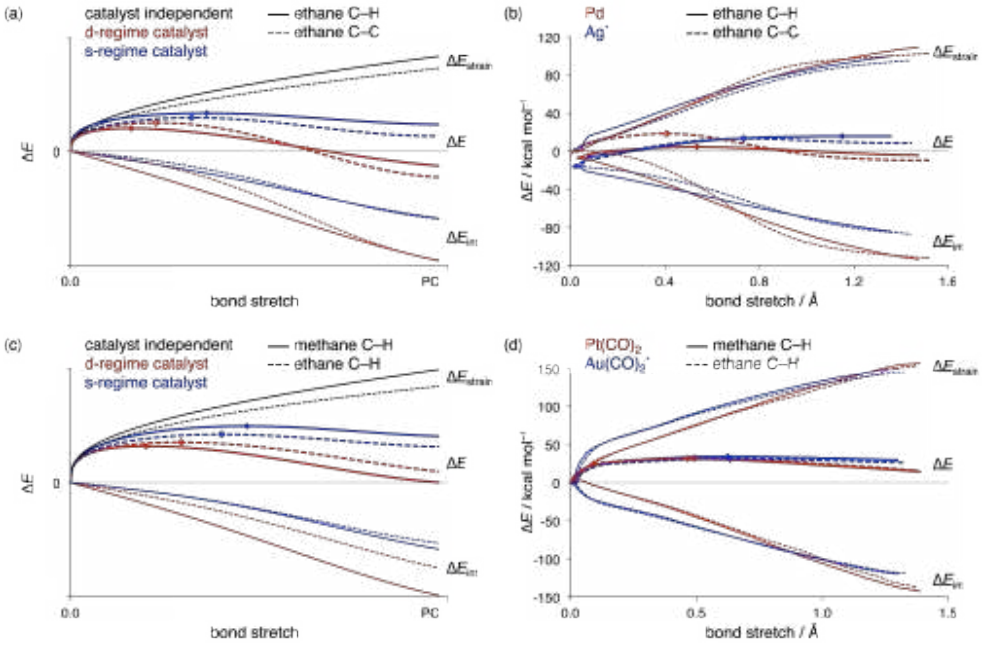

Figure 7.6 Activation strain diagrams (see Equation 2.10), comparing the addition of ethane C–H and C–C bonds to (a) an idealized set of catalysts, and (b) to an actual set of catalysts, as well as a comparison of the methane and ethane C–H bonds to (c) an idealized set of catalysts and (d) an actual set of catalysts. A dot designates the position of the TS.

effect on the stationary points and does not alter the trends.[241] We have performed a preliminary exploration in the aqueous phase (including optimizations) for the model catalysts that are suggested for selective C–H or C–C activation. This has been done by applying the COSMO (Conductor-like Screening Model) method[297,298] as implemented in ADF,[299] using a dielectric constant for water of 78.4, a solvent radius of 1.9 Å, and atomic radii taken from the MM3 van der Waals radii[300] scaled by 0.8333.[301] These results suggest that the ordering of the reaction barriers for these model catalysts is not changed, that is, the observed selectivity in the gas phase is upheld in the aqueous phase. Note that these examples include the charged Ag^+. We choose, however, not to provide the results, because the atomic radii have never been confirmed to give reliable results for ionic species, and, more importantly, coordination of a solvent molecule to the catalyst might occur during the reaction,[41,278,341] which cannot be accounted for using a continuum model.

7.6 Selective Methane C–H versus Ethane C–H Bond Activation

Although the C–H bonds in ethane are very similar to those in methane, there are two important differences. Albeit subtle, these differences appear to have interesting consequences when these bonds interact with the various types of catalysts included in this work. The first difference between these bonds is that the ethane C–H bonds are slightly weaker than the methane C–H bonds (purely electronic BDE of 104.7 kcal mol^{-1}, compared to 109.7 kcal mol^{-1}). Secondly, and importantly, when these bonds are stretched during the oxidative addition, the methane σ^*_{C-H} LUMO energy drops faster than the ethane σ^*_{C-H} LUMO energy. For the elongated C–H bonds, the ethane σ^*_{C-H} LUMO is higher in energy due to the contribution from the singly occupied MO on the ethyl fragment, which is destabilized by the antibonding interaction between its constituting methylene and methyl units. Such an antibonding interaction is absent in the singly occupied MO on the methyl fragment in CH_4, leading to its σ^*_{C-H} LUMO being lower in energy. Figure 7.7 contains the σ^*_{C-H} orbital energies for both substrates as a function of C–H bond stretch, starting from the substrates in their equilibrium geometries and stepwise elongating the C–H bond while all other geometry parameters are optimized. During an oxidative addition, the faster dropping methane σ^*_{C-H} LUMO induces a stronger enhancement of the donor-acceptor orbital interaction with the d hybrid orbital of the catalyst complex.

A comparison of the activation strain analyses (see Figure 7.3 and 7.5), reveals that the weaker C–H bond of ethane translates into a less destabilizing strain term $\Delta E_{strain}(\zeta)$, while the weaker backbonding to the ethane C–H bond translates into a less stabilizing

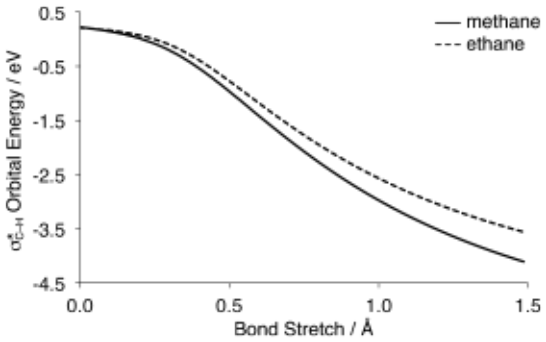

Figure 7.7 Energy of the σ^*_{C-H} orbital as a function of the stretch of the methane (solid line) and ethane (dashed line) C–H bond.

interaction energy term $\Delta E_{int}(\zeta)$. These counteracting effects tend to cancel out, at least partially. However, while the effect on the strain term is essentially equal for each catalyst complex, the effect on the interaction energy is, again, catalyst dependent. Thus, to rationally design selective catalysts, we can take an approach similar to that described above for the ethane C–H and C–C bonds.

To exemplify this, we consider again two cases: (i) a catalyst from the d regime, such as the anionic, or most of the neutral complexes, and (ii) a catalyst from the s regime, such as one of the cationic complexes. Schematic activation strain analyses for these two situations are shown in Figure 7.6c. For both cases, we find a less destabilizing strain term ΔE_{strain} for ethane activation (dashed black line), compared to methane activation (solid black line), due to the slightly lower bond dissociation energy of the former. Going from the methane to the ethane C–H bond, also the catalyst-substrate interaction ΔE_{int} weakens as a result of the weaker catalyst-to-substrate backbonding that goes with the higher orbital energy of the ethane σ^*_{C-H} LUMO (see Figure 7.7). However, this latter effect hinders the catalysts from the d regime more than the catalysts from the s regime, for which this d donation plays a less prominent role (compare the difference between the red ΔE_{int} lines with the difference between the blue ΔE_{int} lines in Figure 7.6c). Thus, the interaction energy ΔE_{int} goes up for both catalysts if one goes from methane to ethane C–H activation, but the difference is greater for the d-regime catalyst, for which it outweighs the less destabilizing ΔE_{strain} and results in an overall higher reaction barrier for ethane C–H activation. For the s-regime catalysts the weakening of the ΔE_{int} curves does not outweigh the lower ΔE_{strain} curve, and these catalysts therefore activate the ethane C–H bond with a lower barrier.

An example of a catalyst from the s regime is $Au(CO)_2^+$, for which the positive charge, the relativistic stabilization of the gold 6s atomic orbital and the π acceptor character of the ligands all contribute to an excellent s-accepting capability. When this catalyst is compared to its group 10 analogue $Pt(CO)_2$, we do indeed find that $Au(CO)_2^+$ prefers ethane C–H activation (+31.3 kcal mol^{-1}, $\Delta G^{\ddagger}$ = +36.5 kcal mol^{-1}) over methane activation (+34.3 kcal mol^{-1}, $\Delta G^{\ddagger}$ = +38.3 kcal mol^{-1}), while for $Pt(CO)_2$ this is the other way around: the barrier of +32.0 kcal mol^{-1} ($\Delta G^{\ddagger}$ = +39.8 kcal mol^{-1}) for ethane C–H activation is higher than the +31.1 kcal mol^{-1} ($\Delta G^{\ddagger}$ = +37.3 kcal mol^{-1}) barrier for methane activation (see Table 7.1). The selectivity is not only observed in the reaction barriers, but also when the stability of the product complexes is considered. Figure 7.6d shows a comparison of the activation strain analyses of the addition of the methane and ethane C–H bond to $Pt(CO)_2$ (red lines) and $Au(CO)_2^+$ (blue lines), which also displays the subtlety of the effect on the

scale of these terms. The most eye-catching features are the stronger strain energy for $Au(CO)_2^+$, due to the greater bite-angle rigidity of the catalyst (see chapter 3), and the stronger interaction in the beginning of the addition to $Au(CO)_2^+$, due to the stronger substrate-to-catalyst donation for this complex. Again, preliminary results indicate that the selectivity observed for these catalyst complexes is also upheld in aqueous solutions.

The above analyses not only confirm earlier observations on the importance of the catalyst-substrate interaction for (regio-)selectivity in C–H bond activation,[342-350] but also provide an explanation and the practical requirements to switch the preferred reaction pathway to the stronger bond: the strength of the interaction has to be sufficiently improved (as in the case of the strongly d-donating catalysts), such that it outweighs the difference in strain energy that originates primarily from the dissociation energy of the bond. By separating and individually analyzing the two different physical factors (*i.e.*, C–H bond strength and catalyst-substrate interaction), we have turned them into tuning parameters for rationally modifying a catalyst's preference from one bond to another. As demonstrated here, this can be done even when the two bonds are very similar in nature.

7.7 Ethane C–C Activation via Ethane C–H Activation

In section 7.2, we already alluded to an alternative, somewhat exotic pathway to C–C activation that proceeds via C–H activation. This reaction pathway is encountered for a number of model catalysts that activate the ethane C–H bond with low barrier, or without barrier, namely, Co^-, Rh^-, Ir^-, Pt and the monocoordinated cobalt- and iridium-based complexes. For the most strongly d-donating catalysts, that is, for Co^-, Rh^-, Ir^-, $CoNH_3^-$ and $IrNH_3^-$, the pathway to the C–C activation product even includes cleavage of two C–H bonds. For $CoPH_3^-$, $CoCO^-$, $IrPH_3^-$ and $IrCO^-$, where the d-donating capability is decreased due to π backbonding to the ligand, only one C–H insertion occurs. In Figure 7.8, we show for Rh^- and C_2H_6 all stationary points and transition states leading to the C–C addition product at –80.0 kcal mol^{-1}, starting from an initial dihapto reactant complex at –44.4 kcal mol^{-1}, and including two reaction steps that involve C–H rupture.

The first reaction step is the oxidative addition of a C–H bond to d^{10}-Rh^-, which takes place from the reactant complex at –44.4 kcal mol^{-1}, via a transition state at –44.3 kcal mol^{-1} to a stable product at –74.4 kcal mol^{-1} (see also Table 7.1). Secondly, the RhH moiety rotates around the Rh–C bond (TS at –72.3 kcal mol^{-1}), followed by a rotation of the methyl group to an eclipsed position (TS at –72.9 kcal mol^{-1}). This establishes an agos-

tic interaction between one of its hydrogens and the rhodium center and furnishes a stable intermediate at –73.8 kcal mol^{-1}. From this intermediate, the second C–H addition occurs, via a TS at –66.8 kcal mol^{-1}, resulting in a product at –84.5 kcal mol^{-1}. This intermediate consists of an ethylene coordinated to a $Rh(H)_2^-$ moiety. Rotation of $Rh(H)_2^-$ leads to a stable intermediate at –68.7 kcal mol^{-1}; this is the minimum listed as the RC in Table 7.2, from which the C–C activation is initiated. The final reaction step occurs via a TS at –30.6 kcal mol^{-1}, in which both the hydrogens are transferred back to the carbon atoms, while simultaneously the C–C bond is cleaved, leading to formation of the common $Rh(CH_3)_2^-$ product complex. Note that this final step constitutes the overall reaction barrier of the complete reaction path.

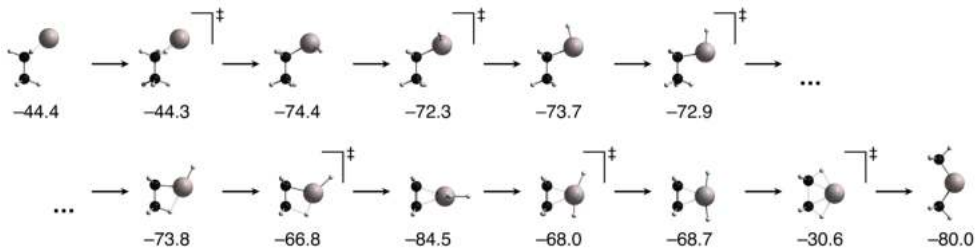

Figure 7.8 Geometries and energies (kcal mol^{-1}, relative to reactants) of the stationary points and transition states along the full reaction path for oxidative addition of the ethane C–C bond to Rh^-.

We expect that the C–C activation product is obtained through a similar reaction path for Co^- and Ir^-, as well as for $CoNH_3^-$ and $IrNH_3^-$, although for the latter two the addition of the second C–H bond leads directly to the RC for C–C addition. For the catalysts that activate the C–C bond via activation of just one C–H bond, we expect the pathway to contain identical reaction steps, up to and including the formation of the first C–H addition product containing an agostic interaction between the metal center and a hydrogen of the adjacent methyl group (such as depicted for Rh^- in Figure 7.8, at –73.8 kcal mol^{-1}). From there, a single transition state leads to the C–C addition product. In this transition state (which corresponds to those listed in Table 7.2), breaking the C–C bond occurs again simultaneously with restoring the C–H bond. We have not further explored each of these alternative reaction pathways, because these more exotic pathways are beyond the scope and purpose of the current work.

7.8 Conclusions

We have developed an approach that allows for rationally tuning a catalyst's preference for activating one particular bond. Here, we have focused on ethane C–H versus C–C activation, as well as on the more subtle balance between the relatively similar C–H bonds of ethane and methane. The tuning parameters are the electronic regime of the catalyst (d regime or s regime) and the effective size of the metal center. This follows from our quantum chemical exploration of almost 200 model reactions using the activation strain model in conjunction with relativistic Kohn-Sham molecular orbital theory.

The physical mechanism behind the tuning is, among others, the difference in stability of the activated bonds and the precise electronic nature of both these bonds and the catalyst complex. The polar C–H bond is more stable and thus yields a higher strain energy curve than the C–C bond. This factor alone would make the barrier for C–H activation higher than that for C–C activation.

The eventual height of the barrier arises as the sum of the above-mentioned activation strain and the interaction between the strained substrate and catalyst. This interaction can therefore modulate the barrier. Unlike the C–H bond, the C–C bond is sterically shielded from all sides by six C–H bonds. This steric shielding requires the C–C bond to stretch first, before the metal d orbitals can overlap with, and donate charge into, the σ^*_{C-C} acceptor orbital. The resulting delay in stabilizing interaction is a factor that works in the direction of giving C–C activation a higher barrier. We have shown that this effect is large for the strongly interacting d-regime catalysts (*i.e.*, with high-energy d orbitals). Thus, d-regime catalysts such as $Pd(PH_3)_2$ favor C–H activation. This can be turned around by going to s-regime catalysts. Now, metal d to substrate σ^*_{C-C} donation is no longer crucial and the delay effect becomes small. Consequently, the difference in strain curves takes over the trend, and the model catalyst activates the weaker C–C bond. Thus, s-regime catalysts, such as those based on Ag^+, favor C–C activation.

The concepts and design principles emerging form this work serve as a proof of principle. They were also successfully applied to the more challenging problem of differentiating between activation of the C–H bonds in ethane versus those in methane. We envisage that these insights contribute to a more rational and efficient approach to catalyst design.

8 Halogen Bonding versus Hydrogen Bonding: A Molecular Orbital Perspective

Previously appeared as

Halogen Bonding versus Hydrogen Bonding: A Molecular Orbital Perspective
L. P. Wolters, F. M. Bickelhaupt
ChemistryOpen **2012**, *1*, 96–105

8.1 Introduction

We have investigated a range of strongly halogen-bonded trihalides $DX\cdots A^-$ and the analogous strongly hydrogen-bonded complexes $DH\cdots A^-$ (D, X, A = F, Cl, Br, I), using relativistic density functional theory (DFT). The purpose of our work is twofold: firstly, we wish to provide a set of consistent structural and energy data from which reliable trends can be inferred for a wide range of model systems. The main objective is to achieve a detailed understanding of the nature of halogen bonds: how they resemble, but also how they differ from the better understood hydrogen bonds in terms of their electronic structure and bonding mechanism. To this end, we first explore how the geometries and energies of our model complexes $DX\cdots A^-$ and, for comparison, $DH\cdots A^-$ vary as either the halogen or hydrogen bond-donating atom D, or the halogen or hydrogen bond-accepting atom A is varied from F to Cl, Br and I. In this way, we arrive at a set of consistent data for a large range of halogen-bonded and hydrogen-bonded complexes.

Next, to understand the origin of the computed trends, we carry out activation strain analyses of the bond formation reaction along the reaction coordinate. The interaction energy and the underlying bonding mechanism are analyzed in the context of quantitative Kohn-Sham molecular orbital theory, in combination with the energy decomposition analysis (EDA) scheme discussed in section 2.6. Our explorations and analyses augment earlier pioneering studies[122,125,129,351,352] through the large variety in our halogen- and hydrogen-

bonded model complexes and the systematic and in-depth analyses along the entire reaction profile for each of the complexation reactions.

8.2 Hydrogen Bonds: Strength and Structure

The results of our ZORA-BP86/TZ2P calculations can be found in Table 8.1 for the hydrogen-bonded DH···A$^-$ model systems, and in Table 8.2 to 8.5 for the fluorine-, chlorine-, bromine- and iodine-bonded DX···A$^-$ model systems, respectively. In the first place, we note that all hydrogen bond formations, as well as halogen bond formations, are associated with single-well potential energy surfaces, that is, there exist no separate energy minima for DX···A$^-$ and D···XA$^-$. In the case that D = A, this leads to the formation of $D_{\infty h}$-symmetric complexes with equal bond distances $r_{D-X} = r_{X\cdots A^-}$.

For the hydrogen-bonded DH···A$^-$ complexes, we find that, as we vary the hydrogen bond-accepting halide A$^-$ down group 17 from F$^-$ to I$^-$, the hydrogen bond strength ΔE is weakened, the H···A$^-$ bond $r_{H\cdots A^-}$ becomes longer, and the D–H bond becomes less elon-

Table 8.1 Bond lengths (in Å), bond energies relative to reactants (in kcal mol^{-1}), and bond analyses of the hydrogen-bonded complexes DH···A$^-$.[a]

	r_{D-H}	Δr_{D-H}	$r_{H\cdots A^-}$	$\Delta r_{H\cdots A^-}$	ΔE	ΔE_{strain}	ΔE_{int}	ΔV_{elstat}	ΔE_{Pauli}	ΔE_{oi}	ΔE_{oi}^{σ}	ΔE_{oi}^{π}	$\langle\sigma^*\vert np\rangle$	σ^* pop.	np pop.	Q_A^{VDD}
FH···F$^-$	1.159	0.226	1.159	0.226	−53.0	19.7	−72.8	−76.4	68.8	−65.1	−58.1	−7.0	0.268	0.27	1.76	−0.51
FH···Cl$^-$	1.012	0.079	1.843	0.550	−26.6	3.3	−29.8	−31.9	24.3	−22.2	−20.0	−2.2	0.359	0.14	1.84	−0.66
FH···Br$^-$	0.994	0.061	2.058	0.625	−21.9	2.0	−23.9	−25.4	18.5	−17.0	−15.4	−1.6	0.390	0.11	1.88	−0.68
FH···I$^-$	0.982	0.049	2.319	0.694	−18.1	1.3	−19.4	−20.2	14.5	−13.7	−12.6	−1.2	0.421	0.13	1.89	−0.69
ClH···F$^-$	1.843	0.550	1.012	0.079	−68.6	43.3	−111.9	−98.2	124.9	−138.7	−128.2	−10.4	0.282	0.54	1.67	−0.36
ClH···Cl$^-$	1.587	0.294	1.587	0.294	−29.3	17.9	−47.2	−45.2	65.4	−67.3	−62.7	−4.7	0.341	0.41	1.63	−0.48
ClH···Br$^-$	1.478	0.185	1.874	0.441	−22.4	8.4	−30.9	−31.5	41.7	−41.1	−38.2	−2.9	0.346	0.30	1.72	−0.56
ClH···I$^-$	1.423	0.130	2.191	0.566	−17.5	4.6	−22.1	−22.6	28.1	−27.6	−25.6	−1.9	0.357	0.27	1.77	−0.62
BrH···F$^-$	2.058	0.625	0.994	0.061	−75.6	43.2	−118.8	−101.8	138.8	−155.9	−144.9	−10.9	0.276	0.60	1.66	−0.33
BrH···Cl$^-$	1.874	0.441	1.478	0.185	−34.1	27.4	−61.5	−54.4	91.9	−99.0	−92.7	−6.3	0.337	0.55	1.53	−0.38
BrH···Br$^-$	1.743	0.310	1.743	0.310	−25.7	15.6	−41.3	−39.2	64.0	−66.2	−62.2	−4.0	0.336	0.44	1.60	−0.46
BrH···I$^-$	1.642	0.209	2.057	0.432	−19.8	8.6	−28.4	−27.1	42.4	−43.7	−41.1	−2.6	0.338	0.39	1.66	−0.53
IH···F$^-$	2.319	0.694	0.982	0.049	−80.6	40.9	−121.4	−104.6	156.9	−173.7	−163.0	−10.7	0.264	0.66	1.65	−0.31
IH···Cl$^-$	2.191	0.566	1.423	0.130	−38.0	31.7	−69.6	−62.1	116.1	−123.6	−116.6	−7.1	0.324	0.66	1.46	−0.32
IH···Br$^-$	2.057	0.432	1.642	0.209	−28.6	21.8	−50.3	−47.8	89.6	−92.1	−87.3	−4.8	0.320	0.57	1.49	−0.38
IH···I$^-$	1.941	0.316	1.941	0.316	−21.8	13.6	−35.4	−33.8	63.0	−64.6	−61.3	−3.2	0.315	0.52	1.55	−0.45

[a] Δr_{D-H} is the stretch of the DH fragment relative to the optimized DH molecule; $\Delta r_{H\cdots A^-}$ is the change in H···A distance compared to the bond length of the optimized HA molecule; for the energy components, see Equations 2.9, 2.11 and 2.13; $\langle\sigma^*\vert np\rangle$ is the overlap of the antibonding σ^* acceptor orbital on DH with the σ lone pair np orbital on A$^-$; pop. is population (in electrons) of the indicated orbital; Q_A^{VDD} is the VDD charge on A$^-$ (in a.u.; see Equation 2.8).

gated from its equilibrium value in an isolated DH molecule ($\Delta r_{D-H} = r_{D-HA^-} - r_{D-H}$). The opposite trend emerges as we vary the hydrogen bond-donating atom D in DH down group 17. Thus, along the hydrogen halides FH to IH, the hydrogen bond strength ΔE is reinforced, the H···A$^-$ bond $r_{H\cdots A^-}$ becomes shorter, and the D–H bond stretch Δr_{D-H} increases.

For example, from FH···F$^-$ to FH···I$^-$, ΔE is weakened from –53 to –18 kcal mol^{-1} while $r_{H\cdots A^-}$ increases from 1.159 to 2.319 Å and the stretch Δr_{D-H} is reduced from 0.226 to 0.049 Å (see Table 8.1). This trend correlates with a systematic weakening of the halide's proton affinity (PA) from 373 kcal mol^{-1} for F$^-$ to 316 kcal mol^{-1} for I$^-$.[353-355] The effect is even more pronounced in the series from IH···F$^-$ to IH···I$^-$ along which ΔE weakens from –81 to –22 kcal mol^{-1}, $r_{H\cdots A^-}$ increases from 0.982 to 1.941 Å, and Δr_{D-H} is reduced from 0.694 to 0.316 Å. Note that, on the other hand, from FH···F$^-$ to IH···F$^-$, ΔE is strengthened from –53 to –81 kcal mol^{-1} while $r_{H\cdots A^-}$ decreases from 1.159 to 0.982 Å and the stretch Δr_{D-H} is increased from 0.226 to 0.694 Å. The higher extent of deformation in the more strongly hydrogen-bonded complexes is also reflected by a more destabilizing strain

Table 8.2 Bond lengths (in Å), bond energies relative to reactants (in kcal mol^{-1}), and bond analyses of the fluorine-bonded complexes DF···A$^-$.[a]

	r_{D-F}	Δr_{D-F}	$r_{F\cdots A^-}$	$\Delta r_{F\cdots A^-}$	ΔE	ΔE_{strain}	ΔE_{int}	ΔV_{elstat}	ΔE_{Pauli}	ΔE_{oi}	ΔE_{oi}^{σ}	ΔE_{oi}^{π}	$\langle\sigma^*\vert np\rangle$	σ^* pop.	np pop.	Q_A^{VDD}
FF···F$^-$	1.755	0.335	1.755	0.335	–51.5	23.5	–75.0	–41.0	73.2	–107.1	–106.2	–1.0	0.125	0.59	1.43	–0.42
FF···Cl$^-$	1.864	0.444	1.965	0.301	–43.3	34.2	–77.5	–52.4	107.8	–132.9	–128.7	–4.2	0.146	0.76	1.26	–0.33
FF···Br$^-$	1.902	0.482	2.049	0.253	–44.0	37.7	–81.7	–53.8	111.7	–139.6	–134.8	–4.8	0.145	0.82	1.20	–0.30
FF···I$^-$	1.993	0.573	2.126	0.181	–48.4	46.0	–94.3	–61.7	132.2	–164.8	–158.0	–6.7	0.145	0.95	1.05	–0.27
ClF···F$^-$	1.965	0.301	1.864	1.965	–30.3	16.4	–46.7	–17.3	51.7	–81.2	–81.2	0.0	0.107	0.54	1.49	–0.48
ClF···Cl$^-$	2.077	0.413	2.077	2.077	–21.2	26.1	–47.3	–30.2	78.3	–95.4	–93.6	–1.7	0.133	0.68	1.35	–0.38
ClF···Br$^-$	2.143	0.479	2.126	2.143	–21.8	31.8	–53.6	–37.6	91.8	–107.8	–105.2	–2.6	0.139	0.77	1.26	–0.33
ClF···I$^-$	2.294	0.630	2.158	2.294	–26.0	44.4	–70.4	–53.4	124.6	–141.6	–136.5	–5.1	0.144	0.95	1.08	–0.27
BrF···F$^-$	2.049	0.253	1.902	2.049	–29.2	11.4	–40.6	–11.0	45.9	–75.5	–75.5	–0.1	0.099	0.52	1.51	–0.49
BrF···Cl$^-$	2.126	0.330	2.143	2.126	–20.0	17.2	–37.2	–21.4	64.3	–80.0	–78.9	–1.1	0.124	0.63	1.40	–0.41
BrF···Br$^-$	2.186	0.390	2.186	2.186	–20.5	21.9	–42.3	–29.1	77.6	–90.9	–89.1	–1.8	0.131	0.71	1.32	–0.37
BrF···I$^-$	2.335	0.539	2.200	2.335	–24.2	33.7	–57.9	–45.9	111.9	–123.8	–119.8	–4.1	0.140	0.89	1.14	–0.29
IF···F$^-$	2.126	0.181	1.993	0.573	–23.9	5.9	–29.8	–1.8	33.7	–61.8	–61.4	–0.4	0.087	0.48	1.55	–0.53
IF···Cl$^-$	2.158	0.213	2.294	0.630	–14.5	7.8	–22.3	–8.3	40.3	–54.4	–53.7	–0.7	0.108	0.53	1.50	–0.49
IF···Br$^-$	2.200	0.255	2.335	0.539	–14.5	10.5	–25.0	–14.6	50.3	–60.7	–59.8	–0.9	0.118	0.59	1.45	–0.44
IF···I$^-$	2.324	0.379	2.324	0.379	–16.9	19.3	–36.2	–29.6	79.8	–86.5	–84.4	–2.1	0.133	0.75	1.29	–0.36

[a] Δr_{D-F} is the stretch of the DF fragment relative to the optimized DF molecule; $\Delta r_{F\cdots A^-}$ is the change in F···A distance compared to the bond length of the optimized FA molecule; for the energy components, see Equations 2.9, 2.11 and 2.13; $\langle\sigma^*\vert np\rangle$ is the overlap of the antibonding σ^* acceptor orbital on DF with the σ lone pair np orbital on A$^-$; pop. is population (in electrons) of the indicated orbital; Q_A^{VDD} is the VDD charge on A$^-$ (in a.u.; see Equation 2.8).

energy ΔE_{strain} (see Table 8.1). This trend correlates with a systematic weakening of the halogen-hydrogen bond from a homolytic bond dissociation energy (BDE) of 144 kcal mol^{-1} in FH to 82 kcal mol^{-1} in IH (see Table 8.6). Furthermore, note that the H···A$^-$ bond distance $r_{H\cdots A^-}$ in DH···A$^-$ is in all cases longer than it is in the diatomic HA molecule, r_{H-A}, as revealed by the corresponding difference in bond distances $\Delta r_{H\cdots A^-} = r_{H\cdots A^-} - r_{H-A}$. This difference $\Delta r_{H\cdots A^-}$ increases from 0.226 Å in FH···F$^-$ to 0.694 Å in FH···I$^-$ and from 0.049 Å in IH···F$^-$ to 0.316 Å in IH···I$^-$.

We conclude that the DH···A$^-$ hydrogen bond becomes stronger and relatively shorter while the D–H bond becomes more elongated in the complex, as the A$^-$ anion is a stronger base and/or the D–H bond is weaker.

8.3 Halogen Bonds: Strength and Structure

The halogen bonds display, in part, trends similar to the hydrogen bonds, but there are also striking differences. In general, and in agreement with *ab initio* results, the fluorine bonds

Table 8.3 Bond lengths (in Å), bond energies relative to reactants (in kcal mol^{-1}), and bond analyses of the chlorine-bonded complexes DCl···A$^-$.[a]

	r_{D-Cl}	Δr_{D-Cl}	$r_{Cl\cdots A^-}$	$\Delta r_{Cl\cdots A^-}$	ΔE	ΔE_{strain}	ΔE_{int}	ΔV_{elstat}	ΔE_{Pauli}	ΔE_{oi}	ΔE_{oi}^{σ}	ΔE_{oi}^{π}	$\langle\sigma^*\vert np\rangle$	σ^* pop.	np pop.	Q_A^{VDD}
FCl···F$^-$	1.909	0.245	1.909	0.245	−64.5	11.9	−76.4	−85.5	107.2	−98.1	−91.1	−7.0	0.187	0.45	1.57	−0.45
FCl···Cl$^-$	1.925	0.261	2.334	0.311	−43.9	13.2	−57.1	−61.6	86.4	−81.9	−76.5	−5.4	0.209	0.53	1.50	−0.46
FCl···Br$^-$	1.933	0.269	2.473	0.300	−40.5	13.8	−54.3	−57.3	82.1	−79.1	−74.3	−4.8	0.207	0.54	1.49	−0.45
FCl···I$^-$	1.955	0.291	2.637	0.285	−38.7	15.6	−54.3	−54.5	81.8	−81.6	−76.8	−4.8	0.206	0.61	1.41	−0.42
ClCl···F$^-$	2.334	0.311	1.925	0.261	−57.2	12.8	−70.0	−74.8	109.3	−104.4	−98.8	−5.6	0.167	0.51	1.55	−0.43
ClCl···Cl$^-$	2.354	0.331	2.354	0.331	−37.5	14.1	−51.6	−54.1	86.2	−83.7	−79.3	−4.3	0.190	0.58	1.46	−0.43
ClCl···Br$^-$	2.366	0.343	2.495	0.322	−34.5	14.8	−49.3	−50.8	81.2	−79.7	−75.9	−3.8	0.191	0.60	1.44	−0.42
ClCl···I$^-$	2.399	0.376	2.654	0.302	−33.4	17.1	−50.5	−49.7	81.7	−82.5	−78.6	−3.9	0.192	0.67	1.35	−0.39
BrCl···F$^-$	2.473	0.300	1.933	0.269	−55.8	10.9	−66.6	−70.1	108.8	−105.3	−100.1	−5.3	0.160	0.52	1.54	−0.43
BrCl···Cl$^-$	2.495	0.322	2.366	0.343	−36.5	12.1	−48.6	−50.5	84.9	−83.1	−79.1	−4.0	0.182	0.59	1.46	−0.42
BrCl···Br$^-$	2.507	0.334	2.507	0.334	−33.7	12.8	−46.4	−47.6	79.9	−78.8	−75.3	−3.5	0.183	0.61	1.43	−0.42
BrCl···I$^-$	2.541	0.368	2.665	0.313	−32.8	14.8	−47.6	−46.9	80.6	−81.3	−77.7	−3.7	0.185	0.68	1.35	−0.38
ICl···F$^-$	2.637	0.285	1.955	0.291	−50.7	8.7	−59.4	−61.3	104.9	−103.0	−98.5	−4.5	0.148	0.53	1.55	−0.43
ICl···Cl$^-$	2.654	0.302	2.399	0.376	−32.2	9.5	−41.7	−43.1	79.1	−77.8	−74.5	−3.2	0.170	0.58	1.47	−0.44
ICl···Br$^-$	2.665	0.313	2.541	0.368	−29.5	10.1	−39.6	−40.9	74.4	−73.1	−70.3	−2.7	0.172	0.60	1.45	−0.43
ICl···I$^-$	2.700	0.348	2.700	0.348	−28.8	11.9	−40.7	−40.9	75.1	−75.0	−72.1	−2.9	0.175	0.67	1.37	−0.39

[a] Δr_{D-Cl} is the stretch of the DCl fragment relative to the optimized DCl molecule; $\Delta r_{Cl\cdots A^-}$ is the change in Cl···A distance compared to the bond length of the optimized ClA molecule; for the energy components, see Equations 2.9, 2.11 and 2.13; $\langle\sigma^*\vert np\rangle$ is the overlap of the antibonding σ^* acceptor orbital on DCl with the σ lone pair np orbital on A$^-$; pop. is population (in electrons) of the indicated orbital; Q_A^{VDD} is the VDD charge on A$^-$ (in a.u.; see Equation 2.8).

are the weakest and the iodine bonds are the strongest halogen bonds.[89-92] The heavier DX···A$^-$ halogen bonds (*i.e.*, X = Cl, Br and I) become weaker and longer as the accepting halide varies from A$^-$ = F$^-$ to I$^-$, just as the corresponding hydrogen bonds do. In the case of the iodine-bonded complexes DI···A$^-$, for example, ΔE weakens from a value around –70 kcal mol^{-1} for A$^-$ = F$^-$ as accepting halide, to a value around –40 kcal mol^{-1} for X$^-$ = I$^-$ (see Table 8.5). However, the fluorine bonds display a more complex dependency of ΔE upon varying the accepting halide A$^-$. From A$^-$ = F$^-$ to Cl$^-$, the fluorine bond strength ΔE still weakens, similar to the situation for the hydrogen bonds and the heavier halogen bonds. But thereafter, along A$^-$ = Cl$^-$, Br$^-$ and I$^-$, the fluorine bond strength ΔE does no longer continue to weaken and instead becomes stronger. This is most clearly seen in the series constituted by the complexes FF···A$^-$ between a fluorine molecule and a halide ion: here, the fluorine bond strength varies from –52 to –43 to –44 to –48 kcal mol^{-1}, along A$^-$ = F$^-$, Cl$^-$, Br$^-$ and I$^-$, respectively (see Table 8.2).

Interestingly, variation of the donating atom D has opposite effects on halogen bonds DX···A$^-$ and hydrogen bonds DH···A$^-$. All halogen bonds studied here become weaker and

Table 8.4 Bond lengths (in Å), bond energies relative to reactants (in kcal mol^{-1}), and bond analyses of the bromine-bonded complexes DBr···A$^-$.[a]

	r_{D-Br}	Δr_{D-Br}	$r_{Br\cdots A^-}$	$\Delta r_{Br\cdots A^-}$	ΔE	ΔE_{strain}	ΔE_{int}	ΔV_{elstat}	ΔE_{Pauli}	ΔE_{oi}	ΔE_{oi}^{σ}	ΔE_{oi}^{π}	$\langle\sigma^*\vert np\rangle$	σ^* pop.	np pop.	Q_A^{VDD}
FBr···F$^-$	2.009	0.213	2.009	0.213	–70.9	8.6	–79.5	–92.3	98.8	–86.0	–77.7	–8.2	0.201	0.43	1.60	–0.45
FBr···Cl$^-$	2.018	0.222	2.454	0.281	–48.7	9.2	–57.8	–65.9	79.1	–71.0	–65.6	–5.5	0.234	0.51	1.50	–0.47
FBr···Br$^-$	2.023	0.227	2.601	0.280	–44.7	9.5	–54.2	–61.5	75.6	–68.3	–63.6	–4.7	0.235	0.52	1.49	–0.46
FBr···I$^-$	2.036	0.240	2.775	0.269	–42.4	10.4	–52.9	–57.9	74.8	–69.8	–65.3	–4.4	0.235	0.58	1.43	–0.44
ClBr···F$^-$	2.454	0.281	2.018	0.222	–65.7	9.7	–75.5	–84.6	103.1	–94.0	–86.9	–7.1	0.181	0.48	1.58	–0.43
ClBr···Cl$^-$	2.465	0.292	2.465	0.292	–44.0	10.4	–54.3	–60.5	81.1	–75.0	–70.2	–4.8	0.212	0.55	1.48	–0.44
ClBr···Br$^-$	2.473	0.300	2.612	0.291	–40.2	10.8	–51.0	–56.8	77.1	–71.3	–67.2	–4.1	0.214	0.57	1.45	–0.44
ClBr···I$^-$	2.495	0.322	2.786	0.280	–38.5	12.1	–50.6	–54.3	76.3	–72.5	–68.6	–3.9	0.216	0.64	1.38	–0.41
BrBr···F$^-$	2.601	0.280	2.023	0.227	–64.3	8.6	–72.9	–80.8	103.9	–96.0	–89.3	–6.7	0.173	0.49	1.57	–0.43
BrBr···Cl$^-$	2.612	0.291	2.473	0.300	–42.8	9.2	–52.1	–57.6	81.1	–75.5	–70.9	–4.5	0.204	0.56	1.47	–0.44
BrBr···Br$^-$	2.621	0.300	2.621	0.300	–39.2	9.7	–48.9	–54.1	76.6	–71.4	–67.6	–3.9	0.206	0.58	1.45	–0.43
BrBr···I$^-$	2.644	0.323	2.794	0.288	–37.7	10.9	–48.6	–52.0	76.0	–72.5	–68.7	–3.8	0.208	0.65	1.36	–0.40
IBr···F$^-$	2.775	0.269	2.036	0.240	–59.8	7.1	–67.0	–74.0	103.2	–96.2	–90.1	–6.1	0.162	0.50	1.57	–0.43
IBr···Cl$^-$	2.786	0.280	2.495	0.322	–38.8	7.6	–46.4	–51.8	78.3	–73.0	–69.0	–3.9	0.192	0.56	1.48	–0.44
IBr···Br$^-$	2.794	0.288	2.644	0.323	–35.5	7.9	–43.4	–48.9	73.9	–68.5	–65.1	–3.3	0.194	0.57	1.46	–0.43
IBr···I$^-$	2.818	0.312	2.818	0.312	–34.0	9.0	–43.1	–47.2	73.1	–68.9	–65.7	–3.2	0.197	0.64	1.39	–0.40

[a] Δr_{D-Br} is the stretch of the DBr fragment relative to the optimized DBr molecule; $\Delta r_{Br\cdots A^-}$ is the change in Br···A distance compared to the bond length of the optimized BrA molecule; for the energy components, see Equations 2.9, 2.11 and 2.13; $\langle\sigma^*\vert np\rangle$ is the overlap of the antibonding σ^* acceptor orbital on DBr with the σ lone pair np orbital on A$^-$; pop. is population (in electrons) of the indicated orbital; Q_A^{VDD} is the VDD charge on A$^-$ (in a.u.; see Equation 2.8).

longer as D runs from F to I (see Table 8.2 to 8.5), whereas the hydrogen bonds were found to become stronger and shorter along this series (see Table 8.1). For example, along the series from FF···F$^-$ to IF···F$^-$, the fluorine bond strength ΔE weakens from –52 to only –24 kcal mol^{-1}, the fluorine bond distance $r_{F\cdots A^-}$ increases from 1.755 to 1.993 Å, and the stretch Δr_{D-F} decreases from 0.335 to 0.181 Å.

8.4 Bond Analyses: Variation of the Accepting Halide

Insight into the bonding mechanism is obtained through activation strain analyses of the various hydrogen bond and halogen bond formation reactions. These complexation reactions are computationally modeled by decreasing the distance between the A$^-$ and the DH or DX fragment, and simultaneously increasing the D–H or D–X bond length. The DH···A$^-$ or DX···A$^-$ distance is decreased from an initial value of 1.8 times the equilibrium bond length in the corresponding HA or XA molecule, to the actual value of the bond in the hydrogen- or halogen-bonded complex ($r_{X\cdots A^-}$). The value 1.8 is based on the ratio of

Table 8.5 Bond lengths (in Å), bond energies relative to reactants (in kcal mol^{-1}), and bond analyses of the iodine-bonded complexes DI···A$^-$.[a]

	r_{D-I}	Δr_{D-I}	$r_{I\cdots A^-}$	$\Delta r_{I\cdots A^-}$	ΔE	ΔE_{strain}	ΔE_{int}	ΔV_{elstat}	ΔE_{Pauli}	ΔE_{oi}	ΔE_{oi}^{σ}	ΔE_{oi}^{π}	$\langle\sigma^*\vert np\rangle$	σ^* pop.	np pop.	Q_A^{VDD}
FI···F$^-$	2.129	0.184	2.129	0.184	–75.0	6.1	–81.1	–103.5	100.0	–77.7	–66.8	–10.9	0.205	0.36	1.66	–0.44
FI···Cl$^-$	2.124	0.179	2.620	0.268	–49.8	5.8	–55.6	–69.1	73.8	–60.3	–54.0	–6.3	0.252	0.44	1.57	–0.49
FI···Br$^-$	2.126	0.181	2.781	0.275	–45.1	5.9	–51.0	–63.7	69.8	–57.0	–51.8	–5.2	0.255	0.45	1.56	–0.49
FI···I$^-$	2.132	0.187	2.977	0.277	–41.9	6.3	–48.2	–58.5	67.1	–56.8	–52.2	–4.6	0.258	0.51	1.51	–0.48
ClI···F$^-$	2.620	0.268	2.124	0.179	–73.3	7.8	–81.1	–101.2	107.6	–87.5	–77.5	–10.0	0.190	0.42	1.64	–0.41
ClI···Cl$^-$	2.615	0.263	2.615	0.263	–48.0	7.6	–55.6	–67.5	78.6	–66.7	–60.9	–5.9	0.232	0.49	1.54	–0.46
ClI···Br$^-$	2.620	0.268	2.776	0.270	–43.5	7.8	–51.3	–62.4	74.0	–62.8	–57.9	–5.0	0.235	0.50	1.52	–0.46
ClI···I$^-$	2.632	0.280	2.971	0.271	–40.6	8.4	–49.0	–57.6	71.0	–62.4	–58.0	–4.4	0.237	0.56	1.46	–0.44
BrI···F$^-$	2.781	0.275	2.126	0.181	–72.2	7.4	–79.6	–98.7	109.6	–90.5	–80.9	–9.6	0.183	0.44	1.64	–0.41
BrI···Cl$^-$	2.776	0.270	2.620	0.268	–47.1	7.2	–54.3	–65.4	79.3	–68.2	–62.5	–5.7	0.223	0.50	1.53	–0.45
BrI···Br$^-$	2.782	0.276	2.782	0.276	–42.7	7.4	–50.1	–60.5	74.4	–64.0	–59.2	–4.8	0.226	0.52	1.51	–0.45
BrI···I$^-$	2.795	0.289	2.976	0.276	–40.0	8.0	–48.0	–56.0	71.3	–63.3	–59.0	–4.3	0.229	0.58	1.54	–0.43
II···F$^-$	2.977	0.277	2.132	0.187	–69.0	6.4	–75.4	–94.0	111.6	–92.9	–83.8	–9.1	0.173	0.45	1.63	–0.40
II···Cl$^-$	2.971	0.271	2.632	0.280	–44.2	6.1	–50.3	–61.3	79.1	–68.1	–62.9	–5.2	0.211	0.51	1.53	–0.45
II···Br$^-$	2.976	0.276	2.795	0.289	–39.9	6.4	–46.3	–56.8	73.9	–63.4	–59.0	–4.4	0.214	0.52	1.51	–0.45
II···I$^-$	2.991	0.291	2.991	0.291	–37.4	6.9	–44.3	–52.6	70.6	–62.3	–58.4	–3.9	0.217	0.58	1.46	–0.43

[a] Δr_{D-I} is the stretch of the DI fragment relative to the optimized DI molecule; $\Delta r_{I\cdots A^-}$ is the change in I···A distance compared to the bond length of the optimized IA molecule; for the energy components, see Equations 2.9, 2.11 and 2.13; $\langle\sigma^*\vert np\rangle$ is the overlap of the antibonding σ^* acceptor orbital on DI with the σ lone pair np orbital on A$^-$; pop. is population (in electrons) of the indicated orbital; Q_A^{VDD} is the VDD charge on A$^-$ (in a.u.; see Equation 2.8).

the distance between the nucleophile and the central carbon atom and the bond length of the central carbon atom to the leaving group in the reactant complexes of the identity S_N2 reactions $X^- + CH_3X$ (with X = F, Cl, Br and I).[205] The DH or DX fragment is stretched from its equilibrium geometry to the geometry it acquires in the hydrogen- or halogen-bonded complex. Thus, each analysis starts from an optimized DH or DX molecule and a halide at a relatively large distance, which is then linearly transformed to the optimized hydrogen- or halogen-bonded complex.

Our analyses show that the weakening of hydrogen bonds DH···A^- and of the heavier halogen bonds DX···A^- (X = Cl, Br, I), as the accepting group varies from A^- = F^- to I^-, is directly related to the concomitant reduction in electron-donating capacity of the A^- hal-

Table 8.6 Geometry (in Å), stability (in kcal mol^{-1}), and electronic structure (in a.u. and eV) of DH and DX molecules.[a]

	r_{D-X}	BDE	Q_X^{VDD}	$\varepsilon(\sigma)$	$\varepsilon(\sigma^*)$	$\varepsilon(\pi)$	$\varepsilon(\pi^*)$
F–H	0.933	143.5	+0.20	–13.57	–0.72	–9.78	–
Cl–H	1.293	107.5	+0.10	–11.79	–0.97	–8.05	–
Br–H	1.433	94.6	+0.07	–11.18	–1.42	–7.51	–
I–H	1.625	81.7	+0.05	–10.31	–1.88	–6.91	–
F–F	1.420	50.1	0.00	–15.61	–6.17	–13.05	–9.74
Cl–F	1.664	69.2	–0.07	–13.61	–4.86	–11.66	–8.04
Br–F	1.796	69.8	–0.11	–12.86	–5.04	–11.01	–7.63
I–F	1.945	75.3	–0.13	–11.95	–4.86	–10.49	–7.03
F–Cl	1.664	69.2	+0.07	–13.61	–4.86	–11.66	–8.04
Cl–Cl	2.023	62.0	0.00	–11.93	–4.51	–9.89	–7.37
Br–Cl	2.173	58.8	–0.03	–11.38	–4.71	–9.36	–7.13
I–Cl	2.352	57.9	–0.08	–10.72	–4.67	–8.93	–6.78
F–Br	1.796	69.8	+0.11	–12.86	–5.04	–11.01	–7.63
Cl–Br	2.173	58.8	+0.03	–11.38	–4.71	–9.36	–7.13
Br–Br	2.321	55.0	0.00	–10.88	–4.82	–8.86	–6.93
I–Br	2.506	53.0	–0.06	–10.26	–4.73	–8.41	–6.62
F–I	1.945	75.3	+0.13	–11.95	–4.86	–10.49	–7.03
Cl–I	2.352	57.9	+0.08	–10.72	–4.67	–8.93	–6.78
Br–I	2.506	53.0	+0.06	–10.26	–4.73	–8.41	–6.62
I–I	2.700	49.0	0.00	–9.68	–4.65	–7.92	–6.39

[a] r_{D-X} = D–X bond length; BDE = homolytic bond dissociation energy without ZPE; Q_X^{VDD} = VDD charge on atom X (see Equation 2.8); ε = orbital energy.

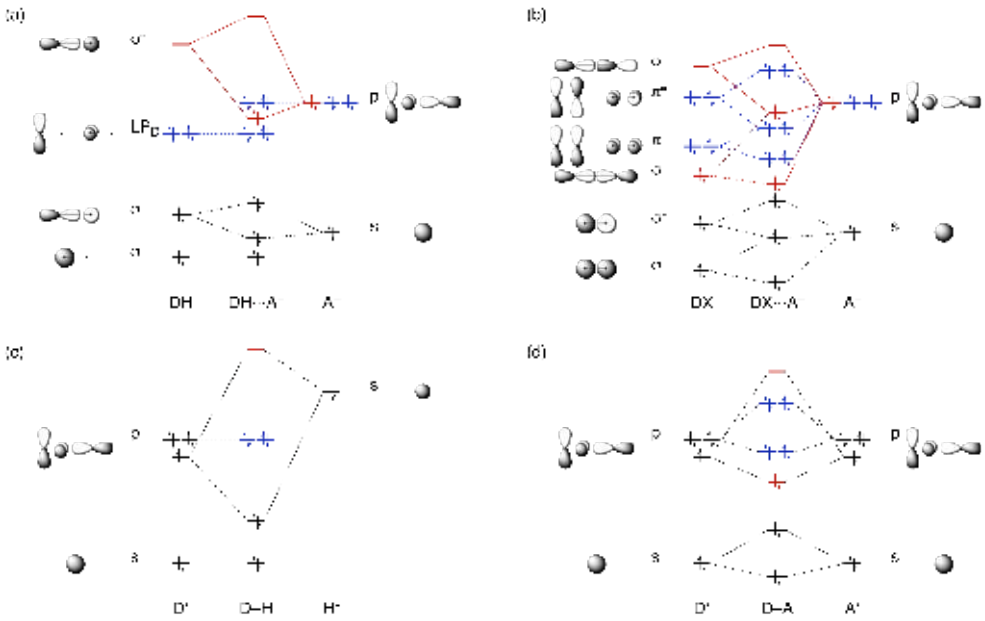

Figure 8.1 Simplified orbital interaction diagrams for (a) hydrogen-bonded complexes DH···A$^-$, (b) halogen-bonded complexes DX···A$^-$, (c) hydrogen halides D–H, and (d) dihalogens D–X, as they emerge from our quantitative Kohn–Sham MO analyses.

ide's np-type highest occupied molecular orbital (HOMO). The hydrogen bonds and halogen bonds appear to have an electrostatic component ΔV_{elstat}, and a covalent component ΔE_{oi} stemming mainly from the HOMO-LUMO interaction between the occupied halide np AO and the DH or DX antibonding σ^* acceptor orbital, shown schematically in Figure 8.1. Both bonding components, ΔV_{elstat} and ΔE_{oi}, are weakened as the halide HOMO becomes more diffuse and effectively lower in energy from A$^-$ = F$^-$ to I$^-$.[356] Consequently, also the interaction energy ΔE_{int}, and thus the net hydrogen or halogen bond strength ΔE, becomes less stabilizing along A$^-$ = F$^-$ to I$^-$ (see Table 8.1, and Table 8.3 to 8.5).

The key to understanding why fluorine bonds DF···A$^-$ show a more complex, partially opposite trend (*i.e.*, the expected weakening from A$^-$ = F$^-$ to Cl$^-$, but thereafter a strengthening along A$^-$ = Cl$^-$, Br$^-$ and I$^-$) is contained in the counteracting effects evolving from D–F bond stretching induced in the diatomic DF as it interacts with the halide A$^-$. Interestingly, activation strain analyses reveal that from early till relatively advanced stages of the complexation reaction, for a given point along the reaction coordinate ζ, we indeed

recover the original trend in interactions, namely, that $\Delta E_{int}(\zeta)$ weakens from $A^- = F^-$ to I^-. This can be nicely seen in Figure 8.2 which, for six representative series, shows the activation strain diagrams along the entire reaction coordinate ζ projected onto the stretch Δr_{D-X} of the complexation reaction between a DX molecule approaching the halogen bond accepting A^-. Each of the six activation strain diagrams in Figure 8.2 refers to one particular DH or DX molecule forming a hydrogen or halogen bond with $A^- = F^-$, Cl^-, Br^- and I^-. Therefore, the strain curves ΔE_{strain} within each of these graphs coincide because they refer to the same diatomic being stretched as the complexation reaction progresses. Consequently, the trend along $A^- = F^-$ to I^- in the total DH···A^- and DX···A^- energy profiles $\Delta E(\zeta)$ in each graph is directly determined by the trend in the corresponding interaction energy curves $\Delta E_{int}(\zeta)$. Also, as can be seen in Figure 8.2, the $\Delta E_{int}(\zeta)$ curve appears to be most stabilizing for $A^- = F^-$ and then weakens along Cl^-, Br^- and I^-, for any given diatomic DH or DX, including all fluorine-bonded DF···A^- complexes.

In other words, fluorine bonds DF···A^- would also show a weakening in interaction ΔE_{int} from $A^- = F^-$ to I^-, as the hydrogen bonds and all other halogen bonds, if it were not for the increasingly stretched D–F bond in the fluorine bond-donating diatomic molecule (see Table 8.2 and Figure 8.2). This structural phenomenon is promoted by a combination of factors: (i) a weak D–X bond that is easily stretched; (ii) a strong interaction with an approaching halide A^-; and importantly, (iii) a DX σ^* acceptor orbital that quickly drops in energy as the D–X bond elongates (see Figure 8.1). The latter generates a driving force for D–X stretching in DX···A^- because it enhances the orbital interactions and thus ΔE_{int} (see Figure 8.1 and 8.2). Indeed, D–X stretching is most pronounced if this bond in the diatomic fragment is weaker, that is, for the weaker halogen-hydrogen bonds (D–X = I–H; see Table 8.1) and the weaker halogen-halogen bonds (D–X = F–F; see Table 8.1). In the latter, it is able to affect the trend in overall bond strength ΔE. The D–F stretching in fluorine-bonded complexes is most pronounced in the FF···A^- series, along which the F–F stretch Δr_{F-F} increases from a value of 0.3 via 0.4 and 0.5 to 0.6 Å. This further stretch is able to induce the reversal of the trend in bond strength ΔE along the equilibrium structures FF···Cl^-, FF···Br^- and FF···I^- (see Table 8.2).

Thus, fluorine bond analyses in DF···A^- equilibrium geometries show that in most cases the interaction energy ΔE_{int} between the stretched D–F molecule and the halide A^-, as well as its components ΔV_{elstat} and ΔE_{oi}, become more stabilizing along the entire series $A^- = F^-$ to I^-, that is, already from F^- to Cl^- (see Table 8.2). This is indeed most pronouncedly so in the series FF···A^-, due to the F–F bond in the DX fragment being relative-

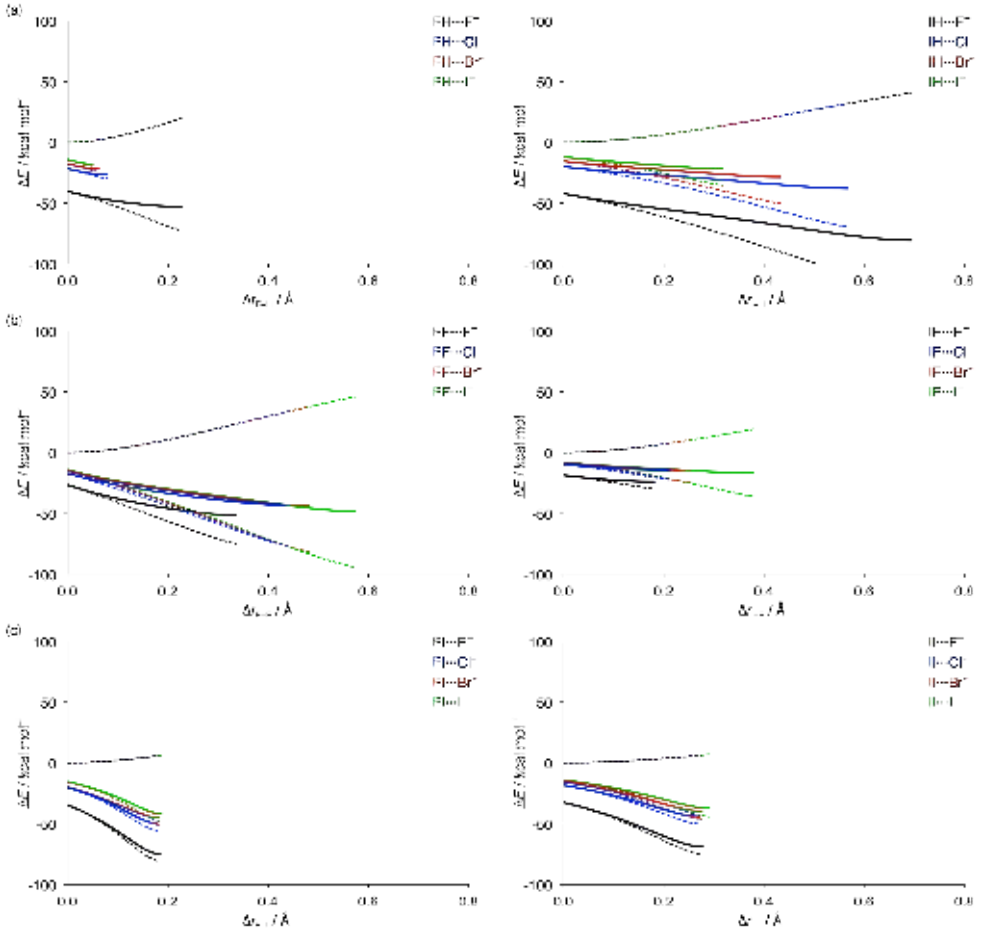

Figure 8.2 Activation strain analyses along the reaction coordinate (Equation 2.10) for DX + A^- complexation as a function of A^- = F^-, Cl^-, Br^- and I^-, projected onto the D–X stretch Δr_{D-X} for (a) hydrogen bonds, (b) fluorine bonds and (c) iodine bonds, with donating groups D = F (left) and D = I (right). Energy profiles ΔE (solid lines) are decomposed into strain energy ΔE_{strain} (dashed lines above ΔE = 0) and interaction energy ΔE_{int} (dashed lines below ΔE = 0).

ly weak. Along the series FF···F^-, FF···Cl^-, FF···Br^- and FF···I^-, ΔE_{int} increases in strength from a value of −75 to −78, −82 and −94 kcal mol^{-1}, respectively. For comparison, along the corresponding series with the much stronger F–I bond in the DX fragment, that is, FI···F^-, FI···Cl^-, FI···Br^- and FI···I^-, the ΔE_{int} weakens from −81 to −56, −51, and −48 kcal mol^{-1}. The overall bond strength ΔE along the fluorine-bonded series shows the aforementioned

initial weakening followed by a strengthening, because the D–F stretching and the concomitant strain energy ΔE_{strain} becomes more destabilizing along the series and, from A^- = F^- to Cl^-, dominates the strengthening in ΔE_{int} (see Table 8.2).

We conclude that, in general, hydrogen bonds DH···A^- and halogen bonds DX···A^- become weaker along A^- = F^- to I^- because the larger radii and lower np AO energies of the halides lead to weaker electrostatic attraction and weaker orbital interactions. Interestingly, for the same reason, F^- is the halide with the strongest gas-phase basicity, the strongest alkyl cation affinity and the lowest barrier for S_N2 reactions with halomethanes.[205,353-356] The trend in DF···A^- fluorine bond strength is partially inverted, that is, ΔE becomes more stabilizing along A^- = Cl^-, Br^- and I^- because of a more subtle interplay of factors. Notably, a significant stretching of the relatively weak D–F bond in the DF···A^- equilibrium structures lowers the DF σ^* acceptor orbital and thus amplifies the donor-acceptor orbital interactions, for example, along FF···Cl^-, FF···Br^- and FF···I^-.

8.5 Bond Analyses: Variation of the Donating Group

We recall that for the hydrogen bonds DH···A^-, a heavier donating halogen D results in a stronger bond, whereas the same variation in D weakens the halogen bonds DX···A^- (see Table 8.1 to 8.5). In both cases, the trend in bond strength ΔE is determined by the interaction energy ΔE_{int}. For example, from FH···F^- to IH···F^-, ΔE_{int} is strengthened from a value of –71 to –121 kcal mol^{-1}, whereas from FI···F^- to II···F^- it is weakened from a value of –75 to –29 kcal mol^{-1} (see Table 8.1 and 8.5). The strain energy ΔE_{strain} is not negligible, but it does not alter the trend set by ΔE_{int}. Our activation strain analyses explain the above differences between hydrogen bonds and halogen bonds, but they also confirm once more that both are very similar in nature (see Figure 8.3).

Starting with some general observations, we find that for hydrogen bonds as well as halogen bonds, the strain energy curves are most unfavorable when D = F and gradually become less destabilizing as the donating atom is varied along D = F, Cl, Br and I (see Figure 8.3). Furthermore, we find that for all DH···A^- and DX···A^- complexes, the interaction energy curves become less stabilizing along D = F, Cl, Br and I. The resulting energy profiles and, therefore, the stability and geometric properties of the complexes DH···A^- and DX···A^- depend on the balance between the ΔE_{strain} and ΔE_{int} curves, which we first discuss individually. The slope and shape of the ΔE_{strain} curves is of course directly related to the D–X bond strength of the diatomic fragment, which in general becomes stronger as the

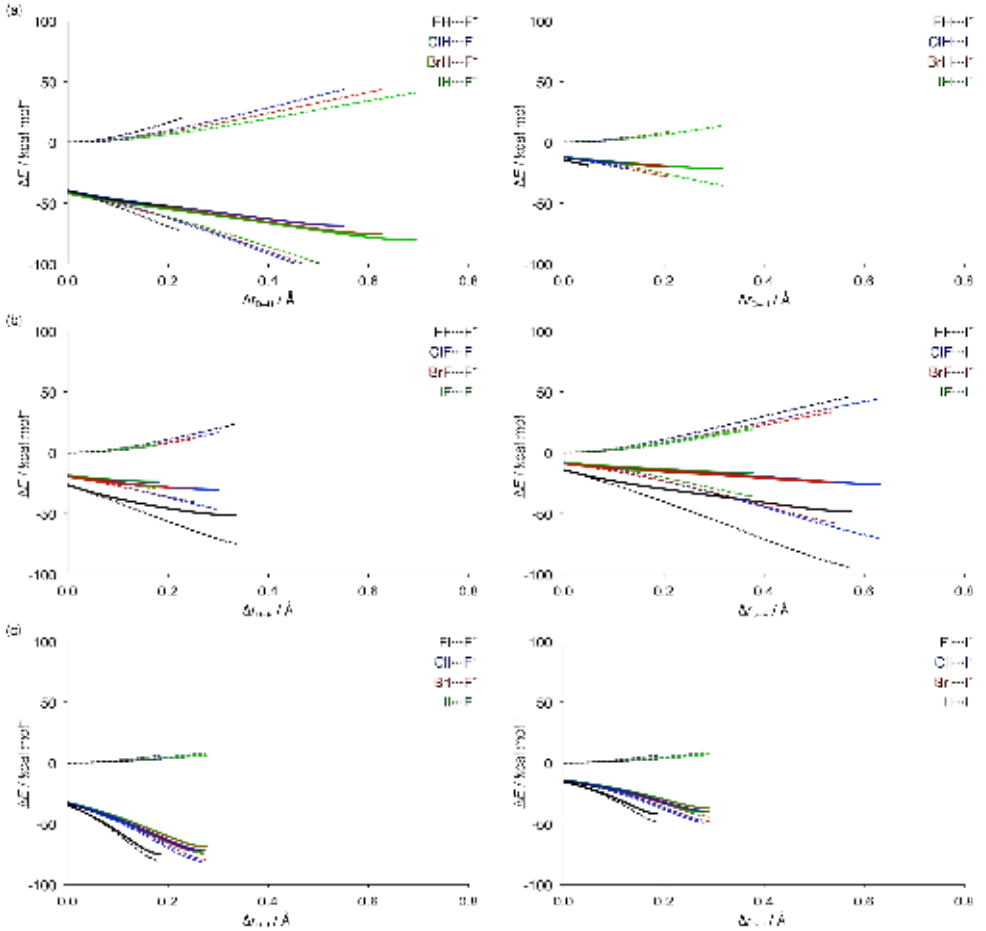

Figure 8.3 Activation strain analyses along the reaction coordinate (Equation 2.10) for DX + A^- complexation as a function of D = F, Cl, Br and I, projected onto the D–X stretch Δr_{D-X} for (a) hydrogen bonds, (b) fluorine bonds and (c) iodine bonds, with accepting groups A^- = F^- (left) and A^- = I^- (right). Energy profiles ΔE (solid lines) are decomposed into strain energy ΔE_{strain} (dashed lines above ΔE = 0) and interaction energy ΔE_{int} (dashed lines below ΔE = 0).

polarity across the D–H or D–X bond increases (see Table 8.6). This is a well-known and understood phenomenon.[357-359] From FH to IH, the halogen-hydrogen bond strength decreases significantly from a value of 143 to 82 kcal mol^{-1} (see Table 8.6). The corresponding halogen-halogen bonds are all much weaker, and variations in the homolytic BDE are also much smaller. From FF to IF, the bond strength increases from 50 kcal mol^{-1}

to 75 kcal mol^{-1}, while for the fragments DX, where X is Cl, Br or I, the bond strength generally decreases from a value of around 70 kcal mol^{-1} for FX to around 50 kcal mol^{-1} for IX. Thus, for the hydrogen-bonded complexes, the ΔE_{strain} curves show a pronounced reduction in slope from FH to IH, which, in the corresponding hydrogen-bonded complexes FH···A$^-$ to IH···A$^-$, translates into an increasing stretch Δr_{D-H} of the diatomic fragment. As the stretch Δr_{D-H} becomes larger from equilibrium structures FH···A$^-$ to IH···A$^-$, the ΔE_{int} curves have been able to descend further, to lower, more stabilizing energies. The final result is an increasing stability of the DH···A$^-$ complexes when the donating atom D is varied from F to I.

For the halogen bonds, the ΔE_{strain} curves are very similar and not decisive. The reason for the decreased stability of the DX···A$^-$ complexes upon the same variation of D from F to I is, therefore, that the ΔE_{int} curves descend more gradually to overall less stabilizing values. The interaction energy ΔE_{int} becomes less stabilizing from FX···A$^-$ to IX···A$^-$ because of decreasing electrostatic attractions (ΔV_{elstat}) and, in some cases, also because of greater Pauli repulsions (ΔE_{Pauli}; see Table 8.1 to 8.5). Both of these effects are easily explained when the electronegativities of the halogens are considered. Along the series FX to IX, the central atom X becomes relatively more electronegative, which will lead to a greater negative charge on this central atom, thus, reducing the electrostatic attraction with the anionic A$^-$, while concomitantly the occupied orbitals will have more X character, which in turn induces stronger Pauli repulsions.

8.6 Bond Analyses: Variation of the Central Atom

A more direct comparison of hydrogen and halogen bonds DX···A$^-$ can be obtained by varying X along H, F, Cl and I (omitting Br for clarity), while keeping the donating atom (D) and the accepting halide (A$^-$) constant (see Figure 8.4). We do this for four combinations of D and A$^-$, giving rise to four graphs in Figure 8.4. There appears to be a regular trend of increasing strength from the fluorine bonds to the iodine bonds. This trend derives again directly from the electronegativity difference across the D–X bond of the diatomic fragment: from DF to DI, the charge distribution on the DX fragment is increasingly polarized towards D, away from A$^-$ (see VDD atomic charges in Table 8.6), whereas the σ^* acceptor orbital achieves a higher amplitude on X (see Figure 8.1). This results in a strengthening of the halogen bond DX···A$^-$ because of greater electrostatic attraction, less Pauli repulsion and more stabilizing orbital interactions (see Table 8.2 to 8.5).

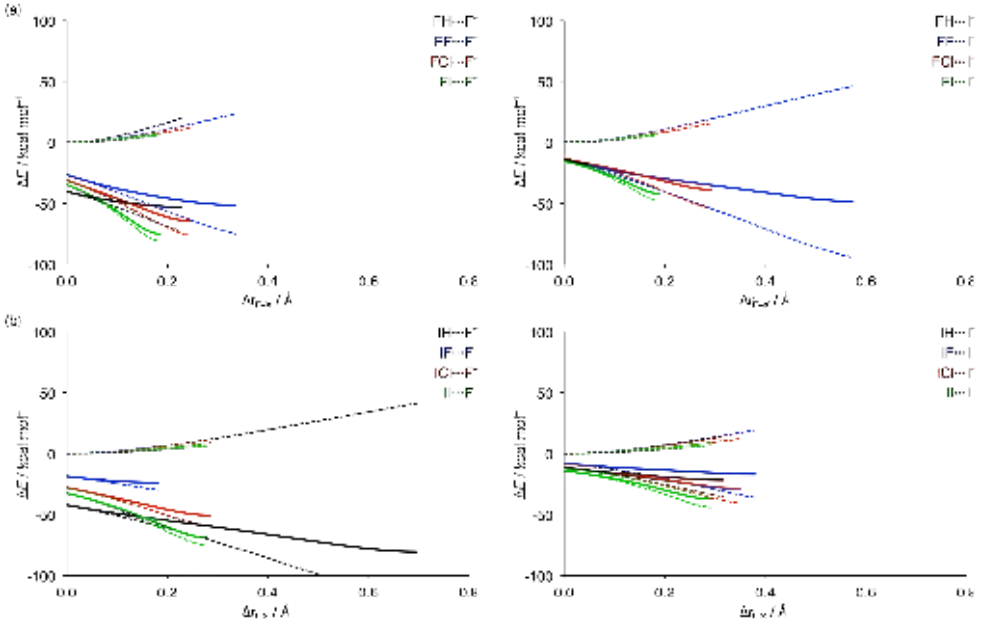

Figure 8.4 Activation strain analyses along the reaction coordinate (Equation 2.10) for DX + A^- complexation as a function of X = H, F, Cl and I, projected onto the D–X stretch Δr_{D-X} for (a) D = F and (b) D = I, and accepting groups A^- = F^- (left) and A^- = I^- (right). Energy profiles ΔE (solid lines) are decomposed into strain energy ΔE_{strain} (dashed lines above ΔE = 0) and interaction energy ΔE_{int} (dashed lines below ΔE = 0).

In analogy to the situation described above, hydrogen bonds might be expected to be much stronger than the halogen bonds due to the large and favorable polarization across the D–H bond, leading to a partially positively charged hydrogen atom in DH. For example, the VDD atomic charge on X in FH, FF and FI amounts to +0.20, 0.00 and +0.13 a.u., respectively (see Table 8.6). The decomposition of the interaction energy into its components shows indeed a stronger contribution from the electrostatic attraction (ΔV_{elstat}) to the bonding energy in the case of the hydrogen bonds (compare results in Table 8.1 to 8.5). Note, however, that this does not imply that hydrogen bonds are always stronger than the corresponding halogen bonds, since in our model systems the bonding mechanism is never purely, or even predominantly, electrostatic. The covalent or orbital interaction term (ΔE_{oi}) is relatively large and crucial for understanding the bonding in our model systems. For the hydrogen-bonded complexes DH···A^-, the ΔE_{oi} term accounts for 40% to 66% of the total bonding interactions (ΔV_{elstat} + ΔE_{oi}). The stabilization due to this term results predomi-

nantly from charge transfer from the np orbitals of the halide into the σ* LUMO of the hydrogen halide (see Figure 8.1). For the halogen-bonded complexes DX···A⁻, the contribution from the orbital interaction term ranges from 43% for FI···F⁻ to as much as 97% for IF···F⁻ at the other end of the spectrum. The larger covalent contribution in the case of the halogen bonds is the result of the low orbital energy of the empty dihalogen σ* orbital (*e.g.*, –0.7 eV for FH and –6.2 eV for FF; see Table 8.6), which directly translates into a stronger donor-acceptor orbital interaction with the halide np orbital (compare results in Table 8.1 to 8.5). Note that, percentagewise, ΔE_{oi} in the halogen bonds appears even larger because of the aforementioned, less favorable electrostatic attraction ΔV_{elstat}.

The nature of the strong hydrogen bonds and halogen bonds discussed so far, strongly resembles that of the weaker, neutral hydrogen and halogen bonds, although contributions from dispersion interactions (ΔE_{disp}) become relatively more important in the latter.[84,86,100,360] Preliminary results of dispersion-corrected ZORA-BP86-D3/TZ2P calculations on FI···FI (ΔE = –4.3 kcal mol^{-1}), ClCl···ClCl (ΔE = –1.3 kcal mol^{-1}) and II···II (ΔE = –6.6 kcal mol^{-1}) show that the covalent component ΔE_{oi} amounts to 43% to 59%, whereas dispersion contributes 2% to 17% to the total of all bonding interactions (ΔE_{oi} + ΔV_{elstat} + ΔE_{disp}). The covalent contribution in these neutral model complexes stems from a donor-acceptor orbital interaction from an occupied π* orbital on one dihalogen fragment into the σ* orbital of the other dihalogen fragment.

We conclude that halogen bonds DX···A⁻ and hydrogen bonds DH···A⁻ have a very similar bonding mechanism consisting of both electrostatic and covalent contributions. The electrostatic attraction is less favorable in the halogen bonds due to a smaller and in some cases less favorably oriented polarization across the dihalogen molecule DX. Nevertheless, halogen bonds can become stronger than hydrogen bonds, because of a more stabilizing covalent component in the former. The reason is the lower orbital energy of the empty σ* orbitals in dihalogen molecules DX leading to a stronger, more favorable donor-acceptor orbital interaction with the halide A⁻ np orbital (see Table 8.6).

8.7 Conclusions

Halogen bonds in DX···A⁻ are very similar in nature to hydrogen bonds in DH···A⁻ (D, X, A = F, Cl, Br, I): both have a sizable covalent component stemming from HOMO-LUMO interactions between the np-type lone pair on the halogen bond- or hydrogen bond-accepting fragment A⁻ and the D–X or D–H antibonding σ* LUMO on the halogen

bond- or hydrogen bond-donating fragment DX or DH, respectively. Neither halogen bonds nor hydrogen bonds are, therefore, predominantly, let alone purely electrostatic phenomena.

Two characteristic differences between the halogen bonds DX···A^- and hydrogen bonds DH···A^- are that halogen bonds are generally associated with (i) a weaker electrostatic attraction (dihalogens DX are less polar than hydrogen halides DH), and (ii) a significantly more stabilizing HOMO-LUMO interaction. The stronger orbital interaction derives from the lower energy of the halogen-halogen σ* LUMO as compared to that of the much stronger halogen-hydrogen bond. Halogen bonds can be stronger, but also weaker, than the corresponding hydrogen bonds.

Finally, hydrogen bonds DH···A^- and halogen bonds DX···A^- become weaker along A^- = F^- to I^-, because the electron-donating capability (and basicity, alkyl cation affinity, nucleophilicity)[205,353-355] of the halide decreases in this order. The trend in DF···A^- fluorine bond strength is partially inverted, that is, Δ*E* becomes more stabilizing along A^- = Cl^-, Br^- and I^-, because of a more subtle interplay of factors, in which a significant stretching of the relatively weak D–F bond lowers the DF σ* acceptor orbital and, thus, amplifies the donor-acceptor orbital interactions.

9 Resonance Assistance and Cooperativity in Halogen-Bonded Complexes

Previously appeared as

Covalency in Resonance-Assisted Halogen Bonds
Demonstrated with Cooperativity in N-Halo-Guanine Quartets
L. P. Wolters, N. W. G. Smits, C. Fonseca Guerra
Phys. Chem. Chem. Phys. **2015**, *17*, 1585–1592

9.1 Introduction

With the computational work presented in this chapter, we continue the analyses of the nature of halogen bonds. The detailed studies on small model complexes in the previous chapter already showed that hydrogen bonds and halogen bonds arise due to a very similar bonding mechanism, consisting of electrostatic attraction and a significant contribution from charge transfer in the σ electron system. Here, we demonstrate that this similar bonding mechanism has equivalent consequences for their bonding characteristics. To this end, we move to much larger model systems, namely the hydrogen-bonded Watson-Crick DNA base pairs adenine-thymine (AT) and guanine-cytosine (GC), as well as the hydrogen-bonded guanine and xanthine quartets (G_4 and Xan_4, respectively). Gilli *et al.* proposed that hydrogen bonds between DNA bases are reinforced by resonance assistance, due to electron delocalization in the π electron system. Therefore, these hydrogen bonds are often referred to as 'resonance-assisted hydrogen bonds' (RAHB).[361] In previous work[114] it has been theoretically established that the hydrogen bonds in Watson-Crick DNA base pairs arise due to roughly equal contributions from electrostatic attraction and charge transfer, and that indeed the π electrons provide some additional stabilization. These findings have later been confirmed by others.[132] Furthermore, the interplay between the delocalization in the π electron system and the donor-acceptor interactions in the σ electron system was

found to be small, that is, the simultaneous occurrence of the σ and π orbital interactions is only slightly stronger than the sum of these interactions occurring individually.

In telomeric DNA, the guanine bases form quadruplexes: stacks consisting of three layers of guanine quartets. The guanine bases in these layers are essentially coplanar and interact through hydrogen bonds. These quadruplexes are furthermore stabilized by the presence of monovalent ions, such as K^+ and Na^+, between the layers. Intriguingly, the hydrogen bond energy of a guanine quartet G_4 is known to be more stabilizing than four times the hydrogen bond energy of one guanine pair G_2. Previously, analyses on telomeric DNA revealed[115] that this cooperativity within the hydrogen bonds originates from the charge separation that goes with donor-acceptor orbital interactions in the σ electron system, and not from the strengthening caused by resonance in the π electron system. In the xanthine quartet, Xan_4, the donor-acceptor interactions run in opposite directions, which does not lead to a charge separation and therefore no cooperativity is observed.

In the following sections, we revisit these analyses on the natural Watson-Crick base pairs as well as the quartets, and compare the results to analyses on their halogen-bonded analogues, in which we have replaced the hydrogen bonds with halogen bonds, resulting in *N*-halo-base pairs (X-AT and X-GC), *N*-halo-guanine quartets (X-G_4) and *N*-halo-xanthine quartets (X-Xan_4), where X indicates the type of halogen bond (*i.e.*, F, Cl, Br or I). Schematic representations of these model systems are shown in Figure 9.1. Chloramines of nucleosides are experimentally known,[362-366] of which the cytidine and adenosine chloramines are the most stable.

Cooperativity and resonance assistance have been explored before in the context of halogen-bonded molecular systems, but mainly on small complexes.[367-375] Here, we investigate these phenomena for larger complexes, by substituting the N–H in the natural G_4 quartets with N–X, and demonstrate that the halogen bonds in an *N*-halo-guanine quartet X-G_4 show the same synergetic enhancement, in quantity and nature, as the hydrogen bonds in G_4. The synergetic enhancement is not observed in X-Xan_4 quartets, similar to the results for hydrogen-bonded quartets. We furthermore present an accurate explanation for the physical mechanism of resonance-assisted halogen bonds (RAXB) and the observed cooperativity, which is again established in terms of Kohn-Sham molecular orbital (MO) theory, and supported by corresponding energy decomposition analyses (EDA) and Voronoi deformation density (VDD) analyses of the charge distribution. The proof of the intrinsic resemblance between hydrogen bonds and halogen bonds will be based on the existence of charge transfer in the halogen bonds, in agreement with the results presented

in the previous chapter. The occurrence of charge transfer can be directly demonstrated with the cooperativity observed within X-G_4 quartets, which follows from unambiguous quantities, namely the interaction energy between hydrogen-bonded fragments, and the electron density deformation that occurs upon formation of these quartets.

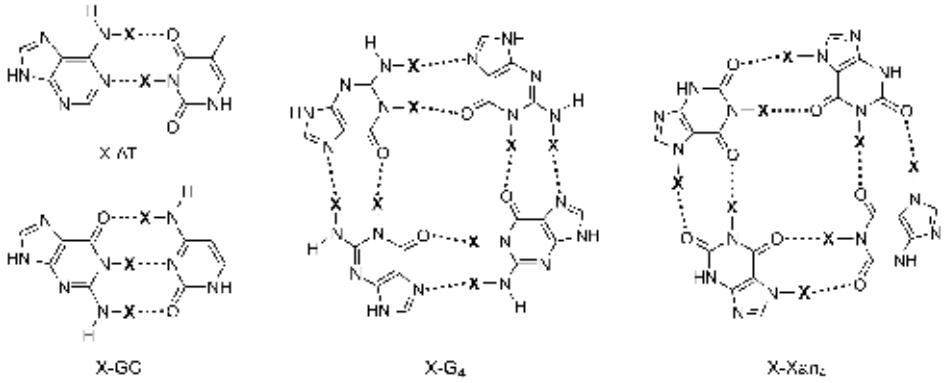

Figure 9.1 Schematic representation of the Watson-Crick base pairs (AT and GC; X = H) and the guanine and xanthine quartets (G_4 and Xan_4; X = H) and the *N*-halo-base pairs (X-AT and X-GC), *N*-halo-guanine quartets (X-G_4) and *N*-halo-xanthine quartets (X-Xan_4) with X = F, Cl, Br or I.

9.2 Bond Analyses: B-DNA Base Pairs

We start with a brief investigation of the nature of the bonding in the halogen-substituted Watson-Crick base pairs. From earlier studies,[376] it is known that the halogen-bonded X-AT and X-GC are weaker bound than the natural AT and GC. Indeed, our computations at ZORA-BLYP-D3(BJ)/TZ2P show that the fluorinated Watson-Crick base pairs are almost unbound (–1.4 kcal mol^{-1} when symmetry constraints are applied to keep the base pair planar, without constraints no halogen-bonded base pair was found, but instead a stacking confirmation), whereas the halogen bonds in the iodine-substituted AT and GC pairs amount to –10.7 kcal mol^{-1} and –17.3 kcal mol^{-1}, respectively (see Table 9.1). Analyses of the hydrogen bonds and halogen bonds for these dimers reveal that the bonding orbital interaction component ΔE_{oi} and the electrostatic attraction ΔV_{elstat} are of comparable magnitude (see Table 9.1).

Table 9.1 Bond energy analyses (in kcal mol^{-1}) for the natural and halogenated Watson-Crick base pairs.[a]

	ΔE	ΔE_{strain}	ΔE_{int}	ΔV_{elstat}	ΔE_{Pauli}	ΔE_{oi}	ΔE_{oi}^{σ}	ΔE_{oi}^{π}	ΔE_{disp}
AT	−16.7	+1.9	−18.5	−32.0	+40.1	−21.2	−19.6	−1.6	−5.4
F-AT	−1.4	+0.1	−1.4	−1.8	+3.7	−1.5	−1.4	−0.2	−1.8
Cl-AT	−6.3	+0.4	−6.7	−13.0	+19.9	−8.9	−8.5	−0.4	−4.8
Br-AT	−9.7	+1.3	−11.0	−22.9	+33.7	−15.6	−14.7	−0.9	−6.3
I-AT	−10.7	+2.0	−12.7	−24.7	+35.4	−16.1	−15.1	−1.0	−7.3
GC	−30.4	+3.5	−34.0	−47.7	+51.9	−31.9	−27.4	−4.5	−6.3
F-GC	−1.4	+0.1	−1.5	−1.3	+4.0	−2.1	−1.8	−0.3	−2.1
Cl-GC	−9.1	+0.6	−9.7	−14.2	+19.3	−8.6	−7.7	−0.8	−6.2
Br-GC	−12.9	+1.2	−14.1	−23.5	+32.5	−15.2	−13.9	−1.3	−7.9
I-GC	−17.3	+2.5	−19.7	−28.7	+38.3	−21.5	−19.5	−2.0	−7.9

[a] See Equations 2.9, 2.11 and 2.13. Energies are computed in C_s symmetry for base pairs and bases. The bond energies for the fully optimized base pairs and bases differ slightly.

We have performed these optimizations and analyses in C_s symmetry to force the base pairs to remain planar, which enables us to separate the orbital interaction energy into contributions from the σ orbitals (A' irrep) and π orbitals (A" irrep), using Equation 2.13. Optimizations without symmetry constraints lead to only slightly different results (data not shown). Similar to the results for hydrogen-bonded bases, and in line with the results in the previous chapter, we found that also for the halogen-bonded bases the largest contribution to the orbital interaction term comes from the σ electrons: resonance assistance by π electron delocalization does not play an important role. We also found that, again in line with

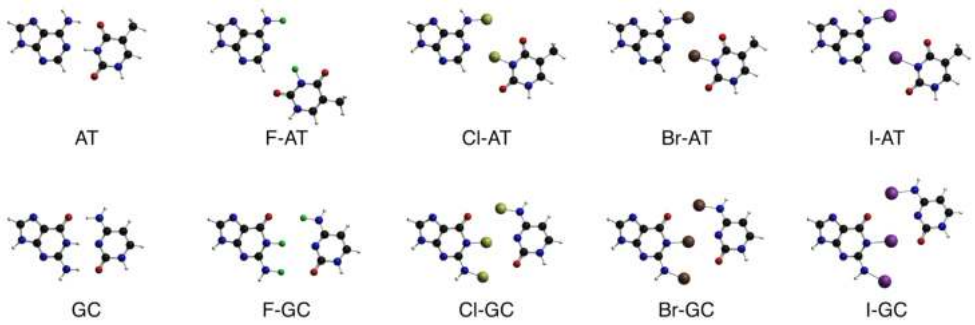

Figure 9.2 Geometries of the hydrogen- and halogen-bonded X-AT and X-GC base pairs in C_s symmetry.

results discussed in section 8.6, the strengthening from the fluorine bonds to the iodine bonds follows from an increase in all bonding components.

The halogen bonds in X-AT and X-GC base pairs differ geometrically from the hydrogen bonds in the natural DNA base pairs. The larger halogen atoms do not pair very well with the other base, because the halogen atoms are too large to fit next to each other. This effect becomes more pronounced from chlorine- to iodine-substituted base pairs, as is visible in Figure 9.2. Due to these geometric differences between the natural base pairs and the halogen-substituted base pairs, it is difficult to make a detailed comparison. However, we do find that there is a large contribution of the σ orbital interactions, which stems from donor-acceptor interactions between the nitrogen or oxygen lone pair orbitals on one base and the σ^*_{N-X} acceptor orbitals on the other base.

9.3 Bond Analyses: G-DNA Quadruplexes

Having established that there is a large contribution of the σ orbital interactions to the bonding of the halogen-substituted base pairs, we extended the investigation to telomeric DNA. The *N*-halo-quartets have, as is the case for the natural guanine and xanthine quartets, an S_4- or C_4-symmetric global minimum structure. However, in the quadruplex, which is the natural occurring structure of guanine quartets, computations showed an almost planar middle layer for the Br-G_4 quartet, which allows for favorable dispersion interactions with the two outer guanine quartets (see Figure 9.3). The Br-G_4 quartet is only 2.3 kcal mol^{-1} lower in energy in the geometry it acquires in the quadruplex G_4-K^+-[Br-G_4]-K^+-G_4, than in a C_{4h}-constrained geometry. Therefore, the quartets have been optimized and analyzed in C_{4h} symmetry (see Figure 9.4) to enable the separation between the σ and π orbital interactions.

The computational experiment to prove the existence of covalency as bonding component in the *N*-halo-guanine quartets started with the comparison of the halogenated guanine and xanthine quartets, as presented in Figure 9.1 and 9.4. We recall from earlier work[115] that natural guanine quartets (G_4) are more strongly bound than xanthine quartets (Xan_4), despite the fact that they have the same number of hydrogen bonds. This is ascribed to a cooperativity effect in the former. The interaction energy of G_4 amounts to −90.6 kcal mol^{-1}, whereas ΔE_{int} of Xan_4 is only −73.4 kcal mol^{-1} (see Table 9.2). Interestingly, the same is true for the Cl-, Br- or I-substituted quartets. The interaction energy of

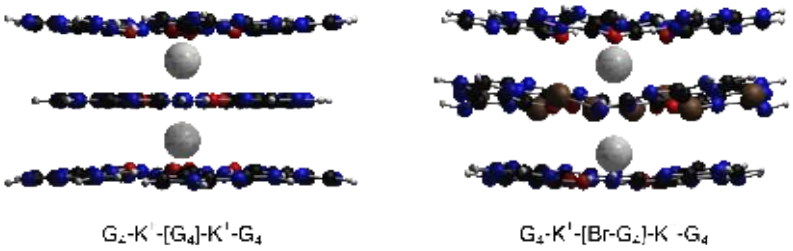

Figure 9.3 Structures of stacked G_4-K^+-[G_4]-K^+-G_4 (left) and G_4-K^+-[Br-G_4]-K^+-G_4 (right) in C_4 symmetry.

X-G_4 for X = Cl, Br and I is, respectively, –13.4 kcal mol^{-1}, –35.0 kcal mol^{-1} and –46.8 kcal mol^{-1} stronger than ΔE_{int} of the analogous X-Xan$_4$.

To investigate whether this is due to a cooperative effect, we compare ΔE_{int} (*i.e.* formation of the quartet from four bases in the geometry they acquire in the quartet) with the sum ΔE_{sum} of the individual pairwise interactions for all possible pairs of bases in the quartet (see Figure 9.5), defined as

$$\Delta E_{sum} = 4\ \Delta E_{pair} + 2\ \Delta E_{diag}\ . \tag{9.1}$$

Here, ΔE_{pair} is the interaction between two neighboring bases (*i.e.*, the interaction between two doubly hydrogen- or halogen-bonded bases in the geometry of the quartet) and ΔE_{diag}

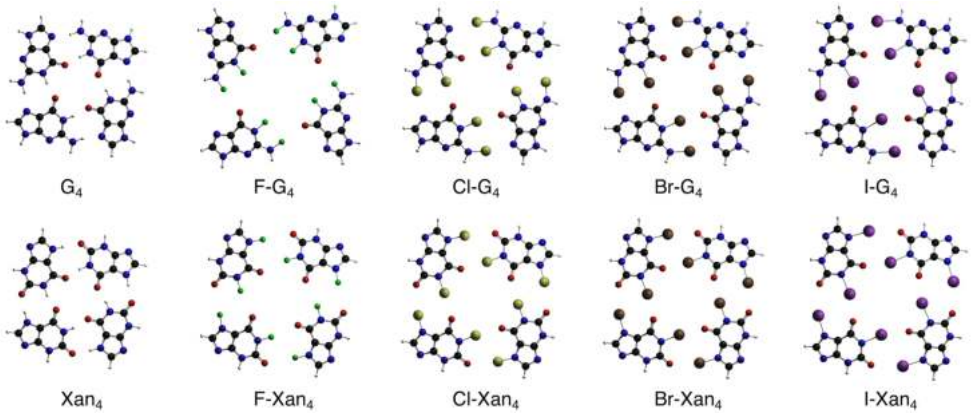

Figure 9.4 Geometries of the hydrogen- and halogen-bonded X-G_4 and X-Xan$_4$ quartets in C_{4h} symmetry.

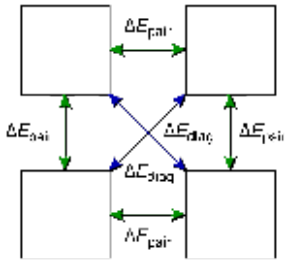

Figure 9.5 Definition of pairwise interaction energy terms ΔE_{pair} (green arrows) and ΔE_{diag} (blue arrows) in quartet of DNA bases (shown as squares).

is the interaction between two diagonally oriented bases (*i.e.*, the interaction between two non-hydrogen-bonded or non-halogen-bonded bases in the geometry of the quartet), as indicated by the green and blue arrows, respectively, in Figure 9.5. The synergy occurring in the quartet is then defined as the difference:

$$\Delta E_{syn} = \Delta E_{int} - \Delta E_{sum} \; . \tag{9.2}$$

Thus, a negative value of ΔE_{syn} corresponds to a stabilizing cooperative effect, that is, a reinforcement of the quartet stability due to the occurrence of all hydrogen bonds or halogen bonds simultaneously.

Analyses of the bonding energy of the C_{4h}-symmetric quartets using these definitions (see Table 9.2), reveal a significant cooperative synergetic effect for chlorine-, bromine-, and iodine-substituted G_4 quartets, but not for any of the Xan_4 quartets. The synergy (Equation 9.2) for Br-G_4 and I-G_4 amounts to –23.5 and –24.9 kcal mol^{-1}, respectively, which is even stronger than for the natural G_4 (–20.9 kcal mol^{-1}). The experiments were extended to the quadruplexes (Figure 9.3) to see how stacking interactions with hydrogen-bonded guanine quartets G_4, and cations K^+ affect the bonding energy of G_4 and Br-G_4, and in particular to see how they affect the cooperativity that is observed for the hydrogen bonds and halogen bonds within these quartets. This is done again using the approach of Equations 9.1 and 9.2 (see also Figure 9.5), but the definitions are modified to account for the presence of the stacking environment. Now, the energy of a base X-B and of a quartet of bases X-B_4 in the stacking environment, are defined as $E_{G_4\text{-}[X\text{-}B]\text{-}G_4} - E_{G_4\text{-}[\ ]\text{-}G_4}$ and $E_{G_4\text{-}[X\text{-}B_4]\text{-}G_4} - E_{G_4\text{-}[\ ]\text{-}G_4}$, respectively, that is, the difference in energy between a stacking environment "occupied" with a central base or quartet and an empty stacking environment. The interaction energy of a quartet in the stacking environment is then given by:

$$\Delta E_{int} = (E_{G_4\text{-}[X\text{-}B_4]\text{-}G_4} - E_{G_4\text{-}[\ ]\text{-}G_4}) - 4\,(E_{G_4\text{-}[X\text{-}B]\text{-}G_4} - E_{G_4\text{-}[\ ]\text{-}G_4})\,. \tag{9.3}$$

Likewise, the sum energy for a quartet in a stacking environment is

$$\begin{aligned}\Delta E_{sum} = 4\,\{(E_{G_4\text{-}[X\text{-}B_2]\text{-}G_4} - E_{G_4\text{-}[\ ]\text{-}G_4}) - 2\,(E_{G_4\text{-}[X\text{-}B]\text{-}G_4} - E_{G_4\text{-}[\ ]\text{-}G_4})\} + \\ 2\,\{(E_{G_4\text{-}[X\text{-}B/X\text{-}B]\text{-}G_4} - E_{G_4\text{-}[\ ]\text{-}G_4}) - 2\,(E_{G_4\text{-}[X\text{-}B]\text{-}G_4} - E_{G_4\text{-}[\ ]\text{-}G_4})\}\end{aligned} \tag{9.4}$$

which contains, in analogy to Equation 9.1 (see also Figure 9.5), four times the interaction energy ΔE_{pair} for a hydrogen- or halogen-bonded pair of bases ($X\text{-}B_2$) in the stacking environment (first line) and twice the interaction energy ΔE_{diag} for a pair of non-adjacent bases (X-B/X-B) in the stacking environment (second line). The effect of stacking and potassium cations can be easily derived from Equations 9.3 and 9.4 by including the cations in the stacking environment.

As shown in Table 9.2, the synergy is barely affected by the molecular environment and nonplanarity: for G_4 and Br-G_4 quartets in the quadruplexes it is –17.9 kcal mol^{-1} and –17.7 kcal mol^{-1}, respectively. These computational experiments confirm the intrinsic resemblance between halogen bonds and hydrogen bonds.

Table 9.2 Interaction energy analyses (in kcal mol^{-1}) for the natural and halogenated X-G_4 and X-Xan_4 quartets.[a]

Environment	Quartet	Symmetry	ΔE_{int}	ΔE_{diag}	ΔE_{pair}	ΔE_{sum}	ΔE_{syn}
Gas phase	G_4	C_{4h}	–90.6	–1.9	–16.5	–69.7	–20.9
	F-G_4	C_{4h}	–3.1	+0.1	–0.7	–2.4	–0.7
	Cl-G_4	C_{4h}	–39.5	–0.1	–7.5	–30.3	–9.2
	Br-G_4	C_{4h}	–77.5	–0.6	–13.2	–54.0	–23.5
	I-G_4	C_{4h}	–97.8	–1.3	–17.6	–72.9	–24.9
	Xan_4	C_{4h}	–73.4	–0.2	–17.9	–71.9	–1.5
	F-Xan_4	C_{4h}	–2.9	+0.4	–0.8	–2.4	–0.5
	Cl-Xan_4	C_{4h}	–26.1	+0.1	–6.5	–25.7	–0.4
	Br-Xan_4	C_{4h}	–42.5	–0.1	–10.4	–41.7	–0.8
	I-Xan_4	C_{4h}	–51.0	–0.3	–12.4	–50.3	–0.8
G_4-[ ]-G_4	G_4	C_4	–89.2	–1.9	–17.4	–73.4	–15.8
	Br-G_4	C_4	–56.0	–0.5	–10.6	–43.4	–12.7
G_4-K^+-[ ]-K^+-G_4	G_4	C_4	–72.7	+0.6	–14.0	–54.8	–17.9
	Br-G_4	C_4	–47.0	+0.3	–7.5	–29.3	–17.7

[a] See Equations 9.1 to 9.4 and Figure 9.5.

The quadruplexes have been subjected to further brief analyses. The stacking interaction in the G_4-K^+-[G_4]-K^+-G_4 quadruplex is smaller than in the G_4-K^+-[Br-G_4]-K^+-G_4 quadruplex. The stacking between the three G_4 layers in G_4-[G_4]-G_4 (no K^+ present) amounts to –66.2 kcal mol^{-1}, and between the G_4, Br-G_4 and G_4 in G_4-[Br-G_4]-G_4 amounts to –72.6 kcal mol^{-1}. When K^+ is present, the interaction between the potassium cations and the stacked quartets is larger for G_4-K^+-[G_4]-K^+-G_4 (–205.6 kcal mol^{-1}) than for G_4-K^+-[Br-G_4]-K^+-G_4 (–176.9 kcal mol^{-1}). The smaller interaction with the cations in G_4-K^+-[Br-G_4]-K^+-G_4 can be attributed to the larger distance between the K^+ ions and the oxygen atoms of the central quartet (3.8 to 3.9 Å). In G_4-K^+-[G_4]-K^+-G_4 quadruplex, the oxygen atoms of the central quartet are considerably closer to the K^+ ions: the distance is only 2.9 Å. The additional lone pairs on the bromines probably do not contribute to the overall stability of the K^+-mediated complex because the bromines are more than 4 Å away from K^+.

9.4 The Origin of Cooperativity in G_4 and X-G_4 Quartets

For the natural quadruplexes, the cooperativity has been shown to originate from the charge separation that goes with donor-acceptor interactions in the σ electron system from N and O lone pair orbitals on one guanine to σ^*_{N-H} acceptor orbitals on another guanine.[115] To trace the origin of the cooperativity in halogen-substituted guanine quartets, we have followed the same procedure: we constructed X-G_4 by taking one of the *N*-halo-guanine bases in the quartet and stepwise adding the other three *N*-halo-guanine bases (always in the geometry of X-G_4), *i.e.*, X-G + X-G = X-G_2; X-G_2 + X-G = X-G_3 and X-G_3 + X-G = X-G_4 (see Figure 9.6a and Table 9.3). The different ways in which the third X-G can bind to X-G_2 are denoted as X-G_3 and X-G^*_3. This stepwise approach enables us to examine accurately why, and at which point, cooperativity begins to show up. Except for F-G_4, which is almost unbound, the *N*-halo-quartets show a trend similar to the natural G_4. For example, the interaction energy in I-G_2 amounts to –17.6 kcal mol^{-1}, between I-G_2 and I-G it is already larger, –24.4 kcal mol^{-1} and the interaction energy for closure of the quartet by the formation of four halogen bonds (that is, between I-G_3 and I-G) is –55.8 kcal mol^{-1}. Thus, the cooperative effect increases systematically and monotonically as the X-G_{n-1} fragment becomes larger. A similar computational experiment with X-Xan$_4$ quartets reveals essentially no cooperativity at all (see Table 9.4). As both quartets have π electrons, this

outcome points towards the σ electron system as the responsible factor for the cooperativity in X-G_4.

To investigate whether the cooperativity in *N*-halo-guanine quartets is caused by a mechanism similar to that in the natural guanine quartets, we subjected the total interaction energy, $\Delta E_{int} = \Delta E_{int}(X\text{-}G_2) + \Delta E_{int}(X\text{-}G_3) + \Delta E_{int}(X\text{-}G_4)$, to an energy decomposition analysis. The synergy in each energy component, for example ΔE_{oi}, is defined, in analogy to Figure 9.5 and 9.6a, as the difference between $\Delta E_{oi}(X\text{-}G_2) + \Delta E_{oi}(X\text{-}G_3) + \Delta E_{oi}(X\text{-}G_4)$ and the sum of the corresponding energy component in the pairwise interactions, that is, $4\ \Delta E_{pair,oi} + 2\ \Delta E_{diag,oi}$. The energy decomposition analyses show that there are two main contributions to this synergy: (i) the synergy in the electrostatic attraction term of –3.8 kcal mol^{-1}, –8.3 kcal mol^{-1} and –6.3 kcal mol^{-1} for Cl-G_4, Br-G_4 and I-G_4, respectively; and (ii) the much stronger synergy in the orbital interactions of –5.8 kcal mol^{-1}, –15.6 kcal mol^{-1}

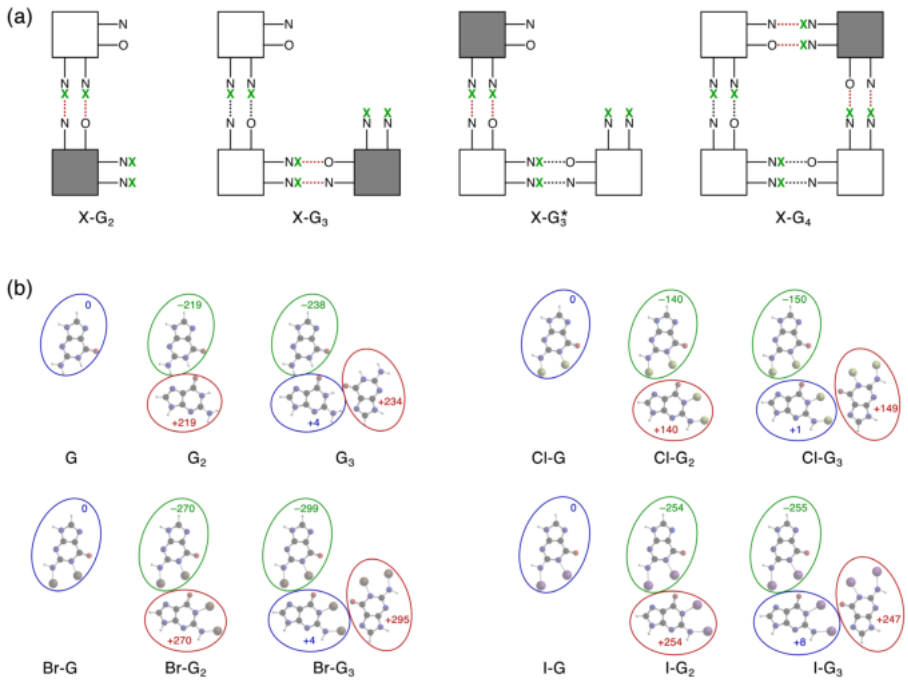

Figure 9.6 (a) Formation of an X-G_4 quartet in three steps: X-G + X-G = X-G_2; X-G_2 + X-G = X-$G_3^{(*)}$; X-$G_3^{(*)}$ + X-G = X-G_4. (b) VDD charges (see Equation 2.8; in milli-electrons) for fragments of the hydrogen-bonded G_4 and halogen-bonded X-G_4 quartets in C_{4h} symmetry.

Table 9.3 Energy decomposition analyses (in kcal mol^{-1}) for the formation of hydrogen-bonded and halogen-bonded G_4 from G_{n-1} + G in C_{4h} symmetry.[a]

		G_2	G_3	G_3^*	G_4	G/G	ΔE_{sum}	ΔE_{syn}
G_4	ΔE_{oi}^{σ}	−14.7	−16.4	−16.1	−36.1	−0.1	−59.1	−8.2
	ΔE_{oi}^{π}	−1.8	−2.4	−2.3	−6.2	−0.1	−7.3	−3.1
	ΔE_{oi}	−16.5	−18.8	−18.5	−42.3	−0.2	−66.4	−11.3
	ΔE_{Pauli}	+30.9	+31.4	+30.2	+61.3	+0.1	+123.8	−0.2
	ΔV_{elstat}	−26.4	−30.9	−30.1	−60.9	−1.6	−108.8	−9.4
	ΔE_{disp}	−4.5	−4.7	−4.7	−9.1	−0.2	−18.3	0.0
	$\Delta E_{int}(G_n)$	−16.5	−23.0	−23.0	−51.1	−1.9	−69.7	−20.9
F-G_4	ΔE_{oi}^{σ}	−0.7	−0.7	−0.7	−1.5	0.0	−2.7	−0.2
	ΔE_{oi}^{π}	−0.1	−0.2	−0.1	−0.4	0.0	−0.5	−0.1
	ΔE_{oi}	−0.8	−0.9	−0.8	−1.8	0.0	−3.2	−0.3
	ΔE_{Pauli}	+1.3	+1.3	+1.3	+2.5	0.0	+5.0	0.0
	ΔV_{elstat}	−0.4	−0.3	−0.4	−1.0	+0.2	−1.3	−0.4
	ΔE_{disp}	−0.7	−0.8	−0.8	−1.5	0.0	−3.0	0.0
	$\Delta E_{int}(G_n)$	−0.7	−0.7	−0.7	−1.8	+0.1	−2.4	−0.7
Cl-G_4	ΔE_{oi}^{σ}	−9.2	−10.3	−9.8	−22.3	0.0	−36.9	−5.0
	ΔE_{oi}^{π}	−0.8	−1.0	−0.9	−2.3	0.0	−3.3	−0.9
	ΔE_{oi}	−10.0	−11.3	−10.8	−24.6	0.0	−40.2	−5.8
	ΔE_{Pauli}	+22.6	+22.9	+22.4	+45.2	0.0	+90.4	+0.4
	ΔV_{elstat}	−15.5	−16.5	−16.5	−33.7	0.0	−61.9	−3.8
	ΔE_{disp}	−4.6	−4.7	−4.7	−9.3	−0.1	−18.5	0.0
	$\Delta E_{int}(G_n)$	−7.5	−9.6	−9.6	−22.4	−0.1	−30.3	−9.2
Br-G_4	ΔE_{oi}^{σ}	−20.2	−23.0	−22.0	−51.5	−0.1	−81.1	−13.7
	ΔE_{oi}^{π}	−1.8	−2.0	−2.1	−5.2	0.0	−7.1	−2.0
	ΔE_{oi}	−22.0	−25.0	−24.2	−56.8	−0.1	−88.1	−15.6
	ΔE_{Pauli}	+47.6	+48.4	+46.8	+95.0	0.0	+190.6	+0.4
	ΔV_{elstat}	−32.6	−35.5	−34.7	−71.2	−0.3	−131.0	−8.3
	ΔE_{disp}	−6.3	−6.4	−6.4	−12.7	−0.2	−25.5	0.0
	$\Delta E_{int}(G_n)$	−13.2	−18.6	−18.6	−45.7	−0.6	−54.0	−23.5
I-G_4	ΔE_{oi}^{σ}	−23.2	−27.0	−27.5	−61.1	−0.1	−93.0	−18.3
	ΔE_{oi}^{π}	−2.4	−2.6	−2.7	−6.2	0.0	−9.5	−1.7
	ΔE_{oi}	−25.6	−29.5	−30.2	−67.3	−0.1	−102.4	−20.0
	ΔE_{Pauli}	+55.2	+55.8	+55.5	+111.4	0.0	+221.0	+1.4
	ΔV_{elstat}	−39.0	−42.1	−41.2	−83.0	−0.9	−157.7	−6.3
	ΔE_{disp}	−8.3	−8.6	−8.6	−16.8	−0.3	−33.7	0.0
	$\Delta E_{int}(G_n)$	−17.6	−24.4	−24.4	−55.8	−1.3	−72.9	−24.9

[a] See Equations 2.11, 2.13, 9.1 and 9.2, and Figures 9.5 and 9.6a. "G/G" represents a pair of diagonally oriented bases.

and −20.0 kcal mol^{-1} for Cl-G_4, Br-G_4 and I-G_4, respectively. The latter originates almost exclusively from the charge transfer orbital interactions in the σ electron system (−5.0, −13.7 and −18.3 kcal mol^{-1} for Cl-G_4, Br-G_4 and I-G_4, respectively), with only minor con-

tributions stemming from synergy in the resonance assistance of the π electron system (see Table 9.3). Therefore, one can conclude that the cooperativity leading to the enhanced stability of the X-G_4 quartets does not stem from resonance assistance.

The synergy in the σ electron system is, for Br-G_4 and I-G_4, even larger than for the natural G_4, for which it amounts to –8.2 kcal mol^{-1}. This is, again, in good agreement with previous results on halogen-bonded complexes (see chapter 8), where it was shown that, upon going from fluorine to iodine bonds, the orbital interactions become more important due to a lower acceptor orbital on the halogen-donating fragment. This can lead to an even larger covalent character for halogen bonds than for the analogous hydrogen bonds.

We have analyzed the electron density for all guanine quartets G_4 and X-G_4, except F-G_4, which is essentially not bound. The analyses provide a straightforward explanation for the cooperativity in halogen-bonded quartets: the donor-acceptor orbital interactions associated with the ΔE_{oi}^{σ} term, induce a charge separation, which in turn enhances both the orbital interactions and the electrostatic attraction with an additional *N*-halo-guanine base. The donor-acceptor interactions between antibonding σ^*_{N-X} acceptor orbitals of the N–X moiety on one X-G and N and O lone pair orbitals on a second X-G lead to a slight but important charge transfer in the resulting X-G_2 complex (see Figure 9.6b). The former X-G base builds up a net negative charge of –140, –270 and –254 milli-electrons for X = Cl, Br, and I, respectively, and the latter base builds up a net positive charge of +140, +270, +254 milli-electrons, respectively (with slightly less charge accumulation for X = I due to backdonation, which we will address later). As a consequence, the orbitals in the former Cl-G base in Cl-G_2 are destabilized due to the net negative charge, making the N and O lone pair orbitals better partners in the donor-acceptor interactions with a third X-G base (see Figure 9.7). The energy of the N and O lone pair orbital (σ HOMO) rises from –6.3 eV in Cl-G to –5.5 eV in Cl-G_2. Also for the fragments of Br-G_4 and I-G_4 a rise of about 1 eV of the σ HOMO is observed upon going from X-G to X-G_2. (see Table 9.5). Likewise, the orbitals on the other X-G base in X-G_2 are stabilized by the net positive charge, making the σ^*_{N-X} orbitals better partners for donor-acceptor interactions with a third X-G base (see Figure 9.7). In the case of Cl-G, for example, the energy of the N–Cl antibonding acceptor orbital (σ LUMO) decreases from –3.2 eV in Cl-G to –3.5 eV in Cl-G_2. These findings are further strengthened by analyses of the orbital populations, which indicate steadily stronger donor-acceptor interactions occurring in X-G_2, X-G_3 and X-G_4, as well as from chlorine- to bromine- to iodine-bonding guanine fragments. For Br-G_4, for example, the combined population of both σ^*_{N-Br} acceptor orbitals increases monotonically

Table 9.4 Energy decomposition analyses (in kcal mol^{-1}) for the formation of hydrogen-bonded and halogen-bonded Xan_4 from Xan_{n-1} + Xan in C_{4h} symmetry.[a]

		Xan_2	Xan_3	Xan_3^*	Xan_4	Xan/Xan	ΔE_{sum}	ΔE_{syn}
Xan_4	ΔE_{oi}^{σ}	−16.6	−16.8	−16.9	−34.0	−0.1	−66.6	−0.8
	ΔE_{oi}^{π}	−2.2	−2.2	−2.3	−4.2	0.0	−8.8	+0.2
	ΔE_{oi}	−18.8	−19.0	−19.2	−38.2	−0.1	−75.4	−0.6
	ΔE_{Pauli}	+31.7	+31.7	+31.9	+63.3	+0.1	+127.2	−0.4
	ΔV_{elstat}	−26.6	−26.7	−26.7	−53.5	0.0	−106.4	−0.5
	ΔE_{disp}	−4.2	−4.4	−4.4	−8.6	−0.2	−17.3	0.0
	$\Delta E_{int}(Xan_n)$	−17.9	−18.5	−18.5	−37.0	−0.2	−71.9	−1.5
F-Xan_4	ΔE_{oi}^{σ}	−0.8	−0.8	−0.8	−1.6	0.0	−3.1	−0.1
	ΔE_{oi}^{π}	−0.1	−0.1	−0.1	−0.2	0.0	−0.4	−0.1
	ΔE_{oi}	−0.9	−0.9	−0.9	−1.8	0.0	−3.5	−0.1
	ΔE_{Pauli}	+1.9	+1.9	+1.9	+3.9	0.0	+7.8	0.0
	ΔV_{elstat}	−0.6	−0.2	−0.2	−0.9	+0.5	−1.3	−0.3
	ΔE_{disp}	−1.3	−1.4	−1.4	−2.7	0.0	−5.4	0.0
	$\Delta E_{int}(Xan_n)$	−0.8	−0.5	−0.5	−1.6	+0.4	−2.4	−0.5
Cl-Xan_4	ΔE_{oi}^{σ}	−4.5	−4.5	−4.6	−9.2	0.0	−18.1	−0.1
	ΔE_{oi}^{π}	−0.5	−0.5	−0.5	−1.0	0.0	−2.1	0.0
	ΔE_{oi}	−5.0	−5.0	−5.1	−10.2	0.0	−20.2	−0.1
	ΔE_{Pauli}	+12.3	+12.3	+12.3	+24.6	0.0	+49.4	−0.1
	ΔV_{elstat}	−9.7	−9.6	−9.5	−19.4	+0.1	−38.4	−0.2
	ΔE_{disp}	−4.1	−4.2	−4.2	−8.3	−0.1	−16.5	0.0
	$\Delta E_{int}(Xan_n)$	−6.5	−6.5	−6.5	−13.2	−0.1	−25.7	−0.4
Br-Xan_4	ΔE_{oi}^{σ}	−9.7	−9.7	−9.8	−19.7	0.0	−38.7	−0.4
	ΔE_{oi}^{π}	−1.1	−1.1	−1.2	−2.2	0.0	−4.6	0.0
	ΔE_{oi}	−10.8	−10.9	−11.0	−22.0	0.0	−43.3	−0.3
	ΔE_{Pauli}	+24.9	+24.8	+24.9	+49.7	0.0	+99.6	−0.2
	ΔV_{elstat}	−18.7	−18.8	−18.7	−37.5	0.0	−74.7	−0.3
	ΔE_{disp}	−5.8	−5.9	−5.9	−11.7	−0.1	−23.3	0.0
	$\Delta E_{int}(Xan_n)$	−10.4	−10.7	−10.7	−21.5	−0.1	−41.7	−0.8
I-Xan_4	ΔE_{oi}^{σ}	−9.8	−9.9	−10.0	−20.0	0.0	−39.3	−0.4
	ΔE_{oi}^{π}	−1.3	−1.3	−1.4	−2.6	0.0	−5.3	+0.1
	ΔE_{oi}	−11.1	−11.2	−11.3	−22.6	0.0	−44.6	−0.3
	ΔE_{Pauli}	+26.5	+26.4	+26.5	+52.8	0.0	+106.0	−0.3
	ΔV_{elstat}	−20.5	−20.7	−20.6	−41.2	−0.1	−82.2	−0.2
	ΔE_{disp}	−7.3	−7.5	−7.5	−14.7	−0.2	−29.5	0.0
	$\Delta E_{int}(Xan_n)$	−12.4	−12.9	−12.9	−25.7	−0.3	−50.3	−0.8

[a] See Equations 2.11, 2.13, 9.1 and 9.2, and Figures 9.5 and 9.6a. "Xan/Xan" represents a pair of diagonally oriented bases.

from 0.20 electrons when two Br-G fragments interact, to 0.22 and 0.26 electrons when the third and fourth fragment are added, respectively.

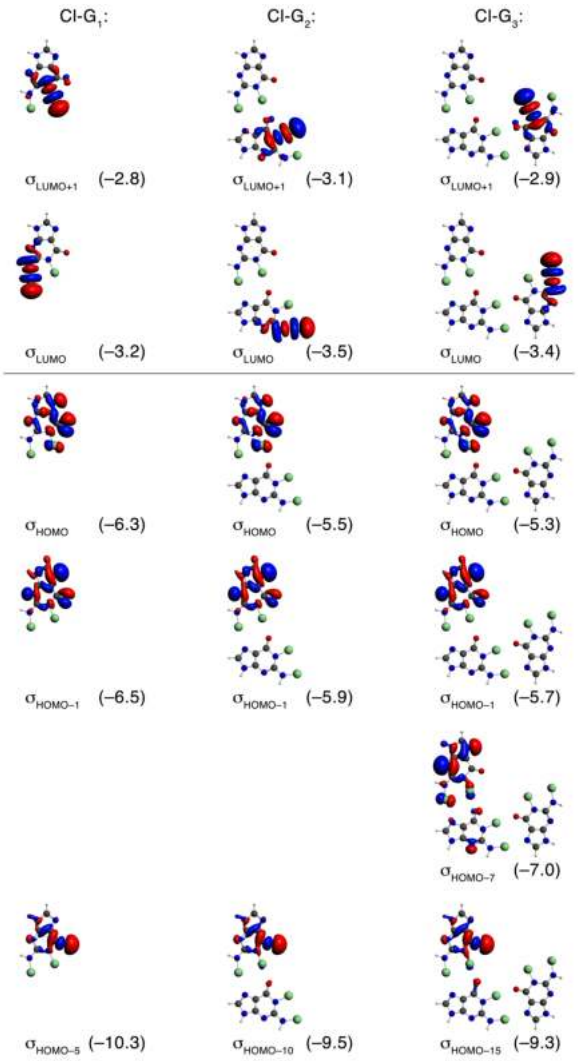

Figure 9.7 Electron-accepting lowest unoccupied molecular orbitals (LUMOs, above separator) and electron-donating highest occupied molecular orbitals (HOMOs, below separator) with their energies (in eV) of the σ electron system on the fragments of the C_{4h}-symmetric Cl-G_4 quartet (see Figure 9.6a).

We now return to the perturbed trend in VDD charges for the iodine-bonded complexes, as shown in Figure 9.6b. The charge separation does not increase significantly from I-G_2 to I-G_3 due to the occurrence of bidirectional charge transfer. The combined population of both σ^*_{N-I} acceptor orbitals on the n^{th} I-G fragment along I-G_2, I-G_3 and I-G_4

Table 9.5 Orbital energies (in eV) of the relevant HOMOs and LUMOs in the σ electron system of the fragments of C_{4h}-symmetric G_4 and X-G_4 (see Figures 9.6a and 9.7).

	G		G_2		G_3	
G_4	σ_{LUMO+3}	+0.8	σ_{LUMO+5}	+0.4	σ_{LUMO+6}	+0.6
	σ_{LUMO+2}	+0.1	σ_{LUMO+2}	−0.3	σ_{LUMO+3}	−0.1
	σ_{LUMO}	−1.1	σ_{LUMO}	−1.4	σ_{LUMO}	−1.2
	σ_{HOMO}	−5.7	σ_{HOMO}	−4.6	σ_{HOMO}	−4.3
	σ_{HOMO-1}	−6.1	σ_{HOMO-1}	−5.2	σ_{HOMO-1}	−5.0
	–		σ_{HOMO-2}	−6.4	σ_{HOMO-3}	−6.2
	σ_{HOMO-3}	−9.7	σ_{HOMO-6}	−8.6	σ_{HOMO-9}	−8.4
Cl-G_4	σ_{LUMO+1}	−2.8	σ_{LUMO+1}	−3.1	σ_{LUMO+1}	−2.9
	σ_{LUMO}	−3.2	σ_{LUMO}	−3.5	σ_{LUMO}	−3.4
	σ_{HOMO}	−6.3	σ_{HOMO}	−5.5	σ_{HOMO}	−5.3
	σ_{HOMO-1}	−6.5	σ_{HOMO-1}	−5.9	σ_{HOMO-1}	−5.7
	–		–		σ_{HOMO-7}	−7.0
	σ_{HOMO-5}	−10.3	$\sigma_{HOMO-10}$	−9.5	$\sigma_{HOMO-15}$	−9.3
Br-G_4	σ_{LUMO+1}	−3.5	σ_{LUMO+1}	−4.0	σ_{LUMO+1}	−4.0
	σ_{LUMO}	−4.2	σ_{LUMO}	−4.6	σ_{LUMO}	−4.6
	σ_{HOMO}	−6.0	σ_{HOMO}	−5.0	σ_{HOMO}	−4.6
	–		–		σ_{HOMO-1}	−5.2
	σ_{HOMO-1}	−6.4	σ_{HOMO-1}	−5.5	σ_{HOMO-2}	−5.3
	–		–		σ_{HOMO-5}	−6.4
	σ_{HOMO-5}	−10.1	$\sigma_{HOMO-10}$	−9.1	$\sigma_{HOMO-14}$	−8.8
I-G_4	σ_{LUMO+1}	−3.7	σ_{LUMO+1}	−4.1	σ_{LUMO+1}	−4.0
	σ_{LUMO}	−4.6	σ_{LUMO}	−4.8	σ_{LUMO}	−4.6
	σ_{HOMO}	−5.7	σ_{HOMO}	−4.8	σ_{HOMO}	−4.6
	σ_{HOMO-1}	−6.3	σ_{HOMO-1}	−5.5	σ_{HOMO-2}	−5.3
	–		σ_{HOMO-2}	−5.7	σ_{HOMO-3}	−5.5
	–		σ_{HOMO-5}	−6.8	σ_{HOMO-6}	−6.5
	σ_{HOMO-5}	−10.0	$\sigma_{HOMO-10}$	−9.1	$\sigma_{HOMO-15}$	−8.9
	–		$\sigma_{HOMO-11}$	−9.5	$\sigma_{HOMO-16}$	−9.3

increases from 0.23 to 0.31 to 0.38 electrons, respectively. This indicates that there is an even larger charge transfer than in the bromine-bonded complexes, which is consistent with previous results (discussed in chapter 8) and the stronger cooperativity that we observe. However, the VDD charges of the fragments in Figure 9.6b do not show an increased charge separation upon going from I-G_2 (±254) to I-G_3 (±255), because the charges as revealed by the VDD analyses are partially quenched due to donor-acceptor interactions running in opposite direction: there is, besides the charge transfer from I-G_{n-1} to I-G, also

charge transfer from I-G to I-G_{n-1}. This is because the σ HOMO on I-G and the σ LUMO on I-G_{n-1} are more delocalized over the molecular fragments and therefore overlap, which does not happen for the natural G_4 or the other X-G_4 quartets.

Thus, cooperativity becomes more pronounced every time an additional X-G base is added because such an addition will amplify the charge separation, and thereby the donor-acceptor interactions (see Figure 9.6 and 9.7). The strongest synergy is found when the fourth and last *N*-halo-guanine base of X-G_4 is introduced, because this quenches the electrostatically unfavorable charge separation in the X-G_3 fragment.

9.5 Conclusions

The computational experiment presented in this chapter, in which we evoked cooperativity in hydrogen- and halogen-bonded compounds, clearly demonstrates the resemblance between halogen and hydrogen bonds. The equivalence between RAHB and RAXB in natural and *N*-halo-guanine quartets is proven by the existence of a small amount of resonance assistance in the π electron system, and significant charge transfer that occurs with donor-acceptor orbital interactions in the σ electron system, from N and O lone pair orbitals on one X-G base to σ^*_{N-H} or σ^*_{N-X} acceptor orbitals on the other X-G base. Thus, whereas the covalency in hydrogen bonds was previously demonstrated by the cooperativity in natural G_4, the even stronger charge transfer present in halogen bonds has now been demonstrated in a similar way. This larger covalent component was already revealed in chapter 8, but within this chapter it is demonstrated that the previously presented description for strong, charge-assisted hydrogen bonds and halogen bonds is equally valid for larger, uncharged, and less strongly bonding model systems. Notably, this is achieved using unambiguous quantities, namely the interaction energy and the density deformation. A physical interpretation of the results has been accomplished using Kohn-Sham MO theory, supported by, but not depending on, a quantitative interaction energy decomposition scheme.

10 Summary

This thesis consists of theoretical studies on various aspects of the oxidative addition reaction, as well as the mechanism of halogen bonding interactions. As stated in the introduction, the purpose of these studies was to not only be descriptive, but to provide insights and reveal causal relationships. Therefore, the following summary will discuss only the most important findings from the preceding chapters, in order to focus on their explanatory character.

All results are obtained using density functional theory (DFT) computations performed with the ADF software package. A red thread throughout this thesis is the interpretation of the numerical results using a combined approach of the activation strain model and molecular orbital (MO) theory. Within the activation strain model (discussed in section 2.5), the energy change that accompanies a chemical process is analyzed in terms of the original reactants. The relative energy is split into two terms: (i) the strain energy that accounts for the geometrical changes that occur during the chemical process, and (ii) the interaction energy between the deformed fragments. Both the strain energy and the interaction energy can be further analyzed using MO theory.

In chapter 3 this approach is used to understand why some d^{10}-ML_2 transition metal complexes have nonlinear equilibrium geometries, that is, bent L–M–L angles, instead of the generally expected linear L–M–L angles. We have investigated the ML_2 complexes where M is varied along Co^-, Rh^-, Ir^-, Ni, Pd, Pt, Cu^+, Ag^+ and Au^+, and the ligands L are varied along NH_3, PH_3 and CO. Based on detailed analyses of the bonding between an ML fragment and a second ligand L, we have traced back the origin of this nonlinearity to π backdonation: when the second ligand L binds to ML perpendicular to the first ligand, its π^* acceptor orbitals interact with d orbitals on the metal that are not yet stabilized by interactions with the first ligand. These d orbitals are therefore higher in energy, resulting in more strongly stabilizing d-π^* donor-acceptor interactions than in the linear L–M–L

geometry. When this additional stabilization is stronger than the induced steric repulsion upon bending, the ML_2 complex obtains a nonlinear L–M–L angle.

In practice, however, catalyst complexes often feature bulkier ligands. Therefore, we have addressed in chapter 4 the effect of steric bulk on the geometry and activity of a series of $Pd(PR_3)_2$ catalyst complexes, where the substituents R are varied along H, Me, *i*Pr (isopropyl), *t*Bu (*tert*-butyl), Cy (cyclohexyl) and Ph (phenyl). From $Pd(PH_3)_2$ to $Pd(PtBu_3)_2$, we find that all complexes have linear L–M–L angles, except $Pd(PiPr_3)_2$ for which it is bent slightly. More interestingly, we find significantly nonlinear L–M–L angles in both $Pd(PCy_3)_2$ and $Pd(PPh_3)_2$. These small angles can not be explained satisfactorily with the electronic mechanism described in chapter 3, although this mechanism does contribute to the flexibility of these complexes. Our analyses show that ligands that are large but to some extent flat (instead of isotropically bulky) build up relatively strong dispersion interactions between their large surfaces ("sticky pancakes") when they bend toward each other. The resulting stabilization, a form of steric attraction, favors bending and thus enhances the flexibility of the bite angle, eventually leading to nonlinear ligand-metal-ligand angles. When methane C–H oxidative addition to these catalyst complexes is investigated, the more flexible, or even nonlinear geometry of these complexes appears to translate into lower reaction barriers.

Chapter 5 discusses yet another series of palladium bisphosphine catalysts, but now the substituents are varied from hydrogen in PH_3, to halogens in the series of PX_3 ligands, where X = F, Cl, Br or I. This series allows to study simultaneously the electronic effects, as described in chapter 3, and the steric effects as described in chapter 4, since both the size and the electronegativity of the substituents is changing significantly. Although $Pd(PH_3)_2$ is linear, all halogenated $Pd(PX_3)_2$ catalyst complexes have nonlinear ligand-metal-ligand angles. Counterintuitively, we also find that, as the size of the halogens increases, the complexes become more bent. This trend originates partly from the attractive dispersion interactions between the ligands, revealing again a contribution from steric attraction. But, besides this steric effect, also the electronic factors have to be taken into account. All halogenated PX_3 ligands are better π acceptors than PH_3, which results in improved π backbonding and nonlinear ligand-metal-ligand angles in the $Pd(PX_3)_2$ complexes. However, our analyses reveal another electronic factor, namely the repulsive overlap between the highest occupied MOs (HOMOs) on the PX_3 and $PdPX_3$ fragments. When the substituents X are varied from F to I, the repulsive HOMO-HOMO overlap decreases, resulting

in less destabilizing Pauli repulsion upon bending the $Pd(PX_3)_2$ complexes, and therefore more strongly bent equilibrium geometries.

Applying the $Pd(PX_3)_2$ complexes for the oxidative addition of the methane C–H bond, we find very similar reaction barriers as for the archetypal $Pd(PH_3)_2$. Activation strain analyses reveal a similar bite-angle effect as described in chapter 4, but also show that this is counteracted by a simultaneous weakening of the catalyst-substrate interaction as one goes from $Pd(PH_3)_2$ to $Pd(PX_3)_2$, and along the $Pd(PX_3)_2$ series as X is varied from F to I. The weaker interaction is a direct result of (i) a decreased electron-donating capability of the catalyst, and (ii) an increase in repulsive catalyst-substrate interactions.

For chapters 6 and 7, we return to the same series of d^{10}-ML_n catalyst complexes that were the subject of chapter 3. In chapter 6, the reactivity of these complexes towards methane oxidative addition is investigated. It is shown that, when going from the anionic group 9 metal complexes to the cationic group 11 metal complexes, reaction barriers go up significantly, due to the decreased electron-donating capability of the catalysts, and therefore weaker catalyst-substrate donor-acceptor interaction. When going from first row to third row transition metal centers, the highest reaction barrier is typically found for the catalyst with a metal center from the second transition metal row. For catalyst complexes with a metal center from the first row the reaction barrier is generally lower, because the d-derived orbital energies of these complexes are higher, leading to stronger donation from catalyst to substrate. When, instead, a catalyst complex with a metal center from the third row is compared to a second transition metal row complex, it is the larger orbital overlap of the former with the substrate σ^* orbital that results in stronger interactions, and consequently a lower reaction barrier. Also relativistic effects become important for third row transition metals. These tend to stabilize the electron-accepting metal s orbital, thereby further enhancing catalyst-substrate interaction.

Ligand effects can be explained by considering their influence on the electron-donating and electron-accepting capabilities of the metal center. Adding a good π-accepting ligand reduces the electron-donating capability of the metal center, whereas a strong σ-donating ligand will enhance the electron-donating capability. To correctly predict how this will affect reaction barriers, we have introduced in chapter 6 the concept of electronic regimes. In what we designate the 'd regime', ligand effects are dictated by their influence on the metal d orbitals. In this regime, reaction barriers become higher when π-accepting ligands are attached to the metal, as these reduce the electron-donating capability of the catalyst. In the 's regime' the reactivity of the catalyst depends to a large extent

on the electron-accepting capability of the s orbital. Adding a strong π-accepting ligand to an s-regime catalyst enhances its electron-accepting capability, and lowers the reaction barrier. It follows that ligands can have completely opposite effects on the reaction barrier, when added to metal centers from different electronic regimes.

Furthermore, in chapter 6 we elaborated on the concept of bite-angle flexibility. We have shown that, for the complexes for which we encountered nonlinear ligand-metal-ligand angles in chapter 3, the reaction barrier for oxidative addition of methane is lowered, due to the smaller amount of catalyst deformation that is required to bend away its ligands. More interestingly, however, we find a similar effect along series of catalysts that all have linear ligand-metal-ligand angles in their equilibrium geometry, but become more flexible towards bending.

In chapter 7, the reaction barriers have been analyzed for oxidative addition of ethane, via activation of either the C–H or the C–C bond. For both bonds, the trends in reaction barriers are very similar to those described for activation of the methane C–H bond in chapter 6. However, there are subtle differences between these bonds, which influence the interaction of the substrates with the catalysts. A detailed understanding of these differences, and the nature of the catalyst-substrate interactions, allowed us to devise catalyst complexes that selectively activate either bond. Thus, starting with the ethane C–H and C–C bonds, activation of the latter usually occurs with a higher reaction barrier, despite the fact that it is weaker. This is due to a delay in the build-up of stabilizing interactions, caused by the additional nodal plane present in the σ^*_{C-C} orbital, compared to the σ^*_{C-H} orbital, which diminishes favorable overlap with the donating metal d orbitals. To shift the selectivity towards activation of the weaker C–C bond, this effect has to be mitigated, which can be achieved by applying a catalyst complex from the s regime, for which donation into the σ* orbitals plays only a moderate role.

To distinguish between the methane and ethane C–H bonds, a similar approach is taken. The ethane C–H bonds are slightly weaker than the methane C–H bonds, but, upon stretching, the methane σ^*_{C-H} LUMO drops faster in energy than the ethane σ^*_{C-H} LUMO. Thus, we found that strongly donating d-regime catalysts prefer activation of the methane C–H bond, because the lower σ^*_{C-H} orbital energy leads to a strengthening of the catalyst-substrate interaction that is significant enough to overcome the higher bond dissociation energy. For s-regime catalysts, the difference between the interaction energy curves for activation of the methane and ethane C–H bonds is smaller, and these catalysts therefore prefer ethane C–H activation, as dictated by the lower strain energy.

The final two chapters of this thesis deal with the bonding mechanism of halogen bonds. Chapter 8 contains detailed analyses of the hydrogen bonds in DH···A^- and halogen bonds in DX···A^- where D, X and A are varied along the halogens F, Cl, Br and I. Consistent comparisons of variations along series of both types of complexes revealed that hydrogen bonds and halogen bonds arise due to a very similar bonding mechanism, which is easily explained in the framework of MO theory. Both halogen bonds and hydrogen bonds have, besides an electrostatic component, a sizable covalent component that originates from charge transfer from the halide lone pair to the DX or DH σ^* orbital. The electrostatic component is usually stronger for hydrogen bonds, due to the more favorable polarization along the DH hydrogen halide, compared to the dihalogen DX. Nevertheless, halogen bonds can be stronger than hydrogen bonds, because of a stronger contribution from the covalent component to the bonding energy. The reason for this is that the empty σ^* orbital on DX is lower in energy than the σ^* orbital on the hydrogen halides DH.

By consistent variation of either D, X or A, and considering how this affects the electronic structure of the fragment, the change in bonding characteristics of DH···A^- and DX···A^- can be readily explained. For example, replacing A^- with a heavier halide, reduces the strength of both the hydrogen bonds and halogen bonds, in part because the electron-donating capability of the halide decreases when going down the periodic table. This is true also for the fluorine-bonded complexes, although the final trend in bond strength is reversed due to a subtle interplay of factors, which are related to the significant stretch of the relatively weak D–F bonds and the low energy of the σ^*_{D-F} acceptor orbitals.

Variation of the hydrogen- or halogen-donating atom D has opposite effects on the bond strength of the hydrogen bonds and halogen bonds. However, activation strain analyses along the bond formation process reveal that the strain and interaction energies follow the same trends as D becomes heavier. The interaction energy weakens, because the increased electropositivity of D results in a less favorable polarization of the electron density across DH or DX, thereby reducing the electrostatic attraction with A^-, and, mainly for the halogen bonds, also strengthening the Pauli repulsion. Simultaneously, the strain energy curves soften, because the D–H and D–X bonds get weaker when D becomes heavier. For the DX fragments, these differences are moderate, and the total bond strength therefore follows the same trend as the interaction energy. The differences in D–H bond strength are, however, much larger. From FH to IH, the D–H stretch upon hydrogen bond formation increases significantly, which allows for a greater build-up of interaction energy, and induc-

es a reversal of the net bond strength: hydrogen bonds DH···A$^-$ become stronger when the donating atom D is varied from F to I.

In the ninth chapter, halogen bonds are again compared to hydrogen bonds, but for significantly larger complexes. Starting from the hydrogen-bonded Watson-Crick DNA base pairs, the hydrogen bonding N–H moieties are replaced with N–X, where X is one of the halogens F, Cl, Br or I, to obtain the halogen-bonded analogues. We have demonstrated that, again, the hydrogen bonds and halogen bonds in these complexes arise due to a very similar mechanism, which involves charge transfer from the N or O lone pair to the σ^* orbitals on N–H or N–X. The similarities not only showed that the bonding mechanism as described in chapter 8 is equally valid for larger complexes, but also suggested that the cooperative effect, as observed in hydrogen-bonded guanine quartets, might also occur in halogen-bonded *N*-halo-guanine quartets. Our computations show that this is indeed the case, that is, the total bond energy of the *N*-halo-guanine quartets is more stabilizing than four times the bond energy of one *N*-halo-guanine base pair. Interestingly, for the bromine-bonded and iodine-bonded guanine quartets, this cooperative effect is even stronger than for the hydrogen-bonded guanine quartets, due to the larger amount of charge transfer that occurs upon formation of these halogen bonds. These conclusions are supported by multiple independent lines of reasoning, based upon a variety of analysis methods.

One can only hope that in the future the insights obtained from the studies in this thesis will contribute to the achievement of new milestones, based on an improved understanding of the chemistry involved. It is most likely that the concepts presented in this thesis will have to be extended, and, when necessary, even be replaced with superior concepts. This process is one of the fundamental pillars of science, and one of the prime reasons why it is such a powerful tool: the scientific method is the only possible way to improve our understanding of natural phenomena. And it has proven to be a very successful one, although only if applied critically.

11 Samenvatting

Chemische Binding en Katalyse
Moleculair-Orbitaalperspectieven op Katalysatorontwerp en Halogeenbruggen

Dit proefschrift omvat theoretisch onderzoek naar verschillende aspecten van de oxidatieve-additiereactie, alsmede naar het bindingsmechanisme van halogeenbruggen. In de introductie is reeds vermeld dat deze studies als doel hebben om niet uitsluitend beschrijvend van aard te zijn, maar ook te voorzien in diepere inzichten, en causale verbanden aan te geven. Deze samenvatting zal daarom uitsluitend de hoofdlijnen en belangrijkste algemene bevindingen vermelden, zodat de aandacht zoveel mogelijk op het verklarende karakter kan worden gevestigd.

Alle resultaten zijn verkregen met behulp van berekeningen op basis van dichtheidsfunctionaaltheorie (DFT), uitgevoerd met het softwarepakket ADF. Een belangrijk onderdeel van dit proefschrift is de interpretatie van de numerieke gegevens die met deze berekeningen zijn verkregen, met behulp van een combinatie van het activeringsspanningsmodel en de moleculair-orbitaaltheorie. Binnen het activeringsspanningsmodel (beschreven in paragraaf 2.5), wordt de verandering in energie, die gepaard gaat met een chemische reactie, geanalyseerd met de karakteristieken van de reactanten als uitgangspunt. Daarvoor wordt de energieverandering opgedeeld in twee componenten: de spanningsenergie en de interactie-energie. De eerste van deze twee termen vindt zijn oorsprong in de verandering van de moleculaire geometrie van de reactanten, de tweede term is het resultaat van de wisselwerkingen die plaatsvinden tussen de vervormde reactanten. Beide termen kunnen vervolgens afzonderlijk uitvoeriger worden geanalyseerd met behulp van moleculair-orbitaaltheorie.

In hoofdstuk 3 is deze methodologie toegepast met het doel te begrijpen waarom enkele overgangsmetaalcomplexen d^{10}-ML_2 een niet-lineaire 'bite angle' hebben, oftewel een gebogen L–M–L-hoek, in plaats van de gebruikelijke lineaire L–M–L hoek. De serie

ML_2-complexen wordt gevormd met M één van de metalen Co^-, Rh^-, Ir^-, Ni, Pd, Pt, Cu^+, Ag^+ of Au^+, en de liganden L zijn NH_3, PH_3 ofwel CO. Onze gedetailleerde analyses van de binding tussen een ML-fragment, en een tweede ligand L tonen aan dat de niet-lineaire geometrie voortkomt uit een toename in π-terugdonatie: als het tweede ligand L zodanig aan ML bindt dat de hoek L–M–L loodrecht is, dan overlappen de accepterende π*-banen met d-orbitalen van het metaal die niet zijn gestabiliseerd door de binding met het andere ligand. Deze d-orbitalen hebben zodoende een hogere energie, hetgeen resulteert in een sterkere stabilisatie door donor-acceptorinteracties dan met een geometrie met een lineaire L–M–L-hoek het geval zou zijn. Indien deze toename in stabilisatie sterker is dan de toename in sterische repulsie, dan resulteert dit in een niet-lineaire geometrie.

In de praktijk worden echter katalysatoren gebruikt met omvangrijkere liganden. In hoofdstuk 4 is daarom bestudeerd wat het effect is van deze grotere liganden op zowel de geometrie als op de activiteit van een aantal katalysatorcomplexen $Pd(PR_3)_2$, met als substituenten R waterstof (H), methyl (Me), isopropyl (*i*Pr), *tert*-butyl (*t*Bu), cyclohexyl (Cy) of fenyl (Ph). Van $Pd(PH_3)_2$ tot $Pd(PtBu_3)_2$ hebben alle complexen lineaire L–M–L-hoeken, behalve het licht gebogen $Pd(PiPr_3)_2$. Interessanter is echter dat $Pd(PCy_3)_2$ en $Pd(PPh_3)_2$ vrij sterk gebogen L–M–L-hoeken blijken te hebben. Het electronische mechanisme, zoals beschreven in hoofdstuk 3, kan dit niet voldoende verklaren, al levert het wel een belangrijke bijdrage aan de flexibiliteit van deze metaalcomplexen. Onze analyses tonen aan dat tussen liganden van vrij forse omvang, maar die toch enigszins plat zijn (in tegenstelling tot isotropisch omvangrijk), relatief sterke dispersie-interacties kunnen optreden als ze naar elkaar toe worden gebogen. Deze dispersie-interacties tussen de contactoppervlakken van de liganden ("plakkerige pannenkoeken"), zijn een vorm van sterische attractie en stabiliseren het metaalcomplex wanneer dit gebogen wordt. Daaruit blijkt, enigszins contra-intuïtief, dat grotere liganden kunnen leiden tot een toename in de flexibiliteit van de L–M–L-hoek (de 'bite-angle flexibility'), en zelfs tot evenwichtsgeometrieën waarin deze hoek gebogen is. In oxidatieve-additiereacties speelt dit effect een aanzienlijke rol. Doordat de complexen minder ver hoeven te worden gebogen of omdat dit buigen door de grotere flexibiliteit minder energie vergt, zijn de reactiebarrières voor deze katalysatoren lager.

In hoofdstuk 5 wordt opnieuw een serie palladiumkatalysatoren onder de loep genomen, maar deze keer betreft het een vergelijking van $Pd(PH_3)_2$ met de serie $Pd(PX_3)_2$, waarbij X één van de halogenen F, Cl, Br of I is. Deze substituenten variëren sterk in electronegativiteit en in omvang, en zodoende kan met deze serie katalysatorcomplexen de wisselwerking tussen de electronische eigenschappen (zoals beschreven in hoofdstuk 3) en de

sterische eigenschappen (zoals beschreven in hoofdstuk 4) worden onderzocht. Hoewel $Pd(PH_3)_2$ een lineaire L–M–L-hoek heeft, blijkt deze hoek in de gehalogeneerde complexen niet lineair te zijn. Ook blijkt opnieuw dat, naarmate de substituenten toenemen in grootte, de complexen meer gebogen zijn. Uit onze analyses blijkt wederom dat deze trend deels wordt veroorzaakt door de attractieve dispersie-interacties tussen de liganden, hetgeen opnieuw duidt op een vorm van sterische aantrekking. De analyses tonen daarnaast ook aan dat de electronische effecten een belangrijke rol spelen. Alle halogeengesubstitueerde liganden zijn betere π-acceptoren dan het archetypische PH_3-ligand, en dat resulteert in gebogen $Pd(PX_3)_2$-complexen, terwijl $Pd(PH_3)_2$ een lineaire L–M–L-hoek heeft. Echter, de reden dat van $Pd(PF_3)_2$ naar $Pd(PI_3)_2$ de complexen sterker gebogen zijn, is de afname in repulsieve overlap van de hoogst gelegen bezette orbitalen van het $PdPX_3$- en het PX_3-fragment.

Wanneer de gehalogeneerde complexen $Pd(PX_3)_2$ als katalysator worden toegepast voor de oxidatieve additie van methaan, blijkt dat de barrières niet veel verschillen van die van het archetypische $Pd(PH_3)_2$. Uit analyses op basis van het activeringsspanningsmodel volgt, in overeenstemming met de bevindingen in hoofdstuk 4, dat er minder energie nodig is voor het buigen van de katalysator indien die reeds enigszins gebogen is. Tegelijkertijd blijkt deze trend te worden tegengewerkt door een verzwakking van de interactie tussen de katalysator en het substraat, wanneer $Pd(PH_3)_2$ wordt vergeleken met de serie $Pd(PX_3)_2$, alsmede wanneer de halogeensubstituenten in $Pd(PX_3)_2$ worden gevariëerd van X naar I. Dit wordt ten eerste veroorzaakt door een afname in electrondonerende capaciteit van de katalysator, en ten tweede door een toename in repulsieve wisselwerkingen.

Voor de hoofdstukken 6 en 7 keren we terug naar de serie katalysatoren met formule d^{10}-ML_n, die het onderwerp waren van het derde hoofdstuk. Hoofdstuk 6 richt zich op de activiteit van deze complexen in de oxidatieve-additiereactie van methaan. De reactiebarrières blijken sterk toe te nemen als het metaal in de katalysator wordt gevariëerd van een negatief geladen metaal uit groep 9 naar een positief geladen metaal uit groep 11, vanwege de afname in electrondonerende capaciteit van de metaalcentra, en dus zwakkere donor-acceptorinteracties met het substraat. Afdalend in het periodiek systeem der elementen, vinden we typisch dat de katalysatoren met metaalcentra uit de tweede rij van overgangsmetalen de hoogste barrière hebben. Katalysatoren met metalen uit de eerste rij van overgangsmetalen hebben doorgaans hogere orbitaalenergieën, hetgeen een sterkere interactie met het substraat teweegbrengt en zodoende een lagere barrière. De metaalcentra uit de derde rij van overgangsmetalen zijn groter, en profiteren van een betere overlap van de

d-orbitalen met het σ*-orbitaal van het substraat, wat leidt tot een sterkere interactie en wederom een lagere barrière. Bovendien spelen voor deze metalen relativistische effecten een rol. Deze effecten stabiliseren het electronaccepterende s-orbitaal en versterken zodoende ook de interactie tussen de katalysator en het substraat.

Het effect van liganden kan worden verklaard aan de hand van hoe de electrondonerende en electronaccepterende eigenschappen van het metaal door de liganden worden beinvloed. Goede π-accepterende liganden reduceren de electrondonerende capaciteit van het metaal, terwijl sterk σ-donerende liganden de electrondonerende kracht van het metaal doen toenemen. Om op betrouwbare wijze te kunnen voorspellen welk effect dit heeft op de hoogte van reactiebarrières is het concept van electronische regimes geïntroduceerd. In het 'd-regime' wordt het effect van liganden bepaald door hoe de energie van de d-orbitalen van het metaal wordt beïnvloed. In dit regime worden activeringsbarrières hoger wanneer π-accepterende liganden binden aan het metaal, omdat deze de electrondonatie naar het substraat verminderen. In het 's-regime', daarentegen, is het belangrijker om het effect van de liganden op de energie van het s-orbitaal te beschouwen, omdat voor deze katalysatoren de electronaccepterende capaciteit een grote rol speelt. Als een sterk π-accepterend ligand bindt aan een metaal uit het s-regime, wordt het electronaccepterende vermogen van het metaal versterkt, wat leidt tot een verlaging van de reactiebarrière. Het blijkt dus dat liganden een volledig tegenovergesteld effect kunnen hebben op de activeringsbarrière, wanneer ze binden aan metalen uit verschillende electronische regimes.

Daarnaast komt in hoofdstuk 6 het concept van de 'bite-angle flexibility' opnieuw aan de orde. Onze analyses tonen aan dat de activeringsbarrières enigszins verlaagd zijn voor de katalysatoren die in hoofdstuk 3 een niet-lineaire L–M–L-hoek bleken te hebben. De reden hiervan is dat er minder energie nodig is om de liganden weg te buigen van het substraat. Een interessantere bevinding is echter dat we eenzelfde soort effect waarnemen bij series katalysatoren met evenwichtsgeometrieën waarin deze hoek lineair is, maar waarvan de flexibiliteit toeneemt en het buigen dus wordt vergemakkelijkt.

Hoofdstuk 7 bevat uitvoerige analyses van de activiteit van de katalysatoren in de oxidatieve additie van ethaan, zowel voor het activeren van de C–H-binding als van de C–C-binding. Voor beide bindingen blijken de trends grotendeels gelijk te zijn aan de trends beschreven in hoofdstuk 6 voor het activeren van de C–H-binding in methaan. De subtiele verschillen tussen deze bindingen hebben echter een verschillende uitwerking op de interactie van de katalysator met het substraat. Op basis van een nauwkeurig begrip van deze verschillen, alsmede van de aard van de wisselwerking tussen de katalysator en het substraat,

zijn we er in geslaagd om metaalcomplexen te vinden waarmee deze bindingen selectief kunnen worden geactiveerd. Uit een vergelijking van de bindingsactivering van de C–H- en C–C-bindingen in ethaan volgt dat activering van de C–C-binding in het algemeen gepaard gaat met hogere reactiebarrières, ondanks het feit dat deze binding zwakker is. Dit is het gevolg van een vertraagde ontwikkeling van de stabiliserende interactie tussen de katalysator en het substraat, veroorzaakt door de aanwezigheid van een extra knoopvlak in het σ^*_{C-C}-orbitaal, in vergelijking met het σ^*_{C-H}-orbitaal. Dit knoopvlak vermindert de overlap met de donerende orbitalen op het metaalcomplex. Om de selectiviteit naar de C–C-binding te verschuiven, is het noodzakelijk deze vertraging in de opbouw van interactie-energie te beperken. Dit is mogelijk door een s-regimekatalysator te kiezen, omdat voor deze katalysatoren de electrondonatie naar het σ^*-orbitaal slechts een geringe rol speelt.

Om selectief de C–H-binding in methaan, als wel in ethaan te verbreken, kan dezelfde strategie worden gebruikt. De C–H-bindingen in ethaan zijn enigszins zwakker dan die in methaan, maar bij oprekking daalt de energie van het σ^*-orbitaal van methaan sneller dan de energie van het σ^*-orbitaal van ethaan. Sterk electrondonerende d-regimekatalysatoren hebben daardoor een voorkeur voor het activeren van de C–H-binding in methaan, omdat de lagere energie van het σ^*-orbitaal de interactie-energie voldoende versterkt om de meer destabiliserende spanningscurve van deze binding te compenseren. Katalysatoren uit het s-regime hebben echter een vergelijkbare interactie-energiecurve voor beide C–H-bindingen en activeren zodoende de zwakkere binding in ethaan met een lagere barrière.

De laatste twee hoofdstukken van dit proefschrift hebben betrekking op het bindingsmechanisme van halogeenbruggen. In hoofdstuk 8 is dit mechanisme uitvoerig geanalyseerd voor zowel de waterstofbruggen in $DH\cdots A^-$, als de halogeenbruggen in $DX\cdots A^-$, waarbij D, X en A de halogenen F, Cl, Br en I kunnen zijn. Consistente vergelijkingen van beide interacties tonen aan dat het bindingsmechanisme van halogeenbruggen grote overeenkomsten vertoont met dat van waterstofbruggen, en dat dit mechanisme eenvoudig kan worden beschreven met behulp van moleculair-orbitaaltheorie. Zowel halogeenbruggen als waterstofbruggen bevatten, naast een electrostatische component, een aanzienlijke covalente component als gevolg van ladingsoverdracht van het ongebonden electronenpaar op het halogenide naar het σ^*-orbitaal op het DX- of DH-fragment. De electrostatische component is doorgaans sterker voor waterstofbruggen, omdat de polarisatie van het DH-fragment gunstiger is dan die van het DX-fragment. Desalniettemin kunnen halogeenbruggen sterker zijn dan waterstofbruggen, vanwege een grotere bijdrage van de covalente

component. De reden hiervan is dat het lege σ*-orbitaal op een dihalogeen DX een lagere energie heeft dan hetzelfde orbitaal op een waterstofhalogenide DH.

Door consistent het D-, X- of A-atoom te variëren en de veranderingen in electronische structuur van de fragmenten te beschouwen is het relatief eenvoudig om het effect op de bindingskarakteristieken van DH···A$^-$ of DX···A$^-$ te verklaren. Het vervangen van, bijvoorbeeld, het A$^-$-ion door een zwaarder halogenide, verzwakt zowel de waterstofbruggen als de halogeenbruggen, onder andere omdat het zwaardere halogenide een minder goede electrondonor is. Dit geldt ook voor de fluorbruggen, hoewel de trend in bindingssterkte daar is omgekeerd door een complexe samenhang van factoren, gerelateerd aan de relatief grote oprekking van de zwakke D–F-bindingen, en de lage energie van de σ^*_{D-F}-orbitalen.

Variatie van de waterstof- of halogeendonerende groep D heeft een tegenovergestelde uitwerking op de bindingssterkte van waterstofbruggen en halogeenbruggen. Wanneer echter het activeringsspanningsmodel wordt toegepast op de vormingsreacties van deze bindingen, blijkt dat deze variatie in beide gevallen hetzelfde effect op de spannings- en interactiecomponenten heeft. De interactie-energie wordt zwakker als D wordt gevariëerd van F naar I, omdat de toegenomen electropositiviteit leidt tot een minder gunstige polarisatie van de electronendichtheid van DH of DX, en dus tot een zwakkere electrostatische aantrekking. Tevens zorgt dit, met name voor de halogeenbruggen, voor een toename in Pauli-repulsie. Tegelijkertijd neemt de spanningsenergie af, omdat de D–H- en D–X-bindingen zwakker worden. Voor de D–X-bindingen zijn de verschillen echter klein, en de uiteindelijke sterkte van de halogeenbruggen volgt zodoende de trend van de interactie-energieën. De verschillen in D–H-bindingssterkte zijn echter beduidend groter. Van FH naar IH wordt het DH-fragment significant verder opgerekt, waardoor een sterkere wisselwerking ontstaat, wat leidt tot een omgekeerde trend in bindingssterkte: de waterstofbruggen in DH···A$^-$ worden juist sterker als het D-atoom wordt gevariëerd van F naar I.

In het negende hoofdstuk wordt opnieuw een vergelijking gemaakt van halogeenbruggen met waterstofbruggen, maar nu aan de hand van aanzienlijk grotere systemen. De systemen bestaan uit de door waterstofbruggen gebonden Watson-Crick-basenparen, zoals voorkomend in DNA, en analoog daaraan de door halogeenbruggen gebonden *N*-halobasenparen. In de laatste zijn de N–H-bindingen van de natuurlijke basen vervangen door N–X-bindingen, waarbij X wederom één van de halogenen F, Cl, Br of I is. We hebben opnieuw aangetoond dat het mechanisme van de waterstofbruggen in deze basenparen grotendeels identiek is aan dat van de halogeenbruggen. In beide gevallen is er een belangrijke bijdrage van ladingsoverdracht van een ongebonden electronenpaar op N of O naar het

σ*-orbitaal van de N–H- of N–X-binding. Deze overeenkomsten bevestigen niet alleen het bindingsmechanisme zoals beschreven in hoofdstuk 8 voor kleinere modelsystemen, maar suggereren ook dat het coöperatieve effect, zoals is aangetoond voor de waterstofbruggen in guanine-kwartetten, eveneens kan plaatsvinden in kwartetten die worden gevormd door halogeenbruggen tussen *N*-halo-guaninebasen. Onze berekeningen tonen aan dat dit inderdaad het geval is: de totale bindingsenergie van de *N*-halo-guanine-kwartetten is meer stabiliserend dan vier maal de bindingsenergie van een *N*-halo-guanine-basenpaar. Voor de kwartetten met broom- en joodbruggen vinden we zelfs dat het coöperatieve effect sterker is dan in het kwartet met waterstofbruggen, vanwege de grotere ladingsoverdracht die plaatsvindt bij het vormen van deze halogeenbruggen. Deze conclusies zijn getrokken naar aanleiding van meerdere onafhankelijke redeneringen, gesterkt door een aantal verschillende analysemethoden.

Men kan slechts hopen dat de inzichten die zijn verworven in deze studies het begrip van de chemie zodanig verbeteren dat ze bijdragen aan het bereiken van nieuwe mijlpalen. Hoogstwaarschijnlijk dienen de concepten gepresenteerd in dit proefschrift te worden aangevuld, verbeterd en waar nodig zelfs te worden vervangen door superieure concepten. Dit proces is een belangrijk onderdeel van wetenschap en één van de voornaamste redenen dat wetenschap zo belangrijk is: de wetenschappelijke methode is het enige instrument waarmee we ons begrip van natuurlijke fenomenen werkelijk kunnen verbeteren. En het heeft reeds bewezen bijzonder succesvol te zijn, mits op kritische wijze toegepast.

12 References

[1] F. Diederich, P. J. Stang, *Metal-Catalyzed Cross-Coupling Reactions*, Wiley-VCH, Weinheim, **1998**.
[2] J. F. Hartwig, *Organotransition Metal Chemistry: From Bonding to Catalysis*, University Science Books, Sausalito, **2010**.
[3] "The Nobel Prize in Chemistry (2010) Press Release", *Nobelprize.org*, http://www.nobelprize.org/nobel_prizes/chemistry/laureates/2010/press.html, **2010**.
[4] A. Suzuki, *Angew. Chem. Int. Ed.* **2011**, *50*, 6722–6737.
[5] E.-I. Negishi, *Angew. Chem. Int. Ed.* **2011**, *50*, 6738–6764.
[6] N. Miyaura, A. Suzuki, *Chem. Rev.* **1995**, *95*, 2457–2483.
[7] M. Torrent, M. Solà, G. Frenking, *Chem. Rev.* **2000**, *100*, 439–493.
[8] A. Dedieu, *Chem. Rev.* **2000**, *100*, 543–600.
[9] I. P. Beletskaya, A. V. Cheprakov, *Chem. Rev.* **2000**, *100*, 3009–3066.
[10] T.-Y. Luh, M.-K. Leung, K.-T. Wong, *Chem. Rev.* **2000**, *100*, 3187–3204.
[11] A. F. Littke, G. C. Fu, *Angew. Chem. Int. Ed.* **2002**, *41*, 4176–4211.
[12] V. Ritleng, C. Sirlin, M. Pfeffer, *Chem. Rev.* **2002**, *102*, 1731–1769.
[13] M. E. van der Boom, D. Milstein, *Chem. Rev.* **2003**, *103*, 1759–1792.
[14] R. B. Bedford, C. S. J. Cazin, D. Holder, *Coordin. Chem. Rev.* **2004**, *248*, 2283–2321.
[15] J.-P. Corbet, G. Mignani, *Chem. Rev.* **2006**, *106*, 2651–2710.
[16] N. T. S. Phan, M. Van Der Sluys, C. W. Jones, *Adv. Synth. Catal.* **2006**, *348*, 609–679.
[17] L. Yin, J. Liebscher, *Chem. Rev.* **2007**, *107*, 133–173.
[18] B. M. Rosen, K. W. Quasdorf, D. A. Wilson, N. Zhang, A.-M. Resmerita, N. K. Garg, V. Percec, *Chem. Rev.* **2011**, *111*, 1346–1416.
[19] R. Jana, T. P. Pathak, M. S. Sigman, *Chem. Rev.* **2011**, *111*, 1417–1492.
[20] A. Molnár, *Chem. Rev.* **2011**, *111*, 2251–2320.
[21] R. F. Heck, J. P. Nolley Jr, *J. Org. Chem.* **1972**, *37*, 2320–2322.
[22] J. K. Stille, *Angew. Chem. Int. Ed.* **1986**, *25*, 508–523.
[23] J. C. Weisshaar, *Acc. Chem. Res.* **1993**, *26*, 213–219.
[24] R. H. Crabtree, *Chem. Rev.* **1995**, *95*, 987–1007.
[25] J. Y. Corey, J. Braddock-Wilking, *Chem. Rev.* **1999**, *99*, 175–292.
[26] A. E. Shilov, G. B. Shul'pin, *Chem. Rev.* **1997**, *97*, 2879–2932.
[27] R. H. Crabtree, *J. Organomet. Chem.* **2004**, *689*, 4083–4091.
[28] I. P. Beletskaya, A. V. Cheprakov, *Coordin. Chem. Rev.* **2004**, *248*, 2337–2364.
[29] M. Lersch, M. Tilset, *Chem. Rev.* **2005**, *105*, 2471–2526.
[30] J. Dupont, C. S. Consorti, J. Spencer, *Chem. Rev.* **2005**, *105*, 2527–2571.
[31] K. C. Nicolaou, P. G. Bulger, D. Sarlah, *Angew. Chem. Int. Ed.* **2005**, *44*, 4442–4489.
[32] T. Ziegler, *Chem. Rev.* **1991**, *91*, 651–667.

[33] A. M. C. Wittborn, M. Costas, M. R. A. Blomberg, P. E. M. Siegbahn, *J. Chem. Phys.* **1997**, *107*, 4318–4328.
[34] S. Niu, M. B. Hall, *Chem. Rev.* **2000**, *100*, 353–405.
[35] L. Xue, Z. Lin, *Chem. Soc. Rev.* **2010**, *39*, 1692–1705.
[36] S. Otsuka, *J. Organomet. Chem.* **1980**, *200*, 191–205.
[37] M.-D. Su, S.-Y. Chu, *Inorg. Chem.* **1998**, *37*, 3400–3406.
[38] C. A. Tolman, *Chem. Rev.* **1977**, *77*, 313–348.
[39] S. Sakaki, N. Mizoe, Y. Musashi, B. Biswas, M. Sugimoto, *J. Phys. Chem. A* **1998**, *102*, 8027–8036.
[40] S. Sakaki, B. Biswas, M. Sugimoto, *Organometallics* **1998**, *17*, 1278–1289.
[41] C. Amatore, A. Jutand, *Acc. Chem. Res.* **2000**, *33*, 314–321.
[42] T. Matsubara, K. Hirao, *Organometallics* **2002**, *21*, 4482–4489.
[43] V. P. Ananikov, D. G. Musaev, K. Morokuma, *J. Am. Chem. Soc.* **2002**, *124*, 2839–2852.
[44] S. Kozuch, C. Amatore, A. Jutand, S. Shaik, *Organometallics* **2005**, *24*, 2319–2330.
[45] V. P. Ananikov, D. G. Musaev, K. Morokuma, *Eur. J. Inorg. Chem.* **2007**, 5390–5399.
[46] J. Jover, N. Fey, M. Purdie, G. C. Lloyd-Jones, J. N. Harvey, *J. Mol. Catal. A: Chem.* **2010**, *324*, 39–47.
[47] S. Kozuch, S. Shaik, *J. Mol. Catal. A: Chem.* **2010**, *324*, 120–126.
[48] C. Amatore, G. Le Duc, A. Jutand, *Chem. Eur. J.* **2013**, *19*, 10082–10093.
[49] P. Hofmann, H. Heiss, G. Müller, *Z. Naturforsch. B* **1987**, *42*, 395–409.
[50] S. Sakaki, B. Biswas, M. Sugimoto, *J. Chem. Soc., Dalton Trans.* **1997**, 803–809.
[51] P. Dierkes, P. W. N. M. van Leeuwen, *J. Chem. Soc., Dalton Trans.* **1999**, 1519–1529.
[52] P. W. N. M. van Leeuwen, P. C. J. Kamer, J. N. H. Reek, P. Dierkes, *Chem. Rev.* **2000**, *100*, 2741–2769.
[53] Z. Freixa, P. W. N. M. van Leeuwen, *Dalton Trans.* **2003**, 1890–1901.
[54] M.-N. Birkholz née Gensow, Z. Freixa, P. W. N. M. van Leeuwen, *Chem. Soc. Rev.* **2009**, *38*, 1099–1118.
[55] J. A. Hageman, J. A. Westerhuis, H. W. Fruhauf, G. Rothenberg, *Adv. Synth. Catal.* **2006**, *348*, 361–369.
[56] N. Fey, A. G. Orpen, J. N. Harvey, *Coordin. Chem. Rev.* **2009**, *253*, 704–722.
[57] A. Diefenbach, G. Th. de Jong, F. M. Bickelhaupt, *Mol. Phys.* **2005**, *103*, 995–998.
[58] A. Diefenbach, *Fragment-Oriented Design of Catalysts: a Theoretical Study on Bond Activation*, Philipps-Universität Marburg, Germany, **2000**.
[59] G. Th. de Jong, *Theoretical Studies on Catalytic Bond Activation*, Vrije Universiteit, Amsterdam, The Netherlands, **2007**.
[60] W.-J. van Zeist, *Activating Bonds: Theoretical Studies of Chemical Bonds and Their Catalytic Activation by Palladium*, Vrije Universiteit, Amsterdam, The Netherlands, **2011**.
[61] C. Amatore, A. Jutand, *J. Organomet. Chem.* **1999**, *576*, 254–278.
[62] S. Kozuch, S. Shaik, *Acc. Chem. Res.* **2011**, *44*, 101–110.
[63] S. Kozuch, *WIREs Comput. Mol. Sci.* **2012**, *2*, 795–815.
[64] G. A. Jeffrey, *An Introduction to Hydrogen Bonding*, Oxford University Press, New York, **1997**.
[65] G. R. Desiraju, T. Steiner, *The Weak Hydrogen Bond*, Oxford University Press, New York, **1999**.
[66] C. A. Coulson, *Valence*, Oxford University Press, London, **1952**.
[67] F. Guthrie, *J. Chem. Soc.* **1863**, *16*, 239–244.
[68] H. A. Bent, *Chem. Rev.* **1968**, *68*, 587–648.
[69] A. C. Legon, *Phys. Chem. Chem. Phys.* **2010**, *12*, 7736–7747.

[70] E. Corradi, S. V. Meille, M. T. Messina, P. Metrangolo, G. Resnati, *Angew. Chem. Int. Ed.* **2000**, *39*, 1782–1786.
[71] P. Metrangolo, G. Resnati, *Chem. Eur. J.* **2001**, *7*, 2511–2519.
[72] P. Metrangolo, H. Neukirch, T. Pilati, G. Resnati, *Acc. Chem. Res.* **2005**, *38*, 386–395.
[73] P. Metrangolo, F. Meyer, T. Pilati, G. Resnati, G. Terraneo, *Angew. Chem. Int. Ed.* **2008**, *47*, 6114–6127.
[74] T. T. T. Bui, S. Dahaoui, C. Lecomte, G. R. Desiraju, E. Espinosa, *Angew. Chem. Int. Ed.* **2009**, *48*, 3838–3841.
[75] C. J. Serpell, N. L. Kilah, P. J. Costa, V. Felix, P. D. Beer, *Angew. Chem. Int. Ed.* **2010**, *49*, 5322–5326.
[76] L. Brammer, G. Mínguez Espallargas, S. Libri, *CrystEngComm* **2008**, *10*, 1712–1727.
[77] G. Mínguez Espallargas, F. Zordan, L. Arroyo Marín, H. Adams, K. Shankland, J. van de Streek, L. Brammer, *Chem. Eur. J.* **2009**, *15*, 7554–7568.
[78] T. Di Paolo, C. Sandorfy, *Chem. Phys. Lett.* **1974**, *26*, 466–473.
[79] T. Di Paolo, C. Sandorfy, *Nature* **1974**, *252*, 471–472.
[80] P. Auffinger, F. A. Hays, E. Westhof, P. S. Ho, *Proc. Natl. Acad. Sci. USA* **2004**, *101*, 16789–16794.
[81] A. R. Voth, F. A. Hays, P. S. Ho, *Proc. Natl. Acad. Sci. USA* **2007**, *104*, 6188–6193.
[82] A. R. Voth, P. Khuu, K. Oishi, P. S. Ho, *Nature Chem.* **2009**, *1*, 74–79.
[83] Y. Lu, Y. Wang, W. Zhu, *Phys. Chem. Chem. Phys.* **2010**, *12*, 4543–4551.
[84] J. P. M. Lommerse, A. J. Stone, R. Taylor, F. Allen, *J. Am. Chem. Soc.* **1996**, *118*, 3108–3116.
[85] A. C. Legon, *Angew. Chem. Int. Ed.* **1999**, *38*, 2687–2714.
[86] P. Romaniello, F. Lelj, *J. Phys. Chem. A* **2002**, *106*, 9114–9119.
[87] C. B. Aakeröy, M. Fasulo, N. Schultheiss, J. Desper, C. Moore, *J. Am. Chem. Soc.* **2007**, *129*, 13772–13773.
[88] P. Cimino, M. Pavone, V. Barone, *J. Phys. Chem. A* **2007**, *111*, 8482–8490.
[89] P. Politzer, P. Lane, M. C. Concha, Y. Ma, J. S. Murray, *J. Mol. Model.* **2007**, *13*, 305–311.
[90] P. Politzer, J. S. Murray, P. Lane, *Int. J. Quantum Chem.* **2007**, *107*, 3046–3052.
[91] I. Alkorta, F. Blanco, M. Solimannejad, J. Elguero, *J. Phys. Chem. A* **2008**, *112*, 10856–10863.
[92] Q. Li, X. Xu, T. Liu, B. Jing, W. Li, J. Cheng, B. Gong, J. Sun, *Phys. Chem. Chem. Phys.* **2010**, *12*, 6837–6843.
[93] T. Sakurai, M. Sundaralingam, G. A. Jeffrey, *Acta Cryst.* **1963**, *16*, 354–363.
[94] S. C. Nyburg, C. H. Faerman, *Acta Cryst. B* **1985**, *41*, 274–279.
[95] A. C. Legon, *Chem. Commun.* **1998**, 2737–2738.
[96] T. Brinck, J. S. Murray, P. Politzer, *Int. J. Quantum Chem.* **1992**, 57–64.
[97] T. Clark, M. Hennemann, J. S. Murray, P. Politzer, *J. Mol. Model.* **2007**, *13*, 291–296.
[98] U. Adhikari, S. Scheiner, *Chem. Phys. Lett.* **2012**, *532*, 31–35.
[99] S. M. Huber, J. D. Scanlon, E. Jimenez-Izal, J. M. Ugalde, I. Infante, *Phys. Chem. Chem. Phys.* **2013**, *15*, 10350–10357.
[100] A. J. Stone, *J. Am. Chem. Soc.* **2013**, *135*, 7005–7009.
[101] S. M. Huber, E. Jimenez-Izal, J. M. Ugalde, I. Infante, *Chem. Commun.* **2012**, *48*, 7708.
[102] M. Hennemann, J. S. Murray, P. Politzer, K. E. Riley, T. Clark, *J. Mol. Model.* **2011**, *18*, 2461–2469.
[103] P. Politzer, J. S. Murray, M. C. Concha, *J. Mol. Model.* **2008**, *14*, 659–665.
[104] P. Politzer, J. S. Murray, *ChemPhysChem* **2013**, *14*, 278–294.
[105] P. Politzer, K. E. Riley, F. A. Bulat, J. S. Murray, *Comp. Theor. Chem.* **2012**, *998*, 2–8.

[106] M. A. A. Ibrahim, *J. Comput. Chem.* **2011**, *32*, 2564–2574.
[107] S. Rendine, S. Pieraccini, A. Forni, M. Sironi, *Phys. Chem. Chem. Phys.* **2011**, *13*, 19508–19516.
[108] M. Kolář, P. Hobza, *J. Chem. Theory Comput.* **2012**, *8*, 1325–1333.
[109] W. L. Jorgensen, P. Schyman, *J. Chem. Theory Comput.* **2012**, *8*, 3895–3901.
[110] K. Morokuma, L. Pedersen, *J. Chem. Phys.* **1968**, *48*, 3275–3282.
[111] H. Umeyama, K. Morokuma, *J. Am. Chem. Soc.* **1977**, *99*, 1316–1332.
[112] K. Morokuma, *Acc. Chem. Res.* **1977**, *10*, 294–300.
[113] C. Fonseca Guerra, F. M. Bickelhaupt, *Angew. Chem. Int. Ed.* **1999**, *38*, 2942–2945.
[114] C. Fonseca Guerra, F. M. Bickelhaupt, J. G. Snijders, E. J. Baerends, *Chem. Eur. J.* **1999**, *5*, 3581–3594.
[115] C. Fonseca Guerra, H. Zijlstra, G. Paragi, F. M. Bickelhaupt, *Chem. Eur. J.* **2011**, *17*, 12612–12622.
[116] S. J. Grabowski, *Chem. Rev.* **2011**, *111*, 2597–2625.
[117] J. Hoja, A. F. Sax, K. Szalewicz, *Chem. Eur. J.* **2014**, *20*, 2292–2300.
[118] R. J. Hach, R. E. Rundle, *J. Am. Chem. Soc.* **1951**, *73*, 4321–4324.
[119] R. S. Mulliken, *J. Am. Chem. Soc.* **1952**, *74*, 811–824.
[120] R. L. Flurry, *J. Phys. Chem.* **1965**, *69*, 1927–1933.
[121] R. L. Flurry, *J. Phys. Chem.* **1969**, *73*, 2111–2117.
[122] J. J. Novoa, F. Mota, S. Alvarez, *J. Phys. Chem.* **1988**, *92*, 6561–6566.
[123] S. L. Price, A. J. Stone, J. Lucas, R. S. Rowland, A. E. Thornley, *J. Am. Chem. Soc.* **1994**, *116*, 4910–4918.
[124] K. E. Riley, P. Hobza, *J. Chem. Theory Comput.* **2008**, *4*, 232–242.
[125] M. Palusiak, *J. Mol. Struc.: THEOCHEM* **2010**, *945*, 89–92.
[126] B. Pintér, N. Nagels, W. A. Herrebout, F. de Proft, *Chem. Eur. J.* **2013**, *19*, 519–530.
[127] C. Wang, D. Danovich, Y. Mo, S. Shaik, *J. Chem. Theory Comput.* **2014**, *10*, 3726–3737.
[128] G. C. Pimentel, *J. Chem. Phys.* **1951**, *19*, 446–448.
[129] N. E. Klepeis, A. L. L. East, A. G. Császár, W. D. Allen, T. J. Lee, D. W. Schwenke, *J. Chem. Phys.* **1993**, *99*, 3865–3897.
[130] I. Alkorta, I. Rozas, J. Elguero, *J. Phys. Chem. A* **1998**, *102*, 9278–9285.
[131] S. J. Grabowski, *Phys. Chem. Chem. Phys.* **2013**, *15*, 7249–7259.
[132] R. Kurczab, M. P. Mitoraj, A. Michalak, T. Ziegler, *J. Phys. Chem. A* **2010**, *114*, 8581–8590.
[133] R. W. Góra, M. Maj, S. J. Grabowski, *Phys. Chem. Chem. Phys.* **2013**, *15*, 2514–2522.
[134] "Theory", *Oxford English Dictionary*, http://www.oed.com/, **2013**.
[135] F. J. Ayala, *Science and Creationism: a View From the National Academy of Sciences*, National Academy Press, Washington, **1999**.
[136] "Model", *Oxford English Dictionary*, http://www.oed.com/, **2013**.
[137] E. Schrödinger, *Phys. Rev.* **1926**, *28*, 1049–1070.
[138] F. Jensen, *Introduction to Computational Chemistry*, Wiley-VCH, Weinheim, **1999**.
[139] C. J. Cramer, *Essentials of Computational Chemistry: Theories and Models*, John Wiley & Sons, Ltd., Chichester, West Sussex, **2004**.
[140] R. McWeeny, *Methods of Molecular Quantum Mechanics*, Academic Press, London, **1992**.
[141] R. G. Parr, W. T. Yang, *Density-Functional Theory of Atoms and Molecules*, Oxford University Press, New York, **1989**.
[142] W. Koch, M. C. Holthausen, *A Chemist's Guide to Density Functional Theory*, Wiley-VCH, Weinheim, **2002**.
[143] P. Hohenberg, W. Kohn, *Phys. Rev. B* **1964**, *136*, B864–B871.

[144] W. Kohn, L. J. Sham, *Phys. Rev.* **1965**, *140*, A1133–A1138.
[145] E. J. Baerends, O. V. Gritsenko, *J. Phys. Chem. A* **1997**, *101*, 5383–5403.
[146] R. Stowasser, R. Hoffmann, *J. Am. Chem. Soc.* **1999**, *121*, 3414–3420.
[147] F. M. Bickelhaupt, E. J. Baerends, in *Reviews in Computational Chemistry, Vol. 15* (Eds.: K.B. Lipkowitz, D.B. Boyd), VCH Publishers Inc., New York, **2000**, pp. 1–86.
[148] E. J. Baerends, O. V. Gritsenko, R. van Meer, *Phys. Chem. Chem. Phys.* **2013**, *15*, 16408–16425.
[149] G. te Velde, F. M. Bickelhaupt, E. J. Baerends, C. Fonseca Guerra, S. J. A. van Gisbergen, J. G. Snijders, T. Ziegler, *J. Comput. Chem.* **2001**, *22*, 931–967.
[150] C. Fonseca Guerra, J. G. Snijders, G. te Velde, E. J. Baerends, *Theor. Chem. Acc.* **1998**, *99*, 391–403.
[151] *ADF*2009, *ADF2010*, *ADF2012*, *ADF2013*. Scientific Computing & Modelling (SCM), Theoretical Chemistry, Vrije Universiteit, Amsterdam, The Netherlands, http://www.scm.com/.
[152] *QUILD*. M. Swart, F. M. Bickelhaupt, Vrije Universiteit, Amsterdam, The Netherlands.
[153] M. Swart, F. M. Bickelhaupt, *Int. J. Quantum Chem.* **2006**, *106*, 2536–2544.
[154] M. Swart, F. M. Bickelhaupt, *J. Comput. Chem.* **2008**, *29*, 724–734.
[155] P. M. Boerrigter, G. te Velde, E. J. Baerends, *Int. J. Quantum Chem.* **1988**, *33*, 87–113.
[156] G. te Velde, E. J. Baerends, *J. Comput. Phys.* **1992**, *99*, 84–98.
[157] A. D. Becke, *J. Chem. Phys.* **1988**, *88*, 2547–2553.
[158] M. Franchini, P. H. T. Philipsen, L. Visscher, *J. Comput. Chem.* **2013**, *34*, 1819–1827.
[159] E. van Lenthe, E. J. Baerends, *J. Comput. Chem.* **2003**, *24*, 1142–1156.
[160] L. Versluis, T. Ziegler, *J. Chem. Phys.* **1988**, *88*, 322–328.
[161] J. C. Slater, *Quantum Theory of Molecules and Solids, Vol. 4*, McGraw-Hill, New York, **1974**.
[162] A. D. Becke, *J. Chem. Phys.* **1986**, *84*, 4524–4529.
[163] A. D. Becke, *Phys. Rev. A* **1988**, *38*, 3098–3100.
[164] C. Lee, W. T. Yang, R. G. Parr, *Phys. Rev. B* **1988**, *37*, 785–789.
[165] S. H. Vosko, L. Wilk, M. Nusair, *Can. J. Phys.* **1980**, *58*, 1200–1211.
[166] J. P. Perdew, *Phys. Rev. B* **1986**, *33*, 8822–8824.
[167] L. Fan, T. Ziegler, *J. Chem. Phys.* **1991**, *94*, 6057–6063.
[168] S. Grimme, J. Antony, S. Ehrlich, H. Krieg, *J. Chem. Phys.* **2010**, *132*, 154104–154119.
[169] S. Grimme, S. Ehrlich, L. Goerigk, *J. Comput. Chem.* **2011**, *32*, 1456–1465.
[170] E. R. Johnson, A. D. Becke, *J. Chem. Phys.* **2005**, *123*, 024101–024107.
[171] E. van Lenthe, E. J. Baerends, J. G. Snijders, *J. Chem. Phys.* **1994**, *101*, 9783–9792.
[172] E. van Lenthe, R. van Leeuwen, E. J. Baerends, J. G. Snijders, *Int. J. Quantum Chem.* **1996**, *57*, 281–293.
[173] B. G. Johnson, P. M. W. Gill, J. A. Pople, *J. Chem. Phys.* **1993**, *98*, 5612–5626.
[174] T. V. Russo, R. L. Martin, P. J. Hay, *J. Chem. Phys.* **1994**, *101*, 7729–7737.
[175] G. Th. de Jong, M. Solà, L. Visscher, F. M. Bickelhaupt, *J. Chem. Phys.* **2004**, *121*, 9982–9992.
[176] G. Th. de Jong, D. P. Geerke, A. Diefenbach, F. M. Bickelhaupt, *Chem. Phys.* **2005**, *313*, 261–270.
[177] G. Th. de Jong, D. P. Geerke, A. Diefenbach, M. Solà, F. M. Bickelhaupt, *J. Comput. Chem.* **2005**, *26*, 1006–1020.
[178] G. Th. de Jong, F. M. Bickelhaupt, *J. Phys. Chem. A* **2005**, *109*, 9685–9699.
[179] G. Th. de Jong, F. M. Bickelhaupt, *J. Chem. Theory Comput.* **2006**, *2*, 322–335.
[180] C. Fonseca Guerra, F. M. Bickelhaupt, J. G. Snijders, E. J. Baerends, *J. Am. Chem. Soc.* **2000**, *122*, 4117–4128.

[181] T. van der Wijst, C. Fonseca Guerra, M. Swart, F. M. Bickelhaupt, B. Lippert, *Angew. Chem. Int. Ed.* **2009**, *48*, 3285–3287.
[182] C. Fonseca Guerra, T. van der Wijst, J. Poater, M. Swart, F. M. Bickelhaupt, *Theor. Chem. Acc.* **2010**, *125*, 245–252.
[183] A. Bérces, R. M. Dickson, L. Fan, H. Jacobsen, D. Swerhone, T. Ziegler, *Comput. Phys. Commun.* **1997**, *100*, 247–262.
[184] H. Jacobsen, A. Bérces, D. P. Swerhone, T. Ziegler, *Comput. Phys. Commun.* **1997**, *100*, 263–276.
[185] S. K. Wolff, *Int. J. Quantum Chem.* **2005**, *104*, 645–659.
[186] K. Fukui, *Acc. Chem. Res.* **1981**, *14*, 363–368.
[187] L. Deng, T. Ziegler, L. Fan, *J. Chem. Phys.* **1993**, *99*, 3823–3835.
[188] W.-J. van Zeist, A. H. Koers, L. P. Wolters, F. M. Bickelhaupt, *J. Chem. Theory Comput.* **2008**, *4*, 920–928.
[189] W.-J. van Zeist, C. Fonseca Guerra, F. M. Bickelhaupt, *J. Comput. Chem.* **2008**, *29*, 312–315.
[190] P. W. Atkins, *Physical Chemistry*, Oxford University Press, Oxford, **1998**.
[191] F. M. Bickelhaupt, N. J. R. van Eikema Hommes, C. Fonseca Guerra, E. J. Baerends, *Organometallics* **1996**, *15*, 2923–2931.
[192] C. Fonseca Guerra, J.-W. Handgraaf, E. J. Baerends, F. M. Bickelhaupt, *J. Comput. Chem.* **2004**, *25*, 189–210.
[193] F. M. Bickelhaupt, *J. Comput. Chem.* **1999**, *20*, 114–128.
[194] G. Th. de Jong, F. M. Bickelhaupt, *ChemPhysChem* **2007**, *8*, 1170–1181.
[195] W.-J. van Zeist, F. M. Bickelhaupt, *Org. Biomol. Chem.* **2010**, *8*, 3118–3127.
[196] I. Fernández, F. M. Bickelhaupt, *Chem. Soc. Rev.* **2014**, *43*, 4953–4967.
[197] T. Ziegler, A. Rauk, *Theor. Chim. Acta* **1977**, *46*, 1–10.
[198] T. Ziegler, A. Rauk, *Inorg. Chem.* **1979**, *18*, 1558–1565.
[199] F. M. Bickelhaupt, E. J. Baerends, N. M. M. Nibbering, *Chem. Eur. J.* **1996**, *2*, 196–207.
[200] A. Diefenbach, F. M. Bickelhaupt, *J. Chem. Phys.* **2001**, *115*, 4030–4040.
[201] A. Diefenbach, G. Th. de Jong, F. M. Bickelhaupt, *J. Chem. Theory Comput.* **2005**, *1*, 286–298.
[202] J. N. P. van Stralen, F. M. Bickelhaupt, *Organometallics* **2006**, *25*, 4260–4268.
[203] G. S. Hammond, *J. Am. Chem. Soc.* **1955**, *77*, 334–338.
[204] B. Galabov, V. Nikolova, J. J. Wilke, H. F. Schaefer III, W. D. Allen, *J. Am. Chem. Soc.* **2008**, *130*, 9887–9896.
[205] A. P. Bento, F. M. Bickelhaupt, *J. Org. Chem.* **2008**, *73*, 7290–7299.
[206] L. P. Wolters, Y. Ren, F. M. Bickelhaupt, *ChemistryOpen* **2014**, *3*, 29–36.
[207] D. H. Ess, K. N. Houk, *J. Am. Chem. Soc.* **2008**, *130*, 10187–10198.
[208] I. Fernández, *Phys. Chem. Chem. Phys.* **2014**, *16*, 7662–7671.
[209] F. M. Bickelhaupt, E. J. Baerends, *Angew. Chem. Int. Ed.* **2003**, *42*, 4183–4188.
[210] J. Poater, M. Solà, F. M. Bickelhaupt, *Chem. Eur. J.* **2006**, *12*, 2889–2895.
[211] I. Fernández, F. M. Bickelhaupt, F. P. Cossío, *Chem. Eur. J.* **2012**, *18*, 12395–12403.
[212] R. Hoffmann, *Angew. Chem. Int. Ed.* **1982**, *21*, 711–724.
[213] T. A. Albright, J. K. Burdett, M. H. Whangbo, *Orbital Interactions in Chemistry*, John Wiley & Sons. Inc., Hoboken, New Jersey, **2013**.
[214] I. Fleming, *Molecular Orbitals and Organic Chemical Reactions, Reference Edition*, John Wiley & Sons, Ltd, Chichester, UK, **2010**.
[215] A. Rauk, *Orbital Interaction Theory of Organic Chemistry*, John Wiley & Sons, New York, **2001**.
[216] K. Morokuma, *J. Chem. Phys.* **1971**, *55*, 1236–1244.

[217] K. Kitaura, K. Morokuma, *Int. J. Quantum Chem.* **1976**, *10*, 325–340.
[218] T. Ziegler, A. Rauk, *Inorg. Chem.* **1979**, *18*, 1755–1759.
[219] A. E. Reed, L. A. Curtiss, F. Weinhold, *Chem. Rev.* **1988**, *88*, 899–926.
[220] E. D. Glendening, A. Streitwieser, *J. Chem. Phys.* **1994**, *100*, 2900–2909.
[221] R. F. W. Bader, *Atoms in Molecules*, Oxford University Press, Oxford, **1990**.
[222] B. Jeziorski, R. Moszynski, K. Szalewicz, *Chem. Rev.* **1994**, *94*, 1887–1930.
[223] K. Szalewicz, *WIREs Comput. Mol. Sci.* **2011**, *2*, 254–272.
[224] M. A. Blanco, A. M. Pendás, E. Francisco, *J. Chem. Theory Comput.* **2005**, *1*, 1096–1109.
[225] R. Z. Khaliullin, E. A. Cobar, R. C. Lochan, A. T. Bell, M. Head-Gordon, *J. Phys. Chem. A* **2007**, *111*, 8753–8765.
[226] M. P. Mitoraj, A. Michalak, T. Ziegler, *J. Chem. Theory Comput.* **2009**, *5*, 962–975.
[227] Y. Mo, P. Bao, J. Gao, *Phys. Chem. Chem. Phys.* **2011**, *13*, 6760–6775.
[228] C. F. Matta, J. Hernández-Trujillo, T. H. Tang, R. F. W. Bader, *Chem. Eur. J.* **2003**, *9*, 1940–1951.
[229] R. F. W. Bader, *Chem. Eur. J.* **2006**, *12*, 2896–2901.
[230] J. Poater, M. Solà, F. M. Bickelhaupt, *Chem. Eur. J.* **2006**, *12*, 2902–2905.
[231] R. Hoffmann, *Solids and Surfaces*, Wiley-VCH, New York, NY, **1988**.
[232] A. Immirzi, A. Musco, *J. Chem. Soc., Chem. Commun.* **1974**, 400–401.
[233] S. Otsuka, T. Yoshida, M. Matsumoto, K. Nakatsu, *J. Am. Chem. Soc.* **1976**, *98*, 5850–5858.
[234] E. Dinjus, W. Leitner, *Appl. Organomet. Chem.* **1995**, *9*, 43–50.
[235] M. Zhou, L. Andrews, *J. Am. Chem. Soc.* **1998**, *120*, 11499–11503.
[236] L. Manceron, M. E. Alikhani, *Chem. Phys.* **1999**, *244*, 215–226.
[237] R. J. Gillespie, R. S. Nyholm, *Q. Rev. Chem. Soc.* **1957**, *11*, 339–380.
[238] R. J. Gillespie, *J. Chem. Ed.* **1963**, *40*, 295–301.
[239] R. J. Gillespie, *Chem. Soc. Rev.* **1992**, *21*, 59–69.
[240] R. J. Gillespie, *Coordin. Chem. Rev.* **2008**, *252*, 1315–1327.
[241] W.-J. van Zeist, F. M. Bickelhaupt, *Dalton Trans.* **2011**, *40*, 3028–3038.
[242] M. Swart, E. Rösler, F. M. Bickelhaupt, *J. Comput. Chem.* **2006**, *27*, 1486–1493.
[243] C. A. Jolly, D. S. Marynick, *Inorg. Chem.* **1989**, *28*, 2893–2895.
[244] M. Kaupp, *Angew. Chem. Int. Ed.* **2001**, *40*, 3534–3565.
[245] R. J. Gillespie, I. Bytheway, R. S. DeWitte, R. F. W. Bader, *Inorg. Chem.* **1994**, *33*, 2115–2121.
[246] M. Kaupp, P. V. R. Schleyer, *J. Am. Chem. Soc.* **1992**, *114*, 491–497.
[247] M. Kaupp, *Chem. Eur. J.* **1999**, *5*, 3631–3643.
[248] J. J. Low, W. A. Goddard III, *J. Am. Chem. Soc.* **1984**, *106*, 6928–6937.
[249] R. Fazaeli, A. Ariafard, S. Jamshidi, E. S. Tabatabaie, K. A. Pishro, *J. Organomet. Chem.* **2007**, *692*, 3984–3993.
[250] P. W. N. M. van Leeuwen, *Homogeneous Catalysis: Understanding the Art*, Kluwer Academic Publishers, Dordrecht, **2004**.
[251] W.-J. van Zeist, R. Visser, F. M. Bickelhaupt, *Chem. Eur. J.* **2009**, *15*, 6112–6115.
[252] E. Zuidema, P. W. N. M. van Leeuwen, C. Bo, *Organometallics* **2005**, *24*, 3703–3710.
[253] M. A. Carvajal, J. J. Novoa, S. Alvarez, *J. Am. Chem. Soc.* **2004**, *126*, 1465–1477.
[254] R. B. King, *Coordin. Chem. Rev.* **2000**, *197*, 141–168.
[255] T. Ziegler, *Inorg. Chem.* **1985**, *24*, 1547–1552.
[256] S. M. Socol, J. G. Verkade, *Inorg. Chem.* **1984**, *23*, 3487–3493.
[257] M. M. Rahman, H. Y. Liu, A. Prock, W. P. Giering, *Organometallics* **1987**, *6*, 650–658.
[258] T. L. Brown, *Inorg. Chem.* **1992**, *31*, 1286–1294.

[259] T. K. Woo, T. Ziegler, *Inorg. Chem.* **1994**, *33*, 1857–1863.
[260] D. Woska, A. Prock, W. P. Giering, *Organometallics* **2000**, *19*, 4629–4638.
[261] C. Suresh, *Inorg. Chem.* **2006**, *45*, 4982–4986.
[262] B. C. Hamann, J. F. Hartwig, *J. Am. Chem. Soc.* **1998**, *120*, 3694–3703.
[263] G. P. F van Strijdonck, M. D. K. Boele, P. C. J. Kamer, J. G. de Vries, P. W. N. M. van Leeuwen, *Eur. J. Inorg. Chem.* **1999**, *1999*, 1073–1076.
[264] J. J. Carbó, F. Maseras, C. Bo, P. W. N. M. van Leeuwen, *J. Am. Chem. Soc.* **2001**, *123*, 7630–7637.
[265] E. Galardon, S. Ramdeehul, J. M. Brown, A. Cowley, K. K. Hii, A. Jutand, *Angew. Chem. Int. Ed.* **2002**, *41*, 1760–1763.
[266] L. Gonsalvi, J. A. Gaunt, H. Adams, A. Castro, G. J. Sunley, A. Haynes, *Organometallics* **2003**, *22*, 1047–1054.
[267] G. Mann, Q. Shelby, A. H. Roy, J. F. Hartwig, *Organometallics* **2003**, *22*, 2775–2789.
[268] J. P. Stambuli, C. D. Incarvito, M. Bühl, J. F. Hartwig, *J. Am. Chem. Soc.* **2004**, *126*, 1184–1194.
[269] F. Barrios-Landeros, J. F. Hartwig, *J. Am. Chem. Soc.* **2005**, *127*, 6944–6945.
[270] S. Moncho, G. Ujaque, A. Lledos, P. Espinet, *Chem. Eur. J.* **2008**, *14*, 8986–8994.
[271] A. Ariafard, B. F. Yates, *J. Am. Chem. Soc.* **2009**, *131*, 13981–13991.
[272] F. Barrios-Landeros, B. P. Carrow, J. F. Hartwig, *J. Am. Chem. Soc.* **2009**, *131*, 8141–8154.
[273] C. E. Kefalidis, O. Baudoin, E. Clot, *Dalton Trans.* **2010**, *39*, 10528–10535.
[274] S. O. Nilsson Lill, P. Ryberg, T. Rein, E. Bennström, P.-O. Norrby, *Chem. Eur. J.* **2012**, *18*, 1640–1649.
[275] A. Kurbangalieva, D. Carmichael, K. K. Hii, A. Jutand, J. M. Brown, *Chem. Eur. J.* **2014**, *20*, 1116–1125.
[276] M. Tanaka, *Acta Cryst. C* **1992**, *48*, 739–740.
[277] A. Immirzi, A. Musco, P. Zambelli, G. Carturan, *Inorg. Chim. Acta* **1975**, *13*, L13–L14.
[278] M. Ahlquist, P. Fristrup, D. Tanner, P.-O. Norrby, *Organometallics* **2006**, *25*, 2066–2073.
[279] Z. Li, Y. Fu, Q.-X. Guo, L. Liu, *Organometallics* **2008**, *27*, 4043–4049.
[280] M. Besora, C. Gourlaouen, B. Yates, F. Maseras, *Dalton Trans.* **2011**, *40*, 11089–11094.
[281] M. S. G. Ahlquist, P.-O. Norrby, *Angew. Chem. Int. Ed.* **2011**, *50*, 11794–11797.
[282] R. Hoffmann, C. C. Levin, R. A. Moss, *J. Am. Chem. Soc.* **1973**, *95*, 629–631.
[283] R. R. Sauers, *J. Chem. Ed.* **1996**, *73*, 114–116.
[284] C. L. McMullin, N. Fey, J. N. Harvey, *Dalton Trans.* **2014**, *43*, 13545–13556.
[285] C. H. Marzabadi, J. E. Anderson, J. Gonzalez-Outeirino, P. R. J. Gaffney, C. G. H. White, D. A. Tocher, L. J. Todaro, *J. Am. Chem. Soc.* **2003**, *125*, 15163–15173.
[286] C.-Y. Lin, J.-D. Guo, J. C. Fettinger, S. Nagase, F. Grandjean, G. J. Long, N. F. Chilton, P. P. Power, *Inorg. Chem.* **2013**, *52*, 13584–13593.
[287] H. Jacobsen, L. Cavallo, *ChemPhysChem* **2011**, *13*, 562–569.
[288] S. Grimme, *ChemPhysChem* **2012**, *13*, 1407–1409.
[289] S. Grimme, J. P. Djukic, *Inorg. Chem.* **2011**, *50*, 2619–2628.
[290] A. Hansen, C. Bannwarth, S. Grimme, P. Petrović, C. Werlé, J.-P. Djukic, *ChemistryOpen* **2014**, *3*, 177–189.
[291] T. L. Brown, K. J. Lee, *Coordin. Chem. Rev.* **1993**, *128*, 89–116.
[292] J. A. Bilbrey, A. H. Kazez, J. Locklin, W. D. Allen, *J. Comput. Chem.* **2013**, *34*, 1189–1197.
[293] J. A. Bilbrey, A. H. Kazez, J. Locklin, W. D. Allen, *J. Chem. Theory Comput.* **2013**, *9*, 5734–5744.
[294] J. Zhang, M. Dolg, *Chem. Eur. J.* **2014**, *20*, 13909–13912.
[295] S. Grimme, P. R. Schreiner, *Angew. Chem. Int. Ed.* **2011**, *50*, 12639–12642.

[296] S. Grimme, *Angew. Chem. Int. Ed.* **2008**, *47*, 3430–3434.
[297] A. Klamt, G. Schüürmann, *J. Chem. Soc., Perkin Trans. 2* **1993**, 799–805.
[298] A. Klamt, *J. Phys. Chem.* **1995**, *99*, 2224–2235.
[299] C. C. Pye, T. Ziegler, *Theor. Chem. Acc.* **1999**, *101*, 396–408.
[300] N. L. Allinger, X. Zhou, J. Bergsma, *J. Mol. Struc.: THEOCHEM* **1994**, *312*, 69–83.
[301] M. Swart, E. Rösler, F. M. Bickelhaupt, *Eur. J. Inorg. Chem.* **2007**, 3646–3654.
[302] K. E. Riley, J. Vondrášek, P. Hobza, *Phys. Chem. Chem. Phys.* **2007**, *9*, 5555–5560.
[303] F. M. Bickelhaupt, R. L. DeKock, E. J. Baerends, *J. Am. Chem. Soc.* **2002**, *124*, 1500–1505.
[304] G. Th. de Jong, A. Kovacs, F. M. Bickelhaupt, *J. Phys. Chem. A* **2006**, *110*, 7943–7951.
[305] G. Th. de Jong, F. M. Bickelhaupt, *J. Chem. Theory Comput.* **2007**, *3*, 514–529.
[306] G. Th. de Jong, F. M. Bickelhaupt, *Can. J. Chem.* **2009**, *87*, 806–817.
[307] S. Wang, Y.-X. Qiu, H. Fang, W. H. E. Schwarz, *Chem. Eur. J.* **2006**, *12*, 4101–4114.
[308] S.-G. Wang, W. H. E. Schwarz, *Angew. Chem. Int. Ed.* **2009**, *48*, 3404–3415.
[309] P. E. M. Siegbahn, *J. Am. Chem. Soc.* **1996**, *118*, 1487–1496.
[310] E. D. Smurnyi, I. P. Gloriozov, Y. A. Ustynyuk, *Russ. J. Phys. Chem.* **2003**, *77*, 1699–1708.
[311] H. Heiberg, O. Gropen, O. Swang, *Int. J. Quantum Chem.* **2003**, *92*, 391–399.
[312] P. Pyykkö, J.-P. Desclaux, *Acc. Chem. Res.* **1979**, *12*, 276–281.
[313] P. Pyykkö, *Chem. Rev.* **1988**, *88*, 563–594.
[314] H. Schwarz, *Angew. Chem. Int. Ed.* **2003**, *42*, 4442–4454.
[315] K. Tatsumi, R. Hoffmann, A. Yamamoto, J. K. Stille, *Bull. Chem. Soc. Jpn.* **1981**, *54*, 1857–1867.
[316] A. Sundermann, O. Uzan, J. M. L. Martin, *Organometallics* **2001**, *20*, 1783–1791.
[317] A. Bader, E. Lindner, *Coordin. Chem. Rev.* **1991**, *108*, 27–110.
[318] P. Braunstein, F. Naud, *Angew. Chem. Int. Ed.* **2001**, *40*, 680–699.
[319] J. W. Faller, H. L. Stokes-Huby, M. A. Albrizzio, *Helv. Chim. Acta* **2001**, *84*, 3031–3042.
[320] R. Lindner, B. van den Bosch, M. Lutz, J. N. H. Reek, J. I. van der Vlugt, *Organometallics* **2011**, *30*, 499–510.
[321] C.-H. Jun, *Chem. Soc. Rev.* **2004**, *33*, 610–618.
[322] M. Tobisu, N. Chatani, *Chem. Soc. Rev.* **2008**, *37*, 300.
[323] T. Seiser, N. Cramer, *Org. Biomol. Chem.* **2009**, *7*, 2835.
[324] M. Murakami, T. Matsuda, *Chem. Commun.* **2011**, *47*, 1100.
[325] Y.-M. Chen, P. B. Armentrout, *J. Phys. Chem.* **1995**, *99*, 11424–11431.
[326] T.-Y. Ju, H.-Q. Yang, F.-M. Li, X.-Y. Li, C.-W. Hu, *Theor. Chem. Acc.* **2013**, *132*, 1387–1400.
[327] P. E. M. Siegbahn, M. R. A. Blomberg, *J. Am. Chem. Soc.* **1992**, *114*, 10548–10556.
[328] B. Rybtchinski, D. Milstein, *Angew. Chem. Int. Ed.* **1999**, *38*, 870–883.
[329] E. Ben-Ari, R. Cohen, M. Gandelman, L. J. W. Shimon, J. M. L. Martin, D. Milstein, *Organometallics* **2006**, *25*, 3190–3210.
[330] D. A. Colby, R. G. Bergman, J. A. Ellman, *Chem. Rev.* **2010**, *110*, 624–655.
[331] T. W. Lyons, M. S. Sanford, *Chem. Rev.* **2010**, *110*, 1147–1169.
[332] T. Satoh, M. Miura, *Chem. Eur. J.* **2010**, *16*, 11212–11222.
[333] K. M. Engle, T.-S. Mei, M. Wasa, J.-Q. Yu, *Acc. Chem. Res.* **2012**, *45*, 788–802.
[334] S. R. Neufeldt, M. S. Sanford, *Acc. Chem. Res.* **2012**, *45*, 936–946.
[335] N. Kuhl, M. N. Hopkinson, J. Wencel-Delord, F. Glorius, *Angew. Chem. Int. Ed.* **2012**, *51*, 10236–10254.
[336] Y. Minami, H. Yoshiyasu, Y. Nakao, T. Hiyama, *Angew. Chem. Int. Ed.* **2013**, *52*, 883–887.
[337] A. Diefenbach, F. M. Bickelhaupt, *J. Phys. Chem. A* **2004**, *108*, 8460–8466.

[338] J.-Y. Saillard, R. Hoffmann, *J. Am. Chem. Soc.* **1984**, *106*, 2006–2026.
[339] M. C. Holthausen, A. Fiedler, H. Schwarz, *J. Phys. Chem.* **1996**, *100*, 6236–6242.
[340] M. C. Holthausen, W. Koch, *J. Am. Chem. Soc.* **1996**, *118*, 9932–9940.
[341] F. Proutiere, F. Schoenebeck, *Angew. Chem. Int. Ed.* **2011**, *50*, 8192–8195.
[342] P. Hofmann, H. Heiss, P. Neiteler, G. Müller, J. Lachmann, *Angew. Chem. Int. Ed.* **1990**, *29*, 880–882.
[343] B. L. Tjelta, P. B. Armentrout, *J. Am. Chem. Soc.* **1996**, *118*, 9652–9660.
[344] M. Reinhold, J. McGrady, R. N. Perutz, *J. Am. Chem. Soc.* **2004**, *126*, 5268–5276.
[345] C. Y. Legault, Y. Garcia, C. A. Merlic, K. N. Houk, *J. Am. Chem. Soc.* **2007**, *129*, 12664–12665.
[346] J. Guihaume, E. Clot, O. Eisenstein, R. N. Perutz, *Dalton Trans.* **2010**, *39*, 10510–10519.
[347] F. Schoenebeck, K. N. Houk, *J. Am. Chem. Soc.* **2010**, *132*, 2496–2497.
[348] A. Petit, J. Flygare, A. T. Miller, G. Winkel, D. H. Ess, *Org. Lett.* **2012**, *14*, 3680–3683.
[349] P. E. Gormisky, M. C. White, *J. Am. Chem. Soc.* **2013**, *135*, 14052–14055.
[350] A. G. Green, P. Liu, C. A. Merlic, K. N. Houk, *J. Am. Chem. Soc.* **2014**, *136*, 4575–4583.
[351] H. Umeyama, K. Kitaura, K. Morokuma, *Chem. Phys. Lett.* **1975**, *36*, 11–15.
[352] G. A. Landrum, N. Goldberg, R. Hoffmann, *J. Chem. Soc., Dalton Trans.* **1997**, 3605–3613.
[353] M. Swart, F. M. Bickelhaupt, *J. Chem. Theory Comput.* **2006**, *2*, 281–287.
[354] R. J. Mulder, C. Fonseca Guerra, F. M. Bickelhaupt, *J. Phys. Chem. A* **2010**, *114*, 7604–7608.
[355] J. M. Ruiz, R. J. Mulder, C. Fonseca Guerra, F. M. Bickelhaupt, *J. Comput. Chem.* **2011**, *32*, 681–688.
[356] W.-J. van Zeist, Y. Ren, F. M. Bickelhaupt, *Sci. China Chem.* **2010**, *53*, 210–215.
[357] F. M. Bickelhaupt, H. L. Hermann, G. Boche, *Angew. Chem. Int. Ed.* **2006**, *45*, 823–826.
[358] F. M. Bickelhaupt, M. Solà, C. Fonseca Guerra, *J. Chem. Theory Comput.* **2006**, *2*, 965–980.
[359] F. M. Bickelhaupt, M. Solà, C. Fonseca Guerra, *Faraday Discuss.* **2007**, *135*, 451–468.
[360] S. Scheiner, *Int. J. Quantum Chem.* **2013**, *113*, 1609–1620.
[361] G. Gilli, F. Bellucci, V. Ferretti, V. Bertolasi, *J. Am. Chem. Soc.* **1989**, *111*, 1023–1028.
[362] C. L. Hawkins, M. J. Davies, *Chem. Res. Toxicol.* **2001**, *14*, 1071–1081.
[363] J. P. Gould, J. T. Richards, M. G. Miles, *Water Res.* **1984**, *18*, 991–999.
[364] A. Ohkubo, Y. Noma, K. Aoki, H. Tsunoda, K. Seio, M. Sekine, *J. Org. Chem.* **2009**, *74*, 2817–2823.
[365] Y. Kawai, Y. Matsui, H. Kondo, H. Morinaga, K. Uchida, N. Miyoshi, Y. Nakamura, T. Osawa, *Chem. Res. Toxicol.* **2008**, *21*, 1407–1414.
[366] M. Ikehara, Y. Ogiso, T. Maruyama, *Chem. Pharm. Bull.* **1977**, *25*, 575–578.
[367] R. D. Parra, *Comp. Theor. Chem.* **2012**, *998*, 183–192.
[368] S. J. Grabowski, E. Bilewicz, *Chem. Phys. Lett.* **2006**, *427*, 51–55.
[369] I. Alkorta, F. Blanco, J. Elguero, *Struct. Chem.* **2009**, *20*, 63–71.
[370] I. Alkorta, F. Blanco, P. M. Deyà, J. Elguero, C. Estarellas, A. Frontera, D. Quiñonero, *Theor. Chem. Acc.* **2009**, *126*, 1–14.
[371] J. George, V. L. Deringer, R. Dronskowski, *J. Phys. Chem. A* **2014**, *118*, 3193–3200.
[372] S. A. C. McDowell, *Chem. Phys. Lett.* **2014**, *598*, 1–4.
[373] M. Domagała, M. Palusiak, *Comp. Theor. Chem.* **2014**, *1027*, 173–178.
[374] X. C. Yan, P. Schyman, W. L. Jorgensen, *J. Phys. Chem. A* **2014**, *118*, 2820–2826.
[375] L. Albrecht, R. J. Boyd, O. Mó, M. Yáñez, *J. Phys. Chem. A* **2014**, 4205–4213.
[376] A. J. Parker, J. Stewart, K. J. Donald, C. A. Parish, *J. Am. Chem. Soc.* **2012**, *134*, 5165–5172.

13 Acknowledgements

First and foremost, I would like to express my gratitude to Matthias, for giving me the opportunity to perform research in a pleasant, and highly skilled environment. You gave me plenty of freedom within the broadly sketched lines of my projects, guiding me when needed and providing crucial insights and suggestions along the way. I always enjoyed discussing results with you, although it was at times frustrating to be forced to not only understand all the results in detail, but also provide a decent, yet elegant explanation. I look forward to continue our collaboration with the few plans that we still have left.

Célia, you were never officially involved in my PhD trajectory, but made a significant contribution with numerous small tips, bits of advice and, ultimately, a fruitful joint project. Thanks for your support, the amusing times when we shared an office, and of course for responding furiously to my politically less correct remarks.

I am grateful to Willem-Jan, Abel and Gabor, who directly worked with me on various projects, but also became good friends. Thanks for all the nice discussions, especially those after working hours. I also like to thank all other collaborators, and those who shared with me their expertise (be it scientific, gastronomic, or otherwise). I thank the entire department and SCM for support on various technical (and bureaucratic) problems and for enjoyable company. I hereby add a special mention for Pier: it is a great honor to have contributed to some of your wonderful compositions, and I hope to do so in the future!

I furthermore want to express my eternal gratitude to my ever-supportive parents and sisters, who, without quite understanding what I was doing, nevertheless shared wholeheartedly in the experience. I take great comfort in being part of such a family.

And finally, I thank my friends: those who came, or returned; those who I had to let go, for various reasons; and, perhaps most of all, those who are still with me. I deeply appreciate who you are.

14 List of Publications

1. *Reaction Coordinates and the Transition-Vector Approximation to the IRC*
   W.-J. van Zeist, A. H. Koers, L. P. Wolters, F. M. Bickelhaupt
   J. Chem. Theory Comput. **2008**, *4*, 920–928
   DOI: 10.1021/ct700214v

2. *Alkali-Metal-Supported Bismuth Polyhedra – Principles and Theoretical Studies*
   K. Yu. Monakhov, G. Linti, L. P. Wolters, F. M. Bickelhaupt
   Inorg. Chem. **2011**, *50*, 5755–5762
   DOI: 10.1021/ic200596c

3. *Halogen Bonding versus Hydrogen Bonding: A Molecular Orbital Perspective*
   L. P. Wolters, F. M. Bickelhaupt
   ChemistryOpen **2012**, *1*, 96–105
   DOI: 10.1002/open.201100015

4. *Nonlinear d^{10}-ML_2 Transition Metal Complexes*
   L. P. Wolters, F. M. Bickelhaupt
   ChemistryOpen **2013**, *2*, 106–114
   DOI: 10.1002/open.201300009

5. *In Silico Design of Heteroaromatic Half-Sandwich Rh^I Catalysts for Acetylene [2+2+2] Cyclotrimerization: Evidence of a Reverse Indenyl Effect*
   L. Orian, L. P. Wolters, F. M. Bickelhaupt
   Chem. Eur. J. **2013**, *19*, 13337–13347
   DOI: 10.1002/chem.201301990

6. *Understanding E2 versus S_N2 Competition under Acidic and Basic Conditions*
   L. P. Wolters, Y. Ren, F. M. Bickelhaupt
   ChemistryOpen **2014**, *3*, 29–36
   DOI: 10.1002/open.201300043

7. *The Many Faces of Halogen Bonding: A Review of Theoretical Models and Methods*
   L. P. Wolters, P. Schyman, M. J. Pavan, W. L. Jorgensen, F. M. Bickelhaupt, S. Kozuch
   WIREs Comput. Mol. Sci. **2014**, *4*, 523–540
   DOI: 10.1002/wcms.1189

8. *d Regime, s Regime and Intrinsic Bite-Angle Flexibility: New Concepts for Designing d^{10}-ML_n Catalysts*
   L. P. Wolters, W.-J. van Zeist, F. M. Bickelhaupt
   Chem. Eur. J. **2014**, *20*, 11370–11381
   DOI: 10.1002/chem.201403237

9. *Controlling the Oxidative Addition of Aryl Halides to Au(I)*
   I. Fernández, L. P. Wolters, F. M. Bickelhaupt
   J. Comput. Chem. **2014**, *35*, 2140–2145
   DOI: 10.1002/jcc.23734

10. *Covalency in Resonance-Assisted Halogen Bonds Demonstrated with Cooperativity in N-Halo-Guanine Quartets*
    L. P. Wolters, N. W. G. Smits, C. Fonseca Guerra
    Phys. Chem. Chem. Phys. **2015**, *17*, 1585–1592
    DOI: 10.1039/c4cp03740e

11. *The Activation Strain Model & Molecular Orbital Theory*
    L. P. Wolters, F. M. Bickelhaupt
    WIREs Comput. Mol. Sci. **2015**, *5*, 323–343
    DOI: 10.1002/wcms.1221

12. *Selective C–H and C–C Bond Activation: Electronic Regimes as a Tool for Designing d^{10} ML_n Catalysts*
    L. P. Wolters, F. M. Bickelhaupt
    Chem. Asian J. **2015**, *5*, 2272–2282
    DOI: 10.1002/asia.201500368

13. *Role of Steric Attraction and Bite-Angle Flexibility in Metal-Mediated C–H Bond Activation*
    L. P. Wolters, R. Koekkoek, F. M. Bickelhaupt
    ACS Catal. **2015**, *5*, 5766–5775
    DOI: 10.1021/acscatal.5b01354

14. *d^{10}-ML_2 Complexes: Structure, Bonding, and Catalytic Activity*
    L. P. Wolters, F. M. Bickelhaupt
    In *Structure and Bonding* (Eds.: O. Eisenstein, S. Macgregor), Springer, Berlin, **2016**
    DOI: 10.1007/430_2014_14